HUNTING FOR SUPERSYMMETRY AND DARK MATTER AT THE ELECTROWEAK SCALE

By

SEBASTIAN MACALUSO

A dissertation submitted to the

School of Graduate Studies

Rutgers, The State University of New Jersey

In partial fulfillment of the requirements

For the degree of

Doctor of Philosophy

Graduate Program in Physics and Astronomy

Written under the direction of

David Shih

And approved by

_____

_____

_____

_____

_____

New Brunswick, New Jersey

October, 2018

ABSTRACT OF THE DISSERTATION

Hunting for Supersymmetry and Dark Matter at the Electroweak Scale

By SEBASTIAN MACALUSO

Dissertation Director:

Professor David Shih

In this thesis, we study models of physics beyond the Standard Model (SM) at the electroweak scale and their phenomenology, motivated by naturalness and the nature of dark matter. Moreover, we introduce analyses and techniques relevant in searches at the Large Hadron Collider (LHC). We start by applying computer vision with deep learning to build a boosted top jets tagger at the LHC that outperforms previous state-of-the-art classifiers by a factor of $\sim$ 2–3 or more in background rejection, over a wide range of tagging efficiencies. Next, we define a cut and count based analysis for supersymmetric top quarks at LHC Run II capable of probing the line in the mass plane where there is just enough phase space to produce an on-shell top quark from the stop decay. We also implement a comprehensive reinterpretation of the 13 TeV ATLAS and CMS searches with the first $\sim$ 15 fb^{-1} of data and derive constraints on various simplified models of natural supersymmetry. We discuss how these constraints affect the fine-tuning of the electroweak scale. Finally, we show how a simple extension of the minimal supersymmetric SM, consisting of a dark sector, can explain the dark matter relic abundance and the Higgs mass in a natural way.

Preface

This thesis is the result of my graduate studies at the New High Energy Theory Center at Rutgers University, under the direction of professor David Shih. This thesis is organized as follows: chapter one contains a brief review of background topics related to the work developed in this thesis, such as the hierarchy problem and thermal dark matter. Chapters two, three, four and five consist of research on the subject that I performed with my collaborators under the supervision of my advisor. Finally, chapter six contains conclusions and outlook. All published papers can be conveniently accessed at http://arxiv.org/.

Acknowledgements

My journey through graduate school at the New High Energy Theory Center (NHETC) at Rutgers University has been an incredible learning experience about physics and life in general. I am grateful to many people who have helped and supported me over the years and without them this process would not have been possible. In the first place, I am deeply grateful to my advisor, David Shih. I was fortunate to work on mainstream and really interesting topics, thanks to David. Most of the physics I learned during graduate school was thanks to David and this happened in different ways, many times directly from him and others from working on problems and ideas during our projects. He showed me how to work rigorously and always pay attention to details. Additionally, I would like to point out that David always kept his office door open for me, always had time to answer my questions and always carefully listened to my ideas and contributions during discussions. I am extremely thankful to him for sharing his ideas and projects with me, for his advice, for the large amount of time he has dedicated to teaching and discussing with me during all these years, and for supporting me every time I wanted to try some new approach or direction. The latter resulted in implementing multiple new packages or writing our own code during our projects together, among other things. Finally, I am very grateful for David's patience and support at moments when things did not go as planned.

At various times throughout my studies I had the opportunity to learn from other mentors in addition to David. I am really grateful to Matt Buckley for the physics I learned during our discussions and collaboration, for sharing his ideas with me and for his continuous support and advice throughout all my time at Rutgers. I am also particularly thankful to Scott Thomas for the physics discussions we had, especially in the early stages of my graduate studies and for pointing me in the right direction when I asked for help with a physics problem. I also want to thank Brock Tweedie and Angelo Monteux. I had the

fortune to collaborate with Brock during my first project and I am immensely grateful for his patience and guidance during my learning process and for teaching me how to design and perform a collider physics analysis. I also learned from Angelo and was lucky to have multiple discussions with him and a really fruitful collaboration. Moreover, I am grateful to Michael Park for his guidance during my first project and my initial attempts to use the relevant computational packages. Finally, I would like to thank Aria Basirnia for his support as well as all the physics I learned from him from our collaboration and multiple discussions during the time we spent together at Rutgers.

I want to thank Eva Halkiadakis and John Paul Chou for physics discussions and helping me understand physics at LHC. I am also thankful to Alejandro Gomez Espinosa, Savvas Kyriacou, Marco Farina, Anthony DiFranzo, Pietro Longhi, Daniel Brennan, and especially Daniel Egana-Ugrinovic, Pouya Asadi and David Feld for all our discussions, collaborations, support and friendship.

Moreover, I want to thank my Licenciatura thesis advisor Martin Schvellinger. He guided me in my early stages and spent a lot of time teaching me physics, and shared his ideas and enthusiasm for physics with me. His continuous support has been particularly important for my career in physics.

I am very grateful for the constant support provided by the NHETC all these years and also by the Physics Department during my initial years at Rutgers. In addition, I am thankful for the funding for summer schools and trips; they were very important for my academic training. In particular, I am grateful to Daniel Friedan and Ronald Gilman for making sure I had a successful time during my graduate studies. I am also thankful to Shirley Hinds, Diane Soyak and Christina Pettola for the many times they helped me solve an administrative problem.

I have been fortunate to have some wonderful friends during this time. Among them, I am especially grateful to Adrian, Kostas, and Juani who supported me in numerous ways during all these years.

Last but not least, my deepest gratitude to my family, who had to live with the consequences of my decision to pursue my studies in a distant place from home. Thanks for the unconditional and constant support.

Dedication

To my parents,
for the unconditional and constant support

Table of Contents

Chapter 1

Introduction

The discovery of a new boson at a mass around 125 GeV at the Large Hadron Collider (LHC) [1, 2] announced on July 4th, 2012, opened a new era leading to the completion of the Standard Model (SM) of particle physics. The SM has been extremely successful in describing particles and their fundamental interactions, and it has survived decades of experiments in particle physics. The SM in principle could be extrapolated up to scales where gravity would become strong at $M_{pl} \approx 10^{18}\,\text{GeV}$. However, there are good reasons to expect to find new physics at the electroweak (EW) scale $(0.1 - 1\,\text{TeV})$.

There are two problems that are not addressed by the SM and have been some of the main areas of research in the field in the last few decades. They are the hierarchy problem and the nature of dark matter (DM) and both strongly suggest the existence of physics beyond the SM around the EW scale. Given the importance and great deal of interest in these problems, in this thesis we explore and propose viable solutions to them. In particular, we study the LHC phenomenology of some of the most promising models of new physics at the EW scale, as well as propose a new model of dark matter that solves both problems and will be fully probed by current and next generation of DM direct detection experiments [3–7]. Also, we propose an analysis that closes an important gap in searches for supersymmetric top quarks (stops) at LHC, contributing to cover the remaining available parameter space of natural supersymmetry. This type of search was implemented by the ATLAS collaboration in [8, 9], obtaining results as expected. Moreover, we introduce machine learning based techniques that significantly outperform previous state-of-the-art classifiers for boosted top

quark jets at LHC. [1]

In this chapter we introduce some topics that constitute background related to the work developed in this thesis. Even though there are detailed reviews on DM [10–13] and the hierarchy problem (for a review and original references, see e.g. [14]), we consider appropriate to briefly describe them. We start by describing the LHC and the CMS detector in section 1.1, given that we present a classification method for jets at the LHC in chapter 2 and that the phenomenology of all the models discussed in this work involves LHC signatures. Next we talk about the Higgs boson and its discovery at LHC in section 1.1.2. We also discuss the top quark phenomenology and its relevance in searches for new physics at LHC in section 1.1.3. In most of this thesis, the phenomenology that we study contains top quark jets.[2] We introduce the hierarchy problem and discuss the implications of a 125 GeV Higgs mass in the minimal supersymetric SM (MSSM) in section 1.2. Finally, we review dark matter as a thermal relic and the viability of thermal neutralino dark matter in section 1.3.

1.1 The Large Hadron Collider

The Large Hadron Collider comprises a 26.7 km tunnel, previously constructed for the Large Electron-Positron Collider (LEP), that lies between 45 m and 170 m underground [15, 16] and is located in the CERN accelerator complex near Geneva, Switzerland. It is the most energetic collider ever built, designed to collide two beams of protons or ions moving in opposite directions. It is expected to achieve a proton-proton center-of-mass energy of 14 TeV, with a maximum current (June 2018) center-of-mass energy of 13 TeV. We consider an event as each time that there is an interaction within a bunch crossing. The total number of events is given by $N_{\text{events}} = L\,\sigma$ where L is the integrated luminosity and σ the cross section.

There are four different points around the LHC beam where the two beams intersect, and four different detectors are built at each interaction point around the ring: ATLAS [17] and CMS [18] for high luminosity proton-proton collisions, LHCb [19] for B-physics and

[1] In section 1.1 we briefly describe jets and how their constituents are reconstructed at the CMS experiment at LHC.

[2] As already mentioned, we design a classifier for boosted top quark jets in chapter 2 and we consider models of new physics that typically involve signatures with top quarks in chapters 3 and 4.

ALICE [20] for ion experiments. Given that in chapter 2 we based our detector simulations on CMS, we will briefly describe this general-purpose detector (the other one being ATLAS).

1.1.1 CMS experiment

The Compact Muon Solenoid (CMS) [21] is built of detectors as cylindrical layers around the point were the beams intersect. It has a total diameter of 15 m, and an overall length of 28.7 m in a cavern located 100 m underground. The central feature of the CMS detector is its superconducting solenoid, with an internal diameter of 6 m and a magnetic field of 3.8 T. A tracker, an electromagnetic calorimeter (ECAL), and a hadron calorimeter (HCAL) are located within the volume of the solenoid. Outside, gas-ionization detectors measure the interactions of muons. The central region is covered by the barrel detector, followed by the endcap detector.

A diagrammatic description of the different components of the CMS detector and the interactions of different particles with them is shown in fig.1.1. These components are described as follows:

- The tracking system finds the position of charged particles in different layers to reconstruct their trajectories. It allows the recognition of long-lived heavy-flavor hadron decays by providing secondary vertex identification.
- The ECAL accurately measures the energy of electrons and photons.
- The HCAL measures the energy deposits of hadrons. Its dense material stops heavy particles that go through the ECAL.
- The muon system is made out of gas that is ionized by muons traveling through the detector.

Starting from the interaction point, we can see in fig. 1.1 that the trajectories (tracks) and the origin (vertices) of charged particles are reconstructed from their interaction with the layers of the tracking system. The particles tracks are bent by the magnetic field and the momenta and charge are measured from the tracks curvature. Electrons and photons are stopped by the ECAL, and their energy and direction are measured from the deposits

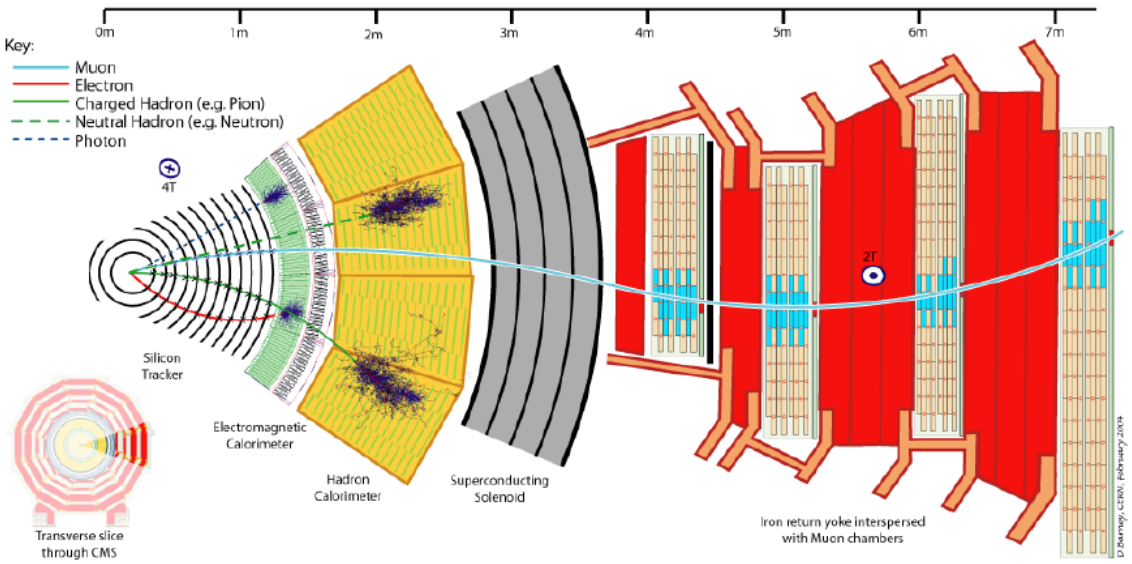

Figure 1.1: Transverse slice of the CMS detector that shows how the different particles interact within the detector [22].

in the ECAL towers. Charged and neutral hadrons leave energy deposits in the ECAL but are completely absorbed at the HCAL towers. Finally, muons go through most of the detector leaving few traces in the calorimeters. Their momenta is estimated from hits left at the tracker and muon system. Regarding neutrinos, they go through the detector without interacting and they are considered missing energy, which is calculated from the imbalance in transverse momenta in an event.

Traditionally, objects are reconstructed by linking the signatures in the different sub-detectors. As already mentioned, electrons and photons are mainly reconstructed from deposits in the ECAL, with electrons also leaving signatures in the tracker. Jets (a collimated spray of energetic charged and neutral hadrons) are identified from energy deposits in the ECAL and HCAL (and tracking hits from the charged hadrons). In particular, b-quark jets are recognized from secondary vertex reconstruction in the tracker. CMS reconstructs each object in an event based on the correlation of the information from the sub-detectors, employing the particle flow algorithm [23].

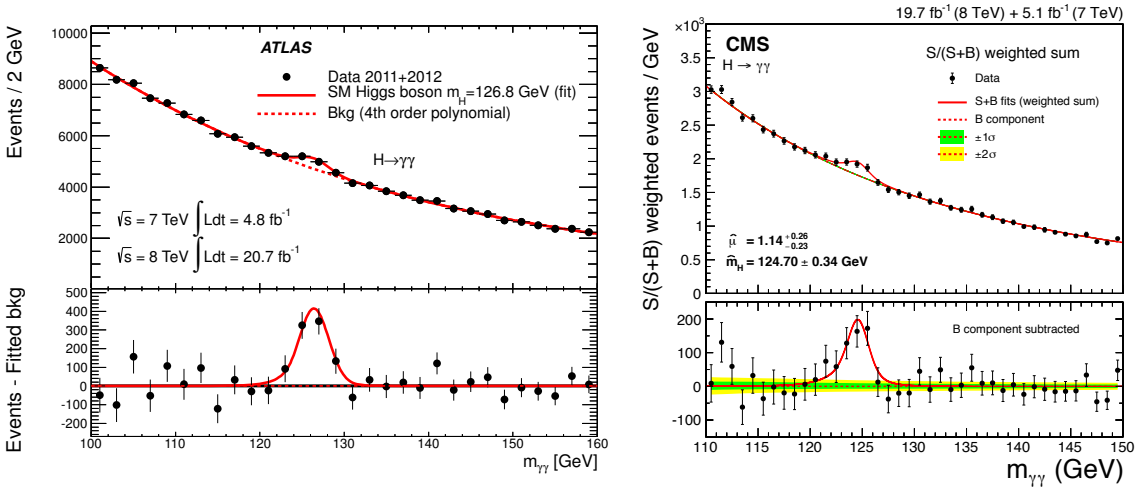

Figure 1.2: Higgs discovery diphoton decay channel observed at the ATLAS (left) [28], and CMS (right) [29] detectors.

1.1.2 Higgs boson and its discovery at LHC

ATLAS [2] and CMS [1] announced the discovery of a new boson with a mass around 125 GeV on July 4th, 2012. The main discovery decay channels where $H \to \gamma\gamma$, $H \to ZZ \to 4\ell$ and $H \to W^+W^- \to 2\ell + 2\nu$ (see fig. 1.2, and 1.3). Until now (June 2018) this new particle properties are in agreement with the SM Higgs boson [24, 25] (for recent reviews on Higgs physics, see e.g. [26, 27]).

Before the Higgs boson was discovered, searches at LEP had implied $m_h \geq 114$ GeV [31], and a range around (160, 170) GeV had been excluded by Tevatron [32]. From a combined analysis of all the information available in 2011, an estimate of $m_h = (125 \pm 10)$ GeV was obtained in [33]. An important motivation for the existence of the Higgs is that in the SM without the Higgs, the scattering amplitudes of the W and Z bosons grow with the square of the center-of-mass energy. This implies that unitarity would be lost at energies above the TeV scale.

The dominant production channel for a SM 125 GeV Higgs at a proton-proton collider is the gluon fusion mechanism $gg \to h$ (ggF), with loops of top quarks giving the main contribution.[3] Subleading processes include the vector boson fusion (VBF) $qq \to hqq$,

[3]This production channel will have an important contribution to the mono(h, Z)+MET cross sections at LHC Run II in the model we propose in chapter 5.

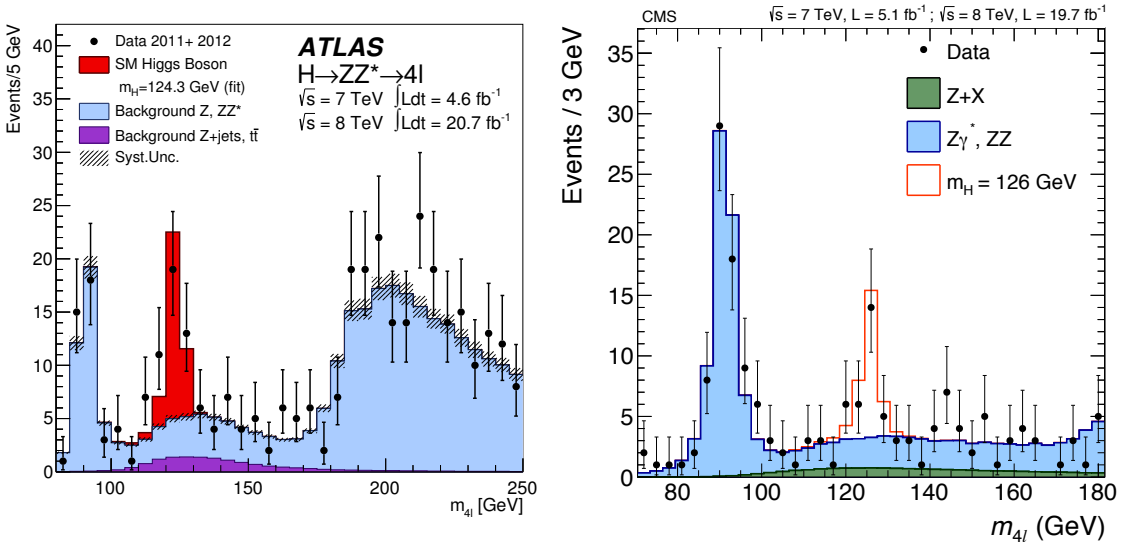

Figure 1.3: Higgs discovery decay channel to four leptons observed at the ATLAS (left) [28], and CMS (right) [30] detectors.

associated production with a gauge boson (HV) $qq \to hV$ with $V = W, Z$ and associated production with a pair of top/antitop quarks $pp \to tth$ and single top.

Regarding decays, as the Higgs couples stronger to heavier particles, we would expect it to decay with a greater ratio to the heaviest particles that are kinematically accessible.[4] The measured value of the 125 GeV Higgs boson mass opens many decay modes that are accessible at LHC. The main decay is to $b\bar{b}$, followed by WW^* as shown in fig. 1.4 [35]. Though the loop induced decay to $\gamma\gamma$ has a small branching ratio, it constitutes a clean channel making this decay one of the most important ones for the Higgs discovery. Thus, the most accurate channels to measure the mass are $H \to \gamma\gamma$ and $H \to ZZ \to 4\ell$. The values obtained are shown in fig. 1.5, giving a combined ATLAS and CMS measurement of $m_h = (125.09 \pm 0.24)$ GeV.[5]

[4]The SM Higgs couplings to fermions (W, Z) are directly (quadratically) proportional to their masses. This property is in excellent agreement with the fit of the data collected at LHC Run I shown in fig. 13 of [34].

[5]This current value of the Higgs mass leads to a metastable solution of the EW vacuum.

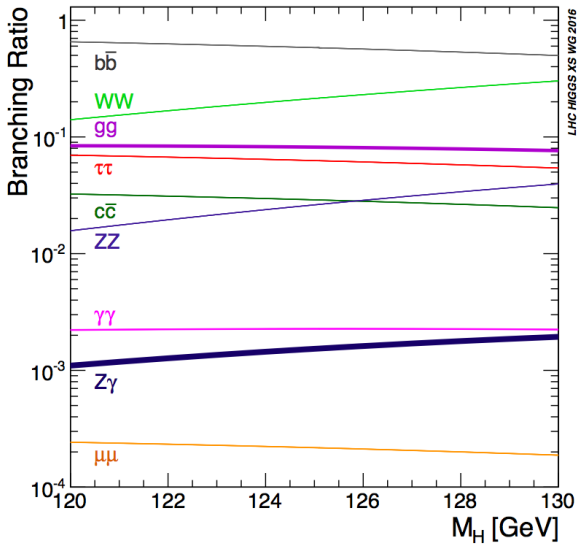

Figure 1.4: Higgs boson branching ratios including QCD and EW corrections for the mass range around 125 GeV. This plot was taken from [35].

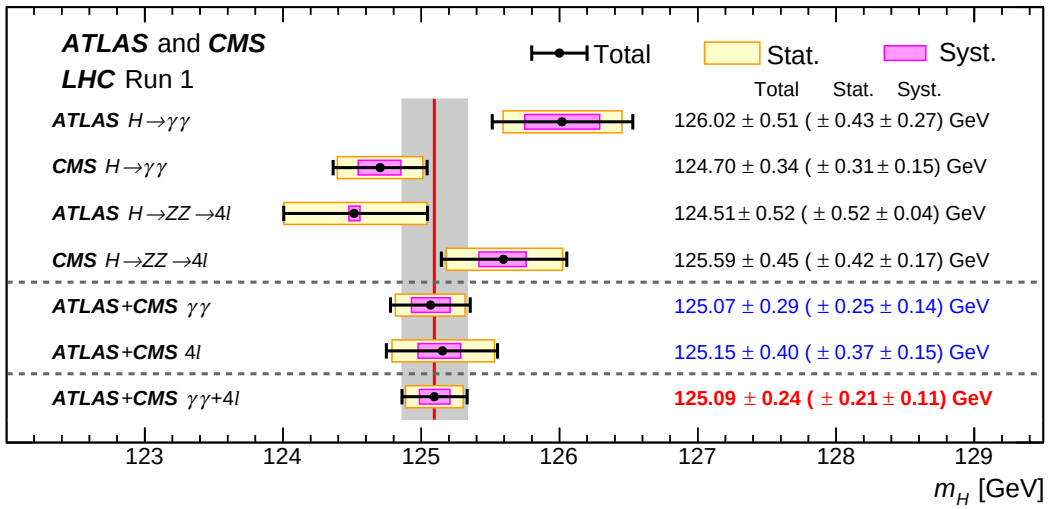

Figure 1.5: Higgs boson mass measurements from the individual analyses of ATLAS and CMS, and from the combined analysis [36].

1.1.3 Top quarks and their collider phenomenology

The heaviest known elementary particle is the top quark, first observed in 1995 at the Tevatron proton-antiproton collider at Fermilab [37, 38]. It has been one of the main objects of interest in high energy physics, given that its large mass implies that it has a sizable coupling to the EW symmetry breaking sector. Measurements confirmed that this

new particle behaves as expected for the predictions of the SM top quark (for recent reviews about top quark physics, see e.g. [39–41]).

The discovery of the Higgs boson, did not answer questions related to the nature of the top quark. Why is the top quark so much heavier than all the other quarks? Why is its mass at the EW scale? Does the top quark play a key role in the mechanism of EW symmetry breaking? If we extrapolate the Standard Model up to the Planck scale, why do the Higgs and the top have masses in a range of values that allow the SM to be stable up to high energies, predicting a metastable state for the Universe? The stability of the electroweak vacuum depends on the top mass value; with the current measured value resulting in a metastable case. Moreover, the large Yukawa coupling y_t between the top and the Higgs is responsible for the main contribution to the running of the quadratic term in the Higgs potential, leading to EW symmetry breaking.

As we will review in section 1.2, the main contribution to one-loop radiative corrections to the Higgs mass comes from loops with top quarks, as a result of the large y_t. So, if there is no new physics up to the Planck scale, unexplained cancellations to many orders are required among the different contributions to the Higgs mass to get a 125 GeV Higgs, which is known as the hierarchy problem. Thus, as the top quark plays an important role in this problem, it may also point towards new physics that solves it. For instance, supersymmetry (SUSY) is one of the main models that could solve the hierarchy problem, where loops of supersymmetric top quarks cancel the top quarks contribution. However, given that the stop quark mass is greater, top quark loops make it possible to go from a tree level bound on the Higgs mass determined by the Z boson mass to a 125 GeV value in the Minimal Supersymmetric SM (MSSM). In this scenario, SUSY phenomenology typically involves signatures with top quarks coming from SUSY particles as they cascade decay down to lighter particles. As a result, there are very good motivations to study top quark physics, couplings, its production and decay channels in detail. Also, it is important to get a direct measurement of the interaction y_t between the top quark and the Higgs boson, for instance from $t\bar{t}h$ production, which is expected to reach a precision of $\mathcal{O}(10\%)$ by the end of the High Luminosity-LHC [42].

The dominant top quark production mechanism at LHC is top pair production $t\bar{t}$. The

main contribution comes from QCD, where at leading order in α_s we have $q\bar{q} \to t\bar{t}$ and $gg \to t\bar{t}$ processes. A subleading production is given by single-top, with the main contribution from W boson exchange. In fig. 1.6 we show LHC and Tevatron top quark pair production cross sections compared with theory predictions with an excellent agreement [43].

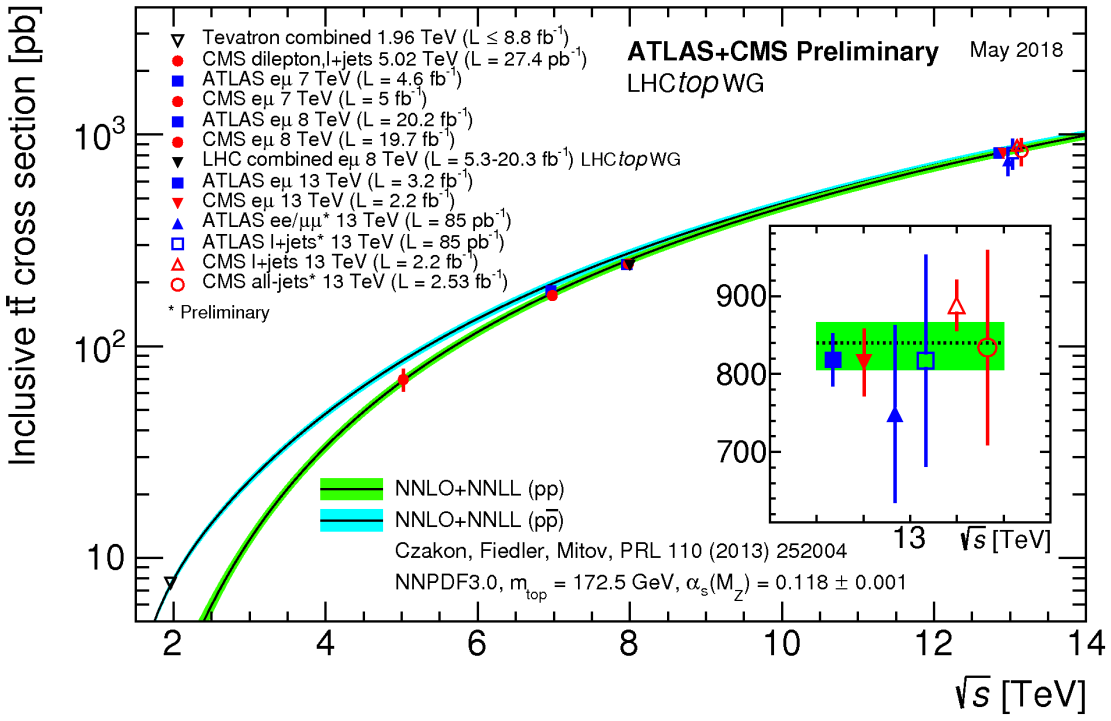

Figure 1.6: LHC and Tevatron measurements of the top-pair production cross-section as a function of the centre-of-mass energy compared to theory predictions. The theory prediction includes uncertainties due to renormalisation and factorization scale, parton density functions and the strong coupling. This plot was taken from [43].

The top quark mass can be reconstructed from collecting jets and leptons from its decay. In fig. 1.7 we show the measured values for the top mass by CMS and Tevatron. Having a mass above the $W\,b$ threshold, and for CKM matrix elements $|V_{tb}| \gg |V_{td}|, |V_{ts}|$, the decay width of the top quark is largely due to the two body channel $t \to W\,b$. As a result of the top mass being much greater than the $W\,b$ threshold, the top width of 1.35 GeV is big enough (lifetime of $\sim 10^{-24}$ s is short enough) for the top to decay before hadronization. Thus, the signature that a top quark leaves in the CMS detector (as described in fig. 1.1) typically includes a secondary vertex in the tracker from the (long-lived) b quark coming from the top decay. Then, if the W decays leptonically to a lepton and a neutrino, the

signature will generally give an isolated lepton, a jet coming from the b quark decay and missing energy (from the neutrino). On the other hand, if the W decays hadronically, there will be tracks left by the charged hadrons coming from the W (and b quark) decay, and energy deposits in the ECAL and HCAL (where hadrons are stopped) coming from the jets made out of the neutral and charged hadrons. Usually, the decay products of the hadronic decay of the top quark are reconstructed as three jets, but for boosted tops they can get collimated into two or even one *fat* jet. In particular, in chapter 2 we propose a machine learning based method to identify boosted top quark jets that are reconstructed as a single fat jet.

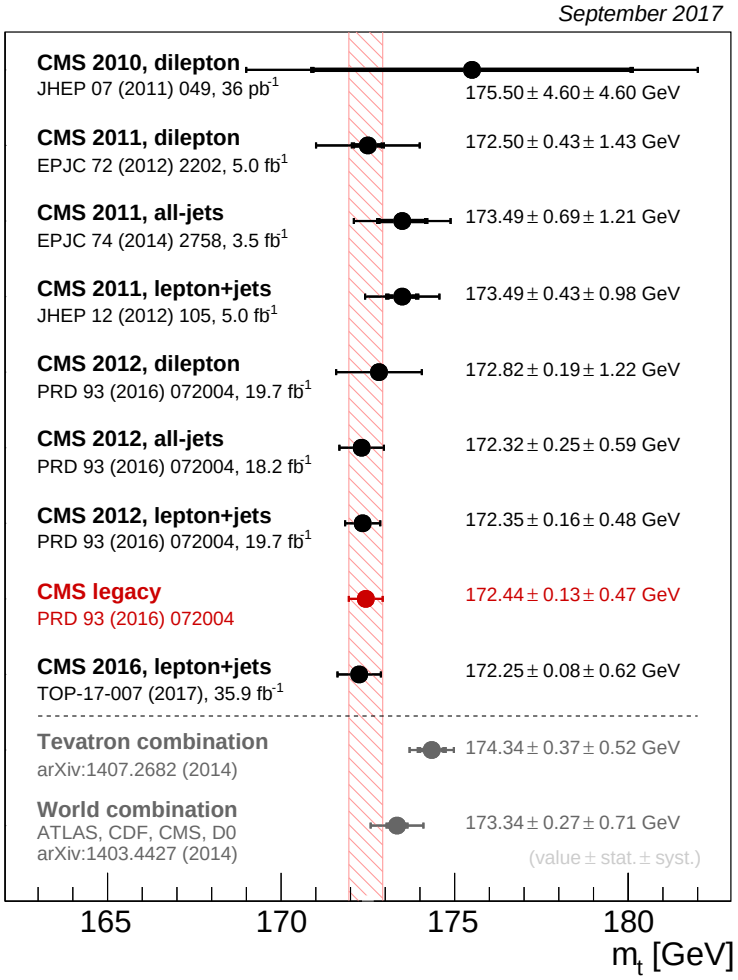

Figure 1.7: Summary of Run-I CMS top mass measurements, their combination, and the world and Tevatron combinations. This plot was taken from [44].

1.2 Hierarchy Problem

Now that we know there is a Higgs boson, there is a hierarchy problem. Given that the Higgs boson is a scalar particle, it has sensitivity to the largest particle masses and to the ultraviolet (UV) cutoff in the theory. In particular, the Higgs mass gets contributions from new heavy particles that couple directly or indirectly to the Higgs. This would lead to a large fine tuning to explain the necessary cancellation among the quantum corrections to obtain a Higgs mass many orders of magnitude smaller. This is known as the *hierarchy* or *naturalness problem.*

In the SM the Higgs field is a complex scalar H with tree level potential

$$V_H = \frac{1}{2}m_H^2|H|^2 + \frac{1}{4}\lambda|H|^4 \tag{1.2.1}$$

The hierarchy problem is usually phrased as the quadratic radiative corrections to m_H^2 from loop diagrams and it appears already at one-loop. The main one-loop contribution to the Higgs mass in the SM comes from top quark loops,

$$\delta m_h^2 \sim \frac{y_t^2}{16\pi^2}\Lambda^2 \tag{1.2.2}$$

where y_t is the top quark Yukawa. Here we are parametrizing our ignorance of physics beyond the SM in just one high energy cutoff Λ for the theory.[6] To avoid fine-tuning, we would expect all the contributions to be of the same size of the Higgs mass itself which gives $\Lambda \sim$ TeV. This is a big motivation for physics beyond the SM at the EW scale.

In general, solutions to the hierarchy problem in the SM either lower the expected cutoff Λ or introduce a symmetry to stabilize the Higgs mass up to much higher energy scales. In particular, if we take the scale of underlying UV physics to be near the Planck scale, radiative corrections to the Higgs mass must cancel one another up to one part in $\sim 10^{32}$, which is unnatural. However, if quantum gravity effects become important not much above the EW scale, there would be no hierarchy in the fundamental scales. Models of large extra dimensions solve the hierarchy problem in this way.

[6] These "quadratic divergences" depend on the regularization technique that we use for the loop-integrals. For instance, in dimensional regularization they do not show up. However, there will be terms proportional to the quadratic masses of the heaviest particles in the theory that couple to the Higgs. As a result, quadratic divergences could be interpreted as the sensitivity of the Higgs mass to higher scales.

Another option is to introduce a new fermion-boson symmetry in nature called supersymmetry, that systematically cancels the dangerous contributions to the Higgs mass. Supersymmetry is the most motivated and studied idea to stabilize the Higgs mass and solve the hierarchy problem; with the minimal realization being the Minimal Supersymmetric Standard Model (MSSM). However, as we discuss in section 1.2.1, the Higgs mass at tree level in the MSSM is bounded above by the Z boson mass, which seems to disagree with a 125 GeV Higgs mass.

1.2.1 Higgs mass in the MSSM

In this section we introduce the Higgs sector in the MSSM (for a pedagogical review of supersymmetry and the MSSM, see e.g. [14]). The Higgs sector is more complicated in the MSSM than in the SM, as now we have two complex Higgs doublets $H_u = (H_u^+, H_u^0)$ and $H_d = (H_d^0, H_d^-)$. So there are eight real scalar degrees of freedom that mix to go from the gauge eigenstates to the Higgs mass eigenstates, obtaining the scalar fields $(h^0, H^0, A^0, H^\pm)$ as well as three Goldstone bosons $(G^\pm, G^0)$. Thus, we have the light and heavy CP-even scalars h^0 and H^0, one CP-odd scalar A^0 and the charged scalars $H^\pm$.

The potential of the neutral Higgs fields in the MSSM is

$$\begin{aligned} V =&(|\mu|^2 + m_{H_u}^2)|H_u^0|^2 + (|\mu|^2 + m_{H_d}^2)|H_d^0|^2 - (b\, H_u^0 H_d^0 + c.c.) \\ &+ \frac{1}{8}(g^2 + g'^2)(|H_u^0|^2 - |H_d^0|^2)^2 \end{aligned} \tag{1.2.3}$$

where μ is the supersymmetric version of the Higgs mass in the SM, and m_{H_u}, m_{H_d} and b come from soft supersymmetry breaking terms. The ratio of the vacuum expectation values (VEVs) can be written as $\tan\beta := \frac{\langle H_u^0 \rangle}{\langle H_d^0 \rangle} = \frac{v_u}{v_d}$. If we find the equations for the minimum, $\partial V/\partial H_u^0 = \partial V/\partial H_d^0 = 0$ we obtain in the large $\tan\beta$ limit, which is motivated as a way to saturate the tree-level Higgs mass as we will see in (1.2.5),

$$m_Z^2 = -2(m_{H_u}^2 + |\mu|^2) + \frac{2}{\tan^2\beta}(m_{H_d}^2 - m_{H_u}^2) + \mathcal{O}(1/\tan^4\beta) \tag{1.2.4}$$

We can see that unless the RHS terms of (1.2.4) have some fine tuned cancelations, they should all be about the same order of magnitude as m_Z^2. However, μ is a supersymmetry respecting parameter coming from the superpotential, while m_{H_u} and m_{H_d} are supersymmetry breaking parameters. So, in principle there is no reason why they should be at the

same scale and this is usually referred to as the "μ problem". We could estimate how fine-tuned the model is from the cancellations needed in (1.2.4).

In order to calculate the Higgs mass in the MSSM, we go to the mass eigenstates basis, where the mass of the light scalar h^0 is bounded above by the Z boson mass and at tree-level is given by

$$m_{h^0} \lesssim m_Z |\cos(2\beta)| \tag{1.2.5}$$

Motivated by the excellent agreement between the SM Higgs couplings and the data from LHC Run I [34], we will focus on the *decoupling limit* that happens when $m_{A^0} \gg m_Z$. In this limit, we saturate the upper bound in (1.2.5) and h^0 has the same couplings to quarks, leptons and EW gauge bosons as the SM Higgs boson.

A priori, the m_Z upper bound in (1.2.5) would be in disagreement with a 125 GeV Higgs.[7] However, the potential in (1.2.3) is defined above the scale of SUSY breaking in the MSSM and needs to be corrected for the threshold corrections and running below the scale of the superparticle masses. The tree-level equation for $m^2_{h^0}$ gets substantial quantum corrections, with the main contributions typically coming from top and stop loops. After including the dominant one-loop radiative corrections to $m^2_{h^0}$ in the MSSM we obtain

$$m^2_{h^0} \lesssim m^2_Z \cos^2(2\beta) + \frac{3m_t^4}{4\pi^2 v^2}\left[\log\left(\frac{M_S^2}{m_t^2}\right) + \frac{X_t^2}{M_S^2}\left(1 - \frac{X_t^2}{12M_S^2}\right)\right] \tag{1.2.6}$$

where $M_S^2 = m_{\tilde{t}_1} m_{\tilde{t}_2}$ with $m_{\tilde{t}_1}$ and $m_{\tilde{t}_2}$ the masses of the stop mass eigenstates. Also, $X_t = A_t - \mu \cot\beta$, where A_t comes from an additional supersymmetry breaking Higgs-stop-stop interaction. In the large $\tan\beta$ limit, this means that we can achieve the Higgs mass of 125 GeV either by taking M_S much greater than the EW scale or by raising the contributions from the A-terms. The latter implies going to the "maximal mixing" condition given by $A_t \sim \sqrt{6} M_S$ and relaxing the required value of stops mass to $\sim$ TeV. In fig. 1.8 we show the Higgs mass calculated at two loops in the MSSM vs the degenerate SUSY scale M_S for two values of X_t, taken from [45]. We can see that top squark mixing is necessary to get a 125 GeV Higgs mass without multi-TeV stops, though the mixing also contributes to fine tuning (for recent reviews and original references, see e.g. [46, 47]).

[7] Any new model of physics beyond the SM should be in agreement with the measured Higgs mass of (125.09 ± 0.24) GeV.

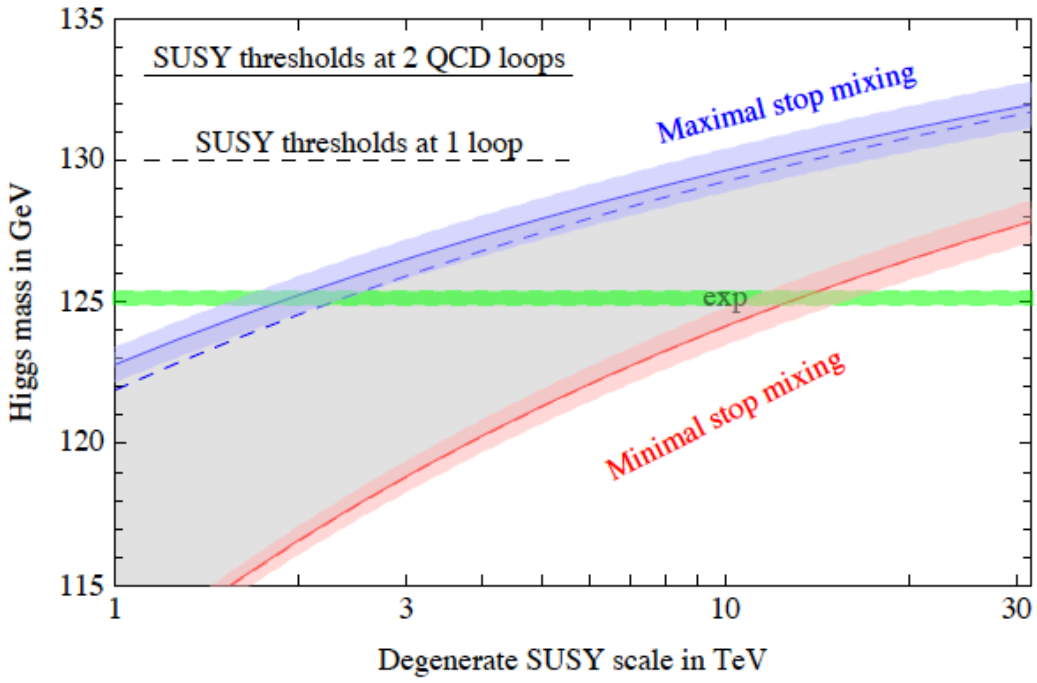

Figure 1.8: The Higgs mass as a function of the SUSY scale, with a degenerate spectrum of superparticles (i.e., all SUSY mass parameters equal to a common mass M_S), and $\tan\beta = 20$. The stop mixing parameter X_t is varied to obtain minimal m_h (red) and maximal m_h (blue). The solid (dashed) lines include (neglect) the effect of the two-loop SUSY-QCD corrections to λ. This plot was taken from [45].

Next, we discuss the degree of fine-tuning in the MSSM to obtain a Higgs of 125 GeV. Typically, $m_{H_u}^2$ is pushed to negative values through RG running which is important to ensure that EW symmetry breaking takes place. However, too large stop masses ($\sim$ 10 TeV or more) make $|m_{H_u}^2|$ take values far from the EW scale. As a result, the parameters of (1.2.4) must be tuned against each other, making the model unnatural. For the tuning calculation, we use the Barbieri-Giudice measure [48],

$$\Delta_{m_h} = \max_i \left| \frac{\partial \ln m_h^2}{\partial \ln M_i^2} \right| \tag{1.2.7}$$

where M_i^2 is a UV squared mass parameter (e.g. μ^2, $m_{Q_3}^2$, $m_{\bar{u}_3}^2$, $m_{H_u}^2$, $m_{H_d}^2$, A_t) defined at the scale Λ. From (1.2.1) we get $m_h^2 = \lambda v^2 = -m_H^2$. We consider the amount of fine-tuning determined by the size of the corrections to the quadratic term in the potential with respect to the Higgs mass. In the MSSM, in the decoupling limit, at large $\tan\beta$, the VEV v is in the H_u direction and we can take $m_H^2 \simeq m_{H_u}^2$. The gluino, stop and Higgsino masses are the most important parameters for fine-tuning. Then, in the leading-log (LL) approximation,

the quadratic sensitivity of the Higgs mass-squared parameter to the higgsino, stop and gluino soft masses arises at tree level, one-loop and two-loops respectively:

- Higgsinos:

$$\delta m_H^2 = |\mu|^2 \tag{1.2.8}$$

- Stops:

$$\delta m_H^2 \sim -\frac{3}{8\pi^2} y_t^2 (m_{Q_3}^2 + m_{\overline{u}_3}^2 + |A_t|^2) \ln \frac{Q}{Q_0} \tag{1.2.9}$$

- Gluinos:

$$\delta m_H^2 \sim -\frac{g_3^2 y_t^2}{4\pi^4} |M_3|^2 \left(\ln \frac{Q}{Q_0} \right)^2 \tag{1.2.10}$$

Here, we identify Q with the messenger scale of SUSY breaking, and Q_0 with the IR scale conventionally taken to be 1 TeV. A number of precision corrections to this LL approximations are studied by my advisor and collaborators in [49]. They introduce a number of improvements, including RGE resummation, two-loop effects, a proper treatment of UV vs. IR masses, and threshold corrections. As a result, they find bounds that can allow for heavier gluinos and stops than previously considered (at a fixed level of tuning).

Now we study the implications on the fine-tuning of the model from the required values of SUSY parameters to get a 125 GeV Higgs. In fig. 1.9 (taken from [50]) we show contours of m_h in the range 124-126 GeV in the $(X_t, m_{\tilde{t}} = m_{Q_3} = m_{\overline{u}_3})$ plane, together with contours of fine-tuning. The fine-tuning contours were obtained by considering only the one-loop LL contribution from (1.2.9). For a 125 GeV Higgs, the smallest viable values give $\Delta_{m_h} \gtrsim 100$ for maximal mixing (for $Q = 10$ TeV) which puts the tuning at the percent level or worse. A possible solution to this problem is to raise the Higgs mass from contributions from a sector beyond the MSSM.[8]

Regarding LHC phenomenology, at Run I of the LHC, ATLAS and CMS collected data from proton-proton collisions for an integrated luminosity of $\sim 5\,\text{fb}^{-1}$ at 7 TeV and $\sim 20\,\text{fb}^{-1}$ at 8 TeV, but only null results were found on SUSY searches. The raise in center-of-mass energy to 13 TeV at LHC Run II, opened new regions of parameter space

[8] We add a dark sector to the MSSM that helps raise the mass of the Higgs in a natural way and gives a thermal dark matter candidate in chapter 5.

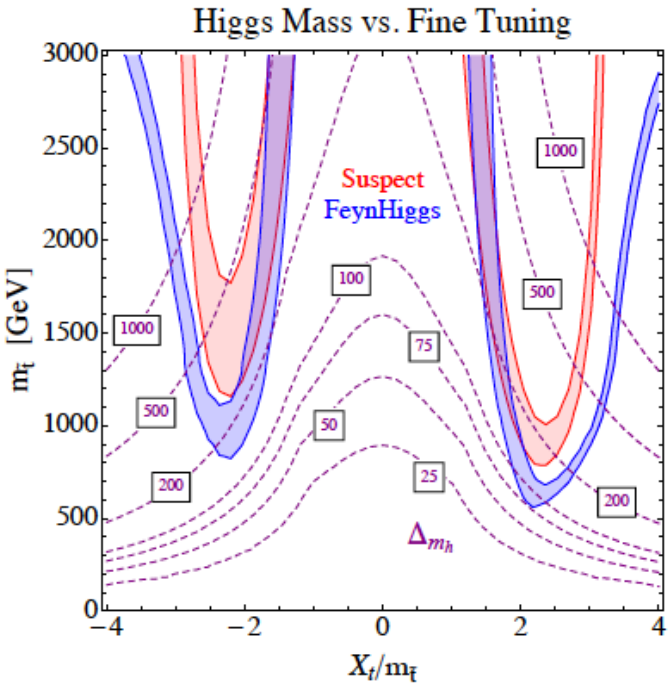

Figure 1.9: Contours of m_h in the MSSM in the $(X_t, m_{\tilde{t}} = m_{Q_3} = m_{\bar{u}_3})$ plane for $\tan\beta = 20$. The red (blue) lines show the result from Suspect [51] (FeynHiggs [52–55]) for m_h in the range 124-126 GeV. Also, contours of fine-tuning of Δ_{m_h} are shown. This plot was taken from [50].

of SUSY models at $\mathcal{O}$(TeV). In particular, in chapter 3 we propose a dedicated search at LHC Run II for supersymmetric top quarks (stops) within the common stop next-to-lightest supersymmetric particle and neutralino lightest supersymmetric particle simplified model. This search extended the coverage to the gap around the line in the mass plane where the phase space from the stop decay to an on-shell top quark is closing off, with S/B ~ 1 and significances often well beyond 5σ. As already mentioned, the ATLAS collaboration performed this type of search obtaining results as expected [8, 9].

There have been many analyses looking for new physics at LHC Run II and most of the latest ones include $\sim 36\,\text{fb}^{-1}$ of integrated luminosity. However, no physics beyond the SM has been found so far (June 2018). These null results have strongly constrained many of the minimal realizations of SUSY at the EW scale while still requiring the models to be natural. Deriving these constraints on various simplified models of natural SUSY from the first ~ 15 fb^{-1} of data has been the subject of study in chapter 4 of this thesis.

1.3 Dark Matter

Multiple observations on astrophysical and cosmological scales indicate that baryonic matter accounts for $\sim 5\%$ whereas dark matter (DM) constitutes $\sim 25\%$ of the content of the Universe (the remaining consists of dark energy). The nature of DM remains one of the primary open questions in physics and searches involve direct and indirect detection experiments as well as searches at particle colliders (for reviews on dark matter, see e.g. [10–13]). The SM of particle physics alone does not explain the nature of this DM, which suggests that the answer lies beyond the SM. The evidence we have in favor of particle DM comes from observations of its gravitational effects on baryonic matter. The first evidence was discovered by Fritz Zwicky in the 1930's from measurements of the velocity dispersion of galaxies in the Coma Cluster [56, 57]. He found that the gravitational attraction of visible matter was not enough to bound these galaxies. A similar argument can be applied to the gas bounded to clusters and also from gravitational lensing [58].

Another important evidence comes from rotation curves of disk galaxies, where the rotational speed v stays constant as a function of the radius beyond the visible disk, instead of getting $v \sim r^{-1/2}$. This suggests that the mass grows with the radius [59]. More evidence is given by the mass distribution of the "Bullet Cluster" [60]. The gravitationally dominant mass component (responsible for weak lensing) was found to be displaced from the hot gas (fluid-like X-ray emitting plasma), implying that some sort of dark matter would be required to explain this effect [61].

There are other observations that give further evidence for the existence of DM. The density fraction $\Omega_i = \rho_i/\rho_c$ gives the ratio of the energy density of each component to the critical density ρ_c, where ρ_c is the value of the total energy density for a spatially flat Universe. From current measurements [62], $\Omega = \sum \Omega_i$ is close to 1. According to the most recent results combining observations from the Planck collaboration of the anisotropies in the Cosmic Microwave Background (CMB) and others in table 4 of [62], we have $\Omega_{DM}h^2 = (0.1186 \pm 0.0020)$ for DM, $\Omega_b h^2 = (0.02226 \pm 0.00023)$ for baryonic matter and $\Omega_{DE}h^2 = (0.692 \pm 0.012)$ for dark energy. The Hubble constant $h = (0.6781 \pm 0.0092)$ is given in units of $100\,\mathrm{km}\,s^{-1}\,\mathrm{Mpc}^{-1}$.

In this section, we introduce the main current paradigm for explaining dark matter in the Universe: Weakly Interactive Massive Particles (WIMPs) as dark matter candidates. We consider DM particle candidates that are produced as *thermal relics*. These particles exist in thermal equilibrium and in abundance in the early Universe, when the temperature of the Universe exceeds the DM mass m_χ. Later, as the Universe cools to a temperature below the mass of the particle, the equilibrium abundance drops exponentially until the rate for the annihilation reaction of DM into lighter particles falls below the expansion rate H (Hubble parameter). At this point the interactions which maintain thermal equilibrium *freeze out* and the number of DM particles becomes fixed (the abundance per comoving volume remains constant).

The evolution of the number density n of thermal DM χ particles is given by the Boltzmann transport equation

$$\frac{dn}{dt} = -3Hn - \langle\sigma_A v\rangle(n^2 - n_{eq}^2) \tag{1.3.1}$$

where σ_A is the $\chi\overline{\chi}$ annihilation cross section, v the relative speed of the annihilating DM particles, n_{eq} is the equilibrium number density at the temperature T of the thermal bath and $\langle\rangle$ denotes an average over the thermal distribution of DM particles. We assumed for simplicity that χ and $\overline{\chi}$ can only annihilate and be created in pairs, $n_\chi = n_{\overline{\chi}} = n$ and there are no coannihilations. Numerical solutions to (1.3.1) are shown in fig. 1.10 for the comoving number density $Y = n/s$ (s is the entropy density) as a function of $x = m_\chi/T$. If the annihilation cross section increases, the WIMPs stay longer in equilibrium and as a result the relic abundance is smaller. The number density n drops exponentially shortly after T drops below m_χ, and the rate for DM annihilation $\Gamma = \langle\sigma_A v\rangle n$ drops below the expansion rate, $\Gamma \lesssim H$. When this happens, the DM falls out of equilibrium and a relic cosmological abundance remains. The temperature T_f at freeze out is obtained from $\Gamma(T_f) = H(T_f)$, giving $T_f \simeq m_\chi/20$ for typical weak-scale numbers. From this freeze out condition $\Gamma(T_f) = H(T_f)$, an approximate equation for the relic abundance can be obtained,

$$\Omega_\chi h^2 = \frac{m_\chi n}{\rho_c} \simeq \frac{3\times 10^{-27}\mathrm{cm}^3 s^{-1}}{\langle\sigma_A v\rangle} \tag{1.3.2}$$

where h is the Hubble constant in units of $100\,\mathrm{km}\,s^{-1}\,\mathrm{Mpc}^{-1}$ and ρ_c the critical density today.

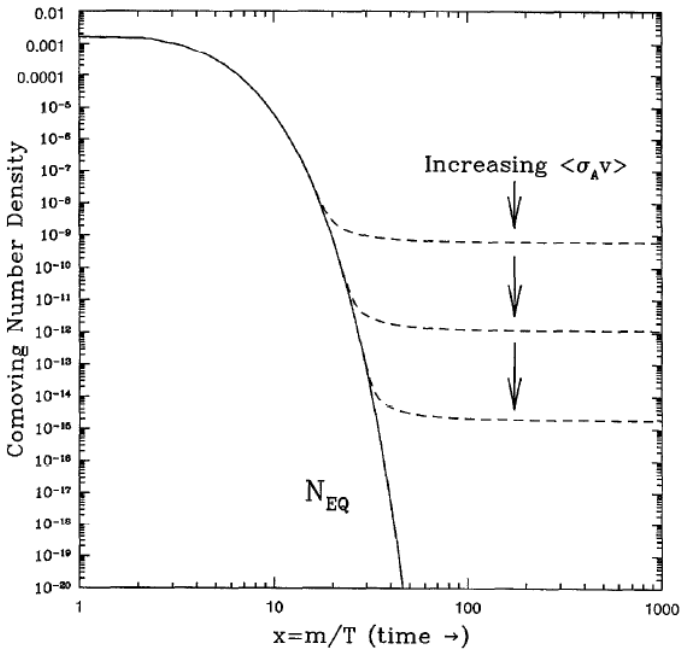

Figure 1.10: Comoving number density of a WIMP in the early Universe as a function of $x = m_\chi/T$. The actual abundance is shown in dashed, and the equilibrium abundance in solid. This plot was taken from [13].

If the DM is a new particle with weak-scale interactions, then we can estimate its annihilation cross section as $\langle\sigma v\rangle \sim \frac{g^4}{16\pi^2 m_\chi^2}$ and we get $\Omega_\chi h^2 \sim 0.1(m_\chi/\text{TeV})^2$, that is about the right relic abundance, even though there is no reason for this to happen. This is usually referred to as the WIMP *miracle*. This coincidence motivates the idea that there could be a new particle associated with DM at the EW scale.

1.3.1 Neutralino dark matter

In this section we consider the main aspects of the phenomenology of SUSY models where the lightest superpartner (LSP) is a stable neutralino that constitutes a DM candidate (for recent studies, see e.g. [63–65]). We decouple all the superpartners (e.g. heavy Higgs bosons, squarks and sleptons) except for a handful that are relevant for DM phenomenology. Thus, we analyze the parameter space for neutralino DM as an admixture of bino ($\tilde{b}$), wino

($\tilde{w}$), and Higgsino ($\tilde{h}$). The neutralino mass matrix is given by

$$\mathcal{M}_\chi = \begin{pmatrix} M_1 & 0 & -\frac{1}{\sqrt{2}}g'v\cos\beta & \frac{1}{\sqrt{2}}g'v\sin\beta \\ 0 & M_2 & \frac{1}{\sqrt{2}}gv\cos\beta & -\frac{1}{\sqrt{2}}gv\sin\beta \\ -\frac{1}{\sqrt{2}}g'v\cos\beta & \frac{1}{\sqrt{2}}gv\cos\beta & 0 & -\mu \\ \frac{1}{\sqrt{2}}g'v\sin\beta & -\frac{1}{\sqrt{2}}gv\sin\beta & -\mu & 0 \end{pmatrix}, \tag{1.3.3}$$

where M_1 and M_2 are the bino and wino mass terms respectively, coming from the soft supersymmetry breaking lagrangian. Also, μ comes from the MSSM superpotential, and g', g are the Higgs-higgsino-gaugino couplings (with the Higgs scalars replaced by their VEVs). Thus, the parameter space is comprised of mass parameters and the ratio of the VEVs, i.e. (M_1, M_2, μ, $\tan\beta$). To saturate the tree level contribution to the Higgs mass, we take the other Higgses to be heavy and in the decoupling limit, and we focus on the large $\tan\beta$ case. This scenario for neutralino DM is valid for different SUSY models, in particular for the MSSM.

For thermal neutralino DM, the right relic abundance constraint typically requires some level of fine-tuning among parameters, as discussed in detail in [63]. We can study three different cases:

- Pure bino: the DM annihilation cross section is too small and DM is overabundant.
- Pure wino or higgsino: DM is under-abundant for $\tilde{h}$ masses below $\sim$ 1 TeV and $\tilde{w}$ masses below $\sim$ 2.7 TeV.
- Well-tempered: in this case we can get the right relic abundance for a precise admixture of bino/higgsino or bino/wino, as shown in fig. 1.11 [63].

We can see in fig. 1.11 that the DM abundance is very sensitive to specific parameter values around the well-tempered cross-over region. The reasons are that the mixing angle changes rapidly in this region and also that the LSP neutralino mass gets close to the next lightest neutralino mass as well as to the charginos, which allows for coannihilation [66].[9]

[9]The coannihilation is exponentially sensitive to the mass difference of the annihilating states.

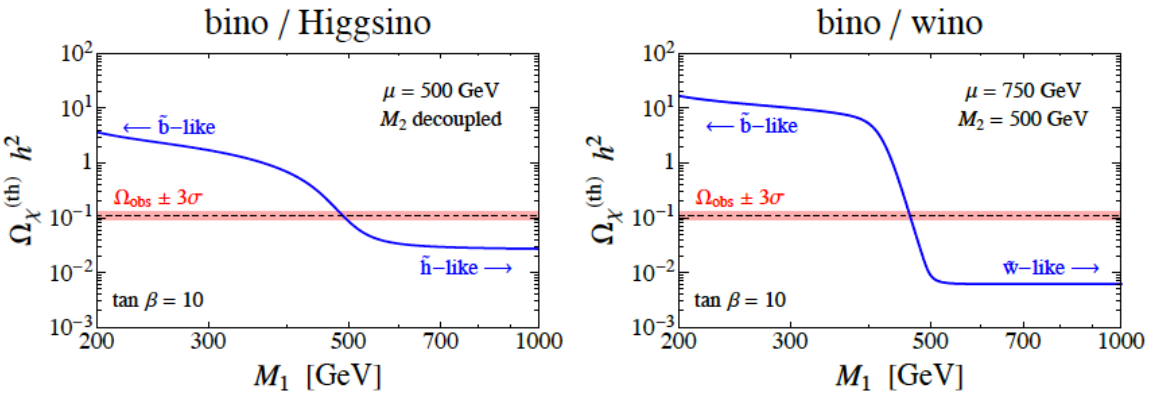

Figure 1.11: Thermal freeze-out abundance for $(\tilde{b},\, \tilde{h})$ (left) and $(\tilde{b},\, \tilde{w})$ (right). This plot was taken from [63].

Next, we show in fig. 1.12 the limits on bino/higgsino DM taken from [63]. Regarding spin independent (SI) direct detection (DD) limits, the cross section is regulated by the Higgs-DM-DM $c_{h\chi\chi}$ coupling. This coupling is suppressed in the pure case where DM is mainly higgsino or bino, as a result that $c_{h\chi\chi}$ originates at tree-level from $h\,\tilde{h}\,\tilde{b}$ and $h\,\tilde{h}\,\tilde{w}$. However, as we just saw, for DM masses below 1 TeV the only option that achieves the right relic abundance is the well-tempered case. Also, $c_{h\chi\chi}$ could cancel for special choices of parameters, named *blind spots*, but for large $\tan\beta$ (as shown in fig. 1.12) the blind spot occurs in a region far from the right relic abundance contour.

As a result, thermal neutralino DM in the well-tempered case relies on coannihilations and numerical coincidences among parameters. Despite of this requirement, this case is being ruled out by current and future direct detection experiments that are pushing down in sensitivity. Higgsino DM at 1 TeV provides the right relic abundance and is allowed by direct detection limits. However, a value of $\mu \sim 1$ TeV would make the model unnatural as discussed in section 1.2.1. Therefore, thermal neutralino DM is under pressure and this strongly motivates looking beyond the MSSM for the source of dark matter, which is the topic of study in chapter 5 of this thesis. In chapter 5, we propose a simple extension of the MSSM that gives a viable thermal dark matter candidate and helps lift the Higgs mass to 125 GeV in a natural way.

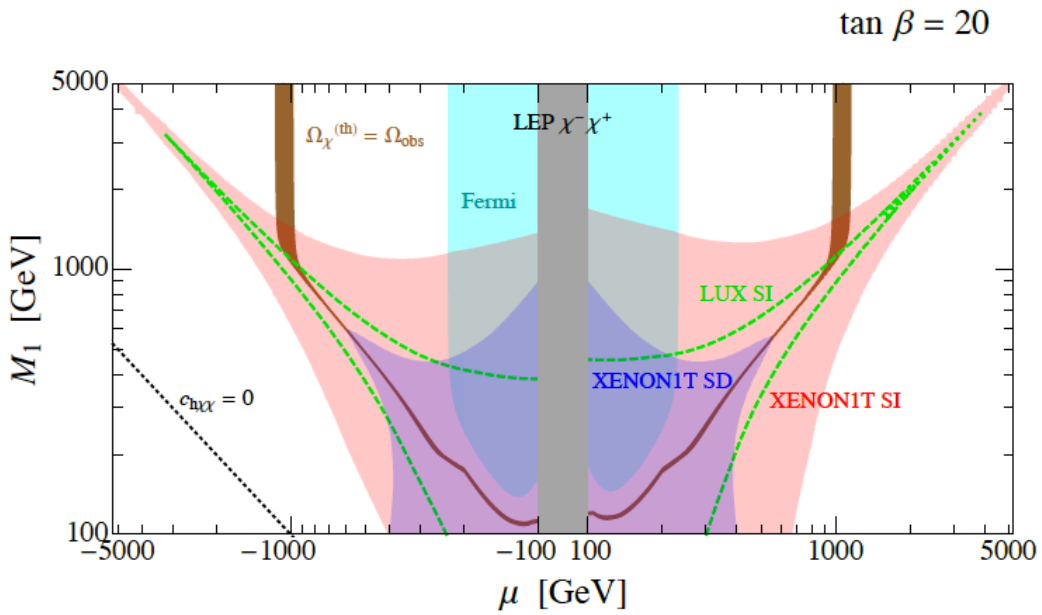

Figure 1.12: Limits on bino/Higgsino DM with for $\tan\beta = 20$ taken from [63]. The brown band is the contour of the right relic abundance within $\pm 3\,\sigma$. An enhancement (dilution) of the DM abundance after freeze-out is necessary for regions above (below) the brown band. The black dashed line is the SI blind spot, $c_{h\chi\chi} = 0$. The plot also shows the projected SI reach of LUX, and both SI and spin dependent reach for XENON1T at the time [63] was published (November 2012).

1.4 Description of the content of each chapter

This thesis is organized as follows. After introducing in this chapter the main background related to the work developed in this thesis, we start by applying two very different techniques for searches at LHC in chapters 2 and 3. Traditional methods start with a set of physical observables, such as jet mass, angular distributions, etc, that can be used to distinguish specific particles. Typically, these high-level features can be implemented in a cut and count analysis or as inputs to various multivariate machine learning algorithms, such as boosted decision trees (BDTs), to further enhance the classification performance. By contrast, in recent years, new approaches using deep neural networks to identify objects at the LHC have been applied. They main difference is that in this case, we can start from much lower level inputs and let the neural network figure out the most useful physical observables for classification, as well as design the optimal set of cuts on these observables. Thus, we apply this second approach in chapter 2, where we use computer vision with deep learning (in the form of a convolutional neural network) to build a highly effective boosted top

quarks tagger. In this case, our goal is to design a single jet classifier for boosted top quarks (that are reconstructed as a single large radius "fat jet") that could be straightforwardly extended to other types of SM jets. In contrast, in chapter 3 we propose a full event analysis using a cut and count method. This search is capable of probing a large patch of the line in the mass plane where there is just enough phase space to produce an on-shell top from the decay of a stop to a top and a neutralino. Next, in chapter 4 we obtain the latest limits on various simplified models of natural SUSY that have light higgsinos, stops and gluinos. We derive these limits from a detailed reinterpretation of 13 TeV ATLAS and CMS searches at LHC Run II with the first ~ 15 fb^{-1} of data. We also study the effects of these constraints on the fine-tuning of the EW scale. Finally, in chapter 5 we propose a simple extension of the MSSM by adding a singlet and a pair of $SU(2)$ doublets. We show that with this new sector, we can obtain a 125 GeV Higgs boson and a dark matter candidate with the right relic abundance in a natural way, while having a region of the parameter space that satisfies the constraints from direct and indirect detection experiments. We finish in chapter 6 with the main conclusions and outlook of the work presented in this thesis. Technical details and validations are reserved for the appendices.

Chapter 2

Pulling Out All the Tops with Computer Vision and Deep Learning

With David Shih

Appeared in arXiv:1803.00107

General context of this chapter

In this chapter, we apply computer vision with deep learning – in the form of a convolutional neural network (CNN) – to build a highly effective boosted top tagger. Previous work (the "DeepTop" tagger of Kasieczka et al) has shown that a CNN-based top tagger can achieve comparable performance to state-of-the-art conventional top taggers based on high-level inputs. Here, we introduce a number of improvements to the DeepTop tagger, including architecture, training, image preprocessing, sample size and color pixels. Our final CNN top tagger outperforms BDTs based on high-level inputs by a factor of $\sim$ 2–3 or more in background rejection, over a wide range of tagging efficiencies and fiducial jet selections. As reference points, we achieve a QCD background rejection factor of 500 (60) at 50% top tagging efficiency for fully-merged (non-merged) top jets with p_T in the 800–900 GeV (350–450 GeV) range. Our CNN can also be straightforwardly extended to the classification of

other types of jets, and the lessons learned here may be useful to others designing their own deep NNs for LHC applications.

2.1 Introduction

Heavy boosted particles play an important role in many analyses at the LHC, including SM precision measurements, Higgs and electroweak physics, and searches for physics beyond the Standard Model (BSM). In general, the collimated decay products of boosted particles are reconstructed as a single large-radius "fat jet". Analyses then attempt to "tag" the origin of the fat jet by looking at its substructure. (For reviews of boosted object tagging and jet substructure, and many original references, see e.g. [67–74].) The ability to accurately tag boosted jets has many benefits. For instance, it can be used to overcome the QCD background and measure $h \to bb$ in associated production [75]. In BSM physics, new heavy particles could be created, which then produce boosted SM objects as they decay. Requiring the presence of these boosted objects is then a useful handle in discriminating signal against SM background.

In this chapter, we will focus on a particularly well-motivated case: boosted top jets. Signatures with energetic top quarks are predicted from SM processes such as single top and top pair production, and in several models of new physics. Top partners are expected to play a key role in solutions to the hierarchy problem, and they can naturally produce boosted top quarks in their decays. Additionally, there are other models that consider the production of dark matter in association with a top quark or top quark pair. Some recent LHC searches based on boosted top jets include [76–79].

Traditional top tagging methods (see [80, 81] for reviews and original references) start with a collection of physical observables, such as jet mass, that can be used to distinguish tops from light-flavor QCD. These high-level features can serve as inputs to various multivariate machine learning algorithms, such as boosted decision trees (BDTs), to further enhance the tagger performance. These algorithms attempt to find a set of complicated boundaries over the phase space that maximizes the classification accuracy. However, as the classification ability is highly dependent on these observables, the main challenge re-

sides in finding ways to systematically come up with a set of observables that are not highly correlated and give the best discriminating power.

By contrast, in recent years, there has been a great deal of interest in using deep neural networks (NNs) to identify objects at the LHC (among many other potential applications). The tantalizing promise of deep learning is the ability to start from much lower level inputs than was previously thought possible, and transform them into meaningful outputs. (For pedagogical introductions to neural networks and deep learning, see e.g. [82, 83].) In the context of boosted jet tagging, the idea is to allow a NN to figure out on its own, from relatively raw data (e.g. momentum four-vectors of all the constituents of the jet), the intrinsic patterns that identify each type of jet and the regions of phase space that distinguish them. In this sense, deep learning attempts to *invent* the most useful physical observables for classification, in addition to designing the optimal set of cuts on these observables.

The interest of the LHC community in deep learning has been spurred by the huge successes of deep NNs in real-world applications (see [84] for a nice overview). One major source of breakthroughs has been in computer vision, from pixel level labeling of images for autonomous vehicles [85, 86] and Google's automatic captioning of images [87, 88], to Facebook's DeepFace project [89] and Microsoft surpassing human-level performance on ImageNet classification [90]. These results were made possible in large part thanks to the invention of convolutional neural networks (CNNs). CNNs are built from two types of layers: *convolutional layers* and *fully connected layers*. The former implement locality (exploit the image's spatially local correlations) and capture the lower level features of the input image (lines, edges, curves, etc.). These are eventually passed on to the latter which are responsible for learning abstract, higher level concepts (such as class probabilities). This independence from hand engineered features is a major advantage of CNNs from more traditional algorithms.

CNNs have a direct application to classifying jets at the LHC, since there is an obvious and natural sense in which jets can be viewed as images. Indeed the calorimeters already provide the requisite pixelization. The intensity of the image can be the per-pixel p_T and can be augmented with other per-pixel quantities such as track multiplicity. This idea of jet images has been explored in a number of works [91–96], with [93, 95, 96] applying CNNs

to W-boson, quark/gluon and top tagging respectively. These works have demonstrated that jet taggers based on computer vision can perform comparably to or slightly better than conventional taggers based on high-level inputs. In particular, the CNN top tagger of [96] (named "DeepTop" there) was trained on grayscale images formed from calorimeter deposits of moderately boosted top jets. The end result was a CNN top tagger with performance comparable to state-of-the-art BDTs built out of SoftDrop variables [97], HEPTopTaggerV2 (HTTV2) variables [98–100], and N-subjettiness [101].

In this chapter, we explore a number of improvements to the DeepTop tagger, including the NN architecture (augmenting the DeepTop CNN with more feature maps and more nodes on dense layers), the NN training (loss function, optimizer algorithm, minibatch size, learning rate), image preprocessing, sample size (increasing the training sample by $10\times$ to $\sim$ 1M jets saturates the NN performance), and adding color (calorimeter p_T, track p_T, track multiplicity and muon multiplicity). The result is a much more effective CNN for top tagging, one that (for the first time) significantly outperforms best-in-use conventional methods. This shows the enormous power and promise of modern deep learning methods as applied to the LHC. We are clearly entering a new era driven by major gains in artificial intelligence.

In order to disentangle any possible correlations between our proposed improvements and the fiducial jet image selection, we consider two very different jet samples in this chapter.[1] The first is the sample of moderately-boosted jets used in the DeepTop paper (350 GeV $< p_T <$ 450 GeV). The second is a sample of high p_T jets (800 GeV $< p_T <$ 900 GeV) that (apart from some minor differences) is taken from a recent note on top tagging methods by CMS [102]. We will refer to these as the "DeepTop sample" and the "CMS sample" throughout this work. Apart from the p_T ranges, an important difference between the two samples is the *merge requirement*. This is a generator-level cut that requires the daughters of the top quark to be contained within the cone of the fat jet. It ensures that all the top jets contain the bulk of the energy from the boosted top quark. Without the merge requirement, the top jet sample is significantly polluted by partially merged top jets that might contain only the W-boson, or only the b quark and a single jet from the W decay.

[1] We thank Gregor Kasieczka for very stimulating discussions on this point.

The CMS sample imposes a merge requirement, while the DeepTop sample does not, and we will see that this has a major impact on the tagger performance.

Combining all of our proposed improvements, we show that the net effect is to increase the background rejection rate of the DeepTop tagger by a factor of $\sim$ 3–10 in the CMS sample, and a factor of $\sim$ 1.5–2.5 in the DeepTop sample. It is perhaps not surprising that the improvement is much more modest in the DeepTop sample, since this was the focus of [96]. In any event, our modifications result in significant gains in performance over the baseline tagger for both jet samples, which is strong evidence for their general applicability. In both cases, the single greatest improvement is actually in the NN training, then followed by the NN architecture and the larger training sample size. This illustrates that the performance of a NN can be determined as much by the methods used to train it and the dataset it is trained on, as it is by the architecture.

We then proceed to a comparison of our CNN top tagger with conventional top taggers that are meant to represent the state-of-the-art and best-in-use. For the DeepTop sample, we compare directly against the "MotherOfTaggers" BDT ROC curve in fig. 8 of [96]. For the CMS sample, we compare against a BDT built out of HTTV2 variables and N-subjettiness. A cut-based version of this tagger was shown in [102] to have optimal performance among cut-based taggers (see also the analogous ATLAS references [103, 104]). The upshot is that our CNN top tagger outperforms these conventional taggers by a factor of $\sim$ 2–3 or more in background rejection, across a wide range of tagging efficiencies.

Very recently there have been several efforts [105–108] to feed the raw jet constituents (as momentum four-vectors) to various deep learning architectures such as recurrent neural networks (RNNs) and dense neural networks (DNNs). These have shown much promise. In [105] they showed that a recurrent neural network (RNN) W/Z tagger can outperform a simple cut-based classifier based on N-subjettiness and jet mass. In [106, 108] they showed that a dense neural network (DNN) and an RNN top tagger can significantly outperform a likelihood-based tagger that takes N-subjettiness and jet mass as inputs. It would be extremely interesting to do a head-to-head comparison of all of these deep learning NNs with each other and with a state-of-the-art conventional tagger.

Although we have focused on top quarks in this work, it can also be viewed as a case

study of boosted object tagging more generally. Our approach could be straightforwardly extended to other types of jets. There are also many other potential applications (many have already begun to be explored), for instance whole-event classification, event generation, weakly-supervised learning, pile-up mitigation to name a few. Furthermore, our optimizations were not systematic due to computational limitations. So perhaps with a more systematic approach (i.e. hyperparameter scans) one could achieve even greater gains.

This chapter is organized as follows. In section 2.2 we describe the details of our simulations and the precise specifications of our top and QCD jet image samples. We also briefly review the original DeepTop CNN which forms the baseline for the CNN tagger developed in this work, as well as the conventional taggers that we benchmark against. In section 2.3 we give an overview of some general "best practices" in the design of NNs, and we show how these can be applied to improve the DeepTop CNN. We hope that, apart from the usefulness of the CNN top tagger itself, this overview of concepts in NN design will prove useful to others. While much or all of it will be known to experts, it may be useful to have it collected in one place.

In Section 2.4, we describe improvements to the image preprocessing steps in the DeepTop paper that are made possible by using the higher-resolution tracks in the jet. In Section 2.5, we examine the dependence of the classification accuracy on the training sample size and multiple intensity channels (colors). Then, in Section 2.6 we put it all together and compare our top tagger against the DeepTop tagger and the conventional taggers built out of high-level inputs. We conclude with a discussion of next steps and promising future directions in Section 2.7. In Appendices A and B we validate our implementation of the DeepTop paper, and the cut-based CMS top tagger (using the HEPTopTaggerV2 and τ_{32} variables) respectively. In Appendix C we discuss the differences in top tagger performance if fully-merged-tops are required or not.

2.2 Methodology

The fat jets used in this chapter are taken from all-hadronic $t\bar{t}$ and QCD dijet events generated in proton-proton collisions using Pythia 8.219 [109], where multiparton interactions

and pileup are turned off for simplicity. After showering and hadronization, the events are passed into DELPHES 3.4.1 [110] for detector simulation. The jets are clustered with FASTJET 3.0.1 [111].

As discussed in the Introduction, we will study improvements to the DeepTop tagger using two very different samples of jet images. These are described in table 2.1. The first is the jet sample used in the DeepTop paper [96], while the second is essentially the same as the high p_T sample used in the CMS note [102].[2] Let's now highlight some of the important differences between the samples:

- The DeepTop sample is much lower p_T than the CMS sample.

- The DeepTop sample uses only calorimeter energies, while the CMS sample uses particle-flow, meaning that the tracks and neutrals (defined to be calorimeter towers minus the track contributions) are counted separately. This is very advantangeous, as the tracks have much higher resolution than the calorimeter towers.

- With the tracking information in the CMS sample, we can use color images along the lines of [95]. In addition to the colors used in [95] (calorimeter p_T of the neutrals, per-pixel track p_T, and per-pixel track multiplicity), we also include muon multiplicity. This is motivated by the presence of muons in a sizable fraction of top quark jets coming from semileptonic b decays. (For comments on b-tagging see Section 2.7.)

- The DeepTop sample used a toy calorimeter with resolution $\Delta\eta = 0.1$, $\Delta\phi = 5^\circ$. For the CMS sample we used the default CMS detector card that comes with DELPHES 3.4.1, which has a slightly higher calorimeter resolution. The number of pixels (37×37) chosen for the high p_T jet images is based on this. In both cases, a large image size is chosen to make absolutely sure the entire fat jet is captured.

- Finally, a crucial difference between the two samples is the merge requirement. DeepTop did not require the daughters of the top quark to fall in the cone of the fat jet, while CMS did. With the merge requirement, the top jets are more "top-like" (otherwise they are significantly contaminated by W jets and b jets), and this increases the

[2] CMS uses 800 GeV $< p_T <$ 1000 GeV jets with $R = 0.8$.

	DeepTop	CMS
Jet sample	14 TeV $p_T \in (350, 450)$ GeV, $\|\eta\| < 1$ $R = 1.5$ anti-k_T calo-only match: $\Delta R(t, j) < 1.2$ merge: NONE	13 TeV $p_T \in (800, 900)$ GeV, $\|\eta\| < 1$ $R = 1$ anti-k_T particle-flow match: $\Delta R(t, j) < 0.6$ merge: $\Delta R(t, q) < 0.6$
Image	40×40 $\Delta\eta = 4$, $\Delta\phi = \frac{10}{9}\pi$	37×37 $\Delta\eta = \Delta\phi = 3.2$
Colors	p_T^{calo}	$(p_T^{neutral}, p_T^{track}, N_{track}, N_{muon})$

Table 2.1: The two jet image samples used in this work.

potential discriminating power against QCD jets. Accordingly, we will see that the ROC curves for the CMS sample look much better than for the DeepTop sample. We explore this further in Appendix C.

We will benchmark our CNN top tagger against BDT taggers built out of high-level inputs. For the DeepTop sample, we directly compare against their "MotherOfTaggers" BDT that takes HTTV2 variables, SoftDropped masses, and N-subjettiness variables (with and without SoftDrop) as inputs. Since we have fully validated the DeepTop minimal tagger, we do not bother to validate the MotherOfTaggers BDT as well, but just take its ROC curve directly from fig. 8 of the DeepTop paper. For the CMS sample, we will consider both a cut-based tagger that combines the HTTV2 variables with the N-subjettiness variable τ_3/τ_2 (motivated by the recent CMS note on top tagging [102]), as well as a BDT trained on these variables. For the former, we varied simple window cuts on each of the variables, as in [102]. We validate our implementation of this by reproducing the ROC curve shown in fig. 7R of [102] using our own simulations (see appendix B for details). For our BDT we used the ROOT package TMVA [112] with the same hyperparameters as in [104] and trained on the same jets as our final CNN tagger.

For the design of our CNN, we took as a starting point the DeepTop tagger of [96]. Its CNN architecture consisted of four identical convolutional layers (8 feature maps, 4×4

kernel) separated in half by one 2×2 max-pooling layer, followed by three fully connected layers of 64 neurons each and an output layer of two softmax neurons. Zero-padding was included before each convolutional layer to prevent spurious boundary effects. The DeepTop CNN was trained on a total of 150k+150k top and QCD jet images, by minimizing a mean-squared-error loss function using the stochastic gradient descent algorithm in minibatches of 1000 jet images and a learning rate of 0.003. In order to validate our implementation of the DeepTop tagger, we have carefully reproduced the ROC curve in fig. 8 of [96], see appendix A for details.

Using the DeepTop tagger, the authors of [96] demonstrated that CNNs could perform comparably to a conventional BDT trained on high-level inputs. In the following sections we will consider a number of improvements to the DeepTop tagger that, taken together, demonstrate for the first time that CNNs can significantly outperform conventional taggers.

2.3 Improvements to the neural network

In the design of an effective neural network, there are countless choices to be made. These include not only decisions about the neural network architecture (how many layers, of what type), but also how it is trained (loss function, optimizer, minibatch size, etc). In general, the many parameters that go into the design of a neural network are referred to as "hyperparameters" (not to be confused with the "parameters" of the NN – weights and biases – that are varied during the training to minimize the loss function).

Through trial and error, we found that many of the hyperparameter choices made in [96] could be improved. (A proper scan of hyperparameters would have been ideal but this requires a GPU cluster which we did not have access to.) While many of these choices are more art than science, and while the best choice may depend heavily on the particular problem domain (e.g. the choice that may be ideal for natural images may not be the best choice for jet images), there is some accumulated lore from the field of deep learning about best practices. In this section we will briefly go over some of this lore and explain how its application to jet tagging can significantly improve the DeepTop tagger performance. While we do make an attempt at a somewhat self-contained treatment, we do not promise

to have succeeded. We refer the interested reader to [82, 83] for any missing definitions and more background material.

2.3.1 Loss function

In any neural network, the goal is to minimize a "loss function" L over the NN parameters θ:

$$L = \sum_i f(a(\theta, x_i), y_i) \tag{2.3.1}$$

The loss function quantifies how well the network is performing. Here $a(\theta, x_i)$ is the NN prediction and is a function of the NN parameters as well as the input x_i (the jet image in our case); y_i is the truth label of example i; and i is summed over all the examples in the training sample. For binary classification problems such as top tagging, we can take $y_i = 0$ for signal (tops) and $y_i = 1$ for background (not-tops).

In DeepTop, f was taken to be the mean-squared-error (MSE) $f(a, y) = (a - y)^2$. However, a better choice in classification problems (that we opt for here) is the cross entropy $f(a, y) = -(y \log a + (1 - y) \log(1 - a))$. Theoretically speaking, MSE is more appropriate and mathematically/statistically sound for Gaussian random variables, while binary cross entropy is more appropriate for discrete (logistic) classification. In more practical terms, using the binary cross entropy for classification tends to avoid the problem of learning slowdown when the predictions are close to zero or one. For more discussion of this see [82].

2.3.2 Optimizer algorithm

Having chosen a loss function, we next need to decide on which algorithm we use to minimize it. The loss function surface of multilayered NNs is typically non-convex and high-dimensional with multiple flat regions and local minima. So the process of training the NN is highly nontrivial. A poor choice of the optimizer can lead to many undesirable outcomes.

Generally, the optimizers used to train deep networks are based on the idea of gradient descent, where the parameters of the NN are updated according to the derivative of the loss function:

$$\Delta\theta = -\eta \nabla L \tag{2.3.2}$$

The learning rate η is a hyperparameter that needs to be tuned: gradient descent would take too many steps if η is too small, but if η is too large one may never converge to a minimum.

Computing the gradient of the full loss function (i.e. summed over the entire training set) – referred to as batch gradient descent – is generally too time consuming. Instead, most optimizers for deep learning involve some form of Stochastic Gradient Descent (SGD), where the training sample is divided into "minibatches", and gradients of the loss function are computed on each minibatch. Stepping through the training sample minibatch by minibatch and updating the weights at each step is then referred to as a "training epoch". While this would appear to provide noisy and inaccurate estimates of the gradient, it actually has many benefits. For instance, introducing some noise into the gradient calculation can prevent the optimizer from becoming stuck in a poor local minimum. Also, while some minibatches may be inaccurate and lead to faulty updates, taken together their cumulative effect can actually greatly speed up the rate of convergence. See [83] for a in-depth discussion of this.

Finally, it is well-known that SGD is very sensitive to the learning rate and other hyperparameters, and optimizing its performance usually requires an in-depth scan and tuning over these quantities (see e.g. [113] for a discussion). Therefore, popular alternatives in deep learning are optimizers such as AdaDelta [114] and Adam [115] that attempt to adaptively determine the optimal learning rate for each parameter and each training epoch. These adaptive versions of SGD usually require little or no manual tuning of a learning rate and are rather insensitive to noisy or large gradients, different model architectures and selection of hyperparameters, etc.

In [96], the optimizer was taken to be vanilla SGD with a minibatch size of 1000 and a fixed learning rate of $\eta = 0.003$. These hyperparameters do not appear to have been tuned. Therefore it is not surprising that switching to AdaDelta (with the default settings in Keras [116]) improves the outcome of training by a considerable amount.[3] We obtained further improvements with a slightly reduced learning rate (0.3 instead of 1) and a learning rate schedule (decreasing the learning rate by $1/\sqrt{2}$ when the validation loss does not decrease by more than 0.0005) as compared to the Keras defaults.

[3] We also tried using Adam and found very similar improvements.

We also found a very significant benefit to training with a smaller minibatch size than was used in the DeepTop paper (128 instead of 1000).[4] This is in line with the small-to-moderate minibatch sizes ($\lesssim \mathcal{O}(10^2)$) that are typically used in the machine learning literature. Smaller minibatches give noisier estimates of the gradient, and as noted above, this is actually beneficial in non-convex optimization, given that it could push the solution out of the saddle points and shallow minima of the loss function.

2.3.3 Architecture

Finally, there are myriad choices involved in specifying the architecture of the neural network. Here we found that the architecture of the DeepTop CNN seemed to be optimal in terms of the number of layers and filter size. But augmenting it with more feature maps (64-128 instead of 8) and more nodes on dense layers (256 instead of 64) improved the performance considerably.

Our NN architecture is shown in fig. 2.1. The input layer is given by an image of 37×37 pixels with (up to) 4 colors. Next, we define a convolutional layer of 128 feature maps with a 4×4 kernel followed by a second convolutional layer of 64 feature maps and similar kernel.[5] Then we have a max-pooling layer with a 2×2 reduction factor. Next we apply two more consecutive convolutional layers with 64 features maps with a 4×4 kernel each, followed by a max-pooling layer with a 2×2 reduction factor. As in [96], we use zero-padding in each convolutional layer to make sure we are not subject to boundary effects. We flatten the 64 maps of the last pooling layer into a single one that is passed into a set of three fully connected dense layers of 64, 256 and 256 neurons each. (Restricting the first dense layer to 64 neurons was motivated by practical considerations. It keeps the number of weights at a manageable level, speeding up training time and ameliorating overfitting.) Finally, the last dense layer is connected to the output layer of 2 neurons which produces the probability that the jet originated from a top or not. We use rectified linear units (ReLU) as the activation

[4] Perhaps an even smaller minibatch size would help even more, but here we were limited by computation time.

[5] The larger number of initial feature maps aims to capture all the possible lower lever features of the images. In computer vision applications these features are different shapes (lines, edges, curves, etc.) that the NN uses to build up to higher-level concepts. Although there is not a direct correspondence between typical computer vision images and our images given that jet images are sparse, raising the number of initial feature maps improved the classification accuracy.

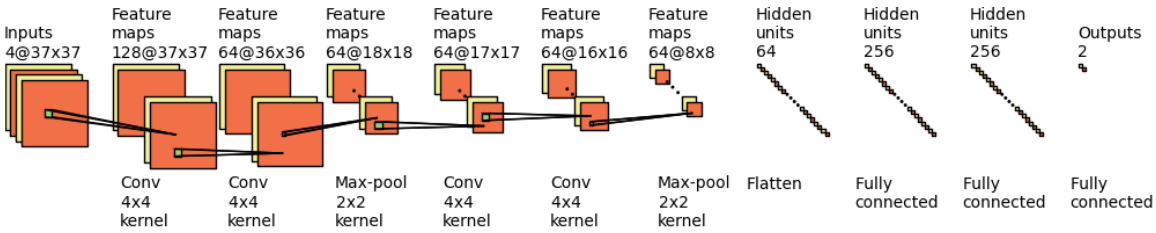

Figure 2.1: Architecture of our CNN top tagger.

functions on all the layers, except for the output layer where we use the softmax function. Also, our final training sample was large enough so that regularization techniques, such as dropout, were not necessary.

The neural network is implemented on an NVidia Tesla K80 GPU using the NVidia CUDA platform (CUDA drivers, toolkit and cuDNN library). The code for the CNN is written in Python, using the deep learning library Keras [116] with the TensorFlow [117] backend. The weights are initialized with the Keras default settings.

We arrived at the NN architecture used in this chapter mainly by trial and error. Due to limited resources, a thorough scan of NN architectures was not possible, however this would obviously be desirable. It is easily possible that further performance gains could be obtained with such a scan.[6]

2.4 Image preprocessing

In the original DeepTop paper [96], the image preprocessing steps were found to actually *decrease* the performance of the tagger. This is surprising since usually preprocessing improves classifier performance.

The DeepTop preprocessing steps were as follows. First they pixelated the image according to their detector resolution. Then they shifted such that the maximum pixel intensity as defined by a 3x3 window was at the origin. Next, they rotated such that the second maximum was in the 12 o'clock position, and they flipped to ensure that the third maximum is in the right half plane. Finally, they normalized each image so that the pixel intensities

[6] We note that a limited scan was carried out in the DeepTop paper. However, they only considered 6, 8 and 10 feature maps per convolutional layer, which does not include the 64-128 feature maps used in this work.

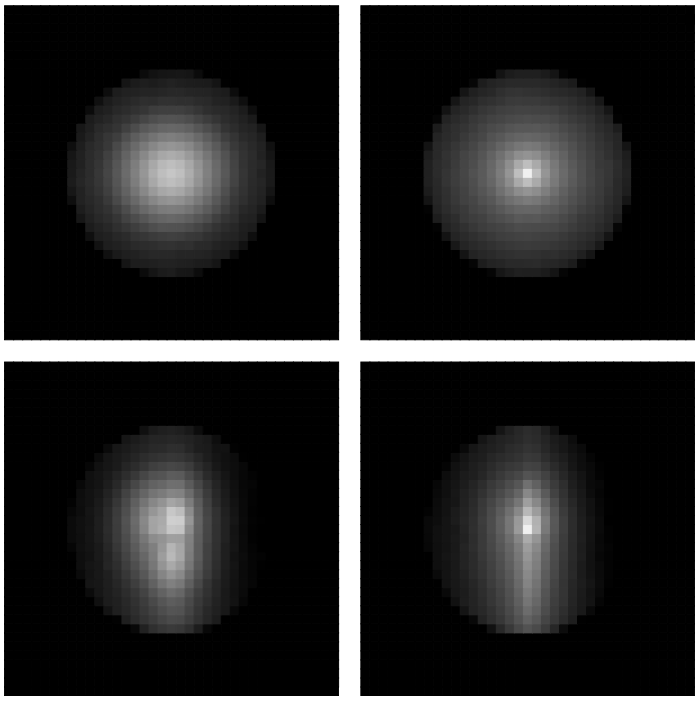

Figure 2.2: The average of 100k jet images drawn from the CMS sample (37×37 pixels spanning $\Delta\eta = \Delta\phi = 3.2$). The grayscale intensity corresponds to the total p_T in each pixel. Upper: no preprocessing besides centering. Lower: with full preprocessing. Left: top jets. Right: QCD jets

are between 0 and 1.

Our preprocessing steps differ from this in the following ways. First of all, we perform all preprocessing *before* pixelating the image. This makes the most sense for the CMS sample which separates the much-higher-resolution tracks from the calorimeter towers. But it also appears to have some benefit even for the calo-only jets of the DeepTop sample. Our first step is to calculate the p_T-weighted centroid of the jet and the p_T-weighted principal axis. Then we shift so that the centroid is at the origin and we rotate so that the major principal axis is vertical. In contrast to DeepTop, we flip along *both* the L-R and the U-D axes so that the maximum intensity is in the upper right quadrant. Finally, after doing all these transformations, we pixelate the image and then normalize it to unit total intensity (i.e. divide by the total p_T).

To demonstrate the effectiveness of our preprocessing steps, we show in fig. 2.2 the average of 100k top and QCD jet images drawn from the high p_T CMS jet sample, with and without preprocessing. Although below we consider color images where the track p_T's

and neutral p_T's are considered separately, here we restrict ourselves to grayscale images where they are added together. We see that even without preprocessing, the average images are quite different, with the QCD jets being much more peaked than the top jets. After our preprocessing steps, the 3-prong substructure of the top jets becomes readily apparent, while the QCD jets remain more dipole-like. (This should be contrasted with the average images in the DeepTop paper, where the 3-prong substructure of the top jets is much less apparent.)

2.5 Other improvements

2.5.1 Sample size

In the DeepTop paper, the training samples were limited to 150k+150k. Here we explore the effect on our CNN top tagger of increasing the training sample size. Shown in fig. 2.3 are the learning curves for the test accuracy vs. training sample size, for our two different jet samples. (The training sample size is defined to be the number of top jets in the training sample; an equal number of QCD jets were used. The test sample size was fixed at 400k+400k jets.) We have shifted the learning curve for the DeepTop sample by a constant 0.075; interestingly, it lines up almost perfectly with the learning curve for the CMS sample. This is evidence that the shape of the learning curve is independent of the fiducial jet selection (although the asymptotic value clearly depends strongly on it). In any event, we see that the performance is basically saturated for $\gtrsim$ 1M jets (for our final CNN tagger, we train on 1.2M+1.2M jets).

We also indicate in fig. 2.3 the result of a least-squares fit of an inverse power law $a + b/N_{train}^c$ to the learning curve. This description of the learning curve may be a general empirical feature of machine learning [118]. However, lacking a precise understanding of the uncertainties on the test accuracies (the sample variance from both the test set and the training set contribute), we cannot provide a detailed description of the fit. Here, to perform the fit, we estimated the uncertainty on each value of the test accuracy using a simple $1/\sqrt{N_{train}}$ scaling.[7] We merely include this fitting function to guide the eye. One

[7] We have tested this scaling using a small number of pseudoexperiments for small values of N_{train} and

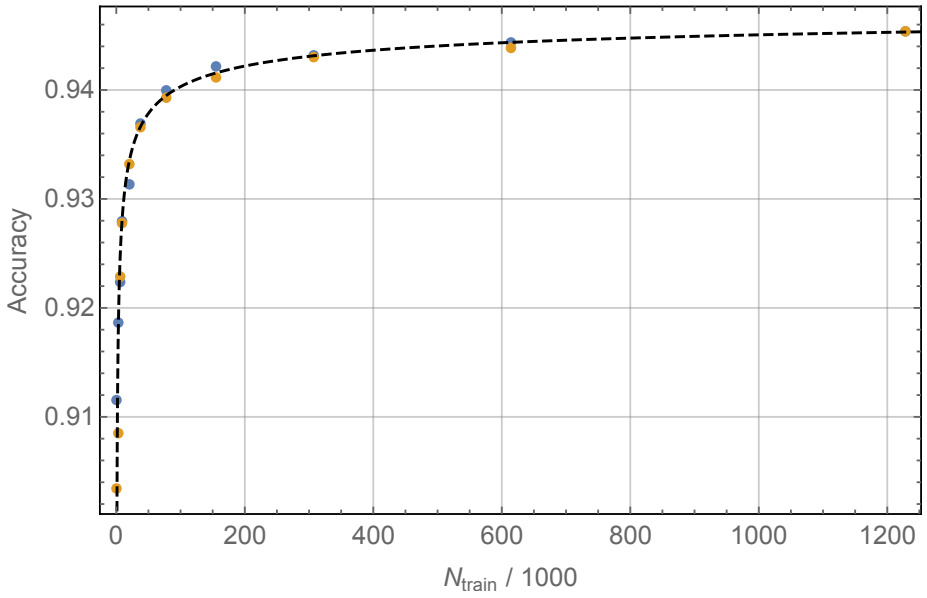

Figure 2.3: In blue (yellow) are the learning curves for the test accuracy vs. training sample size for the CMS jets (DeepTop jets). The CNN used is our final tagger but with grayscale images. The learning curve for DeepTop jets has been shifted up by a constant offset of 0.075. Shown also in black, dashed is a heuristic least-squares fit to an inverse power law with uncertainties given by $1/\sqrt{N_{train}}$.

sees visually that it seems to describe the learning curves well.

2.5.2 Color

Inspired by [95], we also added color to our images from the CMS sample. (The DeepTop sample was calo-only so we could not add color to them.) The four colors we used were neutral and track p_T per pixel, the raw number of tracks per pixel, and the number of muons per pixel. The last color was not considered in [95], which focused on quark vs. gluon tagging. Obviously, muons can be considered a crude proxy for b-tagging and should play a role in any top tagger. (For more comments on b-tagging, see Section 2.7.)

Interestingly, we found that adding color to the images led to significant overfitting for smaller training sample sizes. Evidently, while the color adds information to the images, it also increases the noise, and with too few training examples, the network learns to fit the noise. This problem went away when the training sample was increased to 1.2M+1.2M, which is why we choose to place the color improvement last.

it appears to hold.

	DeepTop minimal	Our final tagger
Training	SGD $\eta = 0.003$ minibatch size=1000 MSE loss	AdaDelta $\eta = 0.3$ with annealing schedule minibatch size=128 cross entropy loss
CNN architecture	8C4-8C4-MP2-8C4-8C4-64N-64N-64N	128C4-64C4-MP2-64C4-64C4-MP2-64N-256N-256N
Preprocessing	pixelate→center → normalize	center→rotate→flip → normalize→pixelate
Sample size	150k+150k	1.2M+1.2M
Color	$p_T^{calo} = p_T^{neutral} + p_T^{track}$	($p_T^{neutral}$, p_T^{track}, N_{track}, N_{muon})

Table 2.2: Summary of our final CNN tagger, together with the original DeepTop tagger.

2.6 Final comparison

The full specifications of our final tagger are summarized in table 2.2 side-by-side with those of the original DeepTop tagger.

Having gone through all the improvements (loss function, optimizer, CNN architecture, image preprocessing, sample size and color) to the DeepTop tagger in the preceding sections, we are now ready to put them all together and quantify their cumulative effects on the tagger performance. Shown in figs. 2.4–2.6 and table 2.3 are ROC curves and aggregate metrics characterizing these effects. The baseline in these plots is always the DeepTop minimal column in table 2.2, applied to the two different jet samples in table 2.1. Each modification is then added cumulatively to this baseline. Here is a more detailed breakdown (each entry here corresponds to moving from left to right sequentially in the corresponding category of table 2.2):

- The end result of all of our improvements to the training (loss function and optimizer) is the blue curves in figs. 2.4-2.6. This gave the single largest boost to the performance of all the different modifications we considered. Furthermore, we find that over half of the improvement here is due solely to the smaller minibatch size. We also note in passing that the better training methods allowed us to vastly speed up the training

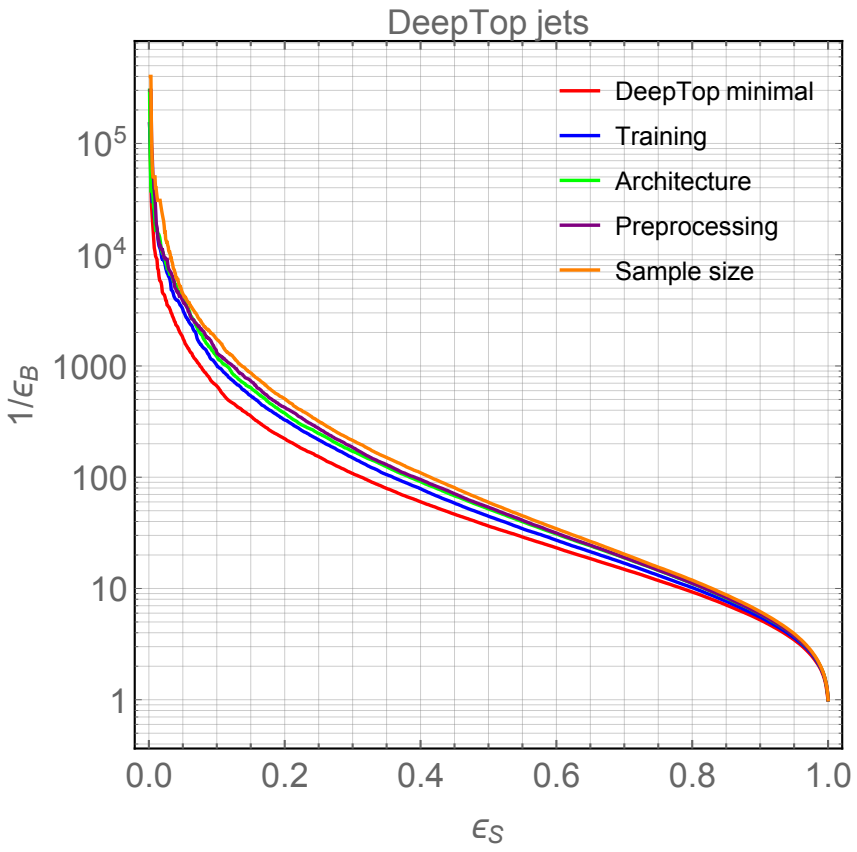

Figure 2.4: Sequence of ROC curves (background rejection $1/\epsilon_B$ vs. tagging efficiency ϵ_S) illustrating the cumulative effects of the various improvements to the DeepTop tagger, for the DeepTop jet sample. Our final tagger including all the improvements is shown in orange.

time, as we only need $\mathcal{O}(10)$ training epochs to converge instead of the $\mathcal{O}(10^3)$ epochs of the DeepTop paper.

- Improving the DeepTop architecture with more feature maps and more nodes on hidden layers brought about another substantial gain in performance, this is indicated in the green curves in figs. 2.4-2.6.

- The result of our image preprocessing steps is a (relatively modest) improvement in tagger performance, as indicated by the purple curves in figs. 2.4-2.6.

- We found that increasing the training sample size by a factor of ~ 10 significantly improved the performance. The improvement using 1.2M+1.2M jets (which according to fig. 2.3 is enough to saturate the best-possible performance of this tagger) is

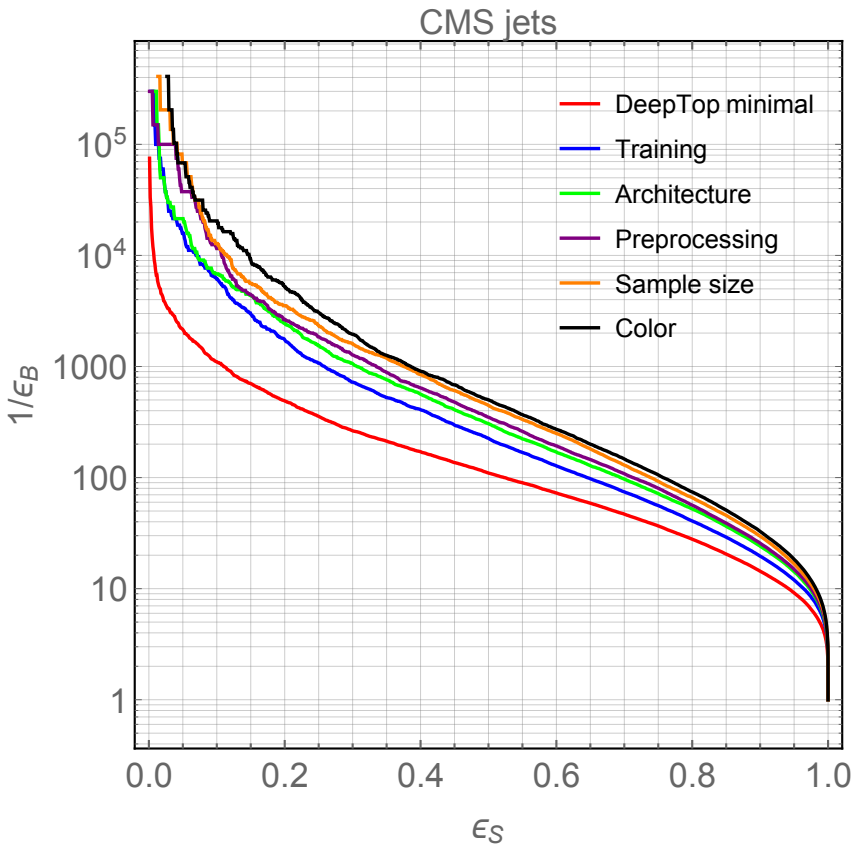

Figure 2.5: Same as fig. 2.4 but for the CMS jet sample.

	DeepTop jets		CMS jets	
Improvement	Accuracy	AUC	Accuracy	AUC
Baseline	85.5%	0.930	91.7%	0.975
Training	86.1%	0.935	93.4%	0.983
Architecture	86.6%	0.939	94.0%	0.985
Preprocessing	86.7%	0.940	94.2%	0.986
Sample Size	87.0%	0.943	94.5%	0.988
Color	—	—	94.8%	0.989

Table 2.3: Accuracy and area under the curve (AUC) of our tagger after adding the modifications over DeepTop minimal.

indicated by the orange curves in figs. 2.4-2.6 (the previous ROC curves were based on the DeepTop training sample size of 150k+150k jets).

- Adding color (only possible for the CMS jet sample that differentiates tracks from

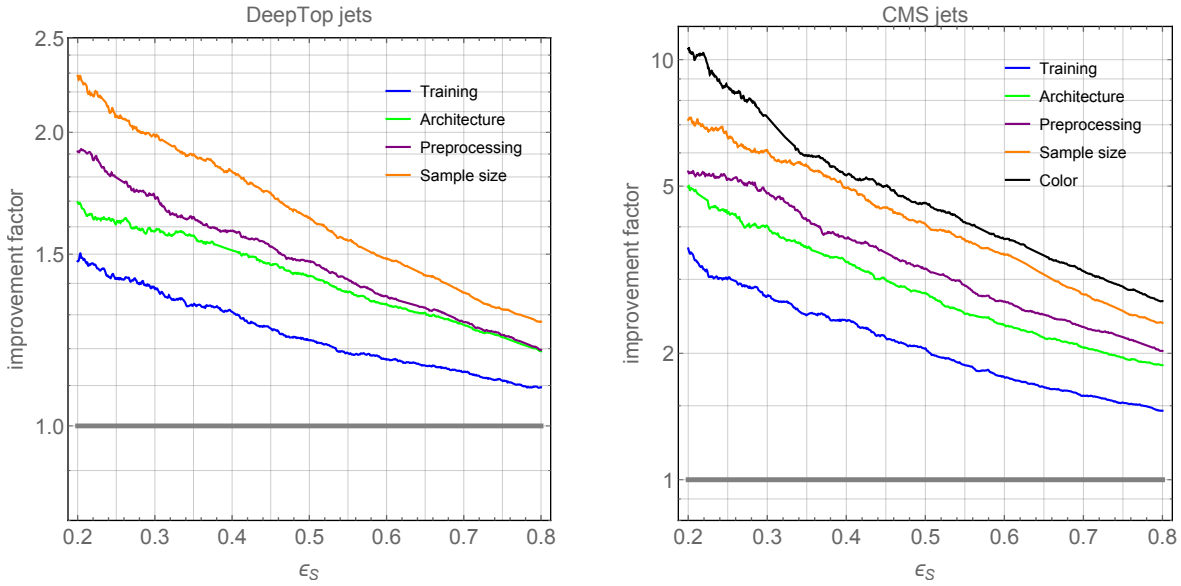

Figure 2.6: Ratio of the ROC curves in figs. 2.4–2.5 over the minimal DeepTop tagger ROC curve, providing another view of the cumulative improvements.

neutrals) resulted in a very modest improvement in the tagger performance, shown in the black curve in figs. 2.5-2.6.

We see that with these modifications we can achieve a factor of $\sim$ 3–10 improvement (depending on the tagging efficiency) in the background rejection rate for the CMS jet sample and a factor of $\sim$ 1.5–2.5 improvement for the DeepTop jet sample.

It is interesting that the improvements are much greater for the CMS jet sample than the DeepTop jet sample. Perhaps the tops vs. QCD jets in the CMS sample have more subtle distinguishing features that can only be learned with the improved methods. Regardless of the reason, this comparison illustrates the strong effect that the fiducial jet selection can have on tagger performance. And although our improvements are more modest for the DeepTop sample, they still do improve it by a factor of $\sim$ 2, which is still quite significant. This demonstrates that the principles described in the previous subsections which motivated these improvements do have general validity.

The comparison between our tagger and state-of-the-art conventional top taggers that use high-level features is shown in fig. 2.7 for the DeepTop jet sample and in fig. 2.8 for the CMS jet sample. As discussed in Section 2.2, for the DeepTop jet sample, we compare

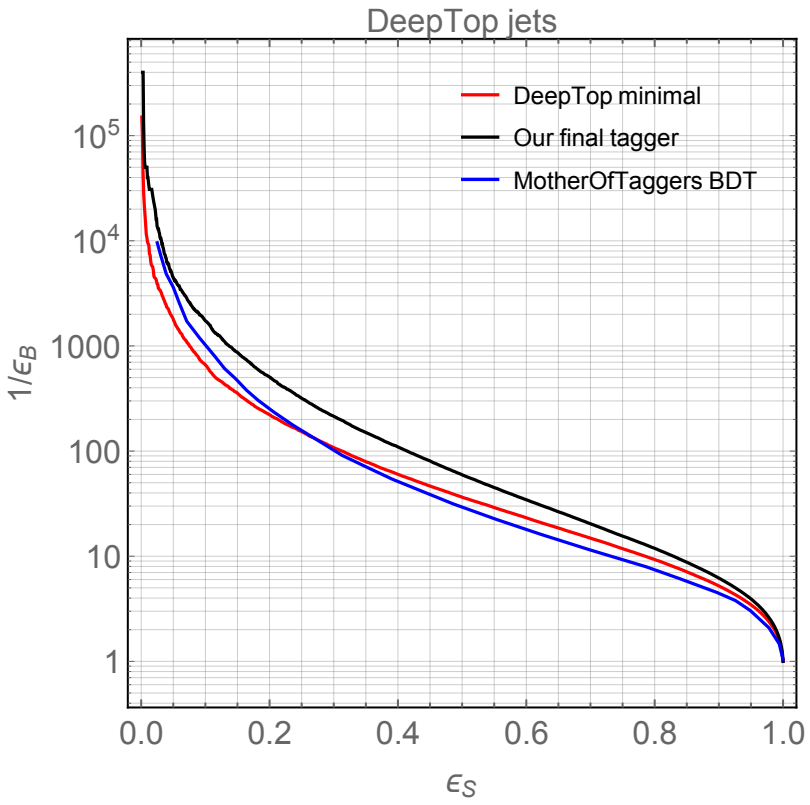

Figure 2.7: ROC curves comparing our best top tagger (black), the original DeepTop tagger (red), and the "MotherOfTaggers" BDT built out of high-level inputs from [96] (blue solid), for the DeepTop jet sample.

directly against their "MotherOfTaggers" BDT ROC curve (i.e. without recasting it). For the CMS jet sample, we include two taggers that are representative of the state-of-the-art in top-tagging with high-level features: a cut-based top-tagger using variables from HTTV2 and N-subjettiness, and a BDT built out of those same variables. The BDT is trained on the same 1.2M+1.2M jets as our final CNN tagger. The BDT improves the performance of the high-level cut-based tagger by a moderate amount.

For the DeepTop jet sample, the baseline tagger was already comparable to the BDT, and our improvements to the former raise it above the BDT by a factor of ~ 2. Meanwhile, for the CMS jet sample, it is surprising to see that the baseline tagger is outperformed by even a simple cut-based tagger at lower tag efficiencies. This again highlights the importance of optimizing a tagger for each fiducial jet selection. Thanks to the factor of 3–10 improvement over the baseline, our final CNN top tagger still shows substantial gains (a factor of ~ 3 in background rejection) compared to the BDT. One exception to this is at the lowest tag

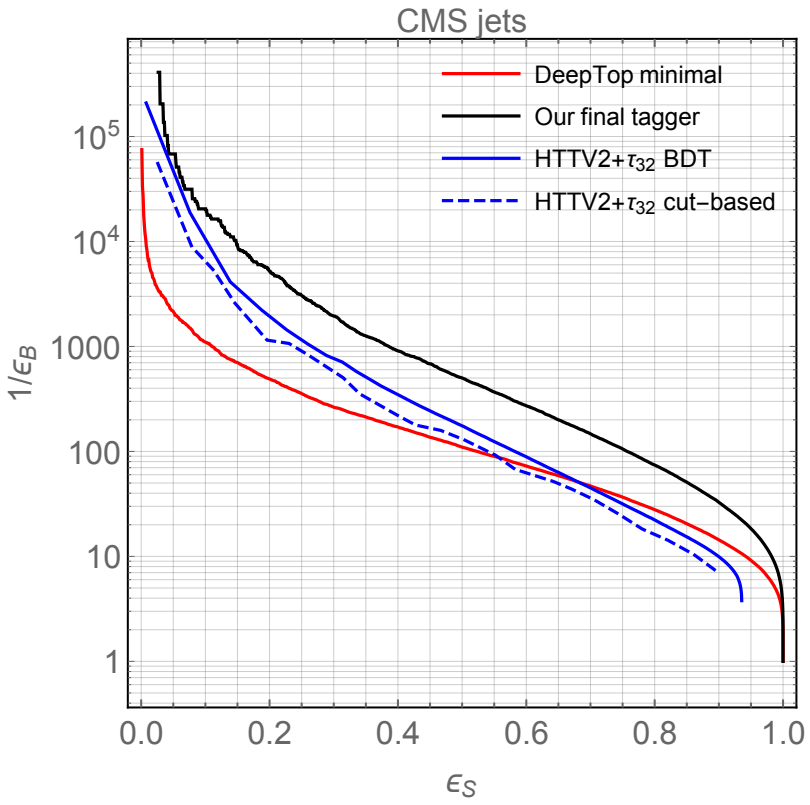

Figure 2.8: ROC curves comparing our best top tagger (black), the original DeepTop tagger (red), the cut-based top-tagger from [102] using variables from HTTV2 and τ_{32} (blue dashed), and a BDT built out of those same variables (blue solid), for the CMS jet sample.

efficiencies ($\epsilon_S \sim 0.1$), where the BDT and the deep learning tagger perform very similarly (this can be seen also in the DeepTop sample). This could be because at these low tag efficiencies, the top is very easy to identify and discriminate against QCD, and so the gain from deep learning is minimized.

2.7 Outlook of this chapter

In this chapter, we showed for the first time how a top tagger based on deep learning and low-level inputs (raw jet images) can significantly outperform state-of-the-art conventional top taggers based on high level inputs. Taking the DeepTop tagger as a starting point, we explored a number of modifications, most of them quite simple, that overall improve the performance by up to a factor of ~ 10 in the ROC curve. Compared to a BDT trained on high-level inputs, our image-based deep-learning top tagger performs better by as much as

a factor of ~ 3.

We believe our work illustrates the enormous promise and potential of modern machine learning. Many more exciting results are sure to follow. In this section we will briefly discuss some of the interesting future directions.

In this work, we made various simplifying assumptions that should be relaxed in future studies. For instance, we ignored pileup. This was motivated by the fact that these are very high p_T jets and we are just trying to classify, instead of trying to measure anything precisely, so we expect pileup to have a negligible effect. But this should be checked – for any actual experimental application one would want to demonstrate the performance of the tagger under realistic pileup conditions. We also restricted to two narrow ranges (350-450 GeV and 800-900 GeV) of top p_Ts. The stability of a tagger performance under a broad range of p_Ts is important to experimentalists, to avoid artificially sculpting the data.

Another glaring omission is b-tagging. Here we have just relied on the momentum four-vectors of the jet constituents, and have not used any impact parameters, displacements or secondary vertex finding. Obviously, since this information is orthogonal to the momenta, we expect that adding b-tagging will give a further boost to the tagger performance. It would be interesting to know whether this boost is enhanced by deep learning or not.

The reason we were not able to add b-tagging is because there is not enough publicly available information to accurately recast the secondary vertex finders used by the experimental collaborations, or even the impact parameters (IPs). The IP resolutions have not been updated past 7 TeV [119], and they are for single isolated tracks or at best very low p_T tops. These IP resolutions are likely to be unrealistically good for tracks in high p_T boosted top environments. Indeed, when we attempted to implement IP significance b-tagging (say, along the lines of [120]) using these publicly available IP resolutions, we found too large of an improvement to the top tagger performance compared to what one sees e.g. in [102].

Another relevant topic that we have not explored in this chapter concerns the issue of overtraining on MC simulations. Clearly, our tagger has no problem generalizing from the training sample to the test sample, but the question is how representative this sample is of the actual data. Since we only used Pythia [109] with some default settings, this question remains unanswered. Some have tried to address it using Herwig [121, 122] as a stand-in

for the data (i.e. training on PYTHIA jets and then testing on HERWIG jets to see if there is any degradation in performance), but this is most meaningful if somehow HERWIG is more realistic than PYTHIA. Otherwise any conclusions from PYTHIA vs. HERWIG comparisons could be misleading.

As noted above, we did not have access to a GPU cluster here. With such computing resources, it would be possible, and important to do a proper architecture and hyperparameter scan to see if the NN performance could be further improved. Our architecture considered here was inspired by the DeepTop paper. However, there are many state-of-the-art CNN architectures out there such as AlexNet [123], Fast-R-CNN [124], VGG [125], ResNet [126], GoogLeNet [127], etc. It would be interesting to test these out and see if any of them offer any further benefit.

It should be straightforward to generalize the top tagger in this work to classify other boosted objects such as W/Z bosons, Higgses, and BSM particles. It would also be interesting to broaden the scope to include partially-merged and fully resolved tops in the list of taggable particles. In this sense, the tagger could have a performance dependent on these two categories, resulting in a greater background rejection at a fixed tag efficiency for merged tops.

Beyond boosted jet tagging, there are countless other potential applications of deep learning to the LHC. For instance, classification of full events is explored in [105]. Furthermore, there are papers that apply Generative Adversarial Networks [128] for simulations in high energy physics in [129–132], where the main purpose is to drastically reduce the event generation time taken by the Geant4 package [133] to emulate the detector response. Other studies focus on extending the ML based classifiers from fully supervised (each event is labeled as signal or background for training purposes) to weakly supervised [134–137]. Another interesting direction to explore would be using unsupervised learning to find all the categories (or discover new ones) of boosted objects or other types of signatures. Given all of these interesting future directions (and more), we believe we are just starting to grasp the scope of the many applications of ML in high energy physics.

Chapter 3

Revealing Compressed Stops Using High-Momentum Recoils

With Michael Park, David Shih, and Brock Tweedie

Appeared in JHEP 1603(2016)151, arXiv:1506.07885

General context of this chapter

In the previous chapter we used computer vision with deep learning to build a single jet classifier for boosted particles starting from low level inputs. In this chapter, we define a full event classifier search instead, using a cut and count method. Searches for supersymmetric top quarks at the LHC have been making great progress in pushing sensitivity out to higher mass, but are famously plagued by gaps in coverage around lower-mass regions where the decay phase space is closing off. Within the common stop-NLSP / neutralino-LSP simplified model, the line in the mass plane where there is just enough phase space to produce an on-shell top quark remains almost completely unconstrained. Here, we show that is possible to define searches capable of probing a large patch of this difficult region, with S/B ~ 1 and significances often well beyond 5σ. The basic strategy is to leverage the large energy gain of LHC Run 2, leading to a sizable population of stop pair events recoiling against a hard jet. The recoil not only re-establishes a $\not{E}_T$ signature, but also leads to a distinctive anti-correlation between the $\not{E}_T$ and the recoil jet transverse vectors when the stops decay

all-hadronically. Accounting for jet combinatorics, backgrounds, and imperfections in $\not{E}_T$ measurements, we estimate that Run 2 will already start to close the gap in exclusion sensitivity with the first few 10s of fb^{-1}. By 300 fb^{-1}, exclusion sensitivity may extend from stop masses of 550 GeV on the high side down to below 200 GeV on the low side, approaching the "stealth" point at $m_{\tilde{t}} = m_t$ and potentially overlapping with limits from $t\bar{t}$ cross section and spin correlation measurements.

3.1 Introduction

Light stops with mass below a TeV are extremely well-motivated by the supersymmetric solution to the hierarchy problem. The uniquely important role of these particles has inspired a growing and increasingly sophisticated set of dedicated searches at the LHC, targeting an array of different possible decay topologies [138–154] (see also [155, 156]). While these searches have already probed significant portions of the possible model space below a TeV, sizable gaps in coverage remain even at $O(100$ GeV), leaving us to consider: Is it possible that light stops have already been produced in abundance in LHC Run 1 but have simply been missed?

In perhaps the most minimalistic benchmark scenario, stops are produced directly in pairs via QCD, and each stop undergoes a one-step R-parity-conserving cascade into an invisible neutralino LSP and an on-shell or off-shell top quark:

$$pp \to \tilde{t}\tilde{t}^*, \qquad \tilde{t} \to t^{(*)} + \tilde{\chi}^0 \tag{3.1.1}$$

The visible composition of the final state is then identical to that of $t\bar{t}$, which serves as a copious background. The main kinematic handle exploited in most searches has been the additional injection of $\not{E}_T$ (or more properly $\not{p}_T$) from the neutralinos. For $m_{\tilde{t}} \gg m_{\tilde{\chi}}$, exclusion limits from $t\bar{t} + \not{E}_T$ searches at Run 1 extend beyond 700 GeV [147]. However, such searches face a major challenge when confronted with lower-mass regions in the stop-neutralino mass plane where the $\not{E}_T$ is squeezed out. In particular, much attention has recently been directed at the "top compression line" $m_{\tilde{t}} \simeq m_{\tilde{\chi}} + m_t$, which defines the boundary between two-body decays into an on-shell top quark and neutralino, and three-

body decays via an off-shell top quark into $Wb\tilde{\chi}^0$. Limits along this compression line are largely nonexistent over a roughly 20 GeV-wide gap in stop mass.

Proposals to probe this region using the total $t\bar{t}$ cross section and spin correlations [157, 158] have led to some inroads near the so-called "stealth" point $(m_{\tilde{t}}, m_{\tilde{\chi}}) = (m_t, 0)$ [138, 141]. But theoretical limitations make it unclear if these searches can be pushed much further, and there are possibly unresolved subtleties in the interplay between top mass and cross section measurements in the presence of a stop signal [158, 159]. The relatively long lifetimes of stops very near to the top compression line has led to a complementary suggestion to use the annihilation-decays of stoponium [160–162], which would lead to distinctive resonant diboson signatures (including, e.g., $\gamma\gamma$ and $Z\gamma$). Projections for Run 2 predict sensitivity up to stop masses of several hundred GeV, depending in detail on the stop chirality admixture. However, these searches become insensitive if the individual stops decay more quickly than the stoponium, which generally occurs as soon as the stop-neutralino mass difference opens up to even $O(\text{GeV})$. Other approaches have sought to use the small amount of $\not{E}_T$ that is available within the bulk of the produced stop pair events. Very detailed measurements of the shapes of the tails of $\not{E}_T$-sensitive observables [163] or their multivariate generalizations [164] may be promising, but a careful accounting of theoretical and experimental errors is not always available, and the one measurement of this type that has been carried out [139] (by ATLAS, in the l+jets channel) does not reach the compression line. A simple cut-and-count style search based on dileptonic m_{T2} [165, 166] or related constrained mass variables [167] should still be viable due to a particularly sharp turnoff of the background, and is also sensitive near the stealth point. But the maximum mass reach of such a search is ultimately limited by low statistics and exhibits a significant dependence on stop chirality. It has also been suggested to utilize electroweak production of stop pairs via VBF, albeit with difficulties in probing stops much heavier than m_t [168, 169].

Given these various limitations, there remains a clear need to consider further alternative options, lest comprehensive exploration of the top compression line be deferred to future precision lepton colliders. To make progress, we may take some inspiration from another compression line, at the very lowest end of the stop mass range: $m_{\tilde{t}} \simeq m_{\tilde{\chi}}$. There, not only

the $\not{E}_T$, but all visible activity is being squeezed out of the decay. Nonetheless, limits exist from the LHC, presently up to roughly 260 GeV [140, 153]. These are obtained using the classic trick of cutting into the region of production phase space where a sparticle pair is produced in association with a visible hard recoil particle, in this case a jet. For an almost completely compressed spectrum, the neutralinos go to zero velocity in the rest frames of their parents, but carry the full energy and therefore take up the full four-momenta. For stop pair production, the $\not{E}_T$ vector in lab-frame is then automatically equal to the net $\tilde{t}\tilde{t}^*$ transverse momentum vector, which in turn approximately balances against the leading jet.

For stop-neutralino spectra near the top compression line, we can define an analogous trick, but now face several novelties. The neutralinos again approach zero velocity in their parent frames, but they share the four-momenta with (almost) on-shell sister top quarks, with fraction $m_{\tilde{\chi}}/m_{\tilde{t}}$ taken up by the neutralinos. Therefore, in the limit of perfectly compressed two-body decay $\tilde{t} \to t\tilde{\chi}^0$, and assuming a single dominant recoil jet with $\vec{p}_T(\text{jet}) \simeq -\vec{p}_T(\tilde{t}\tilde{t}^*)$, we get the following relation,

$$\vec{\not{E}}_T \simeq -\vec{p}_T(\text{jet}) \times \frac{m_{\tilde{\chi}}}{m_{\tilde{t}}}. \tag{3.1.2}$$

The $\not{E}_T$ is now attenuated relative to the recoil p_T, by a factor that can nominally extend down to zero in the massless neutralino limit (corresponding to the stealth stops [157]). This attenuation will generally make searches much more challenging when $m_{\tilde{\chi}} \ll m_{\tilde{t}}$ along the compression line, such that great care will be required in understanding the lower mass reach. For a given neutralino mass, the extra $2m_t$ worth of energy required to make a stop pair also leads to much lower rates relative to conventionally compressed spectra with $m_{\tilde{t}} \simeq m_{\tilde{\chi}}$, especially in association with a proportionately energetic recoil jet. This issue in particular will be greatly ameliorated with the higher beam energy of the upgraded LHC. Finally, the two stop decays produce two on-shell or off-shell top quarks, which add to the visible activity and can inject further $\not{E}_T$ if either W decays leptonically. Perhaps somewhat counterintuitively, the cleanest signal may then be the all-hadronic decay mode, where all of the $\not{E}_T$ comes from the neutralinos, and Eq. 3.1.2 is most closely followed. However, this decay mode also maximizes possible QCD backgrounds, as well as our possible confusion over exactly which jets come from the recoil against the stop pair versus from their decays.

The possible utility of high-momentum recoils in this respect was emphasized relatively recently in [170]. In the present chapter, we seek to put these ideas on firmer phenomenological footing, including a novel set of cuts and treatment of jet combinatorics, a detailed accounting of the various backgrounds, and allowance for a range of possible $\not{E}_T$ measurement performances. Targeting all-hadronic stop decays, we typically find a healthy $S/B \sim 1$, ensuring robustness against systematic errors of up to $O(10\%)$. We proceed to make a detailed forecast for the possible discovery and exclusion coverage in the stop-neutralino mass plane. Our results are summarized in Fig. 3.3, where the proposed search is seen to cover a large portion of the formerly inaccessible top compression line, acting as a bridge between the two-body and three-body search strategies. For the expected 300 fb^{-1} to be delivered through Run 3 of the LHC, exclusion sensitivity extends up to 550 GeV. On the lower end, shrinking $\not{E}_T$ poses a major complication, but we find that exclusion sensitivity down to $m_{\tilde{t}} \simeq m_t + O(10 \text{ GeV})$ may be possible. This would merge our forecasted coverage with that of $t\bar{t}$ cross section measurements and other techniques that perform well in the stealth region, allowing for unbroken coverage. If this can be achieved, it would be a major accomplishment of the LHC, and a further demonstration that the enormous luminosity and broad bandwidth of accessible energies there provides unique opportunities, even for relatively low-mass physics with subtle kinematics.

Our chapter is organized as follows. The next section outlines our proposed analysis strategy and presents our estimated signal sensitivities. Section 3.3 discusses the results and possible extensions. More details of the generation of our event samples are presented in Appendix D.

3.2 Proposed analysis and predicted coverage

Our proposed analysis requires only a few ingredients:

- A veto on isolated leptons.
- A high multiplicity of jets and at least two b-tags.
- An energetic "ISR-jet" candidate.

- Coarsely-reconstructed top-candidates whose masses are not significantly above m_t.
- A strong anticorrelation of ISR-jet and $\vec{\not{E}}_T$ directions.
- A "significant" amount of missing energy, $\not{E}_T/\sqrt{H_T}$, localized near a value set by the ISR-jet p_T cut and $m_{\tilde{\chi}}/m_{\tilde{t}}$.

In more detail, our full reconstruction and selection, applied to 13 TeV simulated data (Appendix D), proceeds as follows.

Reconstructed electrons (muons) are first selected starting from truth leptons with $p_{T,\ell} > 10$ GeV and $|\eta_\ell| < 2.5$, and flat identification efficiency of 0.90 (0.95). (The precise choices for the ID efficiencies are not crucial.) Electrons are then isolated by first computing $\sum_i |p_{T,i}|_{\Delta R<0.2}$ (where the sum is over all other particles within $\Delta R < 0.2$ of the electron) and requiring

$$\frac{\sum_i |p_{T,i}|_{\Delta R<0.2}}{p_{T,\ell}} < 0.1\,. \tag{3.2.1}$$

Electrons that fail this isolation criterion, as well as all other unidentifiable leptons, are returned to the particle list as "hadrons" to be used in jet clustering. Additionally, there must be no jets (defined below) within 0.4 of either an electron or muon. Otherwise, the lepton is vector-summed into the closest jet.[1] Events that contain any surviving isolated leptons are then discarded. This lepton veto significantly reduces important backgrounds where the $\not{E}_T$ arises from a W boson decay, especially l+jets $t\bar{t}$ events and leptonic W+jets. More aggressive approaches than ours are also possible, using τ anti-tagging and/or vetoes on more loosely-identified leptons. Ultimately, we find that our backgrounds containing Ws are moderately dominated by $\tau\nu_\tau$.

Jets are clustered from all truth hadrons, photons, and unidentified leptons (including electrons that fail the initial isolation step). The anti-k_T algorithm [171] in `FastJet` [172] is applied with $R = 0.4$, an initial p_T threshold of 15 GeV, and $|\eta| < 5.0$. Jets from this stage are used for the lepton isolation above. Individual jet energies are then smeared with gaussians according to the expectation for the Run 2 & 3 conditions of $\approx$ 50

[1] While these steps do not explicitly fold in pileup, significant drops in lepton reconstruction and isolation efficiencies in the coming LHC runs are unlikely, especially given the availability of isolation methods that are more tracker-based. It is also important to note that, because of the high recoil p_T cut demanded below, leptons in the dominant backgrounds tend to be quite energetic.

simultaneous pileup events, as projected in the Snowmass 2013 simulation note [173]: $\sigma(p_T)/p_T = (8.2\ \text{GeV})/p_T \oplus (0.55\ \text{GeV}^{1/2})/\sqrt{p_T} \oplus 0.02$.[2] Subsequently, an event must have at least seven reconstructed jets with smeared p_T above 20 GeV and $|\eta| < 2.8$, highly favoring the all-hadronic $\tilde{t}\tilde{t}^*$+jet signal topology and further reducing backgrounds.[3]

Jets with $|\eta| < 2.5$ are b-tagged according to an assumed working point with an efficiency of 0.70 (0.10) for truth b-jets (c-jets). Jets are first truth flavor-tagged by looking for the heaviest overlapping b- or c-hadron in the event record, and then assigned a reconstruction-level identity (b-jet or light-flavor jet) based on the above efficiencies. Mistags of light-flavor jets are not incorporated, nor are backgrounds with less than two heavy-flavor partons in the hard event (see Appendix D). Light-flavor mistags are of subleading importance for both the stop signal and top backgrounds. For W/Z+jets and especially multijets, a complete analysis with light-flavor mistags requires extensive simulation, which we have not undertaken. However, we do not expect this omission to have significant impact on the validity of our background estimates. As a specific corroborating example, we refer to the detailed background composition of the Higgs search $(W/Z)H \to (W/Z)(b\bar{b})$ [176], in which the W/Z+jets backgrounds are dominated by events with two truth b-jets.[4]

Modeling of the $\not{E}_T$ vector is potentially a delicate issue for the low-mass region of this analysis. We employ a nominal model based on $\vec{\not{H}}_T \equiv -\sum_j \vec{p}_T(j)$. This model implicitly incorporates the effects of pileup via the jet energy smearing, and preserves some of the correlations between the $\not{E}_T$ vector and over/under-measured jets. However, it does not account for additional refinements that could come from adding in activity that is not clustered into jets. To provide an approximate indication of how our $\not{E}_T$ modeling affects our results, we also include some comparisons against truth-$\not{E}_T$, denoted $\vec{\not{E}}_T^{\,\text{truth}}$. For both definitions, $\vec{\not{E}}_T$ is not allowed to point along the $\vec{p}_T$ of any of the leading three jets, with a

[2] As of this writing, the most recent version (v1) contains a shifted-decimal typo for the noise coefficient in the written formula.

[3] We do not model "pileup jets" consisting mostly of diffuse pileup particles, of which $O(2)$ per event are expected [174] given our p_T threshold and before dedicated pileup-jet rejection. We anticipate that these will be rejected with reasonable enough efficiency (see, e.g., [175]) so as not to have a major impact on our analysis, though higher thresholds on the individual jet p_Ts would also be an option if necessary.

[4] To give some rough sense of accounting, the "penalty" for QCD to produce a pair of hard, well-separated heavy quarks from a gluon splitting is $O(\alpha_s/\pi)$, which is overall percent-scale. This easily beats the chances of a double-mistag of truth light-flavor jets, which is $O(10^{-4})$. For single-mistag events containing one b-quark at the hard event level, the $O(10^{-2})$ mistag would need to be combined with the very small b PDFs. (Practically such events are paying both α_s/π *and* the mistag rate.)

Baseline Cuts	
lepton veto	no isolated ID'ed leptons with $p_T(l) > 10$ GeV, $\|\eta(l)\| < 2.5$
jets	$p_T(j) > 20$ GeV, $\|\eta(j)\| < 2.8$; $N(j) >= 7$, $N(b\text{-tag}) >= 2$
ISR-jet	$p_T(\text{ISR-jet}) > 550$ GeV
jet/$\not{E}_T$ overlap	$\|\Delta\phi(j_{1,2,3}, \not{E}_T)\| > 0.55$
$\not{H}_T/\sqrt{H_T}$	$\not{H}_T/\sqrt{H_T} > 3$ GeV$^{1/2}$ (including $\not{E}_T^{\text{truth}}$ analysis)
Additional Cuts	
tops	$m(\text{top-candidates}) < 250$ GeV
ISR-jet/$\not{E}_T$ anti-alignment	$\|\Delta\phi(\text{ISR-jet}, \not{E}_T)\| > 2.95$
$\not{E}_T/\sqrt{H_T}$ window	$S/\sqrt{S+B}$ optimized

Table 3.1: Summary of reconstruction cuts.

requirement $|\Delta\phi| > 0.55$. In practice, such a cut is used experimentally to avoid fake $\not{E}_T$ from under-measured jets, as well as real $\not{E}_T$ from heavy flavor decays inside of jets. Within our own multijets samples, the cut is still somewhat advantageous when using $\not{H}_T$. The advantage with $\not{E}_T^{\text{truth}}$ is minor, but we continue to apply the cut to maintain consistency and a higher degree of realism.

Identification of the ISR jet exploits the kinematics of top decay in a simple way. For a b-quark produced in a hadronic top decay, adding in either of the quarks produced in the sister W's decay will produce a subsystem with a mass less than m_t, and more specifically less than $\sqrt{m_t^2 - m_W^2} \simeq 153$ GeV at leading-order with narrow W. These inequalities continue to hold even when the top is below its mass-shell, as the kinematic boundary only becomes lower. The leading two b-jets in the event are taken to be the b-quark candidates. A list of remaining jets in the event is formed which satisfy $m(b + j) > 200$ GeV for *both* b-quark candidates. The highest-p_T jet from this list is then the ISR candidate. Only events with $p_T(\text{ISR-jet}) > 550$ GeV are kept in our analysis. (For an indication of how the signal rate changes with the recoil p_T threshold, see [170].)

Individual top quarks are reconstructed using a procedure borrowed from [142]. Excluding the two leading b-jets and the ISR-jet candidate, the two closest jets in the η-ϕ plane are added to form a "W boson." This in turn is added to the closest b-jet to form a "top quark." The procedure is then repeated amongst the remaining jets and b-jet. In the

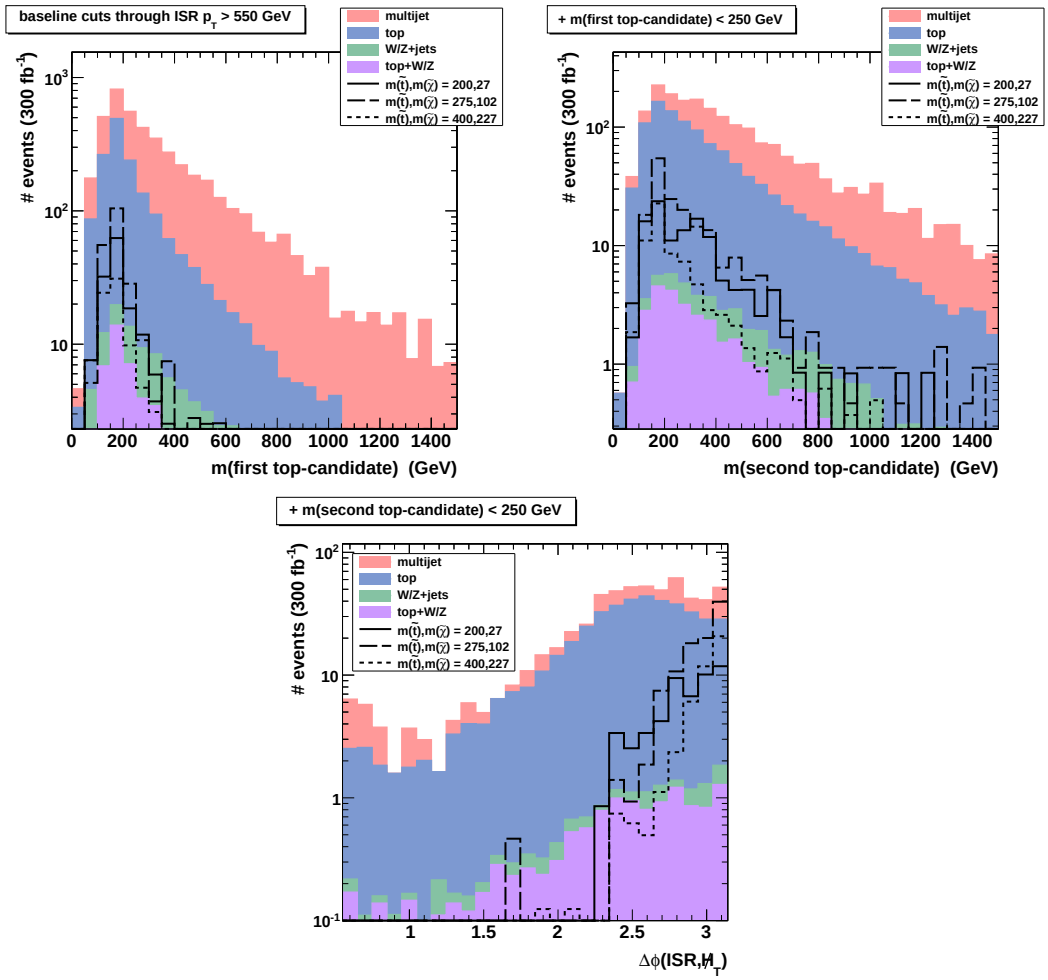

Figure 3.1: Kinematic distributions of stacked backgrounds and some example signal points for the nominal $\not{H}_T$-based analysis, with cumulative cuts. The baseline cuts include the lepton veto, jet counting, ISR-jet p_T cut, jet/$\not{E}_T$ overlap removal, and a cut $\not{H}_T/\sqrt{H_T} > 3$ GeV$^{1/2}$ used to define the simulation samples.

absence of smearings and combinatoric confusions, both top-candidates constructed in this manner would satisfy $m \simeq m_t$ if on-shell, and $m < m_t$ if off-shell. We make a somewhat looser demand of $m < 250$ GeV. The main purpose of this cut is to reduce multijet and W/Z+jet backgrounds, which tend to reconstruct higher masses with a very broad tail.

Finally, we employ the relation in Eq. 3.1.2, which, as per [170], we decompose into angle and magnitude. For the angular component, a strong anticorrelation between the ISR-jet and $\not{E}_T$ directions is demanded: $|\Delta\phi(\text{ISR-jet},\not{E}_T)| > 2.95$. For the magnitude, we expect that the signal $\not{E}_T$ will be approximately equal to $p_T(\text{ISR-jet})\times(m_{\tilde{\chi}}/m_{\tilde{t}})$. Because of the interplay of the hard p_T(ISR-jet) cut and the rapidly-falling production p_T distributions,

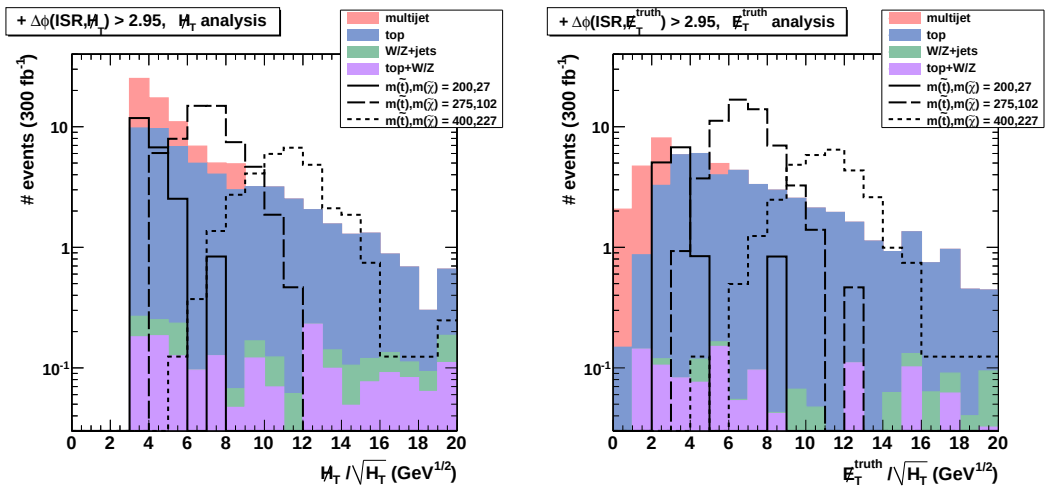

Figure 3.2: Distribution of $\not\!\!E_T$-significance for stacked backgrounds and some example signal points, for the nominal $\not\!\!H_T$-based analysis (left) and the reference $\not\!\!E_T^{\text{truth}}$-based analysis (right). All other cuts have been applied.

	multijet	top	W/Z+jets	top+W/Z	$(m_{\tilde{t}}, m_{\tilde{\chi}})$ $(275, 102)$
baseline cuts	2859	1498	55	46	226
+ m(first top) < 250 GeV	910	1021	19	30	192
+ m(second top) < 250 GeV	151	425	4	12	101
+ $\lvert\Delta\phi(\text{ISR-jet}, \not\!\!E_T)\rvert > 2.95$	32	53	1	2	58
+ $\not\!\!H_T/\sqrt{H_T} \in [4.4, 10.6]$ GeV$^{1/2}$	13	29	< 1	1	57

Table 3.2: Cut flow for the nominal $\not\!\!H_T$-based analysis, normalized to 300 fb^{-1} luminosity, with an example compressed signal point and its optimized $\not\!\!H_T/\sqrt{H_T}$ window.

the signal will appear as a localized bump in $\not\!\!E_T$. Raw $\not\!\!E_T$ can serve as an adequate discriminating variable here, as can other standard $\not\!\!E_T$-sensitive variables such as the ratio $\not\!\!E_T/H_T$ or the "significance" ratio $\not\!\!E_T/\sqrt{H_T}$. We find the last option to be slightly more effective than the others at separating signal from background (at the 10% level in S/B), and choose this for our analysis.

Table 3.1 summarizes the complete set of cuts. Figs. 3.1 and 3.2 show distributions of several of the discriminating variables for backgrounds and some example signal points, illustrating the cumulative purification of the signal. Table 3.2 shows the integrated event counts. Note that, to maintain efficient Monte Carlo generation, a cut of $\not\!\!H_T/\sqrt{H_T} > 3$ GeV$^{1/2}$ has been applied to define a baseline reconstructed sample. (This $\not\!\!H_T$-based cut

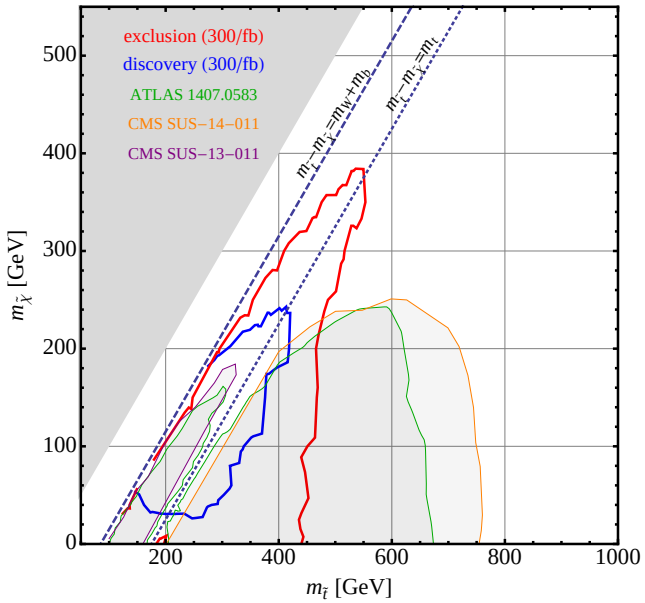

Figure 3.3: Existing Run 1 limits from ATLAS and CMS, and projected 300 fb^{-1} discovery and exclusion sensitivities for our nominal $\not{H}_T$-based analysis. The reference $\not{E}_T^{\text{truth}}$-based analysis (not shown) yields very similar exclusion contours, but somewhat stronger discovery contours at lower masses. Note that our simulation grid does not extend all the way down to the W compression line $m_{\tilde{t}} \simeq m_{\tilde{\chi}} + m_b + m_W$ nor below, where the decay kinematics transitions to four-body. (We also do not indicate existing exclusions in that region. For the stealth exclusions, see Fig. 3.6.)

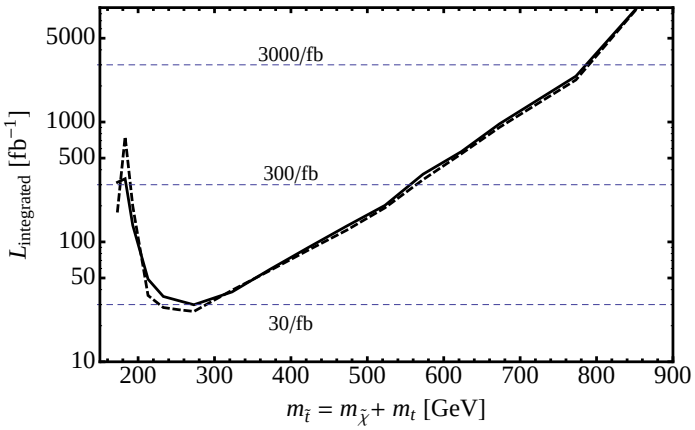

Figure 3.4: Luminosity required for exclusion sensitivity along the top compression line for both our nominal $\not{H}_T$-based analysis (solid) and our reference $\not{E}_T^{\text{truth}}$-based analysis (dashed), assuming 13 TeV and Run 2 & 3 pileup and detector conditions. (Projections beyond 300 fb^{-1} are naive extrapolations, not using HL-LHC conditions.)

is also applied in the $\not{E}_T^{\text{truth}}$-based analysis.)

The analysis thus defined, we scan through the model space of the stop-neutralino mass plane, with finer-grained steps near the top compression line (of order the top quark width). The final $\not{E}_T/\sqrt{H_T}$ window is optimized per sample to maximize the naive statistical signifi-

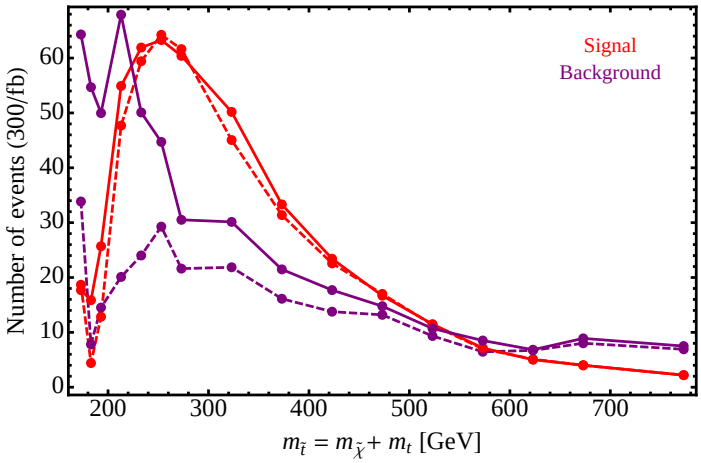

Figure 3.5: Signal (red) and background (purple) counts along the top compression line for 300 fb^{-1}, for both our nominal $\not{H}_T$-based analysis (solid) and our reference $\not{E}_T^{\text{truth}}$-based analysis (dashed).

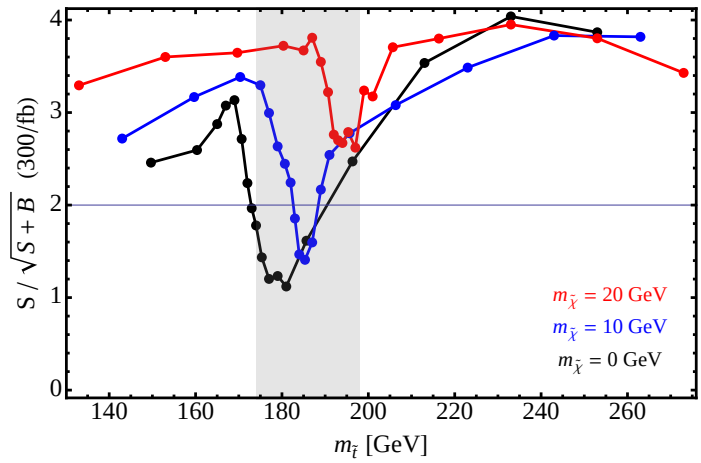

Figure 3.6: Projected 300 fb^{-1} exclusion sensitivity around the stealth point, scanning $m_{\tilde{t}}$ for several fixed $m_{\tilde{\chi}} \ll m_t$, for our nominal $\not{H}_T$-based analysis. The gray shaded region indicates the excluded stop masses from the dedicated ATLAS search for stealth stops [138]. The $\not{E}_T^{\text{truth}}$-based analysis (not shown) yields very similar significances in the dip near the top compression line, but up to $O(1)$ higher significances away from it.

cance $S/\sqrt{S+B}$. We define exclusion threshold as $S/\sqrt{S+B} = 2$, and discovery threshold as $S/\sqrt{B} = 5$. Fig. 3.3 shows our nominal exclusion and discovery contours for 300 fb^{-1}, indicating a near complete closure of the current compression line gap. Fig. 3.4 shows the luminosity required to achieve exclusion-level sensitivity along the compression line. While our simulations are done under Run 2 & 3 conditions, we have also naively extrapolated as far as the HL-LHC luminosity of 3 ab^{-1}. We include as well in Fig. 3.5 a scan of the signal and background rates at 300 fb^{-1} along the top compression line. This indicates $S/B \sim 1$

over most of the range that we study, suggesting good resilience to systematic errors, which we have not attempted to estimate. Finally, in Fig. 3.6 we provide a closer view of the exclusion sensitivity near the stealth point, via a series of scans over $m_{\tilde{t}}$ at fixed neutralino masses.

3.3 Discussion and Outlook of this chapter

Fig. 3.3 suggests that our proposed search strategy can access stops along the top compression line beyond 400 GeV at discovery-level significance, and perhaps up to 550 GeV at exclusion-level significance, over the current phase of LHC running. These numbers already start to approach what was done for non-compressed stops at Run 1. However, unlike those searches, for us the sensitivity is maximized *on* the top compression line. This complementarity is made possible by focusing on the unique kinematic configurations that start to open up at Run 2. It is rather remarkable that the persistent sensitivity gap at the top compression line, which has become a modern benchmark of difficulty in new physics searches, can be covered so quickly and so broadly. Fig 3.4 indicates that the gap will start to close already with a data set comparable in size to Run 1, which should be achievable before the end of 2016.

On the low side, our search very closely surrounds the stealth point $(m_{\tilde{t}}, m_{\tilde{\chi}}) = (m_t, 0)$, as indicated in detail in Fig. 3.6. In fact, we have found that the exclusion-level contour there depends only moderately on whether we use $\not{H}_T$ or $\not{E}_T^{\text{truth}}$, though Fig. 3.5 illustrates that this choice does strongly affect the S/B there. We emphasize the caveat that we have not folded in systematic errors. Ultimately, the major question is how well the multijet background can be controlled and modeled. Given this uncertainty, it is difficult for us to make very concrete statements near the stealth point. But following the discussion in the introduction, it seems highly likely that multiple search strategies will come into play. Even the present state-of-the art searches based on $t\bar{t}$ cross section and spin correlation measurements [138, 141] already overlap with our projections, completing the coverage at exclusion-level.

Our search is also very effective at covering large portions of the three-body region.

While our simulated model points do not extend below the W compression line at $m_{\tilde{t}} \simeq m_{\tilde{\chi}} + m_b + m_W$, and into the four-body region, it seems quite likely that we even continue to have some coverage there. This leaves open the possibility of linking up with monojet and other searches in that region. (See as well [165] for a recast of a soft dilepton search at 7 TeV that already makes some surprising inroads there.) An approach that requires fewer jets and looser hadronic top reconstructions would also likely be fruitful, a possibility that we save for future work.

More generally, we have only very coarsely optimized our analysis, first by fixing most of our selection criteria by-eye on a small subset of model points, and then by selectively scanning over only our final $\not{E}_T/\sqrt{H_T}$ window. With the principle proven, a more carefully optimized suite of cuts would certainly achieve better results, especially for the stealthier model points. Breaking the search into more analysis regions, e.g. binned over p_T(ISR-jet) (or fit over multiple variables), could also be beneficial.

An obvious further extension of the analysis includes HL-LHC, with up to 3 ab^{-1} of luminosity. The very high pileup would likely be a major concern there, as the rate of fake jets rises significantly, and the resolution on $\not{E}_T$ further degrades. Certainly, pushing further into the stealth region will be difficult, although the much higher event rates may allow for more highly-crafted cuts. On the high-mass side, if we naively extrapolate up our 300 fb^{-1} analysis as per Fig. 3.4, we find discovery (exclusion) reach extending to about 800 GeV. Along similar lines, projections for a 100 TeV proton collider are also interesting to pursue. However, as we ultimately scan up to $m_{\tilde{t}} \gg m_t$, we effectively return to the fully compressed situation $m_{\tilde{\chi}} \simeq m_{\tilde{t}}$. All of the compression lines may then practically blur together using more standard "monojet"+$\not{E}_T$ style searches, perhaps supplemented by the additional "soft" activity from the $t^{(*)}$ decays. Such an analysis has been carried out in [177], finding sensitivity to compressed stops up to multiple TeV using the dilepton channel.[5] Finally, all of our results readily generalize to those classes of fermionic top-partner models that exhibit either a conserved or approximately-conserved parity, and contain a

[5] If we naively scale the energies and cross sections from the existing monojet+$\not{E}_T$ searches for fully compressed stops [140, 153] from an 8 TeV machine to a 100 TeV machine (without running the PDFs), we would expect an exclusion of (260 GeV) $\times$ (100/8) $\simeq$ 3 TeV after accumulating a luminosity of 20 fb^{-1} $\times$ $(100/8)^2 \simeq 3$ ab^{-1}. Suggestively, this coarse estimate is very close to that of [177] on the top compression line.

neutral "LSP" boson which plays a role kinematically identical to $\tilde{\chi}^0$ [178]. The only major difference relative to stops, from the perspective of our analysis, is their approximately six times larger cross section at a given mass, yielding commensurately stronger sensitivity.

In conclusion, natural supersymmetry poses some interesting phenomenological challenges, as evidenced by the enduring gaps in coverage of one its simplest incarnations: an NLSP stop and LSP neutralino. While limits continue to push upward in mass in the favorable parameter regions that readily provide lots of $\not{E}_T$, we have seen here that an appropriately constructed analysis at the upgraded LHC, along the lines suggested in [170], can qualitatively extend sensitivity to this model into the more difficult compressed regions at lower masses. Combined, these approaches will leave very little "natural" parameter space unexplored. With its next major phase in progress, the LHC appears poised to provide us with a much more comprehensive perspective on the possible role of supersymmetric top quarks in Nature.

Note added: While this chapter was nearing completion, [179] appeared, which has significant overlap with our results. Their proposed R_M variable (a very close variant of what was originally proposed in [170]) is highly correlated with the $\not{E}_T/\sqrt{H_T}$ variable that we use here, and in general with any variable proportional to $\not{E}_T$ in the presence of a hard ISR-jet p_T cut. There are a number of other differences in our analysis strategy, which lead to a higher S/B with comparable formal statistical significance, and somewhat different sensitivity contours. (E.g., near the specific mass point $m_{\tilde{t}} = m_\chi + m_t \simeq 350$ GeV, we find $S/B \simeq 2$, versus the $S/B \simeq 1$ found in [179].) We also pay additional attention to the approach to the stealth region and the possible role of $\not{E}_T$ resolution. However, we do not make a dedicated study around the W compression line.

Chapter 4

Cornering Natural SUSY at LHC Run II and Beyond

With Matthew R. Buckley, David Feld, Angelo Monteux and David Shih

Appeared in JHEP 1708 (2017) 115, arXiv:1610.08059

General context of this chapter

In this chapter, we derive the latest constraints on various simplified models of natural SUSY with light higgsinos, stops and gluinos, using a detailed and comprehensive reinterpretation of the 13 TeV ATLAS and CMS searches with the first $\sim$ 15 fb^{-1} of data. We discuss the implications of these constraints for fine-tuning of the electroweak scale. While the most "vanilla" version of SUSY (the MSSM with R-parity and flavor-degenerate sfermions) with 10% fine-tuning is ruled out by the current constraints, models with decoupled valence squarks or reduced missing energy can still be fully natural. However, in all of these models, the mediation scale must be extremely low ($<$ 100 TeV). We conclude by considering the prospects for the high-luminosity LHC era, where we expect the current limits on particle masses to improve by up to $\sim$ 1 TeV, and discuss further model-building directions for natural SUSY that are motivated by this work.

4.1 Introduction and Summary

Recently, at the ICHEP 2016 Conference [180], the ATLAS and CMS collaborations presented the results of the search for new physics using the first ~ 15 fb^{-1} at 13 TeV [181, 182]. This represents a significant milestone for the LHC: with this dataset the sensitivity to new physics at the energy frontier begins to truly surpass that achieved at Run I. Now is therefore the perfect time to assess the implications of these results for well-motivated models of new physics such as supersymmetry (SUSY).

Weak-scale SUSY has long occupied a central place in the theoretical expectations for the LHC, as the addition of superpartners to the Standard Model (SM) particles at or near the scale of electroweak symmetry breaking stabilizes the Higgs mass and solves the hierarchy problem (for a review and original references, see e.g. [14]). Given that the superpartners must be heavier than their Standard Model counterparts, the supersymmetric cancellation of loops protecting the Higgs mass cannot be perfect. The heavier the superpartners, the more finely tuned the original bare mass must be against the loop contributions. If we require the theory be fully "natural" – that the level of fine-tuning be less than some fixed amount, taken in this work to be the arbitrary threshold of 10% – then an upper limit can be derived on the mass of the Standard Model SUSY partners [48]. For a recent review on naturalness in SUSY with many original references, see e.g. [183].

While specific realizations of SUSY can have a wide variety of predictions for the spectrum of the superpartner masses, basic requirements of naturalness which hold in a wide class of models include a light higgsino (which directly sets the Higgs mass squared parameter at tree-level), relatively light stop squarks (as the top has an $\mathcal{O}(1)$ Yukawa, leading to large one-loop-corrections to the Higgs), and a relatively light gluino (which corrects the mass of the stop itself, yielding a two-loop correction to the Higgs) [184, 185].

As the higgsino is color-neutral, it is difficult to produce directly and detect at the LHC. However, if the gluino and stop are relatively light as required by naturalness, they will be copiously produced at the LHC. As they cascade decay down to the light higgsinos, they will typically yield at least one or more of the following signatures [186]:

- Significant missing transverse momentum (MET)

- Top quarks
- High object multiplicity

The purpose of this chapter is to investigate the parameter space of natural SUSY that is still allowed by the latest LHC searches. So far, no search has turned up definitive evidence for new physics, and the null results are phrased in terms of limits on a small set of "simplified models". In order to carry these limits over to more general scenarios, e.g. those motivated by natural SUSY, a detailed reinterpretation ("recasting") of the LHC searches is required. In this work, we have performed a comprehensive recasting of the 13 TeV post-ICHEP analyses which are most relevant for natural SUSY (i.e. target the signatures listed above), see Table 4.1 for a complete list. (Previous work that reinterpreted recent 13 TeV LHC results includes [187, 188].) For more details and the validation of our simulations by comparison with the official ATLAS and CMS limits, see Section 4.2 and Appendix E.

Using the recasted searches, we will explore the parameter space of natural SUSY, using a carefully chosen set of representative simplified models. Our philosophy here will be similar to that of [186]: we work purely bottom up, motivated to find the most conservative limits on gluinos, stops and higgsinos. In all the models we consider, the lightest MSSM sparticle is the higgsino, with $\mu \leq 300$ GeV as suggested by naturalness. However, apart from this assumption, we allow ourselves a great deal freedom in the simplified models.[1]

First, as an essential baseline model, we will consider "vanilla SUSY" – the minimal supersymmetric Standard Model (MSSM) with R-parity conservation and flavor-degenerate sfermions. Next we will examine simplified models of natural SUSY that alleviate the latest LHC constraints by either reducing the signal cross section or by reducing the signal acceptance. We will consider the "effective SUSY" scenario [184, 185] where the 1st/2nd generation squarks are decoupled. Decoupling the valence squarks in particular reduces the total SUSY cross section by factors of $\mathcal{O}(10)$ or more in the region of the mass plane near the current LHC limits. We also consider two scenarios that trade MET for jets: baryonic

[1]Since this chapter is focused on the implications of the latest LHC direct searches for natural SUSY, we will not require our simplified models to raise the Higgs mass to 125 GeV, instead remaining agnostic as to the source of this mass. As is well understood, if the SUSY Higgs mass corrections arise only from the MSSM stop squark loop, the level of tuning is at the few percent level or worse (see e.g. [189] for a recent detailed discussion and references).

R-parity violating (RPV) decays of the higgsino (see e.g. [190] for a review and original references); and a hidden-valley (HV) [191, 192] scenario inspired by Stealth SUSY [193, 194]. By trading MET for jets, the signal becomes more difficult to distinguish from QCD, thereby significantly degrading the acceptance.

By examining the LHC limits on these simplified models, we will attempt to draw more general conclusions on viable directions for SUSY models post-ICHEP. For each simplified model, we will overlay the current LHC limits in the gluino/stop mass plane together with the $\Delta \leq 10$ natural regions, for different choices of the higgsino mass μ and the messenger scale Λ. Here Δ is derived from the Barbieri-Giudice fine-tuning measure [48] with respect to a soft SUSY-breaking parameter M, reformulated in terms of m_h instead of m_Z [195] in order to better take into account the effect of radiative corrections to the Higgs quartic:

$$\Delta_{M^2} = \frac{\partial \log m_h^2}{\partial \log M^2} \tag{4.1.1}$$

When multiple sources of tuning are present, we take the maximum tuning as our measure, $\Delta = \max_{\{M_i\}} \Delta_{M_i^2}$.

For the calculation of Δ_{M^2}, it has been conventional in much of the literature to work in the leading-log (LL) approximation (see however [189, 196, 197] for notable exceptions). There the quadratic sensitivity of the Higgs mass-squared parameter to the higgsino, stop and gluino soft masses arises at tree level, one-loop and two-loops respectively:

- Higgsinos:

$$\delta m_H^2 = \mu^2 \tag{4.1.2}$$

- Stops:

$$\delta m_H^2 \sim -\frac{3}{8\pi^2} y_t^2 m_{\text{stop}}^2 \log \frac{\Lambda}{Q} \tag{4.1.3}$$

- Gluinos:

$$\delta m_H^2 \sim -\frac{g_3^2 y_t^2}{4\pi^4} |M_3|^2 \left(\log \frac{\Lambda}{Q} \right)^2 \tag{4.1.4}$$

Here Λ is the messenger scale of SUSY breaking, and Q is the IR scale, conventionally taken to be 1 TeV in many works (see e.g. [189, 198]). Aside from the naturalness bounds this yields on the higgsino, stop and gluino masses, these LL formulas also demonstrate that the

tuning is worsened as the messenger scale is raised. Natural SUSY theories greatly prefer lower values of Λ.

In this work, we go beyond the leading-log approximation and include a number of important higher-order effects, including the full two-loop RGEs, one and two-loop threshold corrections to stop and gluino masses and threshold corrections to the Higgs potential. A detailed description of these effects (and original references) will appear in a companion paper [49]. Here we will summarize the main idea: we translate the tuning bounds on the UV mass parameters M^2 which enter into the Barbieri-Giudice measure into upper limits on pole masses at the IR scale. The physical pole masses are what the LHC sets limits on. Surprisingly, the full set of differences between UV and IR parameters in tuning calculations has largely been neglected in the literature so far, but we find that they have several crucial consequences.

First, they are numerically important and they can raise the tuning bounds on sparticles by $\mathcal{O}(1)$ factors. Second, including these higher-order corrections makes $\Delta_{M_3^2}$ ($\Delta_{m_{Q_3}^2}$) dependent on the stop (gluino) mass. Large gluino masses significantly raise the stop IR mass through the RG, while large stop masses contribute non-negligible threshold corrections to the gluino pole mass. Therefore in a natural spectrum, the stop and gluino mass are actually correlated: a heavy stop implies a heavy gluino, and vice versa. Perhaps it is counterintuitive, but the fact that we have seen neither the stop nor the gluino may be *more* consistent with natural SUSY than the discovery of one and not the other. In any event, this means that the $\Delta \leq 10$ natural region is not simply a rectangle in the gluino/stop mass plane, but instead turns out to be wedge-shaped. Finally, the higher-order corrections include effects from the 1st/2nd generations that become very important in effective SUSY scenarios. At one-loop, heavy 1st/2nd generation squarks appreciably lift the gluino pole mass, which helps to relax the tuning bound on the gluino. At two-loops, the RGEs drive the stop mass lower in the IR, which can strengthen the tuning bound on the stops. See [49] for more details.

We will see that vanilla SUSY is strongly constrained by the current searches and cannot be natural at the 10% level for any choice of the messenger scale – this was true already after Run I. With either Effective SUSY or models that trade MET for jets, the LHC limits

are greatly reduced, but still eliminate most of the parameter space with $\Delta \leq 10$, except at the very lowest messenger scales $\Lambda \lesssim 20$ TeV. Finally, we consider the combination of Effective SUSY with RPV, and show that significant natural parameter space still remains at $\Lambda \lesssim 100$ TeV. As many of models put forward as alternative solutions to the Hierarchy Problem *start* with at least 10% tuning [199–201], the continued survival of natural SUSY serves as a reminder that – despite the lack of discovery – supersymmetry remains one of the least tuned solutions for physics beyond the Standard Model.[2]

Throughout this work, we will neglect the role of the gravitino, and in particular the possibility that the higgsino LSP decays to it within the detector. This is compatible with the low mediation scale $\Lambda \lesssim 100$ TeV provided that the effective SUSY breaking felt by the messengers was much smaller than the ultimate SUSY-breaking scale $\sqrt{F}$ in the hidden sector. (This is the parameter called k in [202].) An assumption along these lines is also necessary to make the baryonic RPV scenario compatible with the low messenger scale; otherwise with very light gravitinos, new proton decay channels such as $p \to \psi_{3/2} K^+$ arise, and proton stability bounds ($\lambda''_{ijk} < (10^{-6} - 10^{-15})(m_{3/2}/1 \text{ eV})$, depending on flavor indices [203]) would preclude the possibility of hiding SUSY by trading MET for RPV jets.

We conclude by showing rough estimates of the LHC reach for sparticles through 300 fb^{-1} and 3 ab^{-1}, using an extrapolation based on the method of [204]. As will be seen, we are situated at approximately the middle of the rapid rise in the superpartner reach due to the increased LHC energy; after reaching approximately 50 fb^{-1} of data (tentatively expected for Moriond 2017), the LHC will have spent most of its energy boost and additional coverage will be slower and more incremental. Overall, we expect the asymptotic improvement in the LHC reach to be an across-the-board increase of $\sim 900 - 1200$ GeV to the current limits, largely independent of the SUSY particle mass. These projections imply

[2] We note that there have been papers in the literature, even during Run I, that have claimed SUSY is at least percent-level tuned in all circumstances. Obviously, given the content of this chapter, we believe these claims were premature. A clear point of reference is with the work of [197]: although we consider a rather similar set of simplified models, we come to completely different conclusions about the tuning. A more in-depth comparison reveals the sources of the discrepancy. Aside from using a different measure of fine-tuning (summing in quadrature and multiplying tunings, vs. taking the max of the EW tuning), the main difference is that in [197], broad conclusions about fine-tuning in SUSY were drawn based on the consideration of a small, limited set of more UV-complete models whose messenger scales never go below $\Lambda = 300$ TeV. Whereas in this chapter, we consider a broad range of messenger scales down to $\Lambda = 20$ TeV, with no attempt at model building. Since we find that only models with $\Lambda < 100$ TeV can be better than 10% fine-tuned after ICHEP, there is in fact no contradiction with the work of [197].

that the high-luminosity LHC (HL-LHC) can exclude or discover all models of fully-natural SUSY that we consider in this work.

These extrapolations assume no qualitatively new analysis techniques will be developed, so there could be room for even greater future improvement. In particular, the recasted limits we have derived on some of our simplified models come from searches that were generally not designed with the phenomenology of the natural SUSY in mind. Perhaps by targeting natural SUSY (and specifically the simplified models considered here), ATLAS and CMS could significantly improve their sensitivity. For example, the RPV and multi-jet searches [205–210] are generally optimized for gluino pair production, but we find them to be also relevant for constraining stop pair production. Since the latter involves a different set of physics objects and object multiplicity, with a greatly reduced cross section, perhaps a re-optimization would better maximize $S/\sqrt{B}$ and further extend the reach in this case. For these reasons, we encourage the LHC collaborations to adopt some or all of our simplified models for natural SUSY, for the purpose of optimizing searches and setting official limits.[3] The question of naturalness is one of the prime motivations for new physics at the LHC, and as such it is too important to be left solely to amateurs such as ourselves!

Our work suggests many future directions that will be interesting and important to explore. On the collider phenomenology side, given the ability of the LHC searches to powerfully constrain conventional natural SUSY models, as demonstrated here, it will be important to examine models with more exotic final states (see [211] for a recent brief review). Possibilities may include displaced decays (for the signatures we study, these were already well constrained by 8 TeV data [212, 213], while displaced leptons are less tested [214]); and collimated particles that fail isolation such as "dirty leptons" [215, 216] and "lepton jets" [217–219]. Also, we have ignored tau leptons in this work, assuming that they will be at least as stringently constrained by either jets+MET or lepton-based searches. It might be worthwhile to test this assumption more rigorously, e.g. in the case of displaced taus where there are important gaps in coverage [214].

On the model building side, there are several, well-known extensions of the MSSM

[3] In our work we have conservatively adopted a 50% "theory uncertainty" on our recasting efficiencies, based on our validations against official limit plots. If ATLAS and CMS made official limits on our simplified models, that alone might "improve" the limits derived in this work by up to 50% in the effective cross section.

(e.g. Dirac gauginos) which provide loopholes to the tuning bounds. These are not considered here, but they are increasingly well-motivated. We will discuss them further in Section 4.5. Even within the more conventional context of natural SUSY with light higgsinos, stops and gluinos, there are many interesting model building directions to pursue. As discussed above, we will show that $\Delta \leq 10$ requires a very low messenger scale ($\Lambda \lesssim 100$ TeV), and this is an important constraint of future models of natural SUSY. This is especially true for models of Effective SUSY, since these constructions generally tie SUSY breaking to the generation of flavor in the SM. This would mean that flavor must also be generated at an extremely low scale, and it is not at all obvious that this is viable. Some examples of previous attempts include Refs. [220–224]. Also, we find that adding a HV/Stealth sector to the MSSM can trade MET for jets and greatly reduce the bounds. It is interesting to speculate whether this additional sector could be used for anything else, such as dark matter or raising the Higgs mass. More generally, obtaining a 125 GeV Higgs is a major issue for natural SUSY and requires going beyond the MSSM, and it is interesting to think about whether extensions of the MSSM which succeed in raising the Higgs mass could also help to hide SUSY at the LHC.

This chapter is organized as follows. In Section 4.2, we describe our methodology for reinterpreting LHC searches (with additional information provided in Appendix E). The models of natural SUSY we consider are described in Section 4.3, and the resulting experimental limits on these models in Section 4.4. We conclude in Section 4.5 with projections for the future reach of the LHC and model-building directions suggested by the existing constraints.

4.2 Recasted searches and methodology

In the following sections, we will consider the status of natural SUSY after the most recent results from the 13 TeV LHC, as mostly reported in the ICHEP 2016 conference [180]. These results, using $12 - 18$ fb^{-1} of data from CMS and ATLAS, greatly extend the experimental reach of the LHC for gluinos and squarks. We concentrate on the searches listed in Table 4.1, each of which has many signal regions (SRs) that target specific mass spectra and

Search	Data (fb^{-1})	Reference
ATLAS 2-6 jets + MET	13.3	ATLAS-CONF-2016-078 [205]
ATLAS 8-10 jets + MET	18.2	ATLAS-CONF-2016-095 [206]
ATLAS b-jets+MET	14.8	ATLAS-CONF-2016-052 [207]
CMS jets + MET (H_T^{miss})	12.9	CMS-PAS-SUS-16-014 [228]
ATLAS SSL/3L	13.2	ATLAS-CONF-2016-037 [208]
ATLAS 1L+jets+MET	14.8	ATLAS-CONF-2016-054 [229]
ATLAS multi-jets (RPV)	14.8	ATLAS-CONF-2016-057 [209]
ATLAS lepton+many jets	14.8	ATLAS-CONF-2016-094 [210]

Table 4.1: Searches most important to our study. All use the 13 TeV LHC data.

supersymmetric production modes.[4]

As in [186], we did not recast searches with photons or two or more opposite-sign leptons, under the assumption that any natural SUSY scenario yielding these signatures would be even more constrained than the simplified models we have considered here.

As can be seen from Table 4.1, we primarily use ATLAS searches. In most cases, the CMS searches have so many signal regions (100+) that they are difficult to reinterpret. A proper approach would require sophisticated statistical methods combining multiple exclusive bins, using information (the correlation matrix of errors) that is not publicly available. In contrast, the ATLAS searches explicitly provide 95% CL limits on number of events due to new physics for each signal region, and generally have far fewer, coarser bins, allowing us to simply use the most sensitive SR to set a conservative (but reasonably accurate) limit.

One important case where CMS did include aggregate signal region information is the jets+MET search with H_T^{miss} [228], which we find to be very powerful. The CMS jets+MET search has b-tagged categories, low-MET and high-MET categories, few jet and many jet categories. As a result, it is equivalent to the union of several different ATLAS jets+MET

[4]We also considered the ATLAS 7-10 jets+MET search [225] with 3.2/fb and the CMS black hole search [226] with 2.2/fb. Due to the strong possibility of control-region contamination, the latter necessitated a conservative reinterpretation along the lines of [186]. Neither search set the strongest limit in any of the simplified models considered in this chapter, so they are not included here. However, an update of the CMS BH search to the full ~ 15 fb^{-1} dataset (especially if optimized for gluino production as in [227]) would likely have competitive sensitivity to high-multiplicity, non-MET simplified models such as the RPV-based scenarios considered here.

searches.[5]

Our simulation methodology is as follows. We generate hard events using MadGraph 5.2.3.3 [232], generating pairs of gluinos, squarks, and antisquarks in all possible combinations. Decay and showering is performed via Pythia 8.219 [109] (with which we implement the RPV and stealth decays of the higgsino), and we use Delphes 3.3.2 [110] with an ATLAS-approximating detector geometry for detector simulation. In order to speed up the event generation, we worked with unmatched samples in most cases.[6] The NLO cross sections for the superparticle production are obtained via Prospino [233–235]. The cutflows for the ATLAS and CMS analyses are recasted using Root 5.34 [236], and validated against the published experimental limits on supersymmetric simplified models.

The details of the simulated analyses, along with the results of these validation checks, are shown in Appendix E. As seen there, while our simulation technique is largely successful in matching the experimental results, sometimes there are slight differences due to the crudeness of our recasting framework. Sources of error could include: the use of Delphes instead of a complete Geant4 [237] detector simulation; the use of the ATLAS detector geometry for CMS searches; or the use of the 70% b-tagging efficiency working point for all searches, while some of the experimental searches use the 77% working point. (This latter choice significantly increases the c-quark mistagging rate: thus, the use of lower efficiency working point will not always reduce our limits when compared to the official searches, especially if the search involves b-vetoes.) Another possible issue is that each of our validation plots (based on a simplified SUSY model) has limits set by a small number of signal regions, while our general models might be sensitive to different signal regions, which are thus never explicitly validated against the experimental efficiencies.

In any event, as can be seen in Appendix E, the addition of a 50% "recasting uncertainty" (i.e. multiplying or dividing the signal efficiencies by a factor of 1.5) around the baseline

[5] Other CMS general-purpose searches [230, 231] provide an equivalent reach on simplified models studied but provide significantly less information. [230] has no aggregate signal regions and does not even provide observed event counts in the text! [231] does have aggregate signal regions, but adds considerable computational complexity in calculating the clustered jets used in the M_{T2} variable, and was beyond the scope of this work.

[6] Because of the choice of models studied in this chapter (in particular, given the high number of jets in the unmatched events), matrix/element/parton-shower matching is usually not necessary: the only case where including extra jets at the generator level makes a difference in the experimental acceptance is for the RPV/Stealth models. We refer to Section 4.4.3 for further comments.

results is sufficient to bring our recast in line with the official limits, in almost every case. For the models of natural SUSY analyzed below, we will show exclusion limits in which we have taken the lower end of our recasting uncertainty. That is, we consider a point in the mass parameter space excluded if it exceeds the observed limit from any of the SRs for each search in Table 4.1, after we have lowered our efficiencies by a factor of 1.5. We use this conservative estimate to make sure that we do not falsely exclude parameter space because of possible inaccuracies in our recasting procedure.

4.3 Overview of simplified models

Here, we will give a brief overview of the various simplified models that we will use in the next section to illustrate the current status of natural SUSY. Although our simplified models are based on the MSSM for the most part (the HV/Stealth scenario is one exception), we expect they are representative of a much broader class of natural SUSY models, and therefore our qualitative conclusions should be much more general.

In all the models we consider, the lightest supersymmetric particle in the MSSM spectrum is the higgsino, which for reasons of naturalness should be lighter than 300 GeV. (We do not consider alternative models where the higgsino mass arises not from μ but from some SUSY-breaking operator [238–242]. We will discuss this possibility further in Section 4.5.2.) At present, the best limits on direct higgsino production are set by LEP, with $\mu \geq 95$ GeV for a stable LSP [243, 244] and $\mu \geq 103$ GeV for RPV decays of the higgsino into udd quarks [245, 246]. (As discussed in the Introduction, we assume that the gravitino is such that the higgsino does not decay to it within the detector.) The recent CMS search with opposite-sign leptons and MET [247] does not yet set limits on direct higgsino production, but bodes well for the future in finally overtaking LEP limits. We will take two benchmark values of the higgsino mass, either $\mu = 300$ GeV (the maximum allowing $\Delta = 10$) or $\mu = 100$ GeV (at the LEP limit).

One might wonder if a stop or gluino LSP (possibly NLSP with a gravitino LSP) is allowed in any part of the parameter space: if the colored partner is (meta-)stable, searches for R-hadrons [248] set limits at 1.6 and 1 TeV for gluinos and stops, respectively. For a

colored NLSP with prompt decays to a gravitino LSP, the usual simplified topologies with a massless neutralino apply (e.g. $\tilde{t} \to t\psi_{3/2}$) and both stops and gluinos limits are well above 300 GeV. If the decays violate R-parity, stop and gluino LSPs are excluded by pair-produced multi-jet resonances, up to 400 GeV [154, 249, 250] and 800 GeV [251, 252], respectively. Similarly, the presence of additional light neutralinos and charginos (as might be expected alongside the higgsino LSP) will only add to the decay chains of colored spartners, with more final states more easily picked up by the searches considered here. Therefore, we do not believe that we have introduced significant blind spots by assuming a natural higgsino LSP.

For each choice of μ, we consider the following models:

1. *"Vanilla SUSY"*: the MSSM with R-parity conservation (RPC) and all three generations of squarks degenerate.[7]

2. *"Effective SUSY"*: The RPC MSSM with all squarks other than the stops and the left-handed sbottom decoupled from the mass spectrum (see Refs. [184, 185]). For the light third-generation fields, their (pole) masses are taken to be the same, but our results will still hold if they are of the same order.

   The key advantage this model has over the vanilla MSSM in evading the LHC constraints is the much reduced cross section for colored SUSY sparticle production, as the 1st and 2nd generation squarks are heavy. With a Majorana gluino, the t-channel gluino-mediated valence-squark cross sections are enormous, assuming the squarks are kinematically accessible. In Fig. 4.1, we show the ratio of the total colored SUSY production cross section in the Effective SUSY scenario over the vanilla SUSY case. In the region of most interest for natural SUSY, when both the gluinos and squarks masses are $\sim 1 - 2$ TeV, the cross section for colored pair production is reduced by more than a factor of 10. Obviously, this significantly reduces the experimental reach for these models.

[7] Note that we set both left- and right-handed squarks at the same scale. A variant of this model would have right-handed down-type squarks decoupled: this does not affect the fine-tuning (which is affected by both chiralities of stops, but not by the right-handed sbottom) but reduces the SUSY cross sections by removing the production of $\tilde{d}_R, \tilde{s}_R$. In this case, the limits on squarks are reduced by about 100 GeV with respect to the Vanilla SUSY model (shown in Fig. 4.2).

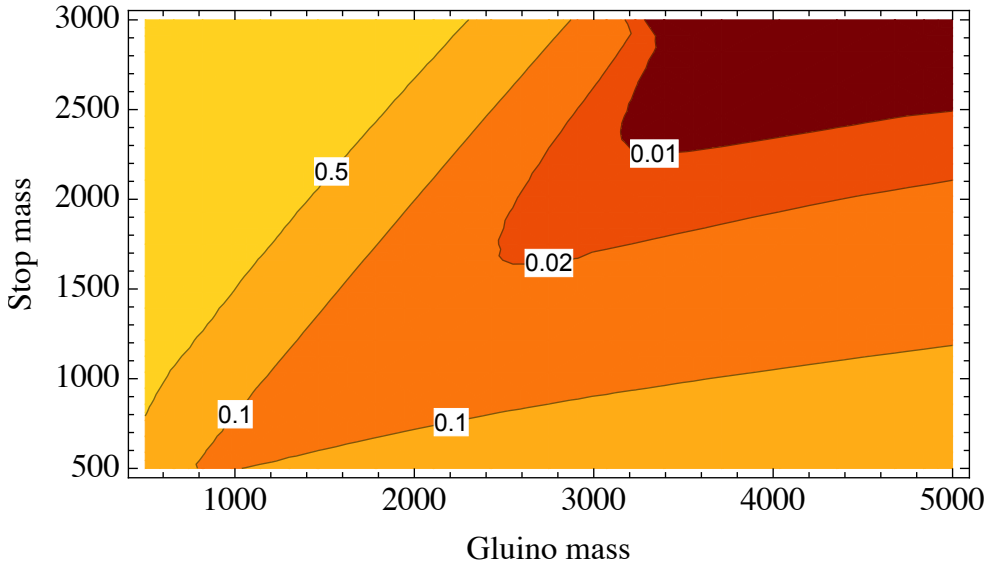

Figure 4.1: Ratio of the 13 TeV total cross section for gluino, squark, and antisquark pair production (in all combinations) in the Effective SUSY model compared to the vanilla SUSY cross section, as a function of gluino and stop masses.

As we briefly discussed in the Introduction (see [49] for details), decoupled 1st/2nd generation squarks tighten (loosen) the naturalness bound on the stops (gluino), because they lower the stop IR masses through the two-loop RGEs (raise the gluino masses through the one-loop pole mass corrections). In the "Effective SUSY" models we consider here, we set 1st/2nd generation squarks to what amounts to a "sweet spot" at 5 TeV: too heavy to be efficiently produced at the LHC, heavy enough to help with the gluino fine tuning, but light enough that they do not reduce the natural stop mass range by much.

3. *RPV SUSY*: The MSSM with baryonic R-parity violation (RPV) in which the lightest higgsino can itself decay promptly to three quarks (see [190] for a review). By turning the MET from the higgsino LSP into more jets via RPV decays, the SUSY signal can be hidden (to some degree) in the larger QCD background. Although there are many possible flavor combinations for UDD RPV, we will focus on the cds operator as the one which is relatively safe from precision constraints [190], yet will relax experimental limits the most. We note that the limits from the will largely carry over to other flavor combinations as well (except for top quarks).[8]

[8]Baryonic RPV scenarios in which the td_id_j operator dominates (e.g. motivated by flavor symmetries

4. *HV/Stealth SUSY*: an R-parity conserving "hidden valley" (HV) extension of the MSSM [191, 192] in which the higgsino can further decay into new gauge-singlet scalar S and its fermionic superpartner $\tilde{S}$:

$$\tilde{H} \to S\tilde{S},\ S \to gg,$$

   The scalar S decays with 100% branching ratio into pairs of gluons, while the fermion is stable due to RPC. This model trades MET for jets, provided that $m_S + m_{\tilde{S}} \approx m_{\tilde{H}}$ and $m_{\tilde{S}} \approx 0$. (We take $m_S = m_{\tilde{H}} - 10$ GeV, and $m_{\tilde{S}} = 5$ GeV.) This simplified model is also a proxy for a number of different well-motivated scenarios. For instance, it could also arise from GMSB with higgsino NLSP, $\tilde{H} \to h + \tilde{G}$, with $m_{\tilde{H}} \approx m_h$ [256]. It can also be thought of as a "lite" version of Stealth SUSY [193, 194]; embedding our particle spectrum into an actual Stealth SUSY construction would provide a natural explanation of the required mass degeneracy, while presumably not modifying the limits significantly.

5. *Effective SUSY with RPV*: a combined Effective-RPV SUSY scenario with first and second generation squarks decoupled and a higgsino LSP decaying to three jets via baryonic RPV. Not surprisingly, this scenario is the least constrained by current searches.

In the models with an unstable higgsino, we assume the conventional cascade decays until reaching the higgsino LSP: for example, the chargino (nearly-mass degenerate with the neutral higgsino) decays to the LSP via an off-shell W and is not allowed to decay directly to jets.

4.4 Results

Finally, we are ready to explore the implications of the latest LHC null results for natural SUSY. We will use our recasting framework to calculate the limits on the simplified models described in the previous section, and then overlay the $\Delta \leq 10$ "fully natural" region (as

[253–255]) result in top-rich final states which either give large-radius jets or leptons. We have checked this case is better constrained: the limits are raised by about 200 GeV for both gluinos and squarks/stops.

determined using the precision calculations in [49]) over these limits to see what range of natural gluino and stop masses are still allowed. As discussed in the Introduction and described in detail in [49], the fully-natural $\Delta \leq 10$ region is wedge shaped, because the physical stop mass now depends sensitively on the gluino mass through the RGEs, while the physical gluino mass depends to a lesser extent on the stop masses through finite thresholds. For other choices of Δ, the limits on the masses scale approximately as $\sqrt{\Delta}$. The extent of these regions depends on the messenger scale Λ, with lower Λ leading to larger allowed masses, see the LL formulas (4.1.2)-(4.1.4) for the rough, qualitative intuition. In our plots, we show the tuning wedges for $\Lambda = 20$ and 100 TeV.[9]

Our results from applying the reinterpreted LHC searches to the natural SUSY models, scanning over gluino and stop masses, are summarized in Fig. 4.2 for vanilla SUSY, Fig. 4.3, for Effective SUSY, Fig. 4.4 for both RPV SUSY and HV/Stealth SUSY, and Fig. 4.5 for Effective RPV SUSY. Of the eight available experimental analyses in Table 4.1, we only show the most constraining for each model, to avoid cluttering the plots. A dashed line indicates the combined nominal limits that we find in absence of any recasting uncertainty; solid lines indicate the limits with the aforementioned conservative reduction in signal efficiency by a factor of 1.5. For reference, we also include the appropriate limit on each model from the 8 TeV data, using the recasting framework developed in Refs. [166, 186, 257].

4.4.1 Vanilla SUSY

In Fig. 4.2 we see that the parameter space for natural vanilla SUSY (i.e. the MSSM with light higgsinos, gluinos, and flavor-degenerate squarks) with $\Delta \leq 10$ is completely excluded by the LHC results, even for $\Lambda = 20$ TeV. In fact, this was basically true even at 8 TeV. Not surprisingly, the most powerful analyses for constraining this scenario are the general-purpose jets+MET searches. The combination of the large production cross section of gluinos and squarks and the large missing momentum carried away by the LSP due to the short decay chain makes vanilla SUSY a rather easy target for these searches.

[9] While $\Lambda = 10^{16}$ GeV is well-motivated, the $\Delta \leq 10$ tuning wedge for this case is so tiny that it would barely show up in the plots, so we do not bother to show it. In fact, for $\Lambda = 10^{16}$ GeV, the $\Delta \leq 100$ tuning region happens to be qualitatively similar to the $\Lambda = 20$ TeV, $\Delta \leq 10$ region, see [49] for details.

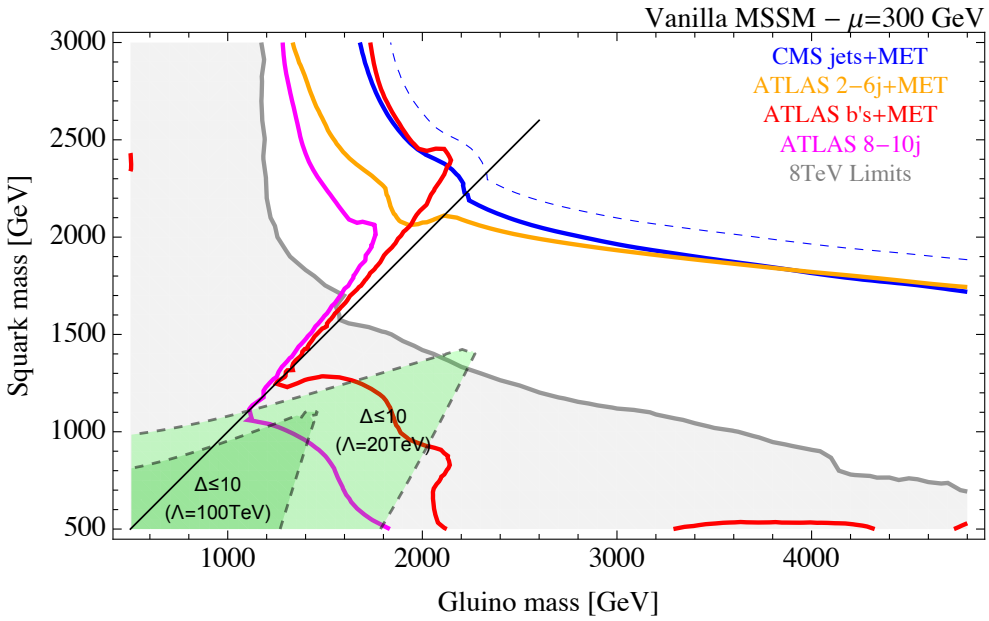

Figure 4.2: Limits on the "vanilla" SUSY model with $m_{\tilde{H}} = \mu = 300$ GeV as a function of the gluino and the degenerate squarks masses. The combined limits for $\mu = 100$ GeV are virtually indistinguishable and we do not show them. All limits are conservative as they already include a factor of 1.5 efficiency reduction to account for possible recasting errors. The nominal limits without recasting uncertainty are shown in dashed blue. The gray shaded area was already excluded by 8 TeV searches (using the framework of Refs. [166, 186, 257]). The shaded green regions with dashed lines show the $\Delta \leq 10$ naturalness bound on the gluino and stop masses for $\Lambda = 20$ and 100 TeV.

Though not shown in Fig. 4.2, we find the current 13 TeV limits correspond to $\Delta = 20$ (i.e. 5% tuning) with a low messenger scale, or $\Delta = 200$ with $\Lambda = 10^{16}$ GeV (this is discussed further in Section 4.4.5). Increasing Λ only reduces the natural region for the gluino and squark masses, as expected from the LL formulas (4.1.2)-(4.1.4).

Some of the limits exhibit a sharp discontinuity along $m_{\tilde{g}} = m_{\tilde{q}}$, becoming much weaker below the diagonal. Above the diagonal, where $m_{\tilde{q}} > m_{\tilde{g}}$, the gluino decays dominantly to Higgsinos via off-shell stops and sbottoms, so the signal is top and bottom rich. Below the diagonal, where $m_{\tilde{q}} < m_{\tilde{g}}$, the gluino decays to all flavors of squarks with nearly equal branching ratio. This reduces the jet multiplicity and the number of b-jets on average, significantly weakening the limits from the searches that require these signatures.

4.4.2 Effective SUSY

We show the limits on the Effective SUSY model (with 1st/2nd generation squarks decoupled to 5 TeV) in Fig. 4.3: gluinos below 1.8 TeV are excluded while limits on direct stop

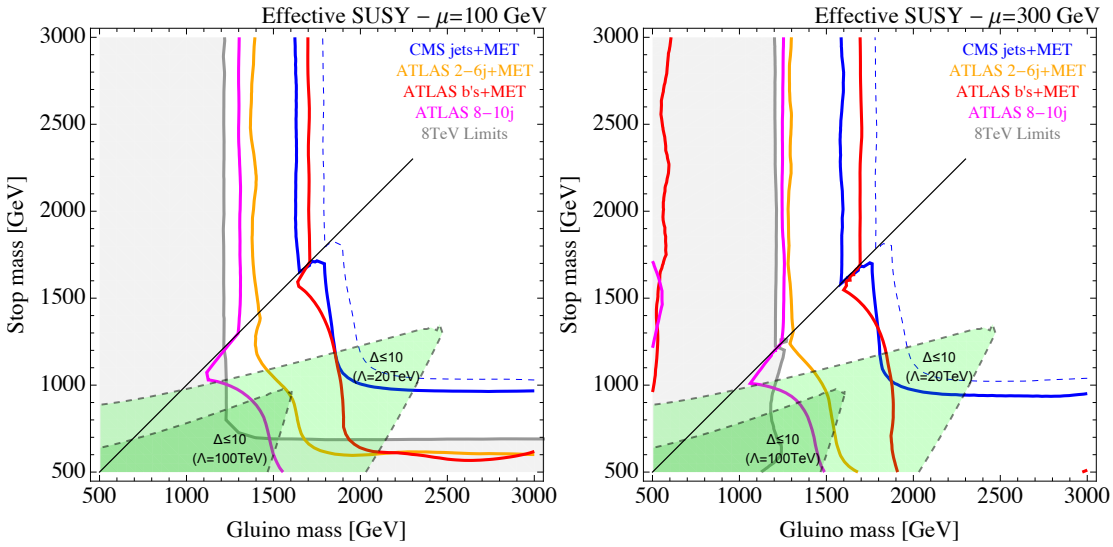

Figure 4.3: Limits on the Effective SUSY model with $\mu = 100$ GeV (left) and 300 GeV (right) as a function of the gluino and the stops and left-handed sbottom masses. The masses of the first and second generation squarks are set to 5 TeV. All other conventions are as in Fig. 4.2.

production are at 900 GeV, significantly raising the previous 8 TeV limits.

Again, we see that the strongest constraints are set by searches targeting large MET, in this case the ATLAS b's+MET and the CMS jets+MET searches. While we did not reinterpret the many dedicated stop searches from ATLAS and CMS for this study, as can be seen, the general SUSY searches are very powerful, excluding stops nearly up to 1 TeV. Indeed, from the CMS official summary plot [258], one sees that the general purpose CMS jets+MET is nearly as effective as the dedicated stop searches in constraining the basic $\tilde{t} \to t + \chi_1^0$ simplified model. So we expect that including the dedicated stop searches would not qualitatively change the conclusions here.

Despite these strong limits, there remains a viable (albeit small) range of natural gluino and stop masses in Effective SUSY, but only for extremely low values of Λ. While $\Lambda = 20$ TeV is not yet ruled out, $\Lambda = 100$ TeV is already excluded. Evidently, reducing the SUSY cross section by a factor of ~ 10 (see Fig. 4.1) by decoupling the first and second generation squarks is not enough to completely relax the constraints from the latest round of searches.

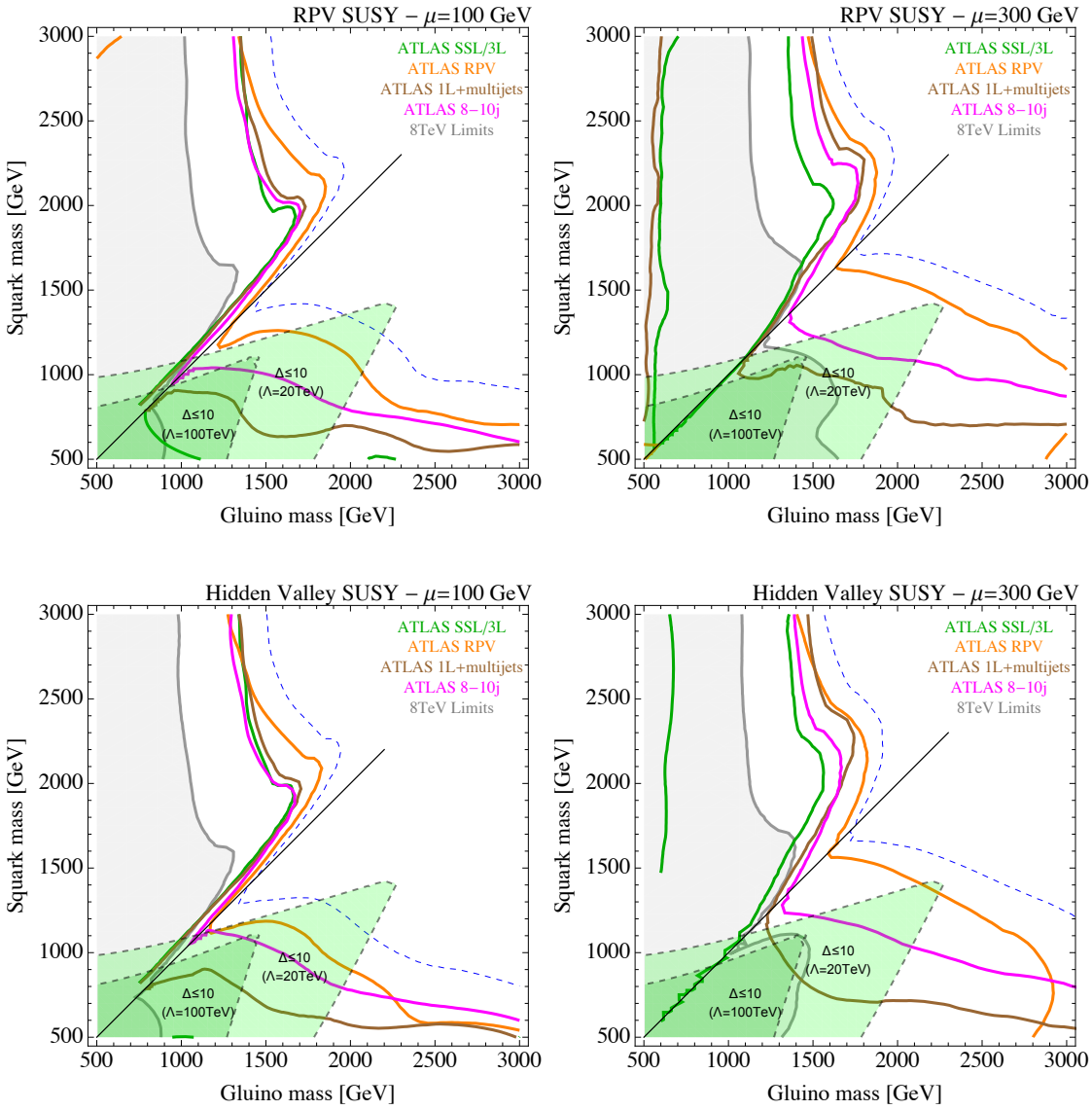

Figure 4.4: Limits on the RPV (top) and HV/Stealth SUSY (bottom) models with $\mu = 100$ GeV (left) and 300 GeV (right) as a function of the gluino and the degenerate squarks masses. All other conventions are as in Fig. 4.2.

4.4.3 RPV and HV/Stealth SUSY

We now turn to SUSY models which trade MET for jets. Obviously, these models are going to be far less constrained by the standard MET-based searches. However, searches which target large multiplicities of high-p_T jets instead of MET (such as the ATLAS 8-10 jets search [206] and the ATLAS RPV search [209]), are still very powerful. In these scenarios, we have included one additional jet at the generator level (and matched the matrix-element and parton-shower calculations in the MLM scheme [259–261]): for squarks, the hard process

would have resulted in 8 final partons, and adding an extra parton raises the reach of the ATLAS RPV and ATLAS 8-10 jets searches by approximately 100 GeV.

In Fig 4.4, top row, we show the limits on RPV SUSY, allowing the higgsino to decay into a trio of *cds* quarks (the results would be similar for any $u_{i\neq 3}d_j d_k$ operator, in particular, for final states with b quarks the ATLAS RPV limits would increase, while ATLAS 8-10 jets would stay the same as it does not involve b-tagging). As can be seen, while the natural masses are excluded for $\Lambda = 100$ TeV, a small region of the $\Lambda = 20$ TeV gluino and squark mass range remains unexplored, assuming the higgsino mass is 100 GeV. If this mass is raised to 300 GeV, the jets resulting from the RPV decay are more effectively captured by the high-multiplicity searches, and the entire $\Delta < 10$ space is excluded. With a lighter higgsino, the quarks in the final states are more collimated and result in significantly fewer resolved jets, which is more difficult to distinguish from the QCD background. This important characteristic was discussed at length in [186].

Again, as in the vanilla SUSY case, there is a pronounced shift in the strength of the limits across the $m_{\tilde{g}} = m_{\tilde{q}}$ diagonal, because the gluino goes from dominantly decaying to Higgsinos via off-shell stops and sbottoms (above), to decaying to all flavors of squarks equally (below). Above the diagonal, where the gluino decays to Higgsino are top-rich, the ATLAS SS dilepton search [208] sets an equally strong limit as the high-multiplicity searches.[10]

The same features are also seen in the HV/Stealth SUSY results, bottom row of Fig. 4.4. As in the RPV case, $\Lambda = 100$ TeV is already ruled out for HV/Stealth, and only lower values of the messenger scale remain viable. The fact that the limits on the RPV and the HV/Stealth scenarios are so quantitatively similar, despite the scenarios having different kinematics and different number of jets in the final state, is evidence that the LHC limits are fairly robust, and that the simplified models we have chosen are representative of a broader class of scenarios that trade MET for jets.

[10]This may come as a slight surprise, as the SS dilepton searches were found to be not as effective for constraining natural SUSY at 8 TeV [186]. The difference is that in the new search, there is a new signal region (SR1b-GG) that does not require any MET. This further highlights the power and importance of doing SUSY searches with low or no MET.

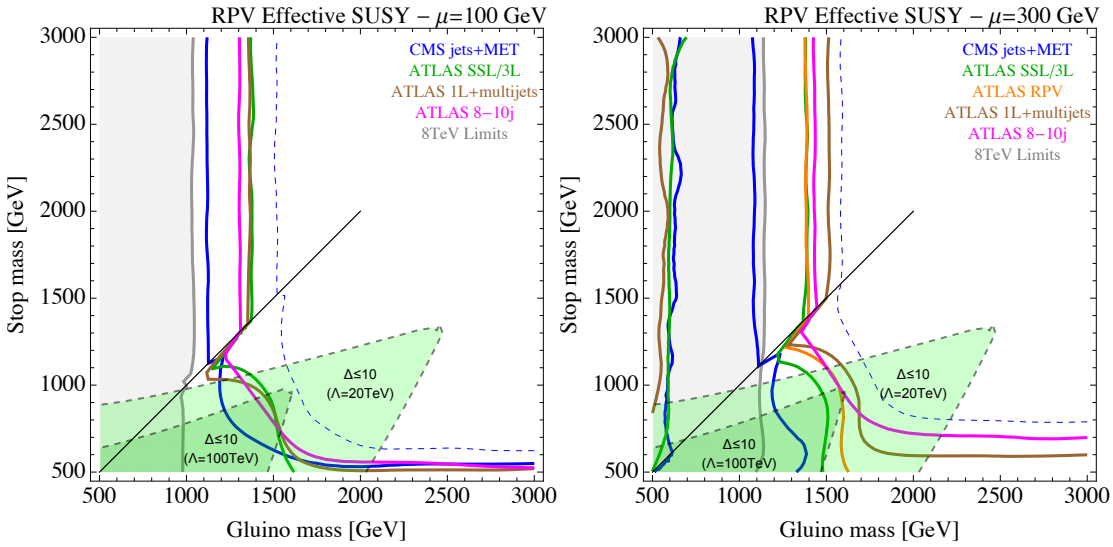

Figure 4.5: Limits on the Effective RPV SUSY model with $\mu = 100$ GeV (left) and 300 GeV (right) as a function of the gluino and the stops and left-handed sbottom masses. All other conventions are as in Fig. 4.2.

4.4.4 RPV Effective SUSY

Finally, having seen the (limited) success of both RPV/HV scenarios and Effective SUSY in evading the LHC bounds on natural SUSY, we consider their combination. In Fig. 4.5, we show the experimental reach for models of Effective RPV SUSY, where the higgsino is unstable and only the two stop squarks and the left-handed sbottom are light, while the remaining sbottom and the first and second generation squarks are decoupled at 5 TeV. As expected, the limits are the weakest of all the models considered so far, with limits on gluinos and third-generation squarks respectively at 1.4–1.5 TeV and 600–800 GeV. (As in the previous subsection, the same limits would apply to any $u_{i\neq 3}d_j d_k$ final state.) Even here, the $\Delta \leq 10$ parameter space for a 100 TeV messenger scale is nearly excluded, but much of the $\Lambda = 20$ TeV parameter space remains viable.

4.4.5 Summary of results and further implications

In the previous sections we have excluded a wide range of gluino, squark and stop masses for a variety of natural SUSY models, and understood the implications for fine-tuning. In Fig. 4.6, we further apply the calculations of [49] in order to show the minimum amount of tuning Δ compatible with a given messenger scale Λ, for each of the natural SUSY models

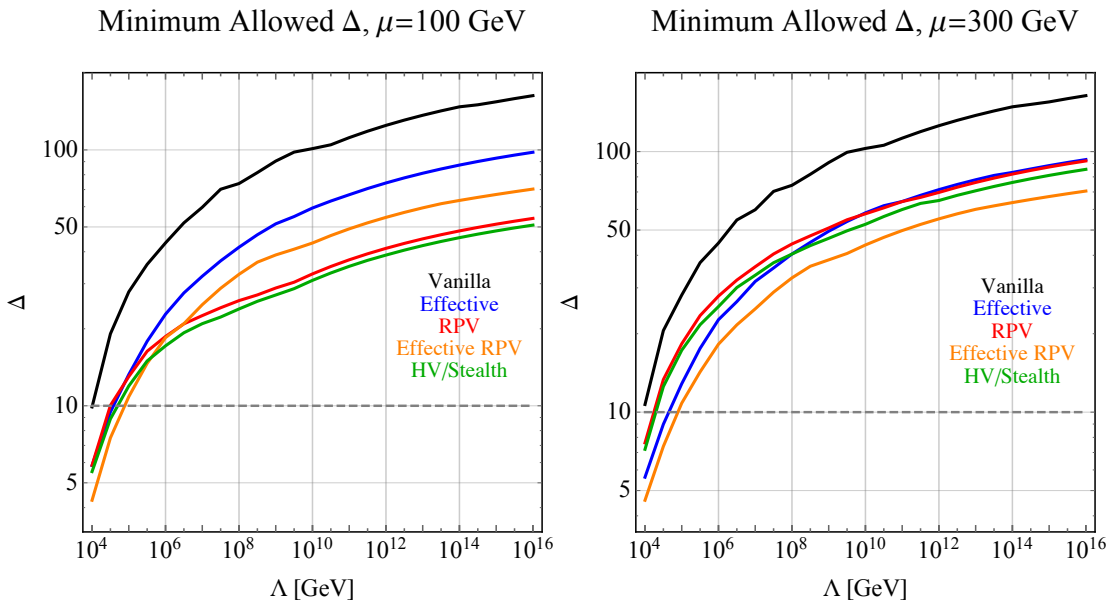

Figure 4.6: Minimum amount of tuning Δ which is experimentally allowed as a function of SUSY breaking scale Λ.

we consider in this chapter. (Qualitatively, these curves can be understood/extrapolated from the results shown in the previous subsections, using the LL formulas (4.1.2)-(4.1.4).) As can be seen, even with our most optimistic scenario (Effective SUSY with RPV decay of higgsinos), the scale Λ must be less than 100 TeV for $\Delta \leq 10$. It should be noted that other choices of "acceptable" levels of fine-tuning allow higher messenger scales. For example every scenario we have considered (except perhaps vanilla SUSY) is only tuned at the percent-level or better, even with messengers at the GUT scale.

Aside from naturalness considerations, the individual recasted limits on each superpartner are noteworthy as they cannot always be obtained from the ATLAS and CMS summary plots (this is particularly true for the RPV/HV/Stealth cases, where the ATLAS RPV and 8-10 jets searches do not consider squark simplified models). For this reason, in Table 4.2 we summarize the asymptotic limits on each colored superpartner (gluinos and either mass degenerate squarks or third-generation squarks); these limits are obtained from the plots above by decoupling either the gluinos or the squarks.[11]

For the models considered so far, we have restricted ourselves to $\mu \leq 300$ GeV, due to the tree-level higgsino contribution to fine-tuning. An obvious question is how the limits scale

[11] We note that, for mass-degenerate squarks, "decoupling" the gluino in practice means taking $m_{\tilde{g}} \gtrsim 10$ TeV, otherwise the gluino t-channel contribution to valence squark production remains non-negligible.

Model	Vanilla SUSY	Effective SUSY		RPV SUSY		Stealth/HV SUSY		RPV Effective SUSY	
μ [GeV]	100 – 300	100	300	100	300	100	300	100	300
$m_{\tilde{g}}$ [GeV]	1730	1690	1690	1310	1500	1330	1440	1350	1490
$m_{\tilde{q},\tilde{t}}$ [GeV]	1500	975	950	700	810	600	750	550	750

Table 4.2: Observed lower limits on the mass of the gluino $m_{\tilde{g}}$ and squarks $m_{\tilde{q}}, m_{\tilde{t}}$ for each model considered above. The limits are asymptotic in the sense that they refer to the case where all other superpartners decouple. The vanilla SUSY limits are independent on the higgsino mass for $\mu < 300$ GeV.

with higher higgsino masses. We find that most of the limits do not change significantly for higgsino masses below $\sim$ 500 GeV, but above $\sim$ 500 GeV, the MET-based scenarios such as vanilla SUSY and effective SUSY start to see some degradation due to compression, with third generation squarks affected first (near 450 GeV), then degenerate squarks (above 600 GeV), and finally gluinos (above 800 GeV). On the other hand, for models with unstable neutralinos, the limits actually *increase* moderately (by $\sim 100 - 200$ GeV) with higher higgsino masses, as the jets neutralino decays are less boosted. These features are fully consistent with the neutralino mass dependence of the validation plots shown in the Appendix.

Before we conclude, a comment is required: in both RPV and HV/Stealth models, it can be seen that fully hadronic MET-based searches set limits that are competitive with searches which do not rely on missing energy. A close inspection at individual events reveals that the source of missing energy is neutrinos in the presence of semi-leptonic W decays (for example, from top quarks or B mesons), where the concurring lepton is not isolated and is therefore removed. The resulting events have non-zero missing energy and no isolated leptons, and are accepted by the all-hadronic searches (in particular, CMS jets and ATLAS 8-10 jets, which have moderate MET requirements). While we have closely mirrored the overlap removal procedures in the experimental papers, our cruder simulation framework might be overestimating the reach of these searches. In any case, the more robust limits from other searches (particularly ATLAS RPV and 1L+multijets) in Figs. 4.4 and 4.5 result in similar exclusions, with differences of at most 50 GeV.

4.5 Conclusions of this chapter and Future Directions

4.5.1 Projections to 300 fb^{-1} and 3 ab^{-1}

We have found in the previous section that while vanilla SUSY has not been fully natural already since Run I, many flavors of SUSY beyond vanilla are currently still viable with $\Delta \leq 10$. Here, we show naive extrapolations of our limits to 300 fb^{-1} and 3 ab^{-1} of integrated luminosity (assuming either 13 and 14 TeV collisions), corresponding approximately to the end of the regular LHC operations and the ultimate end of the HL-LHC runs, respectively.

Our methodology is the same as [204] (we thank A. Weiler for some clarifications in this regard). We assume that the signal cross section is controlled by a single mass scale m, and that signal *efficiencies* and background *counts* remain constant as the integrated luminosity $\mathcal{L}$ and/or center-of-mass (CM) energy $\sqrt{s}$ are increased. The latter makes sense, provided that the mass reach grows in a way that one can always cut harder to keep the backgrounds low, while preserving the sensitivity to new physics at higher and higher mass scales. It also assumes that as $\mathcal{L}$ and/or $\sqrt{s}$ are increased, there are no qualitatively new obstacles that cannot be overcome with more clever analysis techniques. For example, our projections ignore the effect of pile-up: while a challenge for the HL-LHC, it should prove less of a barrier to searches in the mass range above 1 TeV, where SUSY decays typically result in many high-p_T jets and/or large MET.

Using this approach, if the previous limit at CM energy $\sqrt{s_1}$ and integrated luminosity $\mathcal{L}_1$ was at m_1, the extrapolated limit to CM energy $\sqrt{s_2}$ and integrated luminosity $\mathcal{L}_2$ can be obtained by requiring

$$m_1^{-2} f(m_1/\sqrt{s_1})\mathcal{L}_1 = m_2^{-2} f(m_2/\sqrt{s_2})\mathcal{L}_2 \tag{4.5.1}$$

where f is the parton luminosity (taken here to be gg for simplicity – the projections for $q\overline{q}$ initiated production are actually slightly stronger, but qualitatively similar).

Interestingly, under these assumptions, the ultimate improvement in mass reach, compared to current limits, is nearly a constant shift, $m \to m + \Delta m$, across a wide range of masses (1 TeV $\lesssim m \lesssim$ 3 TeV). This can be traced back to the fact that, in this range of $x = m/\sqrt{s}$ values, the parton luminosities at the LHC happen to be dropping nearly expo-

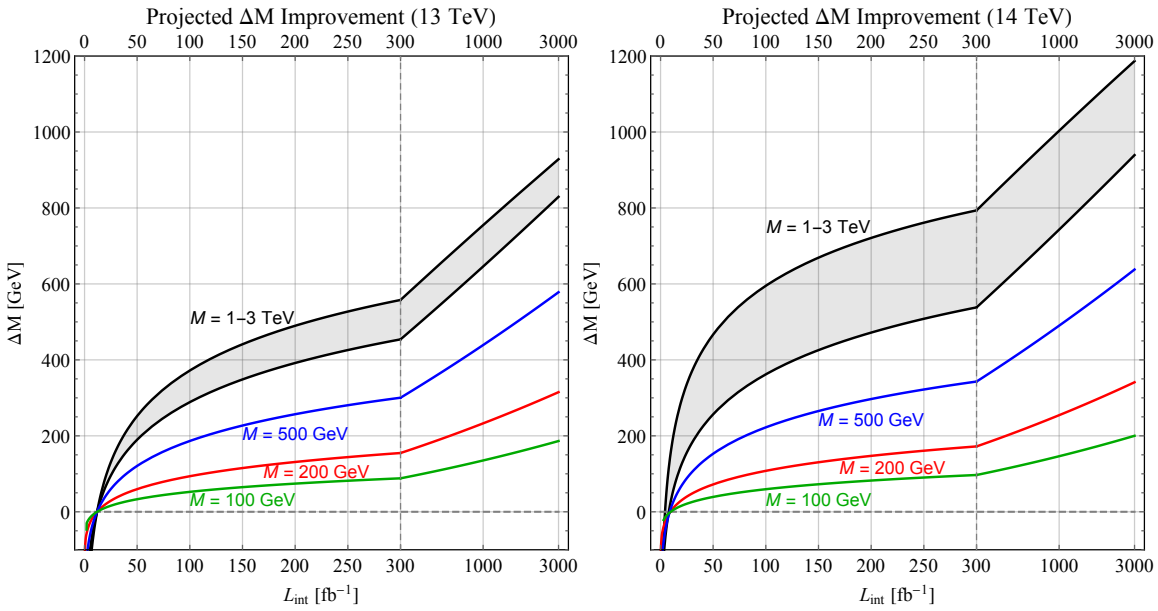

Figure 4.7: Projected improvement ΔM to the experimental 95% CL upper limits on a superpartner excluded by 12 fb^{-1} of 13 TeV data, as a function of integrated 13 TeV (left) or 14 TeV data (right). The black shaded region corresponds to the projected ΔM for an existing limit for a search which currently excludes a particle between 1 and 3 TeV. Here, the improvements are relatively independent of the limit. The green line is the projected improvement for limit which currently excluded a 100 GeV particle, the red line assumes a 200 GeV present limit, and the blue line assumes 500 GeV. The projection technique is as described in the text and [204]. Note the transition from linear to log scale at 300 fb^{-1}.

nentially, $f(x) \sim e^{-ax}$. In Fig. 4.7, we show the increase in mass reach benchmarked against a limit set with 12 fb^{-1} of 13 TeV, as a function of integrated luminosity (for both 13 and 14 TeV LHC running). After 300 fb^{-1} of data is collected at 13 TeV, the rough rule of thumb is that we expect the limits on both gluinos and stops to improve by $\Delta M \sim 500$ GeV from their current levels, with a further improvement to $\Delta M \sim 900 - 1200$ GeV after 3 ab^{-1} at 14 TeV. For example, taking the current best limits on gluino (1.8 TeV) and stop (900 GeV) masses, this would correspond to an ultimate reach of ≈ 3 TeV and ≈ 2 TeV respectively. Using these projections, we see that the $\Delta \leq 10$ regions for all models we consider can be fully explored by the end of the HL-LHC era.

As an aside, while very light particles do not see the full shift in mass reach, the asymptotic improvement would still have a very significant impact, fractionally speaking. This is especially relevant for non-colored particles, where the current limits in many cases are not far beyond the LEP bounds. Here an increase of $\sim 200 - 300$ GeV to the range of experimental sensitivity to these channels would constitute at least a doubling of the existing

bounds, if not more. This provides a strong motivation for the construction of the HL-LHC.

4.5.2 Future directions for model building

One of the principal values of a recasting work on simplified models is that it motivates further model building to populate the allowed parameter space, which could in turn lead to new correlated signatures to explore (or could suggest that the allowed parameter space cannot be realized in UV complete models). So we will conclude by describing some of the model building avenues that are suggested or motivated by our work. This is not an exhaustive list, but highlights some directions of theoretical and experimental interest.

The first (and least interesting) possibility in light of these results is simply to relax the requirement of naturalness. The weak scale may involve a slight numerical accident; after all there are plenty of other percent-level accidents in Nature. This is a logical possibility (perhaps further motivated by the 125 GeV Higgs mass), but it may not be experimentally testable. Tuning at the level of $\Delta \sim 100$ is not well constrained at the LHC, and the relevant parameter space is unlikely to be excluded in most SUSY models in the foreseeable future.

The remaining alternatives all require extending SUSY beyond the vanilla scenario. For instance, in this chapter we have explored two possibilities. The first, effective SUSY, lowers the total SUSY cross section by removing the possibility of valence squark production. As emphasized in our companion paper [49], without the addition of further particles as in [262], the squarks cannot be set to arbitrarily high masses without risking tachyonic 3rd generation sparticles. Decoupling some of the squarks also raises questions about the resolution of the supersymmetric flavor problem. All of these difficulties are compounded by the requirement of very low messenger scales ($\Lambda \lesssim 100$ TeV). It remains to be seen whether any viable model of effective SUSY exists with such low messenger scales. Some promising prior work that explored models in this direction includes [220–224].

The second avenue we explored is RPV/HV/Stealth SUSY, which reduces the signal to background ratio by trading MET for jets. It would be interesting to investigate the HV/Stealth sector further, to see whether it could be useful for anything else, e.g. dark matter or lifting the Higgs mass. Also, further exploration of RPV scenarios is well-motivated. For instance, a potential option to further reduce the constraints on RPV discussed in this

work might be having at least one large coupling, such that squarks decay dominantly to jets instead of higgsinos (searches for paired dijet resonances are then relevant [154, 249]). Although constraints from flavor physics [190] can be important, this can be accomodated in models with hierarchies dictated by flavor symmetries [253–255]. At the same time, this also opens the possibility of resonant squark production via the *udd* operator, with additional signatures and 8 TeV limits recently described in [263]. Nevertheless, a low messenger scale calls for cautious model-building if new flavor-violating interactions are to be present.

As noted previously, in this work we have not considered the possibility of decays to light gravitinos inside the detector. In the high-MET scenarios (vanilla SUSY, effective SUSY), allowing the higgsino to decay to gravitino plus $h/\gamma/Z$ is unlikely to qualitatively change our conclusions on a stable higgsino, with the increase in final state multiplicity possibly reinforcing our limits. One exception would be the compressed scenario $m_{\tilde{\chi}_1^0} \simeq m_h$, where some of this phenomenology would be covered by our Hidden Valley model, as already noted above. In any event, for what concerns experimental limits, it would be interesting to see if opening a gravitino decay channel would significantly change the limits presented in this work.

Finally, another interesting direction would be to challenge the underlying assumptions going into the tuning calculations: for example the SUSY production cross section can be reduced by introducing "super-safe" Dirac gluinos [264, 265] (which eliminate valence squark diagrams with t-channel gluinos). Alternatively, models where the higgsino mass is not set primarily by the μ term, e.g. [238–242] are increasingly well-motivated. A higgsino LSP above 600 GeV can lead to compressed spectra and greatly weakened limits, as discussed in Section 4.4.5; for instance the gluino could be as light as $\sim$ 800 GeV given the current bounds on the $\tilde{g} \to qq\chi_1^0$ simplified model. Also, if the higgsino was not the LSP, it could lead to weakened bounds if the gluino can decay directly to a HV/Stealth sector [266].

In this work, we have explored simplified models motivated by natural SUSY where cascade decays of accessible gluinos and stops down to a light higgsino produce collections of ordinary jets, leptons, etc. We have considered scenarios with and without MET. While limits from current searches may still allow fully natural SUSY models, it is a testament to the breadth of the ATLAS and CMS experimental programs that much of the $\Delta \leq 10$

parameter space is fully excluded already, while what remains (at $\Lambda \lesssim 100$ TeV) can be completely covered by the end of the HL-LHC run.

Note Added The first preprint version of this chapter differed with respect to the present published version in two aspects: first, it did not include matching, which led to an underestimation of some limits, especially for the ATLAS RPV search constrains on unstable neutralino scenarios of Sec. 4.4.3. Second, a bug was found in Delphes 3.3.2 which caused an overestimation of the ATLAS 8-10 jets search limits on the same RPV and Hidden Valley scenarios.[12] The neutralino, which had a significant boost originating from the large mass splitting with the squarks or gluinos, decays to boosted quarks and in the ensuing parton shower a small (but significant enough) fraction of events had long-lived unstable hadrons, with a nominal lifetime large enough to escape the detector. While at the LHC those would deposit all their energy in the hadronic calorimeter and then decay, Delphes would throw away their daughter particles as it used only the list of final stable particles within the detector volume for each event. Given these missing high-momentum particles in some events, the resulting $E_T^{\text{miss}}/\sqrt{H_T}$ spectrum was not as steeply falling as it should be, and the requirement $E_T^{\text{miss}}/\sqrt{H_T} > 4\,\text{GeV}^{1/2}$ of Ref. [206] was satisfied in a larger fraction of events, resulting in stronger limits from that search. Fixing this bug reduced the ATLAS 8-10 jets limits by $200 - 400$ GeV, especially for the squarks. The net effect of these two changes is negligible in most of the parameter space of Fig. 4.4 with no differences in the combined limits in the natural regions of parameter space and of at most 100 GeV elsewhere.

[12] For more details and the bug-fix appearing in Delphes 3.4.1, see `https://cp3.irmp.ucl.ac.be/projects/delphes/ticket/1084`.

Chapter 5

Dark Matter and the Higgs in Natural SUSY

With Aria Basirnia and David Shih

Appeared in JHEP 1703 (2017) 073, arXiv:1605.08442

General context of this chapter

In addition to the 125 Higgs mass, null results from dark matter direct detection experiments pose serious challenges to minimal supersymmetry. In this chapter, we propose a simple extension of the MSSM that economically solves both problems: a "dark sector" consisting of a singlet and a pair of $SU(2)$ doublets. Loops of the dark sector fields help lift the Higgs mass to 125 GeV consistent with naturalness, while the lightest fermion in the dark sector can be viable thermal relic DM, provided that it is mostly singlet. The DM relic abundance is controlled by s-wave annihilation to tops and Higgsinos, leading to a tight relation between the relic abundance and the spin-dependent direct detection cross section. As a result, the model will be fully probed by the next generation of direct detection experiments. Finally we discuss the discovery potential at LHC Run II.

5.1 Introduction and Summary

The MSSM paradigm is under siege from both the LHC and dark matter (DM) direct detection. The Higgs mass at tree-level in the MSSM is famously bounded by m_Z, and relying on radiative corrections from stops and other particles in the MSSM forces the stops to be either at least $\sim$ 10 TeV or their A-terms to be multi-TeV (for recent reviews and original references, see e.g. [14, 46, 47]). Together with the null direct search results at the LHC, this puts the fine-tuning in the MSSM at the percent level or worse. Meanwhile, to evade stringent direct and indirect detection bounds, thermal relic neutralino DM in the MSSM must rely on increasingly contrived numerical accidents (well-tempering, blind spots, funnels, co-annihilations) or an increasingly heavy SUSY scale (e.g. $\sim$ 1 TeV Higgsinos or $\sim 2-3$ TeV winos) (see e.g. [63–65] for recent comprehensive studies). The latter constitutes a DM version of the little hierarchy problem, whereby the WIMP miracle's preference for TeV-scale DM (as opposed to 100 GeV scale DM) is in tension with naturalness.

This strongly motivates looking beyond the MSSM for both the source of the Higgs mass and dark matter. Although it is logically possible that different sectors are independently responsible for the Higgs mass and dark matter, it is interesting to contemplate more elegant and economical models where a single sector generates both. In this chapter, we will study such a model. We will show how to achieve a 125 GeV Higgs and thermal relic WIMP DM consistent with all existing constraints, while greatly ameliorating the fine-tuning, by just adding a pair of $SU(2)$ doublets L, $\overline{L}$ and a singlet S to the MSSM. With a Z_2 "DM parity" that keeps the lightest state in the dark sector stable, together with matter parity from the MSSM, the most general renormalizable superpotential for this "dark sector" is:

$$W = \frac{1}{2}M_S S^2 + M_L L\overline{L} + k_u H_u L S - k_d H_d \overline{L} S \tag{5.1.1}$$

Although it would be interesting to also consider phases, we will focus on real couplings in this chapter for simplicity. Then without loss of further generality, we can take M_S and M_L to be positive.

The idea of extending the Standard Model (SM) with a "singlet-doublet DM" sector has been studied previously in [267–274], motivated by minimality and by the fact that it is a simple generalization of the well-studied bino/Higgsino system of the MSSM. The idea of

lifting the Higgs mass with loops of vector-like matter has also been well-studied [275–292]. But to our knowledge, the two ideas have never been combined before.[1] Combining these two ideas leads to some important differences with previous works.

First, unlike in previous works on lifting the Higgs mass, our dark sector cannot be truly vector-like. The scalar soft mass-squareds of the dark sector must be positive in order to lift the Higgs mass, making our DM the lightest fermion in the dark sector. It cannot be a Dirac fermion, otherwise it would be ruled out by many orders of magnitude by Z-mediated spin-independent (SI) direct detection. Instead, we make the dark sector fermions Majorana (as shown in (5.1.1)) by having only one singlet and not a vector-like pair of them. This only has a minor effect on the contribution to the Higgs mass in this model, which we fully take into account. We will find that a $m_h = 125$ GeV Higgs can be achieved with the fine-tuning coming from the DM being only $\sim$10%, provided that $k_u \sim \mathcal{O}(1)$.

Second, we differ from the singlet-doublet DM models in that we are supersymmetrizing everything.[2] A priori, the parameter space of the entire model (MSSM+dark sector) is vast, but most of the soft parameters do not play a significant role in the analysis. As seen in (5.1.1), our dark sector only couples directly to the Higgs sector and the EW gauge sector of the MSSM. We will keep the Higgsinos light ($\lesssim 300$ GeV), since they contribute to the fine-tuning of the EW scale at tree level. As a result, DM annihilation to light Higgsinos through superpartners in the dark sector plays a major role in determining the relic abundance of the DM. Meanwhile, it does not change our analysis qualitatively to decouple all other MSSM superpartners (effectively at the $\sim$ TeV scale). This is further motivated by the null results from the LHC. (We will remain completely agnostic as to the origin of the SUSY-breaking soft masses in this model. UV completing this with a viable messenger and hidden sector will be an interesting direction for future work.)

We will further simplify the analysis of the model by focusing on the regime where the dark matter χ is mostly-singlet, i.e. $M_S < M_L$ and $v \ll M_L$, $M_L - M_S$. As we will argue

[1] A related idea [293, 294] is to use vector-like matter to boost the Higgs mass while simultaneously opening up new annihilation channels for bino-like DM.

[2] Actually, in [268] they also added singlets and doublets to the MSSM. However, they considered soft masses purely from GMSB (whereas we are agnostic) and therefore they never have mostly-singlet fermionic DM. Moreover they fix $k_u = k_d = 0.3$ whereas we have them as free parameters. Finally, they do not calculate the contribution to the Higgs mass from the dark sector.

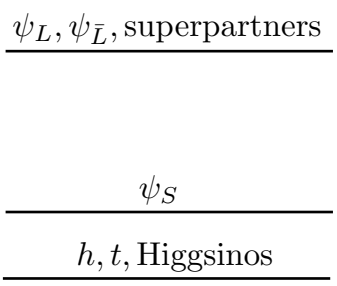

Figure 5.1: A typical, viable spectrum of the model. ψ_S, ψ_L, $\psi_{\overline{L}}$ are the fermionic components of the dark sector fields. Superpartners include scalar components of the dark sector and superparticles in MSSM.

in much more detail in section 5.5, this regime is absolutely necessary in order to evade direct detection bounds while raising the Higgs mass without fine-tuning. A key part of the argument, which distinguishes this from the bino/Higgsino system in the MSSM, is that k_u must be $\mathcal{O}(1)$ in order to lift the Higgs mass without fine-tuning. This eliminates both the well-tempered regime and the mostly-doublet regime vis a vis DM direct detection. The mostly-doublet regime is further unpromising because (by analogy with pure Higgsino DM in the MSSM) it would require a DM mass in excess of 1 TeV, and this would greatly exacerbate the fine-tuning problem, since the rest of the dark sector would have to be even heavier. This leaves the mostly-singlet regime, where the analysis of the model greatly simplifies, and we are able to understand all the features of the model with simple analytic formulas. A cartoon spectrum of the model that describes these hierarchies qualitatively is shown in fig. 5.1.

In this work, we will assume the simplest DM scenario, namely that χ is a thermal relic comprising all of the DM. In the mostly-singlet limit with $k_u \sim 1$, we will show that the thermal relic abundance is controlled by just two DM annihilation channels: s-wave $t\bar{t}$ (through s-channel Z exchange) and s-wave Higgsinos (through t-channel superpartner exchange). Assuming $M_S \ll M_L$ for simplicity, we find:

$$\sigma v_\chi \approx \frac{3k_u^4 m_t^2}{32\pi M_L^4} + \frac{(k_u^2 + k_d^2)^2 \mu^2}{16\pi (M_L^2 + m^2)^2} \tag{5.1.2}$$

where m is a common soft mass for the dark sector scalars. As noted above, the second term

coming from Higgsinos is a major difference from the non-supersymmetric singlet-doublet DM models that have been studied previously. Having more annihilation channels increases σv_χ, making it possible to have smaller effective couplings between the DM and the SM. This opens up more parameter space that is not ruled out by direct detection experiments and yet still has the correct thermal relic abundance, as compared to the non-SUSY singlet-doublet models.

Interestingly, the DM mass drops out of the annihilation cross section (5.1.2) in the mostly-singlet limit. The WIMP miracle becomes one for the mediator scale, not the WIMP mass! With $k_u \sim k_d \sim 1$, $m \sim M_L$ and $\mu \lesssim 300$ GeV, mediator scales of $M_L \sim 1 - 2$ TeV are implied by the thermal relic constraint. Meanwhile the DM can be much lighter than this, alleviating the DM little hierarchy problem. It is also interesting to contrast this with the mostly bino limit of the bino/Higgsino system in the MSSM. There the annihilation cross section is not large enough, being suppressed by g_1^4 instead of k_u^4. Our model (and singlet-doublet DM more generally) gets around this in the mostly-singlet regime with $\mathcal{O}(1)$ Yukawa couplings that are free parameters, not fixed to be g_1 by supersymmetry.

Meanwhile, DM direct detection in these models is completely controlled by the effective couplings of the DM to the Higgs and Z respectively:

$$\delta\mathcal{L} = c_h h\overline{\psi}_\chi\psi_\chi + c_Z Z_\mu\overline{\psi}_\chi\gamma^\mu\gamma^5\psi_\chi \tag{5.1.3}$$

As is well-known, c_h (c_Z) controls the SI (SD) direct detection cross section. For direct detection, as we will review, the current best bounds for our DM mass range of interest ($100 \lesssim m_{DM} \lesssim 1000$ GeV) come from LUX [4] and IceCube [295]. We will convert the official experimental results, which are phrased in terms of the DM-nucleon cross section, into limits on c_h and c_Z. Furthermore, in the mostly-singlet limit, we will obtain simple analytic expressions for c_h and c_Z. We will see that c_h can be naturally small enough for mostly-singlet DM, due to suppression from the heavier doublet scale, as well as a mild blind-spot cancellation:

$$c_h \approx -\frac{m_\chi + \frac{2k_d M_L}{k_u \tan\beta}}{\sqrt{2}v}\frac{k_u^2 v^2}{M_L^2} \tag{5.1.4}$$

provided that $k_u \sim k_d$. We should emphasize here that the Higgs mass depends not just on c_h but also on the effective Yukawa couplings between the Higgs and the other dark sector

particles. So even dialing $c_h \to 0$ does not qualitatively affect the Higgs mass calculation. Meanwhile c_Z is given in the mostly-singlet limit by:

$$c_Z \approx -\frac{g_2}{4c_W}\frac{k_u^2 v^2}{M_L^2} \tag{5.1.5}$$

According to our discussion above, after fixing the thermal relic density constraint $\Omega_{DM}^{obs}h^2 \approx 0.12$, c_Z is essentially fixed to lie within a narrow range which depends primarily on the Higgsino mass μ. Therefore imposing the relic density constraint essentially fixes the SD cross section. Fortunately, this value is not ruled out yet, but the next generation of DM experiments (e.g. Xenon1T [6], LZ [7]) should completely rule out or discover this model.

Although direct detection is controlled by c_Z and c_h, the other facets of the model (relic abundance, Higgs mass) depend on more than just these couplings, so our model does not fit completely into the framework of Z- and h-portal DM. For instance, we mentioned above that the Higgsino cross section arises entirely from t-channel superpartner exchange. Also, we find that DM annihilation to dibosons is suppressed more than would be the case in Z and h portal models, in part due to t-channel exchange of doublet fermions. Similar comments apply to the effective operator formalism: our DM is generally not light enough compared to the mediator scale (the doublet mass) for the annihilation to be accurately captured by effective operators. Evidently, the complete model (5.1.1) is required for an accurate analysis. This illustrates the shortcomings and limitations of both simplified models and effective operator approaches to dark matter.

We have focused primarily on the standard direct detection searches in this work, because other indirect probes of our dark sector are far less sensitive. For example, the Fermi experiment and others have searched for energetic photons produced through DM annihilating at the centers of dwarf galaxies. For DM masses above 100 GeV, Fermi does not constrain any point with the right relic-abundance [296], assuming (as is the case for us) that the relic abundance is determined by s-wave annihilation. Meanwhile, searches at colliders and electroweak precision tests (EWPT) could have put constraints on our model. However as we will discuss further in section 5.8.2, LHC bounds [297–300] on c_h and c_Z from monojets+MET and monophoton+MET are orders of magnitude weaker than direct detection for the range of DM masses that we are interested in. We will briefly discuss mono-

(W,Z,h)+MET and show how it could probe the low end of DM masses ($m_{DM} \sim 200$ GeV) in our model, with 300/fb at LHC Run II. Finally, limits from Higgs and Z invisible width do not apply to the mass range of DM that we consider in this work, and we checked that contributions to the S and T parameters are well within the acceptable range, in agreement with previous studies of these variables in closely-related models [271, 279].

In this chapter, we will analyze the model using a combination of simple, approximate analytic expressions valid in the mostly-singlet regime, and more precise numerical methods that take into account the full suite of one (and even two) loop threshold corrections. The analytic approach, while being reasonably accurate, is primarily a source of intuition and understanding. The numerical approach is meant to be more accurate and to provide us with the quantitative results. Clearly, having both numerics and analytics is a vital source of cross-checks, giving us greater confidence in our results.

Our numerical methods are based on publicly available codes. Our starting point was the powerful SARAH 4.5.8 framework [301] for automated analysis of general models. Once we properly defined our model, SARAH automatically generated source code for SPheno 3.3.7 [302, 303] and for micrOMEGAs 4.1.8 [304].[3] The former calculates the spectrum while the latter calculates the DM relic abundance and direct detection cross sections. In our numerical calculations, all MSSM soft masses as well as gauginos are taken to be at 1 TeV, and the A-terms are set to zero. As noted earlier, since μ appears at tree level in fine-tuning of the electroweak scale we treat it differently. We pick $\mu = 300\,\text{GeV}$ in our numerical calculations which corresponds roughly to 10% fine-tuning. We also consider $\mu = 100\,\text{GeV}$ to see the effect of μ on our analysis. Finally, to saturate the tree level contribution to the Higgs mass, we take the other Higgses to be heavy and in the decoupling limit, and we take $\tan\beta = 10$.

The outline of our chapter is as follows. In section 5.2 we introduce the model. Then in section 5.3, we derive direct detection limits from LUX and IceCube on the effective couplings c_h and c_Z. We will emphasize that these results are general and are not limited to the model we consider in this work. In section 5.4 we compute the one-loop corrections to

[3] We are extremely grateful to Florian Staub for his time and patience in helping us set up the SARAH model and link it to these other codes.

the Higgs mass from the new particles in our model, and we discuss fine-tuning. We argue in section 5.5 that the mostly singlet case is the only viable scenario. In the mostly singlet limit, we provide analytic expressions for dark matter annihilation in the early universe for our model in section 5.6. In section 5.7 we put everything together to show the viable parameter space that satisfies all direct detection constraints while having the right relic abundance and Higgs mass. Here we demonstrate quantitatively that requiring χ to be all of the DM essentially fixes c_Z (and hence σ^{SD}) to a unique value which is not yet ruled out by direct detection, but will be fully within reach of the next generation of experiments. We conclude by studying the collider signatures for LHC Run II and the UV behavior of the model, and giving suggestions on future directions on section 5.8. Technical details and validations are reserved for three appendices. In appendix F we review the derivation of the direct detection cross sections from effective DM nucleon couplings. We validate our numerical and analytical calculations of the Higgs mass in appendix G. Finally we provide analytical cross sections for DM production at LHC II in appendix H.

5.2 The Model

We begin by describing the model in more detail. We add to the MSSM a "dark sector" consisting of a vector-like pair of $SU(2)$ doublets L, $\overline{L}$ and a gauge singlet S.[4] The dark sector is equipped with an unbroken Z_2^{DM} parity symmetry under which all new fields are odd and all MSSM fields are even. This makes the lightest new state stable and a DM candidate. Finally, we assume MSSM matter parity, under which all the dark sector fields have the same charge; otherwise there will be additional, potentially dangerous terms.[5] The transformation properties of the dark sector under the gauge and global symmetries is summarized in tab. 5.1.

The most generic superpotential consistent with these symmetries is:

$$\delta W = \frac{1}{2} M_S S^2 + M_L L\overline{L} + k_u H_u L S - k_d H_d \overline{L} S \tag{5.2.1}$$

[4] To keep gauge coupling unification as in MSSM, we can assume L and $\overline{L}$ are part of complete $\mathbf{5}$ and $\overline{\mathbf{5}}$ multiplets of $SU(5)$. We take their colored partners to be heavy and decoupled for simplicity.

[5] The assumption of matter parity implies another stable particle – either the LSP in the MSSM, or the gravitino. Either way, we assume the parameters and cosmological history are such that this will add a negligible additional component to the dark matter relic density.

	$SU(3)_c$	$SU(2)_L$	$U(1)_Y$	Z_2^{DM}	Z_2^M
L	**1**	**2**	$-\frac{1}{2}$	-1	1
$\overline{L}$	**1**	**2**	$\frac{1}{2}$	-1	1
S	**1**	**1**	0	-1	1

Table 5.1: Gauge and global symmetries of the dark sector.

The superpotential has four new parameters in addition to the MSSM: M_L, M_S, k_u, k_d. There is one physical complex phase, but as discussed in the introduction, we will take these parameters to be real in this chapter. In this case, there is still a physical sign. We will take M_L, M_S and k_u to be positive and put the sign into k_d.

For the soft SUSY-breaking Lagrangian, for simplicity we take the minimal case with equal soft mass-squareds and no A- or B-terms:

$$\delta\mathcal{L}_{\text{soft}} = -m^2(|\overline{\ell}|^2 + |\ell|^2 + |s|^2) \tag{5.2.2}$$

(We denote the scalar components of the dark sector superfields with lowercase letters.) Allowing different soft masses for the different fields will not change most of the discussion in this chapter, only the contributions to Higgs mass.

As we want this new sector to increase the lightest Higgs mass analogous to the MSSM stops, we assume that $m^2 > 0$. This implies that the DM candidate is a fermion. Furthermore it is Majorana, thanks to the fact that we have included only one singlet in the theory. Had we started with a Dirac pair of S and $\overline{S}$ and defined the mass term as $M_S S\overline{S}$, our dark matter would have had a vector-like coupling to the Z. In that case it would have been impossible to hide it from SI direct detection experiments while keeping the interesting features of our model.

After EWSB, neutral fields in the dark sector mix through the Yukawa couplings in

(5.2.1). The fermion mass matrix of the neutral states is:

$$\mathcal{M} = \begin{pmatrix} M_S & \hat{k}_u v & \hat{k}_d v \\ \hat{k}_u v & 0 & M_L \\ \hat{k}_d v & M_L & 0 \end{pmatrix}, \tag{5.2.3}$$

where we have introduced $\hat{k}_u \equiv k_u \sin\beta$ and $\hat{k}_d \equiv k_d \cos\beta$, with $\tan\beta = v_u/v_d$ and $v_u^2 + v_d^2 = v^2 \approx (174\,\text{GeV})^2$ as usual. We take large $\tan\beta = 10$ in this chapter to saturate the upper bound on the tree level Higgs mass. The mass matrix is diagonalized by $U\mathcal{M}U^\dagger = \mathcal{M}_{\text{diag}}$. The spectrum of the model consists of three Majorana fermions with masses $m_{\chi_1} < m_{\chi_2} < m_{\chi_3}$ and a Dirac charged fermion with mass $m_{\chi^\pm} = M_L$. The dark matter candidate is then $\chi \equiv \chi_1$.

We note that the fermionic part of our dark sector is analogous to Bino-Higgsino DM in the MSSM (with everything else decoupled), except that in the Bino-Higgsino system, we effectively have $k_u = k_d = g'/\sqrt{2}$, whereas here k_u and k_d are general. In fact, as discussed in the introduction, here we will be primarily interested in k_u, $k_d \sim \mathcal{O}(1)$.

After rotating to the mass eigenbasis, DM-Z and DM-Higgs couplings are generated:

$$\delta\mathcal{L} = c_h h \overline{\psi}_\chi \psi_\chi + c_Z Z_\mu \overline{\psi}_\chi \gamma^\mu \gamma^5 \psi_\chi \tag{5.2.4}$$

where $\psi_\chi = (\chi, \chi^\dagger)^T$ is a 4-component Majorana fermion and c_h and c_Z are given by:

$$\begin{aligned} c_h &= \frac{1}{\sqrt{2}} \text{Re}(\hat{k}_u U_{11}^* U_{12}^* + \hat{k}_d U_{11}^* U_{13}^*) \\ &= \frac{v}{\sqrt{2}} \left(\frac{m_\chi(\hat{k}_d^2 + \hat{k}_u^2) + 2\hat{k}_d \hat{k}_u M_L}{M_L^2 + 2M_S m_\chi - 3m_\chi^2 + v^2(\hat{k}_d^2 + \hat{k}_u^2)} \right) \end{aligned} \tag{5.2.5}$$

and

$$\begin{aligned} c_Z &= \frac{g_2}{4c_W} \left(|U_{12}|^2 - |U_{13}|^2 \right) \\ &= \frac{g_2}{4c_W} \frac{(M_L^2 - m_\chi^2) v^2 (\hat{k}_d^2 - \hat{k}_u^2)}{(M_L^2 - m_\chi^2)^2 + v^2((\hat{k}_u^2 + \hat{k}_d^2)(M_L^2 + m_\chi^2) + 4\hat{k}_d \hat{k}_u M_L m_\chi)} \end{aligned} \tag{5.2.6}$$

As is well-known [269–273], c_h and c_Z play an important role in the analysis of singlet-doublet DM: they are entirely responsible for SI and SD direct detection, respectively. In the next section, we will review the current direct detection constraints on c_h and c_Z.

5.3 DM Direct Detection through the h and Z Portals

In the DM mass range of interest (100 GeV $\lesssim m_{DM} \lesssim$ 1 TeV), the LUX experiment currently sets the best bound on SI elastic WIMP-nucleon scattering [4]. Meanwhile, the best limits for SD elastic WIMP-proton (WIMP-neutron) scattering come from IceCube [295] and LUX [4]. The IceCube limits depend on an assumption of DM s-wave annihilation in the sun exclusively to a single SM final state. As we will show in section 5.6, our DM annihilates in the s-wave to both $t\bar{t}$ and Higgsinos. Annihilation to Higgsinos could weaken the limits somewhat if the Higgsinos are stable, but that depends in detail on the other parameters of the model (such as μ, k_u and k_d). Here we consider the simplest case where annihilation is only to $t\bar{t}$; this will provide the "worst case scenario" where the SD bound from IceCube is strongest. In section 5.7 we will also take into account annihilation to stable Higgsinos.

In this section, we will recast these constraints in terms of the couplings c_h and c_Z. The discussion here can be viewed as an update of the nice treatment in [63] with the latest experimental results (in particular LUX). It is worth emphasizing that these bounds on c_h and c_Z are quite model independent. Any WIMP DM that couples to SM mainly through Higgs and Z (including MSSM neutralinos) should satisfy these bounds.

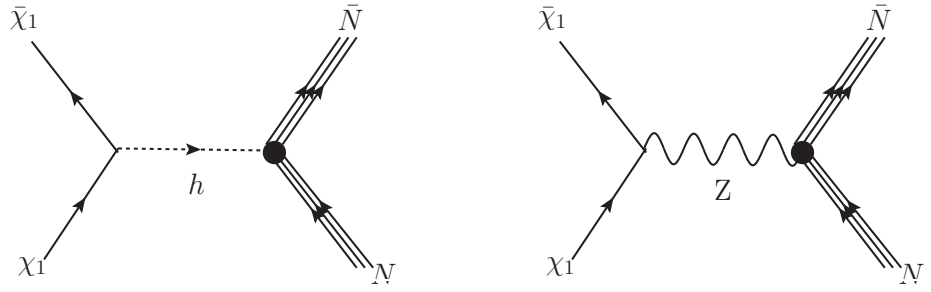

Figure 5.2: Higgs (Z) exchange diagrams contributing to SI (SD) cross sections

To convert the results of these experiments into bounds on c_Z and c_h, we first translate c_Z and c_h into the couplings appearing in the effective Lagrangian for direct detection:

$$\delta\mathcal{L} \supset \sum_q \left(\xi_q^{SI} (\overline{\psi}_\chi \psi_\chi)(\overline{q} q) + \xi_q^{SD} (\overline{\psi}_\chi \gamma^\mu \gamma_5 \psi_\chi)(\overline{q} \gamma_\mu \gamma_5 q) \right). \tag{5.3.1}$$

In Higgs and Z-portal DM models, the SI (SD) terms arise from Higgs (Z) exchange, as shown in fig. 5.2. The coefficients of the effective operators are given in terms of c_h and c_Z as:

$$\xi_q^{SI} = y_q \frac{c_h}{m_h^2} \ , \qquad \xi_q^{SD} = \frac{g_2 \eta_q}{4 c_W} \frac{c_Z}{m_Z^2} \tag{5.3.2}$$

with y_q being the Yukawa coupling and $\eta_q = 1$ (-1) for down-type (up-type) quarks.

Then we use standard formulas that relate the DM-nucleon cross sections to $\xi_q^{SI,SD}$ (see appendix F for our conventions and parameter choices). The result, assuming $m_{DM} \gg m_{p,n}$ is given by:

$$\begin{aligned} \sigma^{SI} &= c_h^2 \times (2.11 \times 10^3 \text{ zb}) \\ \sigma_p^{SD} &= c_Z^2 \times (1.17 \times 10^9 \text{ zb}) \\ \sigma_n^{SD} &= c_Z^2 \times (8.97 \times 10^8 \text{ zb}) \end{aligned} \tag{5.3.3}$$

In principle, σ_p^{SI} and σ_n^{SI} are slightly different but the difference is negligible, so we only take σ_p^{SI} to represent both.

The resulting limits on c_h and c_Z are shown in fig. 5.3.[6] Amusingly, we note that although the constraint on the SI cross section is $\sim 10^5$ stronger than the SD cross-section, translated constraints on c_h and c_Z are of the same order of magnitude. This is because the Higgs-nucleon effective Yukawa coupling (y_{hNN}) is much weaker than the Z-nucleon effective coupling ($\sim g_2$). Recall that the Higgs-nucleon coupling is mainly due to Higgs-gluon-gluon loop-induced interaction with heavy quarks running in the loop

$$y_{hNN} = \frac{\sqrt{2}\alpha_s N_H}{24\pi v} \langle N | G^{a\mu\nu} G^a_{\mu\nu} | N \rangle = \frac{\sqrt{2} N_H m_N}{3 b v} \simeq 10^{-3} \tag{5.3.4}$$

where $N_H = 3$ is the number of heavy quarks and $b = 11 - \frac{2}{3} N_H$ comes from QCD beta function at one loop. The second equality can be calculated using QCD scale anomaly that relates the QCD beta function to nucleon mass (see [307] for the original references).

[6] We agree with the limits from [63] after taking into account a factor of 2 in both c_Z and c_h from 4-component vs. 2-component notation. We also agree with limits on operators from [305] modulo a factor of 4 between Dirac and Majorana fermions and a factor of a few difference between [305] and the latest LUX bounds. We do not agree with the limits on g_A (related to our c_Z via $g_A = \frac{c_w}{g_2} c_Z$) reported in fig. 3 of [306]. Their limit on g_A, derived from essentially the same LUX results, is over an order of magnitude weaker than ours.

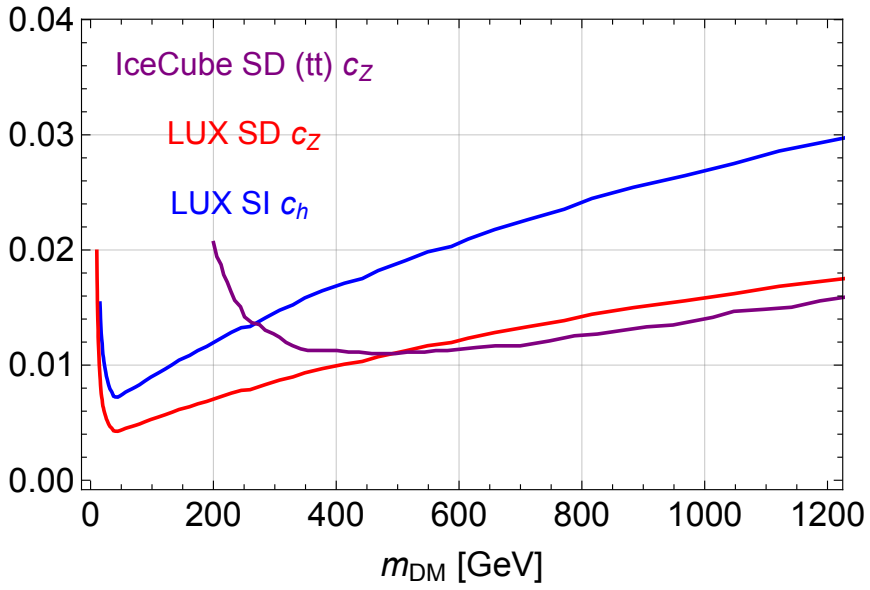

Figure 5.3: Limits on c_h from LUX [4] (blue) and c_Z from LUX [4] (red) and IceCube $t\bar{t}$ [295] supposing DM only annihilates to $t\bar{t}$ (purple).

5.4 Higgs mass and Fine-Tuning

In this section we will describe our calculation of the Higgs mass in the model and its implication for the fine-tuning of the EW scale. As described in the introduction, we used SARAH 4.5.8 [301] and SPheno 3.3.7 [302, 303] to include all the loop corrections (contributions up to two loops both from the MSSM and the dark sector [308, 309]). Here we will describe an analytic treatment of the dominant one-loop contributions from k_u and k_d. This will serve as a valuable source of intuition, as well as a validation of the full two-loop numerical calculation (for more details on the validation, see appendix G).

The one-loop Higgs mass was previously computed in the literature using the Coleman-Weinberg potential in closely-related vector-like extensions of the MSSM [277–279, 281]. However, there are some key differences with our case that necessitate a fresh look. First, as noted above, in these past works, the vector-like extension was Dirac, while ours is Majorana (the difference between $W \supset MS\tilde{S}$ and $W \supset \frac{1}{2}MS^2$). This leads to small differences in the formula for the Higgs mass. Second, previous works presented analytic formulas for the one-loop Higgs mass only in the simplified limit with common fermion masses ($M_L = M_S$). Motivated by the DM side of the story, we will need the Higgs mass in a rather different regime, the mostly-singlet regime where $M_S \ll M_L$.

Other effects that we will ignore in our discussion here, but that are taken into account in the full numerical SARAH-SPheno calculation, include $g_{1,2}^2$ corrections, two-loop corrections, and the effective A-terms due to μ. The effects of g^2 are about a 10-20% correction to δm_h^2, which amounts to a 2 GeV shift in m_h. That matters for our calculations quantitively but not qualitatively. The μ values we consider in this chapter motivated by naturalness are small enough that μ has a negligible effect on the Higgs mass. Finally, we are interested in moderately-large values of $\tan\beta$ (e.g. $\tan\beta = 10$) but for simplicity we will present the $\tan\beta \to \infty$ limit here. The corrections due to $1/\tan\beta$ also do not make a qualitative difference. (In particular, there are no blind-spot cancellations here.)

With all of these simplifying assumptions, the result of our one-loop Coleman-Weinberg calculation is:

$$\delta m_h^2 = \frac{1}{4\pi^2} k_u^4 v^2 \left(f_1 \log(1+x_L^2) + f_2 \log(1+x_S^2) + f_3 \log \frac{x_S^2}{x_L^2} \right) \tag{5.4.1}$$

with

$$\begin{aligned} f_1 &= \frac{(2x_L^4 + x_L^6 + 3x_L^2 x_S^2 + 3x_L^4 x_S^2 - x_S^4) x_S^2}{(x_L^2 - x_S^2)^3} \\ f_2 &= \frac{(x_L^2 - 5x_S^2 - x_L^2 x_S^2 - 3x_S^4) x_L^4}{(x_L^2 - x_S^2)^3} \\ f_3 &= \frac{x_L^4 x_S^2 (x_L^2 + 3x_S^2)}{(x_L^2 - x_S^2)^3} \end{aligned} \tag{5.4.2}$$

where $x_L = m/M_L$ and $x_S = m/M_S$. A plot of $k_u^{-4}\delta m_h^2$ is shown in fig. 5.4 (left). We see that δm_h^2 asymptotes to a finite value as $x_L \to \infty$ or $x_S \to \infty$. In these limits (corresponding to mostly-doublet and mostly-singlet DM respectively), the dependence on the DM mass drops out, and δm_h^2 is controlled by the ratio of the soft mass to the heavier mediator scale (M_S or M_L respectively).

To raise the Higgs to 125 GeV in this chapter, we rely on a combination of the extra vector-like matter and MSSM stops. For stops at 1 TeV, which satisfy the current experimental bounds and imply about a $\sim 10\%$ tuning of the EW VEV, the MSSM contribution to the Higgs mass is about 110 GeV (for a recent review see e.g. [47]). Therefore the target for δm_h^2 from the dark sector is:

$$\delta m_h^2 \approx 3500 \text{ GeV}^2 \tag{5.4.3}$$

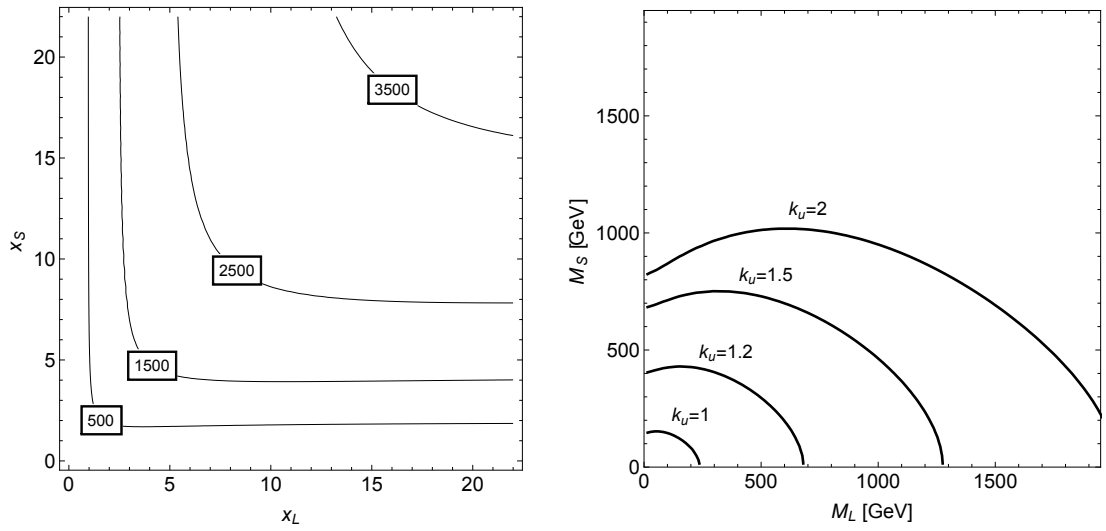

Figure 5.4: Left: contours of $k_u^{-4}\delta m_h^2$ in GeV^2 in the (x_L, x_S) plane, according to (5.4.1). Right: contours of $\Delta = 20$ in the (M_L, M_S) plane for different values of k_u that have a Higgs mass at 125 GeV.

This selects out a contour in the (x_S, x_L) plane as shown in fig. 5.4 (left), according to the value of k_u.

This has the following implications for the fine-tuning of the EW scale. Just as the dark sector lifts the physical Higgs mass analogous to stops in the MSSM, it also contributes to the fine-tuning of the EW scale through the renormalization of $m_{H_u}^2$. Following [50, 310], we define the measure of fine-tuning to be:

$$\Delta = \frac{2\delta m_{H_u}^2}{m_h^2} \tag{5.4.4}$$

where $\delta m_{H_u}^2$ is the running of $m_{H_u}^2$ due to the new fields

$$\delta m_{H_u}^2 = \frac{k_u^2 m^2}{8\pi^2} \log \frac{\Lambda_{UV}}{\Lambda_{IR}} \tag{5.4.5}$$

Optimistically we take $\Lambda_{UV} = 10\,\Lambda_{IR} \sim 10\,\text{TeV}$. We can combine this with (5.4.1) and (5.4.3) as follows. For a given value of k_u and a given point in the (M_S, M_L) plane, we can solve (5.4.3) for the soft mass m. Then substituting this into (5.4.4), we get a value for Δ. Regions of $\Delta \leq 20$ are shown in fig. 5.4 (right) for different representative values of k_u. We see that we need $k_u \gtrsim 1$ to have any viable parameter space at all for a natural SUSY 125 GeV Higgs. This is not surprising, since from (5.4.1), we see that k_u plays the role that y_t

plays for the MSSM stops. Of course, corrections we have neglected such as the D-terms and two-loop effects will modify this quantitatively. However, we will see that the same qualitative implications for fine-tuning and k_u will persist in our final plots.

5.5 The need for mostly-singlet DM

In section 5.2, we derived formulas for c_h and c_Z in terms of the parameters of the model, while in section 5.3 we showed that direct detection limits on c_h and c_Z are at the $\mathcal{O}(10^{-2})$ level. Finally, in section 5.4, we argued that we need $k_u \gtrsim 1$ in order to have any viable parameter space for a natural SUSY Higgs at 125 GeV. Here we will combine these facts and show that the DM must be mostly singlet in order to be consistent with all the constraints.

Basically there are three possibilities: the well-tempered regime where $|M_L - M_S| \lesssim v$ (recall our convention is that M_S and M_L are positive), the mostly-doublet regime where $M_L < M_S$ and $v \ll M_S,\ M_S - M_L$, and the mostly-singlet regime where $M_S < M_L$ and $v \ll M_L,\ M_L - M_S$. Keeping in mind that we need $k_u \gtrsim 1$ and large $\tan\beta$ for a natural Higgs mass, the challenge is to decrease c_h and c_Z to the 10^{-2} level. In fact, c_h alone is enough to rule out all but the mostly-singlet case. We will comment on the implications for c_Z in sections 5.6 and 5.7.

Examining the formula for c_h (5.2.5), we see that for $|M_L - M_S| \sim v$ and $\hat{k}_u \sim 1$, we have $c_h \sim \mathcal{O}(1)$. (In particular, there is a cancellation in the denominator, leaving it $\mathcal{O}(vM_S)$). This rules out the well-tempered case.

The mostly-doublet case is ruled out separately by two independent considerations. First, from fig. 5.4, we see that in order to be natural and mostly-doublet, we must have the DM mass below ~ 800 GeV. However, we know by analogy with pure Higgsinos in the MSSM that the thermal relic density constraint requires $M_L \geq 1$ TeV. (The mostly-doublet DM in this model has additional annihilation modes due to k_u and k_d, so M_L will be even larger.) So the mostly-doublet scenario is not promising for naturalness.

Also, from direct detection, we are basically forced into the mostly-singlet regime. In order to lower c_h by two orders of magnitude, we must either (a) raise M_L or M_S to increase the denominator of (5.2.5), or (b) cancel the two terms in the numerator of (5.2.5).

(a) Increasing the denominator of (5.2.5) necessitates either M_L or $M_S \gg v$. In the former, corresponding to mostly-singlet DM, we see that $c_h \propto 1/M_L^2$ and we can achieve the required level of suppression for $M_L \sim 1-2$ TeV for $M_S \sim v$ and $k_u \sim 1$. Meanwhile for the latter, corresponding to mostly-doublet DM, we see that $c_h \propto 1/M_S$ and therefore much larger $M_S \sim 2-5$ TeV is required for $M_L \sim v$ and $k_u \sim 1$. The latter is greatly disfavored by naturalness (it would likely be as fine-tuned as 10 TeV stops in the MSSM).

(b) Cancelling the two terms in the numerator requires

$$\frac{M_L}{m_\chi} \sim -\frac{1}{2}\frac{k_u}{k_d}\tan\beta \tag{5.5.1}$$

This is the blind spot. Since $k_u \gtrsim 1$ and we are in the large $\tan\beta$ limit, the RHS is generally much greater than one for any reasonable value of k_d. Therefore we must be in the mostly-singlet DM regime to realize the blind spot.

We conclude that several different constraints independently point at mostly-singlet DM as the only viable possibility.

For later reference we exhibit c_h and c_Z in the mostly-singlet limit

$$\begin{aligned} c_h &= -\frac{m_\chi + \frac{2k_d M_L}{k_u \tan\beta}}{\sqrt{2}v}\frac{k_u^2 v^2}{M_L^2} + \dots \\ c_Z &= -\frac{g_2}{4c_W}\frac{k_u^2 v^2}{M_L^2} + \dots \end{aligned} \tag{5.5.2}$$

Here we have taken $M_L \to \infty$ and $\tan\beta \to \infty$ holding fixed $M_L/\tan\beta$ and all the other mass scales. In fig. 5.5, we exhibit the amount of blind spot cancellation that is required by the SI bounds, for a typical choice of parameters that will lead to a viable relic density. We show this behavior by varying k_d keeping other parameters fixed. We can see that the constraint on c_h is satisfied in a fairly wide window of k_d values ($-1.8 \leq k_d \leq -1$). As for the two terms in c_h in (5.5.2), this amounts to a mild cancellation at the level of one part in 3-4. This could be viewed as another source of fine-tuning in the model, but it will be in general subdominant to the tuning of the EW scale, so we will not comment on it further. Most of the suppression of c_h is coming from large M_L, which as we will see in the next section is fixed by the thermal relic abundance constraint.

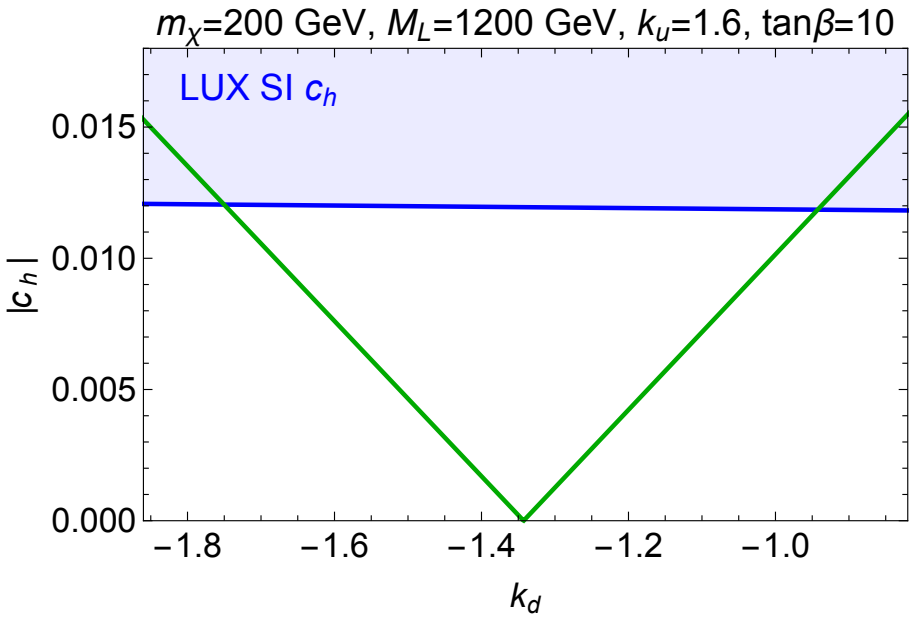

Figure 5.5: Values of the coupling c_h while varying k_d for a sample point of the parameter space. The values on the shaded area are excluded by LUX.

In the same mostly-singlet regime, we also exhibit δm_h^2:

$$\delta m_h^2 = \frac{k_u^4 v^2}{4\pi^2} \log(1 + x_L^2) - \frac{3k_u^4 v^2 x_L^4}{4\pi^2 x_S^2} \log \frac{1 + x_L^2}{x_L^2} + \mathcal{O}(x_S^{-4}) \tag{5.5.3}$$

As noted in the previous subsection, the Higgs mass in this limit to leading order does not depend at all on the DM mass M_S. So the Higgs mass constraint to leading order in the mostly-singlet regime becomes a constraint on k_u and m/M_L. For example, according to (5.5.3), in order to achieve $\delta m_h^2 = 3500$ GeV^2 for $k_u = 1.6$, we need $x_L \approx 1$.

5.6 DM annihilation in the mostly-singlet regime

An attractive feature of WIMP dark matter is its potential to naturally explain the observed relic abundance via the thermal freeze-out mechanism. Following the usual procedure (see e.g. the classic review [13]), we have

$$\Omega_{DM} h^2 \approx 9.2 \times 10^{-12} \text{ GeV}^{-2} \times \left(\int_{x_f}^{\infty} dx \, \frac{\langle \sigma v_\chi \rangle}{x^2} \right)^{-1} \tag{5.6.1}$$

The integral over x takes into account annihilation after freeze-out, and $x_f = m_\chi / T_f \approx 25$ parametrizes the freeze-out temperature. $\langle \sigma v_\chi \rangle$ is the thermally-averaged DM annihilation

cross section $\chi\chi \to XY$, summed over all final states X and Y. This is usually expanded in the small velocity limit:

$$\sigma_{XY}\, v_\chi = r_{XY}(a_{XY} + b_{XY}\, v_\chi^2 + O(v_\chi^4)), \tag{5.6.2}$$

where $r_{XY} \equiv \sqrt{1-(m_X+m_Y)^2/4m_\chi^2}$ is a kinematic phase space factor. At the time of freeze-out, the DM relative velocity is typically $v_\chi^2 \sim 0.1$. Therefore, the annihilation cross section is generally controlled by the s-wave contributions a_{XY}, unless they are suppressed for some reason.

In our model, the dark matter has many interactions and annihilation channels that should all be considered in full generality. As described in the introduction, for numerical calculations we use micrOMEGAs 4.1.8 [304] source code generated by SARAH 4.5.8 [301] to accurately take these into account. However in the mostly singlet limit that we are interested in, the cross sections simplify and we can have an analytic understanding of the behaviour of our model. We will assume that DM is lighter than all MSSM superpartners except possibly the Higgsinos, which are forced to be light $\mu \sim v$ by naturalness. In this case, the freeze-out process happens only through annihilation to SM particles and the Higgsinos. Including the Higgsinos in the story is a major difference from simplified-model-analyses of singlet-doublet dark matter, which generally just add the singlet and doublets to the SM. As we will see, the Higgsinos can be a major part of the DM annihilation in the early universe.

The full cross sections are too complicated to print here. Instead, we will expand in the mostly-singlet limit $M_S < M_L$, $v \ll M_L$, $M_L - M_S$ with the further assumption that $v \ll M_S$. This suffices for our purposes and results in relatively simple expressions. (One exception is the tree-level, s-wave $t\bar{t}$ cross section in the next subsection, for which we can write down an extremely simple exact expression in terms of c_Z.)

5.6.1 DM annihilation to fermions

The fermions have s-wave contributions

$$\begin{aligned} a_{f\bar{f}} &= \frac{3k_u^4}{32\pi}\frac{m_f^2}{M_L^4(1-\epsilon^2)^2} \\ a_{\psi_H\psi_H} &= \frac{(k_d^2+k_u^2)^2}{16\pi}\frac{\mu^2}{M_L^4(1+\epsilon^2+x_L^2)^2} \end{aligned} \tag{5.6.3}$$

where $\epsilon \equiv M_S/M_L$, and $x_L \equiv m/M_L$ was defined in section 5.4. In the second line, we have summed over the various Higgsino final states including both neutralinos and charginos, assuming a pure MSSM Higgsino (i.e. $M_{1,2}$ decoupled). The fermion b coefficients are always subdominant (suppressed by both v_χ^2 and v^2/M_L^2), so we have not included them here.

The fermion cross sections are all suppressed by the square of the fermion mass, so $t\bar{t}$ and Higgsinos are the dominant channels. This is the famous s-wave helicity suppression of DM annihilation to fermion pairs.

Although $t\bar{t}$ and Higgsinos are parametrically similar, their diagrammatic origin is entirely different. The former (latter) arise from s-channel Z (t-channel superpartner) exchange. As a result, the Higgsinos are suppressed by the soft mass m. For $k_u = 1.6$, we saw in section 5.5 that we need $x_L \approx 1$ for $m_h = 125$ GeV, so the suppression is not large. Also, μ is constrained to be $\lesssim 300$ GeV by naturalness. So all in all, the Higgsino contribution ends up generally of the same order or smaller than $t\bar{t}$.

The fact that the SM fermions all arise from s-channel Z diagrams means that they have a simple exact expression *beyond* the small v approximation:

$$a_{f\bar{f}} = c_Z^2 \frac{3y_f^2}{4\pi m_Z^2} \tag{5.6.4}$$

In other words, c_Z controls both the SD direct detection cross section and the annihilation to $t\bar{t}$. Therefore, we expect to see a fairly direct correlation between the SD direct detection limits and the relic density constraint.

5.6.2 DM annihilation to bosons

Meanwhile the diboson cross sections are all p-wave to leading order:

$$\begin{aligned} b_{hh} &= b_{ZZ} = \frac{k_u^4}{384\pi}\frac{\epsilon^2(3+2\epsilon^2+3\epsilon^4)}{M_L^2(1+\epsilon^2)^4} \\ b_{hZ} &= \frac{k_u^4}{96\pi}\frac{\epsilon^2}{M_L^2(1+\epsilon^2)^2} \\ b_{WW} &= 2b_{hh} + b_{hZ} \end{aligned} \tag{5.6.5}$$

Here we took $\tan\beta \to \infty$ for simplicity; we checked that the $1/\tan\beta$ corrections are irrelevant. The s-wave contributions are suppressed by v^4/M_L^4 so they are always subdominant to the p-wave contributions shown here.

Clearly, the diboson cross sections exhibit some interesting features. They are nonvanishing even in the $v \to 0$ limit, so they can be understood as a consequence of $SU(2)_L \times U(1)_Y$ symmetry. These tree-level cross sections arise entirely due to the longitudinal components of the $W^\pm$ and Z bosons, which by the Goldstone equivalence theorem are also equivalent to the charged and neutral Goldstones $G^\pm$ and G^0 respectively. Under a $U(1)_Y$ rotation, $h \to G^0$ and $G^0 \to -h$, while under an $SU(2)_L$ rotation, $W^\pm \to h \pm iG^0$. This explains both relations in (5.6.5).

Comparing $t\bar{t}$ and Higgsinos to the total diboson cross section, we see that parametrically the latter can be larger than the former, for sufficiently large M_L. However the cross over point is generally at very large M_L and M_S. For instance, for $\epsilon = 1/2$ and $x_L = 1$, we find the cross over to be in the range $M_L \sim 2.7 - 3.6$ TeV for $\mu \sim 100 - 300$ GeV. This is well beyond the naturalness-motivated part of the parameter space that we are focusing on in this chapter. Therefore we conclude that the total σv_χ is always dominated by $t\bar{t}$ and Higgsinos, and dibosons are always a subdominant part of it.

5.6.3 Total annihilation cross section

We have shown analytically that the relic density is dominated by s-wave annihilation to $t\bar{t}$ and Higgsinos (assuming of course that the DM is above the respective thresholds):

$$\sigma v_\chi \approx a_{t\bar{t}} + a_{\psi_H\psi_H} = \frac{3k_u^4}{32\pi}\frac{m_f^2}{M_L^4(1-\epsilon^2)^2} + \frac{(k_d^2+k_u^2)^2}{16\pi}\frac{\mu^2}{M_L^4(1+\epsilon^2+x_L^2)^2} \tag{5.6.6}$$

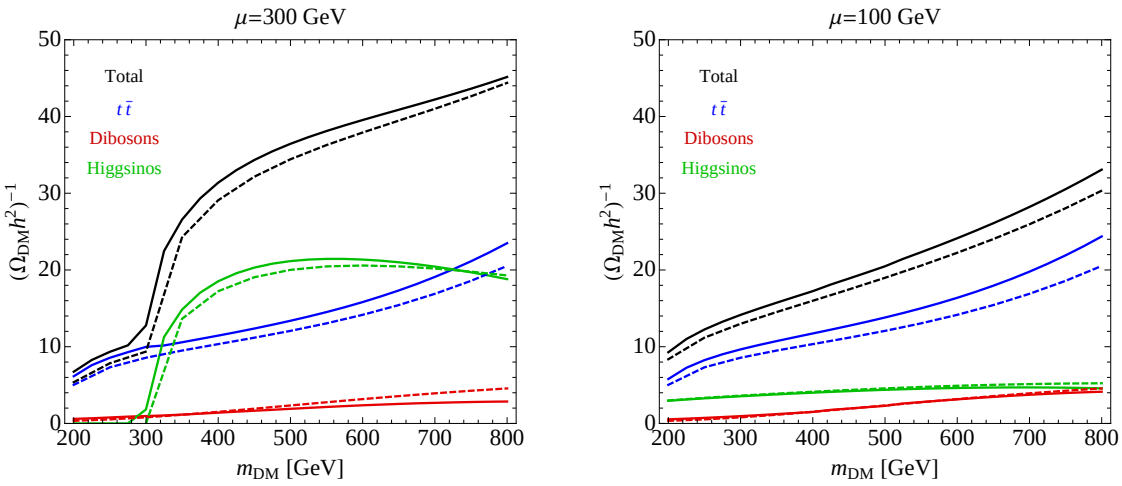

Figure 5.6: Inverses of the total relic abundance (black) as well as the individual contributions from $t\bar{t}$ (blue) and dibosons (red) as calculated numerically by micrOMEGAs 4.1.8 (solid) and the analytic equations (5.6.3) and (5.6.5) (dashed), for $M_L = 1.2$ TeV, $k_u = 1.6$, $k_d = -1.5$ and $\tan\beta = 10$.

A plot comparing our analytics to micrOMEGAs is shown in fig. 5.6 for fixed choices of the parameters; we see there is excellent agreement across the entire range of relevant DM masses. We confirm that the dibosons are never more than $\sim 10\%$ of the relic density across the entire parameter range of interest. Higgsinos and $t\bar{t}$ are comparable for $\mu \sim 300$ GeV, while for $\mu \sim 100$ GeV, $t\bar{t}$ dominates, as expected from the μ dependence of the Higgsino cross section (5.6.3).

One very interesting consequence of (5.6.6) is that in the limit of large M_L, the DM mass drops out of the annihilation cross section. Furthermore, we have seen that we need $k_d \sim k_u$ for the blind spot, $x_L \approx 1$ for the Higgs mass, and $\mu \sim m_t$ for naturalness. Thus the WIMP miracle transforms from being a constraint on the WIMP mass to being a constraint on the mediator scale M_L! This helps to relieve the "WIMP little hierarchy problem", whereby the preference of the thermal relic constraint for TeV-scale WIMPs is in tension with naturalness. Comparing with (5.5.2), we also expect that the relic density constraint will essentially fix c_Z to a unique value. We will confirm this in the next section with our full numerical scans and discuss its implications for SD direct detection.

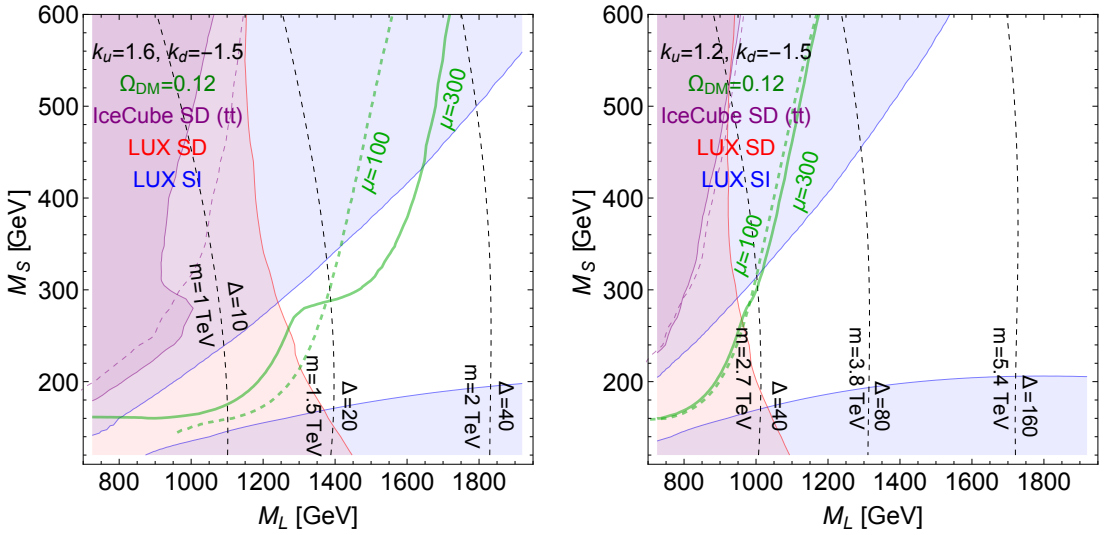

Figure 5.7: $M_L - M_S$ parameter space scan with micrOMEGAs 4.1.8 [304] for $k_u = 1.6$, $k_d = -1.5$ (left) and $k_u = 1.2$, $k_d = -1.5$ (right), $\tan\beta = 10$ and all MSSM soft masses and gauginos at 1 TeV. We show the exclusion regions from σ^{SI} in blue and σ_n^{SD} in red, both from LUX [4] and for σ_p^{SD} from IceCube $t\bar{t}$ with $\mu = 300$ GeV ($\mu = 100$ GeV)[295] in solid (dashed) purple. The dashed black lines are the fine-tuning contours for $\mu = 300$ GeV. The contour of $\Omega_{DM} = 0.12$ with $\mu = 300$ GeV ($\mu = 100$ GeV) is in solid (dashed) green.

5.7 Putting it all together

5.7.1 Plots in the M_L-M_S plane

Having described the various individual components of the analysis of the model (direct detection, the Higgs mass, and the relic abundance), we will now combine them and describe how the different constraints interact to produce the viable parameter space of the model.

In fig. 5.7 we show contour plots for numerical scans over the (M_L, M_S) plane for fixed values of k_u, k_d and μ. We choose four sets of benchmark parameters: large coupling ($k_u = 1.6$, $k_d = -1.5$) and small coupling ($k_u = 1.2$, $k_d = -1.5$); and large μ ($\mu = 300$ GeV) and small μ ($\mu = 100$ GeV).

We see the impact of the direct detection limits on the parameter space of the model.[7] The LUX SI and SD limits are strongest almost everywhere except a tiny sliver for large

[7] We have not overlaid indirect detection limits on this plot. As already mentioned in the introduction, for DM masses above ~ 100 GeV, there are no constraints from Fermi [296] for points with the correct relic abundance. For points with $\Omega_{DM} > 0.12$, $\langle\sigma v_\chi\rangle$ would be even smaller and Fermi would not constrain any of these points either. Finally, for points with $\Omega_{DM} < 0.12$ there could be indirect detection constraints, but in this case the model should be completed by having multi-component DM and/or non-thermal processes, giving many possible new signatures. We leave a detailed analysis of these extensions of our model for future work.

M_S in the $k_u = 1.2$, $k_d = -1.5$ case where IceCube has an impact. (Note that the LUX limits assume the singlet-doublet sector comprises all of the DM, regardless of whether it is thermal or not.) The SD (SI) limits primarily cover the lighter (heavier) DM mass region. The heavier DM region is ruled out because we are holding fixed k_d, so as one increases m_χ the blind spot cancellation shown in (5.5.2) becomes less effective.

For every point in the plane we numerically solved (using SPheno) the $m_h = 125$ GeV constraint for the common soft mass m; these contours are shown in fig. 5.7 along with their corresponding tuning. These contours are mostly vertical; as discussed in section 5.4, the soft mass and Δ depend primarily on M_L since the dependence on M_S drops out to leading order at large M_L.

Finally, we used micrOMEGAs to numerically solve the thermal relic density constraint $\Omega_{DM} = 0.12$ [62]; this fixes M_L as a function of M_S and these contours are shown in green for various choices of the parameters. Note the rapid increase in M_L across the top and Higgsino thresholds. Here new s-wave annihilation channels open up, and so larger values of M_L are needed to maintain the overall annihilation rate at the thermal relic value. This effect is more pronounced for larger values of $k_{u,d}$ and for larger values of μ. Indeed, in section 5.6 we saw that the annihilation cross sections to $t\bar{t}$ and Higgsinos are enhanced for greater $k_{u,d}$, and the Higgsino cross section in particular is proportional to $(k_d^2 + k_u^2)^2\mu^2$.

Since larger M_L decreases direct detection cross sections, increasing $k_{u,d}$ and μ also increases the viable parameter space for thermal relic DM. The Higgsino channels in particular allow the model to survive the direct detection limits over a wider range of parameter space than would have been the case for non-supersymmetric singlet-doublet DM. Fig. 5.7 also shows that larger $k_{u,d}$ is better for fine-tuning, confirming our discussion in section 5.4. The only potential drawback of the larger coupling choice is (as we will discuss in section 5.8.1) that the former has a lower Landau pole ($\Lambda \sim 10^2$ TeV vs $\Lambda \sim 10^3$ TeV).

Away from the top and Higgsino thresholds, we see that the relic density contours are mostly vertical, meaning that the relic density constraint becomes a constraint primarily on M_L, once the other parameters (k_u, k_d, m, μ) are fixed, i.e. the WIMP DM mass drops out to leading order. This confirms our analytics in the previous section.

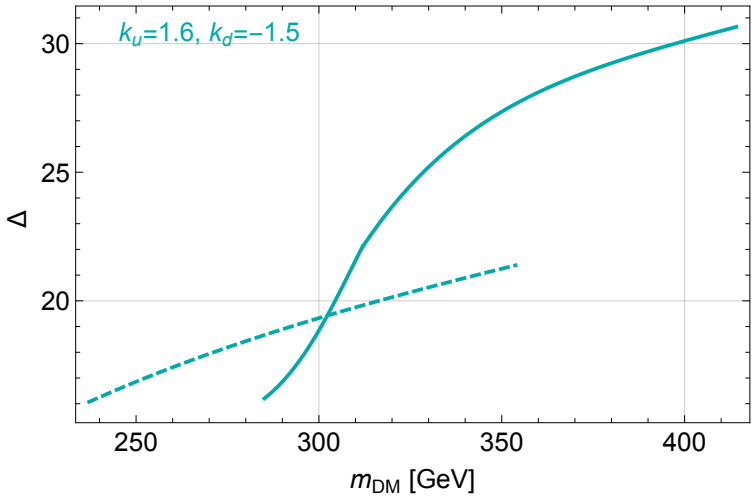

Figure 5.8: Fine-tuning for the right relic abundance contours of fig. 5.7 (left) that are allowed by direct detection. We show the case for $\mu = 300$ GeV (solid) and $\mu = 100$ GeV (dashed).

5.7.2 Projecting onto the thermal relic contour

Finally let us impose the relic density constraint $\Omega_{DM} = 0.12$ and see how various parameters vary along the green contours in fig. 5.7. In fig. 5.8 we show the fine-tuning for the points with the correct relic abundance. It is remarkable that there are allowed regions of the parameter space with $\Delta \lesssim 20$, making this model much less tuned than the MSSM.

In fig. 5.9 we show c_h for the points of the parameter space that satisfy $\Omega_{DM} = 0.12$ (including both allowed and excluded points from direct detection limits). We see that varying k_d we can move toward the blind spot and satisfy the SI direct detection bounds.

Similarly, in fig. 5.10 we show c_Z for the points of the parameter space with $\Omega_{DM} = 0.12$ (including both allowed and excluded points from direct detection limits). We can see that for $m_{DM} > \mu$ contours of constant Ω_{DM} have an approximately constant c_Z. This confirms the discussion based on analytics in section 5.6.3. Indeed, using (5.6.6) with the parameter choices here, we find that for 100 GeV $\leq \mu \leq$ 300 GeV, c_Z ranges from $0.005 \lesssim c_Z \lesssim 0.008$. These values are clearly illustrated in fig. 5.10.

We conclude that c_Z (and consequently σ^{SD}) is basically fixed by the relic density constraint. Requiring χ to be all the dark matter leads to a nearly unique prediction for the SD cross section! Fortunately, as shown in fig. 5.10, these values of c_Z are still allowed by the current direct detection experiments, IceCube in particular.[8] With factor of 10-100

[8]It is quite crucial that our DM annihilates almost exclusively to $t\bar{t}$ and Higgsinos. The IceCube bound

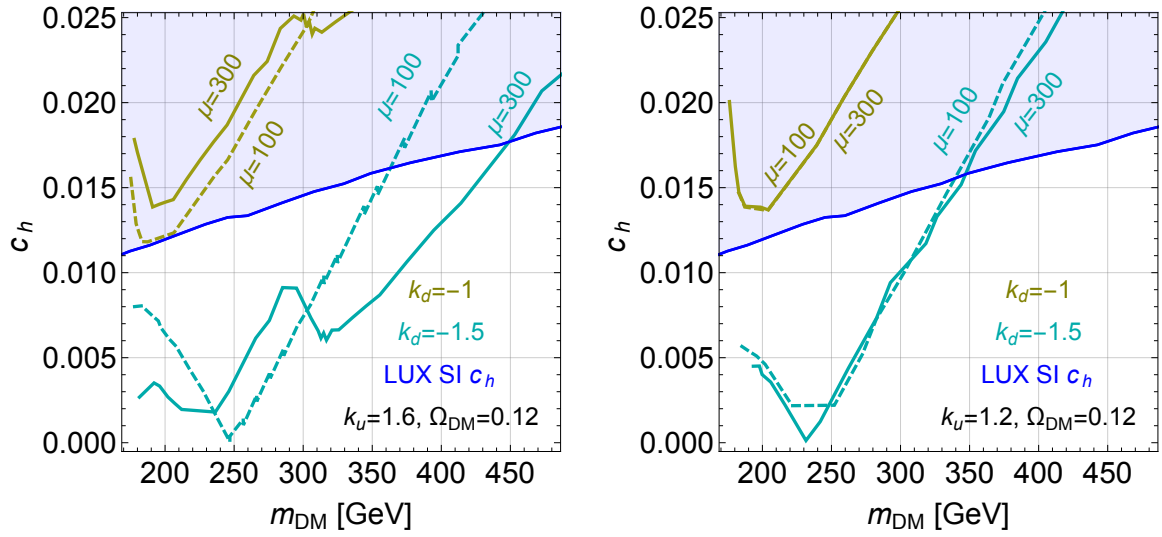

Figure 5.9: Values of the coupling c_h for the points with $\Omega_{DM} = 0.12$ for different values of k_d. We show the values for $k_u = 1.6$ (left) and $k_u = 1.2$ (right). The exclusion region from σ^{SI} is in blue.

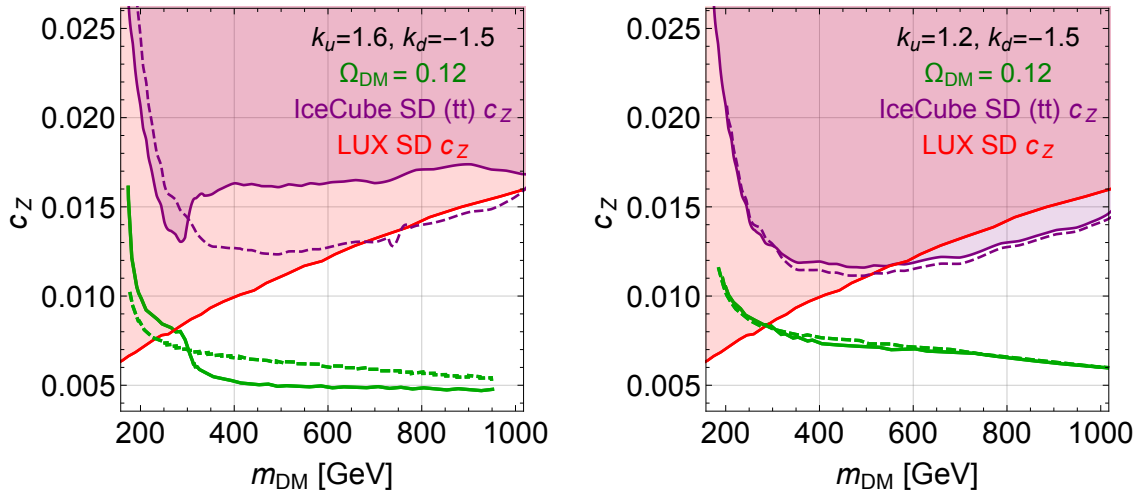

Figure 5.10: Values of the coupling c_Z for the points with $\Omega_{DM} = 0.12$ for $\mu = 300\,\text{GeV}$ ($\mu = 100\,\text{GeV}$) in solid (dashed) green. The exclusion region from σ_n^{SD} is in red and from σ_p^{SD} with $\mu = 300$ GeV ($\mu = 100$ GeV) is in solid (dashed) purple.

improvements in cross section expected from Xenon1T [6] and LZ [7], the next generation of

on $t\bar{t}$ is by a factor of a few weaker than the W^+W^- cross section, and it saves the model from being already ruled out. The case of Higgsinos decaying to Higgs and gravitino does not introduce any new regions of parameter space that were not already ruled out by LUX [4] in fig. 5.7. (Also, as the DM annihilation to Higgsinos arises from t-channel superpartner exchange, there would be no constraints on c_Z from this channel.)

DM direct detection experiments will be sensitive to essentially the entire parameter space of this model (assuming χ is a thermal relic and is all the DM). A discovery might be right around the corner!

5.8 Outlook of this chapter

In this section we briefly discuss the UV behavior of the model (in particular the Landau poles) and the potential sensitivity from LHC Run II. Finally we conclude with some thoughts on future directions.

5.8.1 UV considerations

So far we have been exploring our model at the EW scale and have identified the interesting parts of the parameter space around $k_u \sim k_d \sim 1.2 - 1.6$. Here we want to examine the UV consequences of such large Yukawa couplings and comment on possible solutions to the Landau pole problem.

Let's focus on the most important couplings, $(g_1, g_2, g_3, y_t, k_u, k_d)$ and neglect the effect of the other couplings in finding the scale of Landau poles. Starting from one loop beta functions above the scale of the new fields (including spectator color triplets for unification) we have

$$\begin{aligned}
\beta_{g_i} &= \frac{b_i}{16\pi^2} g_i^3 \qquad\qquad (b_1, b_2, b_3) = (\frac{36}{5}, 2, -2) \\
\beta_{k_u} &= \frac{k_u}{16\pi^2}(2k_d^2 + 4k_u^2 + 3y_t^2 - \frac{3}{5}g_1^2 - 3g_2^2) \\
\beta_{k_d} &= \frac{k_d}{16\pi^2}(4k_d^2 + 2k_u^2 - \frac{3}{5}g_1^2 - 3g_2^2) \\
\beta_{y_t} &= \frac{y_t}{16\pi^2}(6y_t^2 + k_u^2 - \frac{16g_3^2}{3} - \frac{13}{15}g_1^2 - 3g_2^2)
\end{aligned} \tag{5.8.1}$$

Solving the RGE's of our model numerically, we can find the lowest scale at which one of the couplings hits its Landau pole. In fig. 5.11 we show this scale as a function of the Yukawa couplings at 1 TeV.

Note that for $k_u \lesssim 2$ (as we have considered in this work), the Landau poles are above 100 TeV. Now we might ask: how can we understand physics above the Landau pole scale, or how can we postpone it to higher energies e.g. the GUT scale? One idea is to use non-Abelian

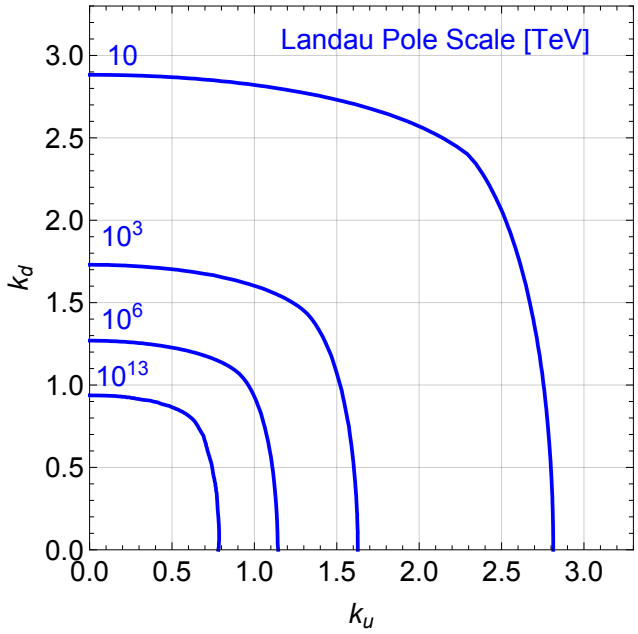

Figure 5.11: Scale of Landau poles with one-loop RGE's in terms of k_d, k_u at the IR scale. We are assuming for each point on the plot that k_u and k_d are given at $\Lambda_{IR} = 1$ TeV.

gauge interactions for the new sector to reduce the beta functions of the Yukawa couplings: if we include multiple copies of S, L, $\overline{L}$ and charge them under a non-Abelian gauge group, the corresponding gauge coupling appears with negative sign in the beta function of k_u, k_d (see e.g. [292] for a recent implementation of this idea). As S is Majorana, we need S to be in a real representation of the new gauge group. A simple example is when the gauge group is $SO(N)$ and S is in the fundamental representation. Another possibility might be to match our model to the magnetic side of a Seiberg duality and interpret physics above the scale of the Landau pole by the electric theory. It will be interesting to explore these ideas further in the future.

5.8.2 LHC Phenomenology

In addition to direct detection experiments, DM models are also probed by the LHC. In principle, monojet+MET [297, 298] and monophoton+MET [299, 300] searches for direct DM production could be sensitive to our model. Since quarks and gluons only talk to χ through s-channel diagrams involving Z's and Higgses, these searches constrain the same c_Z and c_h couplings as direct detection. However, these constraints are weaker by several

orders of magnitude than those from direct detection under the assumption that our DM candidate χ is all of the relic density, for the mass range we consider. See e.g. [311, 312] for a recent discussion in terms of simplified DM models.

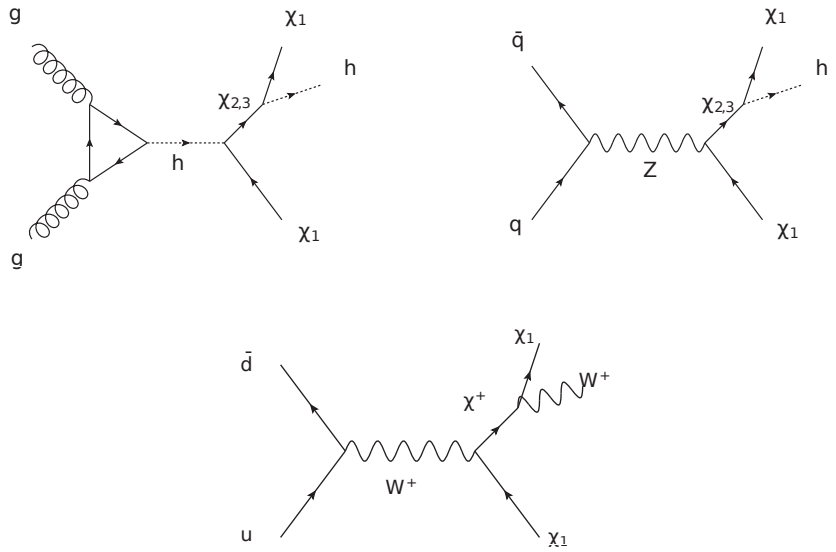

Figure 5.12: Diagrams contributing to mono-Higgs/Z/W+MET in our model.

Instead, let us briefly consider mono(h, W, Z)+MET. This can occur in our model through production of $\chi_1\chi^0_{2,3}$ and $\chi_1\chi^\pm$ and subsequent decay of the (mostly-doublet) $\chi^0_{2,3}$ and $\chi^\pm$. (Here all χ's refer to dark sector fermion mass eigenstates, not MSSM neutralinos and charginos.) A full treatment including estimation of SM backgrounds, detector acceptances, etc. is beyond the scope of this work. Here we will just present the raw production cross sections in our model.

Diagrams contributing to mono-Higgs/W+MET are shown in fig. 5.12 (mono-Z+MET is the same as mono-Higgs with the final state Higgs replaced by Z). Note that we have included the one-loop gluon fusion diagram.[9] Because of the large, $\mathcal{O}(1)$ Yukawas k_u, k_d in this model, this contribution can be as much as 60% of the total $\chi_1\chi^0_{2,3}$ cross section. We calculated the gluon fusion contribution analytically, and the tree level contributions both analytically and with MadGraph5 [232] using the model file generated by SARAH and the spectrum files generated by SPheno. More details on the analytics are given in appendix H. In both cases, we used the NNPDF2.3 [313] PDF set. Fig. 5.13 shows the sum of tree

[9] We thank Matt Reece for bringing this to our attention.

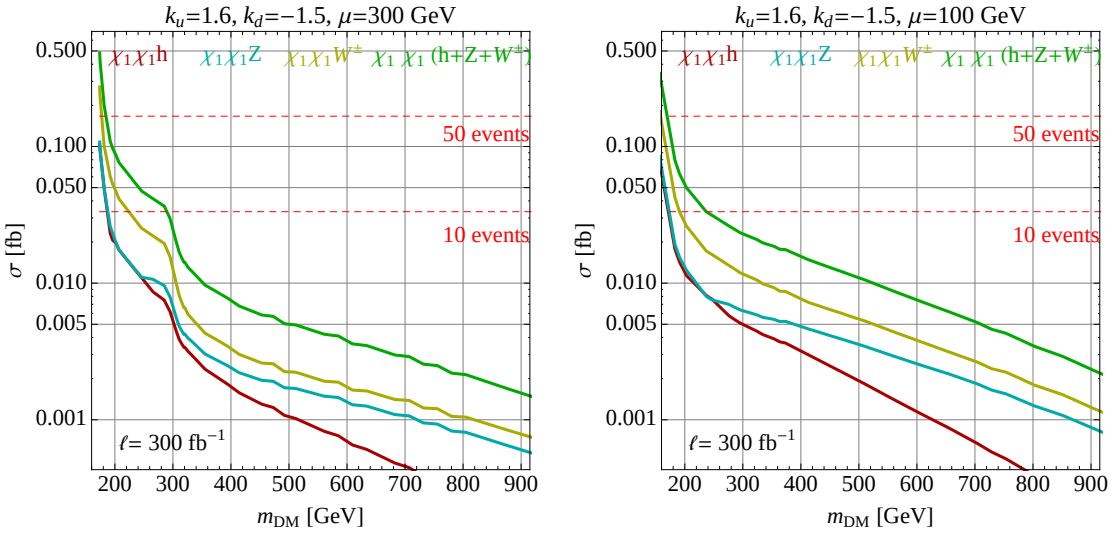

Figure 5.13: Final state cross sections for LHC13 for the points with $\Omega_{DM} = 0.12$ from fig. 5.7 (left), $\tan\beta = 10$ and all superpartners decoupled. As these points depend on the annihilation cross section to Higgsinos, we specify the value of $\mu = 300$ GeV (left) and $\mu = 100$ GeV (right). We show in green the total cross section (adding h, Z and $W^{\pm}$ channels). For the W cross section we are showing the sum of W^+ and W^- final states.

level contributions and gluon fusion along the $\Omega_{DM} = 0.12$ contour. We see that LHC13 will ultimately be able to probe the small mass region. Of course, if χ is all of the dark matter, then direct detection experiments will discover the model first. In that case, the LHC will only be useful as a post-discovery confirmation of the model. However, since the LHC is producing χ directly, it does not depend on the relic density. Therefore if our dark sector is only one component of Ω_{DM}, the direct detection limits could be greatly relaxed while the LHC would remain sensitive.

5.8.3 Future directions

The work presented in this chapter is a simple realization of a general idea: economically extending the MSSM with a single sector that provides both thermal WIMP dark matter and the 125 GeV Higgs mass. Here we took this sector to be a singlet and a pair of doublets, but one could easily imagine many other possibilities. For instance, very popular ideas for lifting the Higgs mass include the NMSSM (see e.g. [314] for a review and original references) and non-decoupling D-terms [315, 316]. While dark matter in the NMSSM is a well-studied topic, it would be very interesting to try to connect non-decoupling D-terms to dark matter.

Even within the context of our specific singlet-doublet model, there are many interesting open questions. In this work we made some simplifying assumptions in our analysis, and it would be interesting to explore the consequences of relaxing these assumptions. For example, we took all model parameters to be real, but in general there is one physical CP-violating phase. The effect of this phase on direct detection and annihilation cross sections can qualitatively change the model's behavior. Furthermore, we took all the soft mass-squareds to be positive to increase the Higgs mass. One might wonder how the phenomenology of the model would change if one of the soft masses is negative and the DM is a scalar instead of a fermion. We also assumed negligible A-terms in the dark sector. By analogy to stops, having substantial A-terms can help in raising the Higgs mass, see e.g. [279]. This could allow for smaller k_u, k_d and open up more of the parameter space. Additionally, we focused on dark matter above ~ 100 GeV. It could be interesting to study the phenomenology of the model for lighter dark matter masses. In particular the annihilations through the Higgs and Z resonances could be large enough while still having suppressed direct detection signals. Finally, one could relax the assumption that χ is thermal and is all of the DM, and consider non-thermal relics or multi-component DM scenarios. All of these directions will become especially well-motivated if nothing is discovered at the next round of direct detection experiments, as discussed in section 5.7.

There are also many interesting model-building directions in the UV. For example, enlarging the dark sector to accommodate a non-Abelian gauge symmetry could have potentially interesting consequences. As noted in section 5.8.1, this may help postpone the Landau pole of the Yukawa couplings, and the new gauge interactions could play an important role in the dynamics of the dark sector. Additionally we have two supersymmetric masses M_L and M_S at the electroweak scale. Perhaps the same dynamics that generates μ in the MSSM is responsible for generating these masses as well.

Chapter 6

Conclusions and outlook

In this thesis we proposed and studied searches at LHC, as well as built and studied the phenomenology of models of new physics at the electroweak scale. As already discussed in chapter 1 there are strong motivations to expect new physics at the EW scale from solutions to the hierarchy problem and a WIMP dark matter candidate with masses around $(0.1 - 1)$ TeV that would give the right relic abundance.

The 13 TeV center of mass energy reached at LHC Run II started to probe new regions of parameter space, e.g. regions with heavy boosted particles. Designing better classifiers to accurately identify boosted jets can help in experimental searches, such as in discriminating the QCD background in SM and beyond SM analyses. In chapter 2 we developed and showed for the first time that a top quark jets tagger based on deep learning and low-level inputs (raw jet images) can significantly outperform state-of-the-art conventional top taggers based on high level inputs. Specifically, our tagger outperforms boosted decision trees based on high-level inputs by a factor of $\sim$ 2–3 or more in background rejection, over a wide range of tagging efficiencies. Moreover, our methodology could be straightforwardly extended to the classification of other types of boosted jets, such as W/Z bosons, Higgses, and BSM particles. A relevant area that we have not studied concerns the issue of overtraining on Monte Carlo simulations. Thus, an interesting future direction would be to explore unsupervised learning techniques, applied on real data, to find all the categories (or discover new ones) of boosted objects or other types of collider signatures. We believe that there will be many new applications of machine learning in high energy physics in the near future.

Regarding supersymmetric searches at LHC, the experimental collaborations have been making great progress in pushing sensitivity out to higher mass values. However, there have been phenomenological challenges related to the remaining gaps in coverage. In particular, searches for supersymmetric top quarks have had gaps in coverage around lower-mass regions where the decay phase space is closing off. In chapter 3 we proposed an analysis that can extend sensitivity to the stop next-to-lightest supersymmetric particle and neutralino lightest supersymmetric particle model into the more difficult compressed regions at lower masses, with S/B ~ 1 and significances often well beyond 5σ. Our proposed search strategy could access, stops along the top compression line beyond 400 GeV at discovery-level significance, and perhaps up to 550 GeV at exclusion-level significance by the end of LHC Run II, though the gap was expected to start to close much earlier. In fact, this type of search was applied by the ATLAS collaboration for the first 13.3 fb^{-1} of data at LHC Run II in [8] and updated for 36.1 fb^{-1} in [9], obtaining results as expected.

Next, in chapter 4 we explored experimental constraints on simplified models motivated by natural SUSY where cascade decays of accessible gluinos and stops down to a light higgsino typically produce one or more of the following signatures: high object multiplicities, top quarks and significant missing transverse momentum. We derived these limits from a detailed reinterpretation of 13 TeV ATLAS and CMS searches at LHC Run II with the first ~ 15 fb^{-1} of data presented at the ICHEP 2016 Conference. We also studied the effects of these constraints on the fine-tuning of the EW scale and found that much of the parameter space at a 10% tuning has been already excluded.

As previously mentioned, null results from Run II at LHC keep pushing superpartner masses to higher values, making at least the most vanilla realization of supersymmetry unnatural (the MSSM with R-parity and flavor-degenerate sfermions). Other alternatives require extending SUSY beyond the vanilla case to lower the experimental constraints. In chapter 4 we have explored two options. The first, effective SUSY (the RPC MSSM with all squarks other than the stops and the left-handed sbottom decoupled from the mass spectrum), decreases the total SUSY cross section. The second case, RPV/HV/Stealth SUSY trades MET for jets reducing the signal to background ratio. Future directions could include exploring if the HV/Stealth SUSY sector could provide a dark matter candidate or

help lifting the Higgs mass.

If we consider only the MSSM, to get the 125 GeV Higgs mass the model is typically already tuned at about 1% level or worse (see fig. 1.9). Possible solutions that lead to a more natural model are to consider minimal extensions of the MSSM that could raise the mass of the Higgs through loops including the new particles. In addition to the Higgs mass, the MSSM is under pressure from null results of dark matter direct detection experiments (if we try to obtain the dark matter relic abundance coming only from the MSSM). As a viable solution to both issues, in chapter 5 we introduced a new model by adding a dark sector containing a singlet and a pair of $SU(2)$ doublets to the MSSM. This dark sector could naturally explain the 125 GeV Higgs mass with an $\mathcal{O}(1)$ coupling to H_u and at the same time provides a thermal dark matter candidate with the correct relic abundance. We showed that our model allows for a small enough dark matter coupling to Higgs to satisfy spin independent direct detection experiments for Majorana WIMP dark matter while the rest of the dark sector has a large enough coupling to Higgs to help raise the Higgs mass to 125 GeV. We found that, in our model, the main contribution to the DM relic abundance comes from s-wave annihilation to tops and Higgsinos, which results in a tight relation between the relic abundance and the spin dependent direct detection cross section. Additionally, it would be interesting to study other extensions of the MSSM with similar motivations, such as trying to connect non-decoupling D-terms to dark matter. There are also interesting directions within our singlet-doublet model, such as allowing for sizable A-terms in the dark sector or studying lighter DM masses (below 100 GeV).

Given that SUSY has not been found so far, very little natural parameter space is left in most supersymmetric models. However, supersymmetry can still explain the large hierarchy between the EW scale and the Planck scale in a natural way. Thus, SUSY is still strongly motivated and perhaps the weak scale may involve a slight numerical accident. In any case, working on building new models that predict physics beyond the Standard Model at the EW scale and studying their phenomenology is especially relevant in present times (June 2018), given that the LHC Run II can probe the parameter space of models at these energies. Finally, with the rise in luminosity at LHC in the near future, analyses will be able to apply much stronger cuts on physics variables while still having enough statistics, opening

new regions in searches for new physics. On another front, current and next generation of DM direct detection experiments will push down the sensitivity with a factor of 10-100 improvements in cross section in the near future. As a result, new physics at the electroweak scale could be just around the corner!

Appendix A

Validating our DeepTop implementation

Here we will validate our implementation of the DeepTop tagger [96] that forms the basis of this work. Following their specifications, as described in table 2.1 (14 TeV collisions, 350 GeV $< p_T <$ 450 GeV, $|\eta| < 1$, anti-k_T $R = 1.5$ calo jets, $\Delta R(t, j) < 1.2$ match requirement, no merge requirement, $\Delta\eta \times \Delta\phi = 0.1 \times 5^\circ$ toy calorimeter, 40×40 pixel images), with the "minimal" preprocessing option described in their paper (centering only), we produced 600k+600k top and QCD jet images, split 25%/25%/50% into training, validation and test samples as in [96].

We used the "default architecture" shown in fig. 4 of [96]. This, together with the training methods used in the DeepTop paper were described in section 2.2. Following these same methods, the result of our validation is shown in fig. A.1. We see that the agreement is excellent.

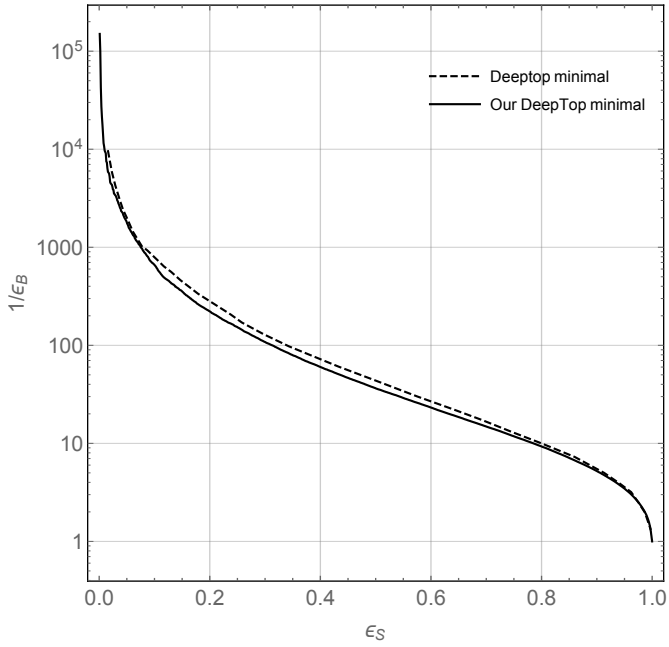

Figure A.1: ROC curves validating our implementation of the DeepTop tagger with minimal preprocessing (solid) against the original (dashed). The latter was obtained by digitizing the "DeepTop minimal" curve in fig. 8 of [96]. We see that the agreement is excellent.

Appendix B

Validating our HEPTopTaggerV2 implementation

Next we turn to validating our implementation of HEPTopTaggerV2 (HTTV2) and Nsubjettiness as used in [102]. As described in section 2.2, their jet samples are in line with our CMS sample, except for some slight differences, specifically $800 < p_T < 1000$ and $R = 0.8$.

The HTTV2 algorithm takes the constituents of a jet as input, attempts to cluster them into subjets consistent with a b and a W, and outputs a short list of kinematic variables, m_{jet}, f_{rec} and R_{opt}. The first is the jet mass and obviously should be close to the top mass. The second is a measure of how W-like a subjet is. The third is a measure of the optimal jet radius which may be different than the input jet radius.[1] Finally, the N-subjettiness variables τ_i are observables built out of the jet constituents that measures how likely the jet is to have a given number of subjets.

Using m_{jet}, f_{rec} and $\tau_{32} \equiv \tau_3/\tau_2$, CMS scans over simple window cuts to produce the optimal mistag rate for a given tag efficiency. The resulting ROC curve is shown in fig. 7R of [102].[2] Our version of this overlaid on the CMS ROC curve is shown in fig. B.1. We again see that the agreement is pretty good.

[1] For some jets, the HTTV2 may fail to find three or more subjets, in which case it produces no outputs. This failure mode must be included in the efficiency calculation of any HTTV2-based tagger.

[2] CMS also cuts on a ΔR_{opt} variable but they say this has the least discriminating power. We omit the cut on this variable for simplicity.

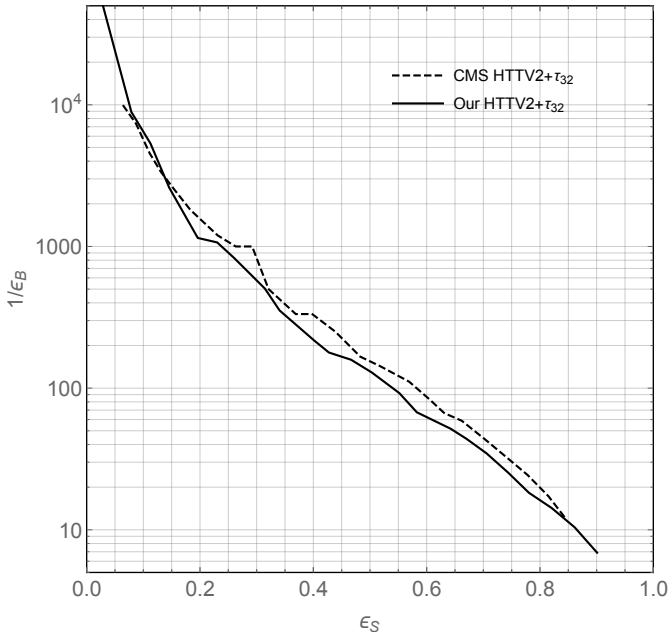

Figure B.1: ROC curves validating our implementation (solid) of the HTTV2+N-subjettiness cut-based tagger described in [102]. The CMS curve (dashed) was digitized from fig. 7R of [102]. We see that the agreement is pretty good.

Appendix C

Importance of the merge requirement

Here we will elaborate further on the importance of the requirement ($\Delta R(t, q) < 0.6$ in chapter 2, following [102]) that the decay products of the top be "fully merged". Tops failing the merge requirement generally result in fat jets that do not contain the full energy from the top quark decay. One can see this e.g. in fig. 2 of [102] where histograms of the jet mass are shown with and without the merge requirement. Without the merge requirement, there is a clear peak and lower tail around the W mass, indicating that some of the top jets are actually W jets or the b and only part of the W.

Restricting the signal sample to fully-merged tops will clearly boost the tagger performance, since the differences with QCD are more accentuated (the top jets are more top-like). This is illustrated in fig. C.1 which compares the ROC curve for our CMS sample with preprocessing (the purple curve in fig. 2.5) with and without the merge requirement. We see that the performance gain with the merge requirement is indeed substantial.

We remark in passing that the merge requirement could explain a puzzling discrepancy between the results in the DeepTop paper [96] and the CMS note [102]. Comparing the DeepTop ROC curve fig. A.1 against the CMS ROC curves defined for a similar jet sample (fig. 7L of [102]), we see that the DeepTop tagger performs considerably worse, by a factor of ~ 3 or more. This is despite the DeepTop tagger being shown to outperform a BDT trained

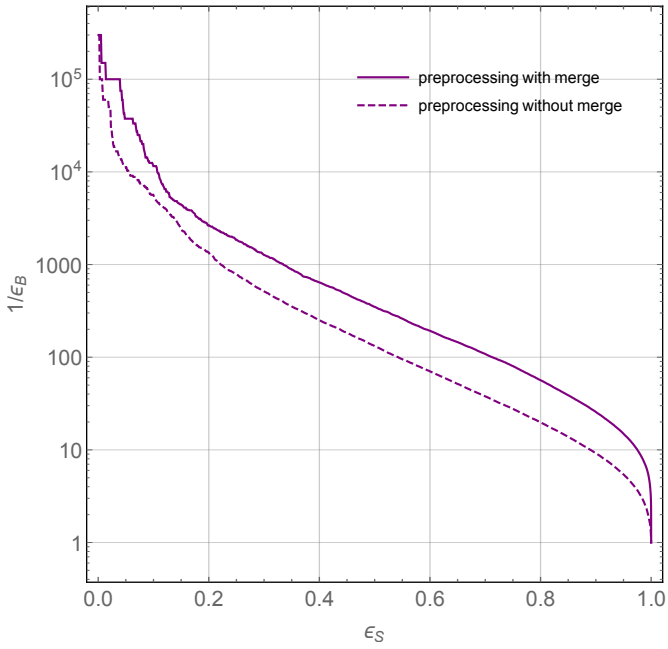

Figure C.1: ROC curves showing the performance of our top tagger on the CMS sample with and without the merge requirement.

on HTTV2 variables, which is among the best ROC curves shown in the CMS reference. We believe the crucial difference between the two ROC curves is the merge requirement. CMS requires their low p_T tops to satisfy $\Delta R(t, q) < 0.8$, while DeepTop [96] does not include this requirement.

Appendix D

Event Generation

Our event generation is performed using `MadGraph5_aMC@NLO` [232] at 13 TeV and showered with `PYTHIA 6` [317], using leading-order matrix elements (without K-factors). We set the top quark mass to 173 GeV, and width to 1.5 GeV.

For our signal samples, we choose mostly-right-handed stop and mostly-Bino neutralino. (Spin effects on our all-hadronic analysis are expected to be modest.) Most samples are generated as $\tilde{t}\tilde{t}^* j$, with only a parton-level cut of 400 GeV on the accompanying jet. Both stops are decayed using three-body phase space $\tilde{t} \to W b \tilde{\chi}^0$, regardless of mass point, which is crucial for modeling the kinematic transition at the top compression line. A complete decay chain is therefore, e.g., `t1 > W+ b n1, W+ > j j`. The stop width for each model point is computed separately using $1 \to 3$ parton-level decay simulations. A subset of models along the compression line have been simulated over their full production phase space, using k_T-MLM matching with a threshold of 100 GeV. Perhaps unsurprisingly, the events passing our final selections are highly dominated by the $1j$ subsample, and are in close agreement with our simple unmatched simulations. Similarly, we find very low relative pass rates for decay modes other than all-hadronic.

The backgrounds are generated as follows.[1] Our $t\bar{t}$ sample is matched up to one (two) jets for all-hadronic (partially leptonic or τ) decays, again using a 100 GeV threshold. We also generate $t\bar{t}W$ and $t\bar{t}Z$ matched up to one jet. For W/Z+jets and multijet backgrounds,

[1] We do not generate single-top nor diboson backgrounds, which, given our reconstruction criteria, we expect to be subdominant to $t\bar{t}$ and W/Z+jets, respectively. Cf. the background composition in ATLAS's all-hadronic stop search [142].

we concentrate on production with at least two heavy quarks (bottom or charm) in the hard event. Because of the difficulties of computing very high-multiplicity matrix elements, we mainly use the parton shower to generate extra partons, and do not employ any matching. The W/Z+jets sample specifically starts with W/Z (decaying to $l\nu$, $\tau\nu$, or $\nu\nu$) plus three hard partons, while the multijet sample starts with four hard partons. We have also cross-checked the multijets against `AlpGen` [318] samples, generated with identical criteria. For each sample we impose cuts at the parton level that treat the b and j partons democratically, requiring $p_T(j) > 15$, $\Delta R(j, j) > 0.4$ (where j here includes b) as well as a p_T cut on the hardest jet of 350 GeV.

Appendix E

Recasting Details and Validation

Here, we discuss the details of our reinterpretation of each of the ATLAS and CMS experimental searches used in chapter 4. Each search has provided details of the cut-flow for the various signal regions, along with the expected and observed number of events, allowing us to apply the results to the supersymmetric models of interest. In order to validate our implementation of each search, we apply our recast to the simplified supersymmetric models used by the experiments themselves. These simplified models typically have only two or three supersymmetric particles kinematically accessible. As such, they are not appropriate for our study of naturalness in SUSY.

As in the study of the full supersymmetric theories, described in Section 4.2, we generate hard events for the simplified models using MadGraph5 [232], with NLO cross sections from Prospino [233–235]; we have not noticed appreciable differences in the validation plots between generating matched and unmatched samples. We decay and shower these events with Pythia8 [109]. Detector simulation is via Delphes3 [110], which makes use of the FastJet [111] package for jet finding. We use the same jet-clustering algorithms as in each experimental search, namely the longitudinally invariant k_t algorithm [319, 320] and the anti-k_t algorithm [171], as well as jet trimming [321] on reclustered jets [322]. In Delphes, we reconstruct the missing energy vector as the negative sum of all calorimeter deposits and all muons. In Delphes a ParticleFlow algorithm is also present, which combines the tracker and the calorimeter information to define physics objects. The differences in the missing energy are usually small, but we choose the former method as it results in validation

plots that are in slightly better agreement with the official results, although the differences are within our "theory error" estimate.

In most cases, recasting the searches requires only a straight-forward implementation of the cut-flow described in the relevant conference note. Where necessary, we note any deviations we were forced to take from the search as reported by the experimental collaboration. In the following, we show our validation plots, comparing the experimental exclusion region with the exclusion region we find on simplified supersymmetric models. As in the original experimental searches, limits are set by taking observed limits on the number of signal events in the signal region which has the best expected limits.

E.0.1 ATLAS Same-sign Lepton/Three Lepton

The ATLAS note CONF-2016-037 [208] is a search for supersymmetric particles decaying to jets and leptons, requiring either two same sign leptons or three leptons in the final state. A number of signal regions are defined, separated by number of b-tagged jets, lepton multiplicity and missing transverse momentum.

We validate our recasting of the search by generating events using one of the supersymmetric simplified models considered by [208]: gluino pair production decaying to top pairs and a neutralino $\tilde{g} \to t\bar{t}\tilde{\chi}_1^0$. The published limits are shown in Fig. E.1 with the results of our recasted search on simulated data, along with a 50% "recasting uncertainty" on the number of events in each signal region.

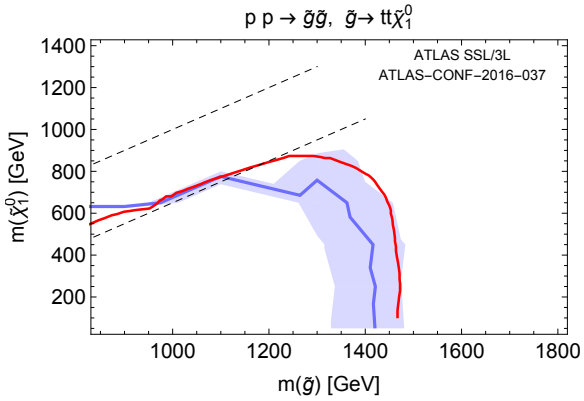

Figure E.1: Limits on a supersymmetric simplified model from our recasted search of [208] (blue line) with 50% error on the number of events in the signal regions (blue shaded region), compared to the experimental results (red line).

E.0.2 ATLAS Lepton Plus Jets

The ATLAS note CONF-2016-054 [229] is a search for gluinos and squarks decaying through $W^{\pm}$ bosons (via charginos), requiring one lepton in the final state, along with jets and missing transverse momentum. A number of signal regions are defined, separated by number of jets, b-tagged jets, and missing transverse momentum.

We validate our recasting of the search by generating events using the supersymmetric simplified model considered by [229]: gluino pair production decaying to light-flavor quarks and a chargino, which itself decays to a neutralino and a W boson: $\tilde{g} \to q\overline{q}'\tilde{\chi}_1^{\pm}$, $\tilde{\chi}_1^{\pm} \to W^{\pm}\tilde{\chi}_1^0$. The chargino mass is set to be the average of the gluino and neutralino mass. The published limits are shown in Fig. E.2 with the results of our recasted search on simulated data, along with a 50% "recasting uncertainty" on the number of events in each signal region.

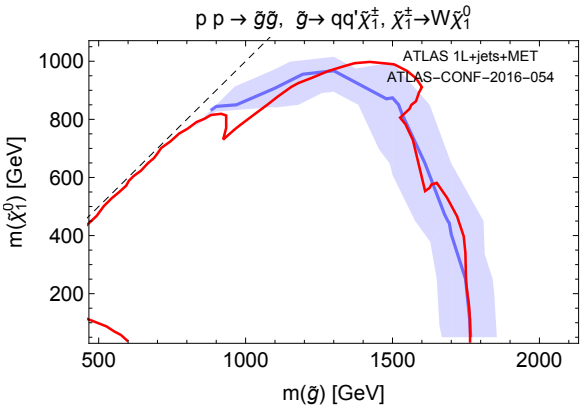

Figure E.2: Limits on supersymmetric simplified models from our recasted search of [229] (blue line) with 50% error on the number of events in the signal regions (blue shaded region), compared to the experimental results (red line).

E.0.3 ATLAS Multi-b

The ATLAS note CONF-2016-052 [207] is a search for gluinos decaying to third generation quarks (tops or bottoms) and missing transverse momentum. At least three b-jets must be identified in the final state. Some signal regions further require "fat" jets which have topological similarities to top quarks. We followed the procedure outlined in [207] by re-clustering the $\Delta R = 0.4$ jets into jets of radius 0.8 using the anti-k_T algorithm in DELPHES, and then further trimming the resulting jets by removing subjets whose p_T falls below 10% of the p_T of the re-clustered jet.

We validate our recasting of the search by generating events using the supersymmetric simplified model considered by [207]: (i) gluino pair production decaying to top pairs and a neutralino $\tilde{g} \to t\bar{t}\tilde{\chi}_1^0$ and (ii) gluino pair production decaying to bottom pairs and a neutralino $\tilde{g} \to b\bar{b}\tilde{\chi}_1^0$. The published limits are shown in Fig. E.3 with the results of our recasted search on simulated data, along with a 50% "recasting uncertainty" on the number of events in each signal region.

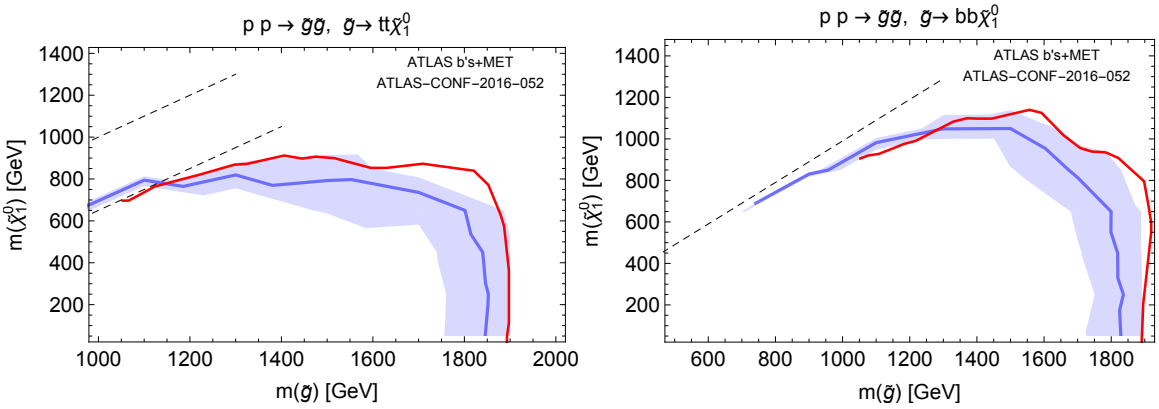

Figure E.3: Limits on supersymmetric simplified models from our recasted search of [207] (blue lines) with 50% error on the number of events in the signal regions (blue shaded regions), compared to the experimental results (red lines).

E.0.4 ATLAS RPV

The ATLAS note CONF-2016-057 [209] is a search for RPV SUSY. A number of signal regions are identified with varying number of jets, b-tagged jets, and large radius jets. These "fat" jets are simulated in DELPHES by reclustering the calorimeter jets into jets of radius 1.0 using the anti-k_T algorithm. Then, the resulting large jets are trimmed by re-clustering their components using the k_T algorithm with a sub-jet radius parameter of 0.2 and discarding sub-jets carrying less than 5% of the original large jet. The surviving sub-jets are used to calculate the "fat" jet energy and momentum, which is then further corrected by the jet energy scale.

We validate our recasting of the search by generating events using the supersymmetric simplified model considered by [209]: (i) gluino pair production decaying to all quark pairs and a neutralino $\tilde{g} \to q\bar{q}\tilde{\chi}_1^0$ followed by neutralino decay via RPV operators into three quarks $\tilde{\chi}_1^0 \to qqq$ (with equal branching ratios to all available flavor combinations), and (ii)

gluino pair production decaying directly to three quarks $\tilde{g} \to qqq$. The published limits are shown in Fig. E.4 with the results of our recasted search on simulated data, along with a 50% "recasting uncertainty" on the number of events in each signal region.

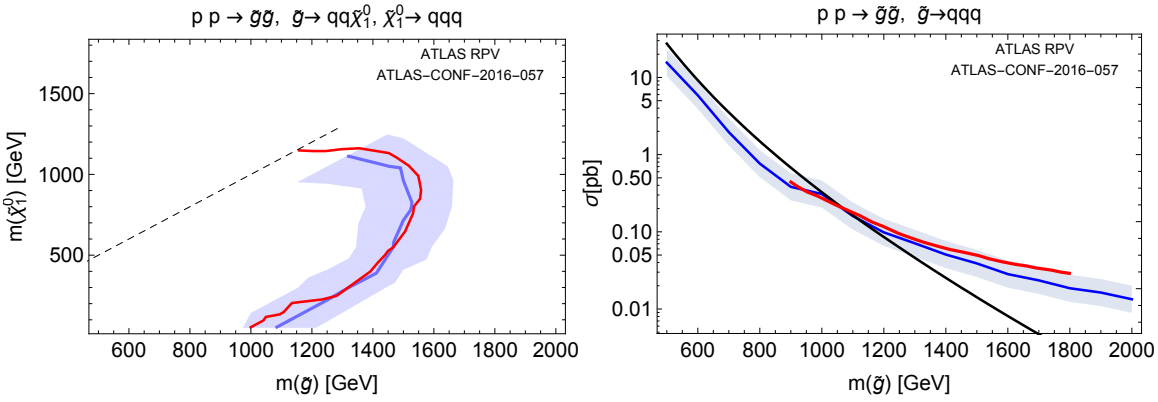

Figure E.4: Limits on supersymmetric simplified models from our recasted search of [209] (blue lines) with 50% error on the number of events in the signal regions (blue shaded regions), compared to the experimental results (red lines). On the right-hand plot, the expect gluino pair production cross section is shown in black.

E.0.5 ATLAS 2–6 Jets Plus MET

The ATLAS note CONF-2016-078 [205] is a search for gluinos and squarks decaying to jets and missing energy, requiring between two and six jets, significant missing energy, and vetoing on leptons. Two search strategies are employed in [205]: one using a m_{eff} variable to separate signal and background, and a second using RJR variables [323]. For simplicity, we use the former search signal regions, which sets bounds as competitive as the latter.

We validate our recasting of the search by generating events using the supersymmetric simplified models considered by [205]: (i) gluino pair production decaying to light-flavor quarks and a neutralino $\tilde{g} \to q\bar{q}\tilde{\chi}_1^0$, (ii) light-flavor squark pair production decaying to quarks and a neutralino $\tilde{q} \to q\tilde{\chi}_1^0$, (iii) and gluino pair production decaying to light-flavor quarks and a chargino, which itself decays to a neutralino and a W boson: $\tilde{g} \to q\bar{q}'\tilde{\chi}_1^\pm$, $\tilde{\chi}_1^\pm \to W^\pm\tilde{\chi}_0^1$. In the latter case, the chargino mass is set to be the average of the gluino and neutralino mass. The published limits are shown in Fig. E.5 with the results of our recasted search on simulated data, along with a 50% "recasting uncertainty" on the number of events in each signal region.

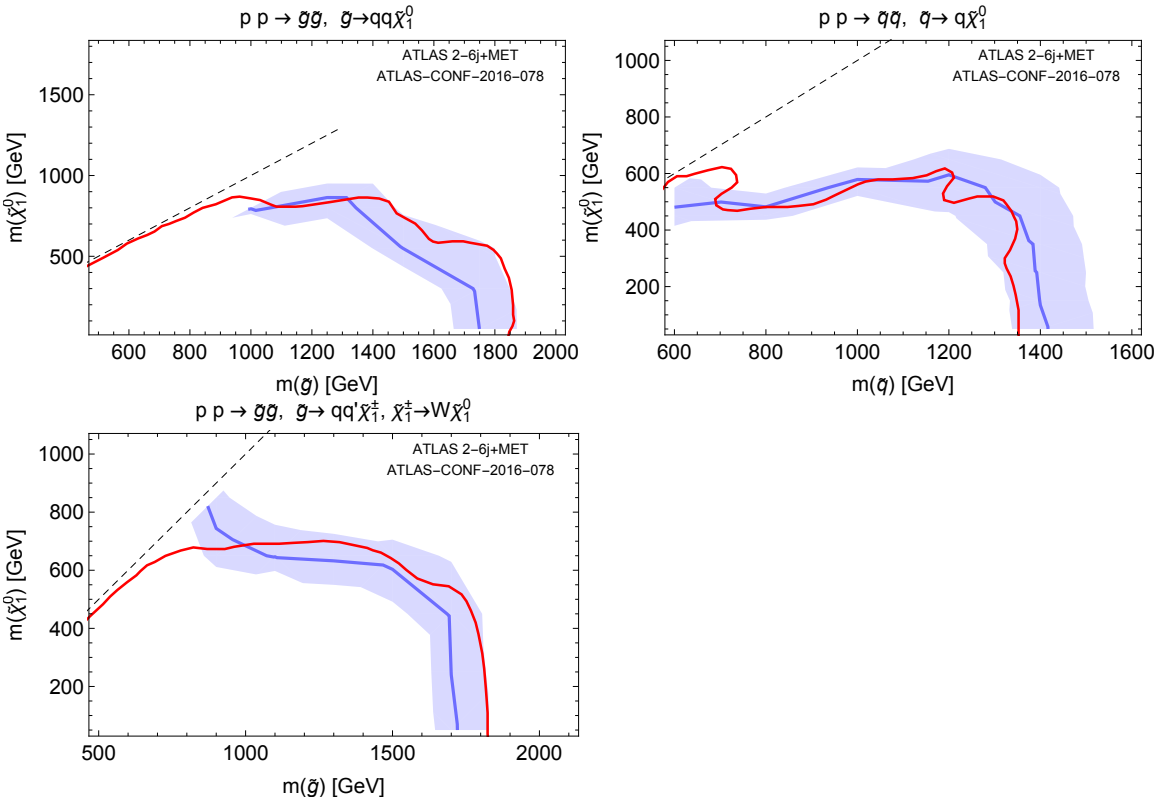

Figure E.5: Limits on supersymmetric simplified models from our recasted search of [205] (blue lines) with 50% error on the number of events in the signal regions (blue shaded regions), compared to the experimental results (red lines).

E.0.6 CMS Multi-Jet + MET

There are three searches from the CMS Collaboration which search for gluinos and squarks decaying to jets and missing energy which were presented at ICHEP in 2016 [228, 230, 231]. We chose to work with [228] (CMS-SUS-16-014), which has equivalent reach as the other two searches. This search requires at least three jets, no leptons, and significant missing transverse momentum. The full analysis uses 160 signal regions, separated by minimum jet, b-tagged jet, H_T, and H_T^{miss}. However, this large number of signal regions can be simplified to twelve aggregated regions. In each region, we calculate the maximum number of signal events which can be accommodated at 95% CL from the published background expectation and observation (Appendix A.5 of [228]) using the CL_s method.

We validate our recasting of the search by generating events using the supersymmetric simplified models considered by [228]: (i) gluino pair production decaying to light-flavor quarks and a neutralino $\tilde{g} \to q\bar{q}\tilde{\chi}_1^0$, (ii) light-flavor squark pair production decaying to

quarks and a neutralino $\tilde{q} \to q\tilde{\chi}_1^0$, (iii) gluino pair production decaying to top pairs and a neutralino $\tilde{g} \to t\bar{t}\tilde{\chi}_1^0$, and (iv) gluino pair production decaying to bottom pairs and a neutralino $\tilde{g} \to b\bar{b}\tilde{\chi}_1^0$. The published limits are shown in Fig. E.6 with the results of our recasted search on simulated data, along with a 50% "recasting uncertainty" on the number of events in each signal region.

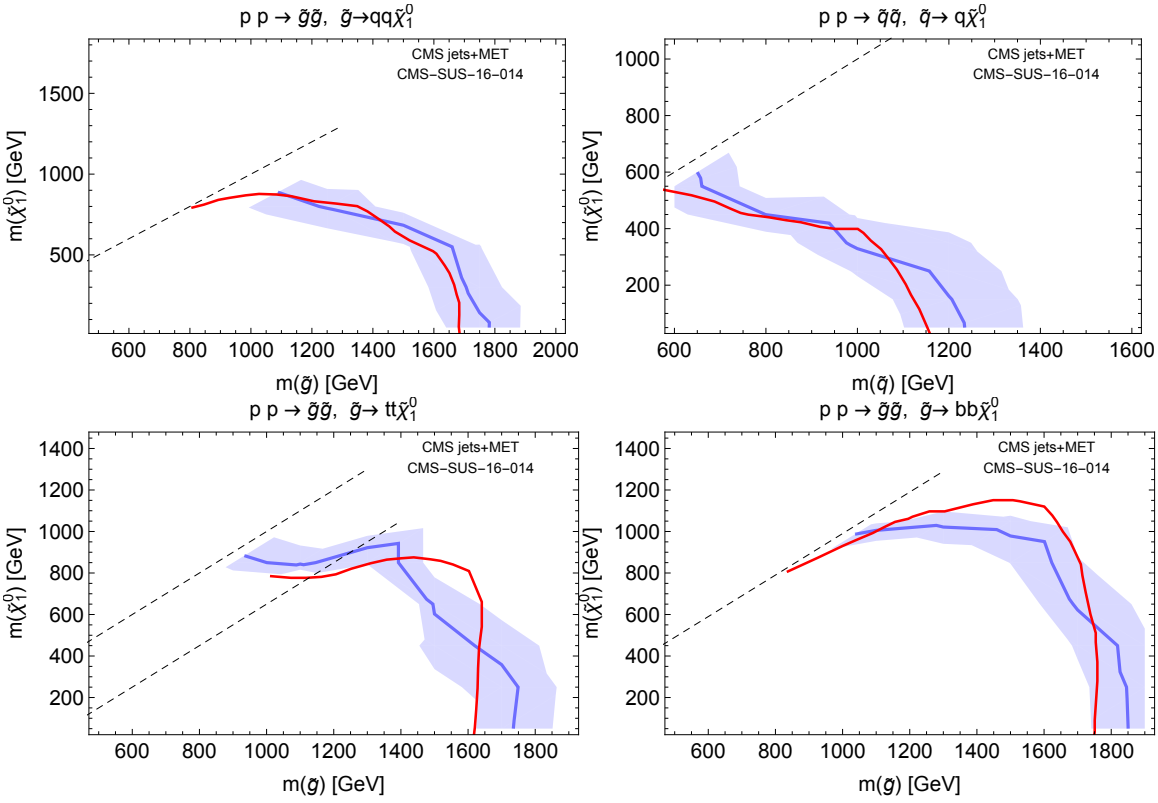

Figure E.6: Limits on supersymmetric simplified models from our recasted search of [228] (blue lines) with 50% error on the number of events in the signal regions (blue shaded regions), compared to the experimental results (red lines).

E.0.7 ATLAS 8–10 Jets Plus MET

The ATLAS note CONF-2016-095 [206] (which is the direct update of the 7–10 jet search in [225] with an increased luminosity of 18.2 fb^{-1}) is a search for gluinos decaying to jets and missing energy, requiring between eight and ten jets, some missing energy, and vetoing on leptons. "Fat" jets are used to discriminate over the background, in addition to the ratio $E_T^{\text{miss}}/\sqrt{H_T}$. A number of signal regions are defined, with varying jet multiplicity and requirements on the sum of the fat jet masses. These large-R jets are found by reclustering

the small-R jets with the anti-k_t algorithm and a radius $R = 1.0$ in DELPHES. Then, the sum of the masses of the reclustered jets is used to define the signal regions.

We validate our recasting of the search by generating events using the supersymmetric simplified models considered by [206], (*i*) gluino pair production decaying to light-flavor quarks and a chargino, which itself decays to a neutralino and a W boson, $\tilde{g} \to q\overline{q}'\tilde{\chi}_1^{\pm}$, $\tilde{\chi}_1^{\pm} \to W^{\pm}\tilde{\chi}_0^1$, with the chargino mass set to be the average of the gluino and neutralino mass, and (*ii*) gluino pair production decaying to light-flavor quarks and a chargino, which then decays to a W boson and a neutralino $\tilde{\chi}_2^0$, followed by the neutralino decay to a Z boson and the lightest neutralino $\tilde{\chi}_1^0$, $\tilde{g} \to q\overline{q}'\tilde{\chi}_1^{\pm}$, $\tilde{\chi}_1^{\pm} \to W^{\pm}\tilde{\chi}_0^2, \tilde{\chi}_0^2 \to Z\tilde{\chi}_0^1$. The published limits are shown in Fig. E.7 with the results of our recasted search on simulated data, along with a 50% "recasting uncertainty" on the number of events in each signal region.

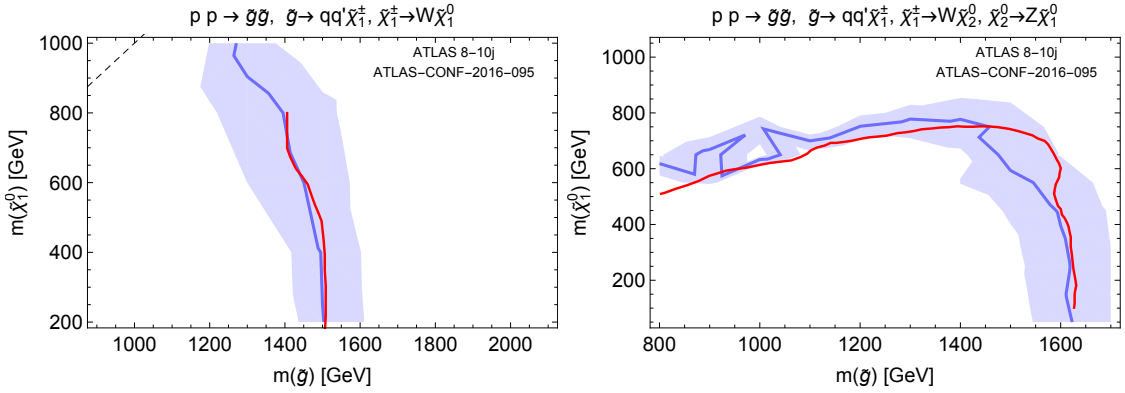

Figure E.7: Limits on supersymmetric simplified models from our recasted search of [225] (blue line) with 50% error on the number of events in the signal regions (blue shaded region), compared to the experimental results (red line).

E.0.8 ATLAS Lepton Plus Many Jets

The ATLAS note CONF-2016-094 [210] is a search for gluinos decaying to top-rich final states and little missing transverse momentum, requiring one lepton and multiple jets in the final state. A number of signal regions are defined, separated by number of jets and b-tagged jets.

We validate our recasting of the search by generating events using the supersymmetric simplified model considered by [210]: gluino pair production decaying to top quarks and a neutralino, which itself decays via RPV to three light quarks: $\tilde{g} \to t\overline{t}'\tilde{\chi}_1^0$, $\tilde{\chi}_1^0 \to uds$. The

published limits are shown in Fig. E.8 with the results of our recasted search on simulated data, along with a 50% "recasting uncertainty" on the number of events in each signal region.

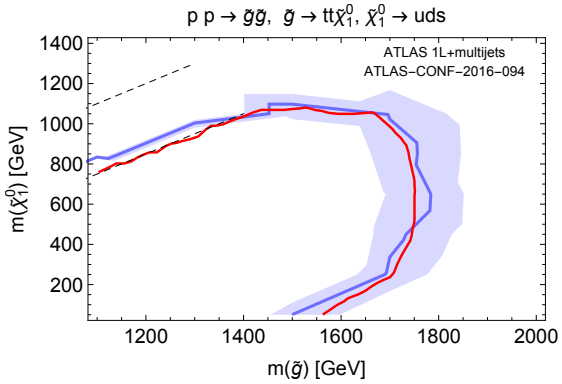

Figure E.8: Limits on supersymmetric simplified models from our recasted search of [210] (blue line) with 50% error on the number of events in the signal regions (blue shaded region), compared to the experimental results (red line).

Appendix F

Connecting model parameters to DD cross sections

In this appendix, we will review how to relate the SI and SD DM-nucleon cross sections to the couplings ξ_q^{SI} and ξ_q^{SD} appearing in the effective Lagrangian (5.3.1). To check our results we verify that by calculating SI and SD cross sections analytically, we get the same result as the one we get from micrOMEGAs.

Following [13], the SI and SD cross sections are

$$\sigma_{p,n}^{SI} = \frac{x m_r^2}{\pi} f_{p,n}^2, \qquad \sigma_{p,n}^{SD} = \frac{3 x m_r^2}{\pi} a_{p,n}^2 \tag{F.0.1}$$

where $x = 4$ for Majorana ($x = 1$ for Dirac) fermions, m_r is the reduced mass of the DM-nucleon system, and $a_{p,n}^{SD}, f_{p,n}^{SI}$ are the effective DM-nucleon couplings:

$$\begin{aligned} f_{p,n} &= \sum_{q=u,d,s} \xi_q^{SI} f_q^{p,n} \frac{m_{p,n}}{m_q} + \frac{2}{27}\left(1 - \sum_{q=u,d,s} f_q^{p,n}\right) \sum_{q=c,b,t} \xi_q^{SI} \frac{m_{p,n}}{m_q} \\ a_{p,n} &= \sum_{q=u,d,s} \xi_q^{SD} \, \Delta_q^{p,n}, \end{aligned} \tag{F.0.2}$$

Here m_q is the quark mass, $f_q^{p,n}$, and Δ_q are hadronic parameters calculated for example by lattice simulations in QCD. We use the values in tab. F.1 according to [324]. The difference between SI cross sections for proton and neutron is negligible as the main contribution comes from f_s which is the same in both cases.

In fig. F.1, we compare our analytic cross sections to micrOMEGAs. We see that the agreement is excellent.

	Δ_u	Δ_d	Δ_s	f_u	f_d	f_s
p	0.842	-0.427	-0.085	0.0153	0.0191	0.0447
n	-0.427	0.842	-0.085	0.011	0.0273	0.0447

Table F.1: Nucleon quark form factors.

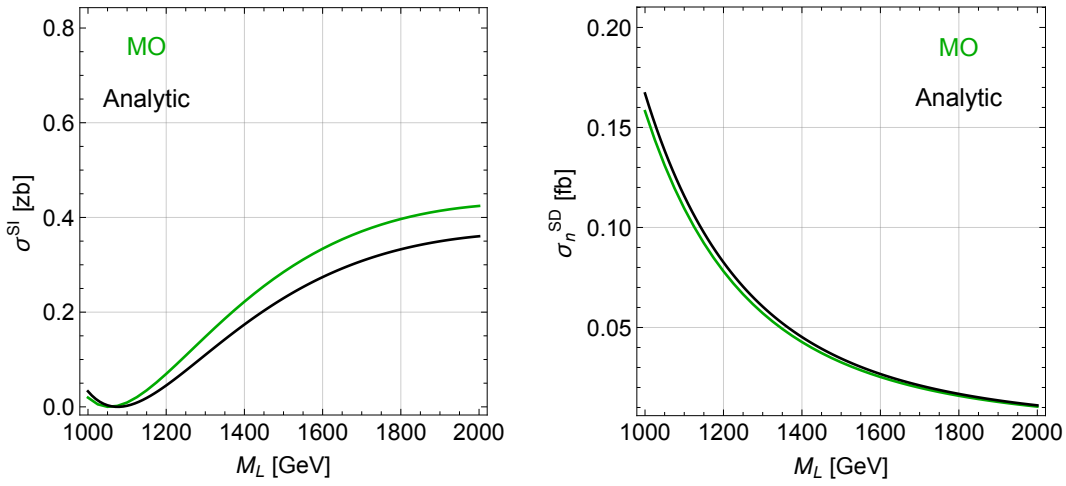

Figure F.1: Comparing (F.0.1) with micrOMEGAs 4.1.8 for $M_S = 200$ GeV, $k_u = 1.6$, $k_d = -1.5$.

Appendix G

Validating SPheno one loop Higgs mass

In this appendix we validate the contributions to the Higgs mass from the dark sector as calculated by SPheno against the analytic one-loop calculation through the Coleman-Weinberg (CW) potential. We consider the simplified one-loop CW result from (5.4.1), where we ignored $g_{1,2}$ and μ and took the $\tan\beta \to \infty$ limit. We will show that both one-loop and two-loop results from SPheno match quite well with our analytical result. As SPheno outputs the total Higgs mass and not just the contributions from the dark sector, we extract these contributions as follows:

$$\delta m_h^2 = m_h^2 - m_h^2|_{MSSM} \tag{G.0.1}$$

where $m_h^2|_{MSSM}$ is the contribution to m_h^2 from the MSSM with superpartners at 1 TeV.

Since the Higgs mass depends primarily on k_u, M_L, M_S, we will demonstrate here that SPheno and our CW calculation agree well as these parameters are varied. From (5.4.1) we expect $\delta m_h^2 \sim k_u^4$. As we can see in fig. G.1 (left), SPheno confirms this behavior. After fixing the k_u dependence, we need to check that our analytical equations and SPheno match as we change M_L and M_S. That is shown in fig. G.1 (right) for two values of M_S as we scan over M_L.

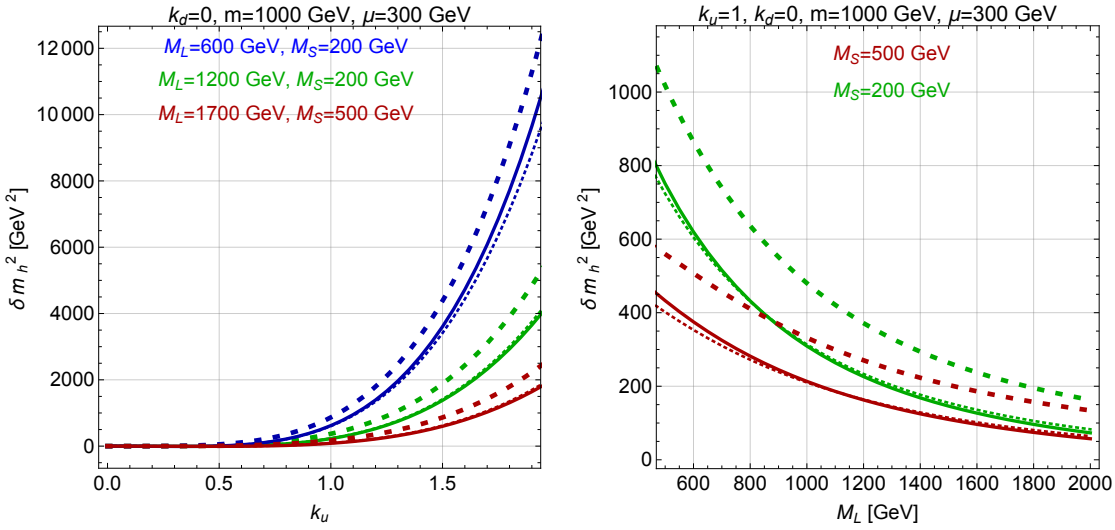

Figure G.1: Thick dashed: analytical one-loop result (5.4.1). Dotted: SPheno one-loop. Solid: SPheno two-loop.

Appendix H

LHC cross section analytics

Here we will provide some analytic details for the calculation of the $pp \to \chi_1\chi_{2,3}$ and $pp \to \chi_1\chi^{\pm}$ LHC cross sections useful for section 5.8.2. The former receives contributions from both tree-level Z's with $q\overline{q}$ initial state, as well as one-loop gluon fusion. The latter comes from tree-level $W^{\pm}$'s with $q\overline{q}'$ initial state.

The tree-level, quark-initiated cross sections are given by:

$$\begin{aligned}\sigma(q\overline{q} \to \chi_1\chi_i) &= \frac{g_2^4|\vec{p}_f|}{144\pi c_W^4 S^{3/2}}\left(c^2_{Zq_Lq_L} + c^2_{Zq_Rq_R}\right)\times \\ &\qquad ((\mathrm{Re}\, R_i)^2 f_Z(S, m_1, m_i) + (\mathrm{Im}\, R_i)^2 f_Z(S, m_1, -m_i)) \\ \sigma(q\overline{q}' \to \chi_1\chi^+) &= \frac{g_2^4|\vec{p_f}|}{576\pi S^{3/2}}\left(f_W(S, m_1, m_+)|R_+|^2 + f_W(S, m_1, -m_+)|R_-|^2\right)\end{aligned} \tag{H.0.1}$$

where

$$\begin{aligned}R_i &= (U^*_{1,2}U_{i,2} - U^*_{1,3}U_{i,3}) \\ R_\pm &= U_{1,2} \pm U^*_{1,3} \\ f_A(S, x, y) &= \frac{(S - (x+y)^2)(S + \frac{(x-y)^2}{2})}{(S - m_A^2)^2}\end{aligned} \tag{H.0.2}$$

and

$$c_{Z\overline{u}_Lu_L} = \frac{1}{2} - \frac{2}{3}s_W^2, \quad c_{Z\overline{d}_Ld_L} = -\frac{1}{2} + \frac{1}{3}s_W^2, \quad c_{Z\overline{u}_Ru_R} = \frac{2}{3}s_W^2, \quad c_{Z\overline{d}_Rd_R} = -\frac{1}{3}s_W^2 \tag{H.0.3}$$

The parton level gluon fusion cross section (as can be calculated e.g. using [307]) is

$$\sigma(gg \to \chi_1\chi_i) = \frac{|\vec{p_f}|m_t^2}{128\pi S^{5/2}}\left|\frac{\lambda_t\alpha_3 c_{\chi_1\chi_i h}F(S/m_t^2)}{4\pi}\right|^2 g(S, m_1, m_i) \tag{H.0.4}$$

where

$$\begin{aligned} g(S, m_1, m_2) &= \frac{(1 - \frac{(m_1+m_2)^2}{S})}{(1 - \frac{m_h^2}{S})^2} \\ F(x) &= 2\sqrt{2}\left(1 + \left(1 - \frac{4}{x}\right)\left[\sin^{-1}\sqrt{\frac{x}{4}}\right]^2\right). \end{aligned} \tag{H.0.5}$$

and $c_{\chi_1\chi_i h}$ is the coupling between Higgs and $\chi_1\chi_i$ $(i = 2, 3)$ defined in the same way as c_h in (5.2.4):

$$\begin{aligned} \mathcal{L} &\supset c_{\chi_1\chi_i h} h \overline{\psi}_{\chi_1} \psi_{\chi_i} \\ c_{\chi_1\chi_i h} &= \frac{1}{\sqrt{2}}\left(\hat{k}_u(U^*_{1,1}U^*_{i,2} + U^*_{1,2}U^*_{i,1}) + \hat{k}_d(U^*_{1,1}U^*_{i,3} + U^*_{1,3}U^*_{i,1})\right), \end{aligned} \tag{H.0.6}$$

Bibliography

[1] Serguei Chatrchyan et al. "Observation of a new boson at a mass of 125 GeV with the CMS experiment at the LHC". In: *Phys. Lett.* B716 (2012), pp. 30–61. DOI: 10.1016/j.physletb.2012.08.021. arXiv: 1207.7235 [hep-ex].

[2] Georges Aad et al. "Observation of a new particle in the search for the Standard Model Higgs boson with the ATLAS detector at the LHC". In: *Phys. Lett.* B716 (2012), pp. 1–29. DOI: 10.1016/j.physletb.2012.08.020. arXiv: 1207.7214 [hep-ex].

[3] E. Aprile et al. "First Dark Matter Search Results from the XENON1T Experiment". In: *Phys. Rev. Lett.* 119.18 (2017), p. 181301. DOI: 10.1103/PhysRevLett.119.181301. arXiv: 1705.06655 [astro-ph.CO].

[4] D. S. Akerib et al. "Results from a search for dark matter in the complete LUX exposure". In: (2016). arXiv: 1608.07648 [astro-ph.CO].

[5] Xiangyi Cui et al. "Dark Matter Results from 54-Ton-Day Exposure of PandaX-II Experiment". In: *Phys. Rev. Lett.* 119 (18 2017), p. 181302. DOI: 10.1103/PhysRevLett.119.181302. URL: https://link.aps.org/doi/10.1103/PhysRevLett.119.181302.

[6] E. Aprile et al. "Physics reach of the XENON1T dark matter experiment". In: *JCAP* 1604.04 (2016), p. 027. DOI: 10.1088/1475-7516/2016/04/027. arXiv: 1512.07501 [physics.ins-det].

[7] D. S. Akerib et al. "LUX-ZEPLIN (LZ) Conceptual Design Report". In: (2015). arXiv: 1509.02910 [physics.ins-det].

[8] *Search for the Supersymmetric Partner of the Top Quark in the Jets+Emiss Final State at sqrt(s) = 13 TeV*. Tech. rep. ATLAS-CONF-2016-077. Geneva: CERN, 2016. URL: https://cds.cern.ch/record/2206250.

[9] Morad Aaboud et al. "Search for a scalar partner of the top quark in the jets plus missing transverse momentum final state at $\sqrt{s}$=13 TeV with the ATLAS detector". In: *JHEP* 12 (2017), p. 085. DOI: 10.1007/JHEP12(2017)085. arXiv: 1709.04183 [hep-ex].

[10] Gianfranco Bertone, Dan Hooper, and Joseph Silk. "Particle dark matter: Evidence, candidates and constraints". In: *Phys. Rept.* 405 (2005), pp. 279–390. DOI: 10.1016/j.physrep.2004.08.031. arXiv: hep-ph/0404175 [hep-ph].

[11] Hitoshi Murayama. "Physics Beyond the Standard Model and Dark Matter". In: *Les Houches Summer School - Session 86: Particle Physics and Cosmology: The Fabric of Spacetime Les Houches, France, July 31-August 25, 2006*. 2007. arXiv: 0704.2276 [hep-ph]. URL: https://inspirehep.net/record/748786/files/arXiv:0704.2276.pdf.

[12] Graciela B. Gelmini. "The Hunt for Dark Matter". In: *Proceedings, Theoretical Advanced Study Institute in Elementary Particle Physics: Journeys Through the Precision Frontier: Amplitudes for Colliders (TASI 2014): Boulder, Colorado, June 2-27, 2014*. 2015, pp. 559–616. DOI: 10.1142/9789814678766_0012. arXiv: 1502.01320 [hep-ph]. URL: https://inspirehep.net/record/1342951/files/arXiv:1502.01320.pdf.

[13] Gerard Jungman, Marc Kamionkowski, and Kim Griest. "Supersymmetric dark matter". In: *Phys. Rept.* 267 (1996), pp. 195–373. DOI: 10.1016/0370-1573(95)00058-5. arXiv: hep-ph/9506380 [hep-ph].

[14] Stephen P. Martin. "A Supersymmetry primer". In: (1997). [Adv. Ser. Direct. High Energy Phys.18,1(1998)], pp. 1–98. DOI: 10.1142/9789812839657_0001,10.1142/9789814307505_0001. arXiv: hep-ph/9709356 [hep-ph].

[15] Lyndon R Evans and Philip Bryant. "LHC Machine". In: *JINST* 3 (2008). This report is an abridged version of the LHC Design Report (CERN-2004-003), S08001. 164 p. URL: http://cds.cern.ch/record/1129806.

[16] Tirso Alejandro Gomez Espinosa. "Search for pair-produced diquark resonances in proton-proton collisions with the CMS detector at $\sqrt{S}$= 13TeV". In: (2018). URL: https://cernbox.cern.ch/index.php/s/gz672amTVmbQ0sS#pdfviewer.

[17] *ATLAS: technical proposal for a general-purpose pp experiment at the Large Hadron Collider at CERN*. LHC Tech. Proposal. Geneva: CERN, 1994. URL: http://cds.cern.ch/record/290968.

[18] *Technical proposal*. LHC Tech. Proposal. Cover title : CMS, the Compact Muon Solenoid : technical proposal. Geneva: CERN, 1994. URL: http://cds.cern.ch/record/290969.

[19] *LHCb : Technical Proposal*. Tech. Proposal. Geneva: CERN, 1998. URL: http://cds.cern.ch/record/622031.

[20] *ALICE: Technical proposal for a Large Ion collider Experiment at the CERN LHC*. LHC Tech. Proposal. Geneva: CERN, 1995. URL: http://cds.cern.ch/record/293391.

[21] S. Chatrchyan et al. "The CMS Experiment at the CERN LHC". In: *JINST* 3 (2008), S08004. DOI: 10.1088/1748-0221/3/08/S08004.

[22] Siona Ruth Davis. "Interactive Slice of the CMS detector". In: (2016). URL: https://cds.cern.ch/record/2205172.

[23] A. M. Sirunyan et al. "Particle-flow reconstruction and global event description with the CMS detector". In: *JINST* 12.10 (2017), P10003. DOI: 10.1088/1748-0221/12/10/P10003. arXiv: 1706.04965 [physics.ins-det].

[24] Georges Aad et al. "Evidence for the spin-0 nature of the Higgs boson using ATLAS data". In: *Phys. Lett.* B726 (2013), pp. 120–144. DOI: 10.1016/j.physletb.2013.08.026. arXiv: 1307.1432 [hep-ex].

[25] "Combination of standard model Higgs boson searches and measurements of the properties of the new boson with a mass near 125 GeV". In: (2012). URL: http://inspirehep.net/record/1230268/files/HIG-12-045-pas.pdf.

[26] Abdelhak Djouadi. "Higgs Physics". In: *PoS* CORFU2014 (2015), p. 018. arXiv: 1505.01059 [hep-ph].

[27] John Ellis. "Topics in Higgs Physics". In: *3rd Asia-Europe-Pacific School of High-Energy Physics (AEPSHEP 2016) Beijing, China, October 12-25, 2016*. 2017. arXiv: 1702.05436 [hep-ph]. URL: https://inspirehep.net/record/1514038/files/arXiv:1702.05436.pdf.

[28] Georges Aad et al. "Measurements of Higgs boson production and couplings in diboson final states with the ATLAS detector at the LHC". In: *Phys. Lett.* B726 (2013). [Erratum: Phys. Lett.B734,406(2014)], pp. 88–119. DOI: 10.1016/j.physletb.2014.05.011,10.1016/j.physletb.2013.08.010. arXiv: 1307.1427 [hep-ex].

[29] Vardan Khachatryan et al. "Observation of the diphoton decay of the Higgs boson and measurement of its properties". In: *Eur. Phys. J.* C74.10 (2014), p. 3076. DOI: 10.1140/epjc/s10052-014-3076-z. arXiv: 1407.0558 [hep-ex].

[30] Serguei Chatrchyan et al. "Measurement of the properties of a Higgs boson in the four-lepton final state". In: *Phys. Rev.* D89.9 (2014), p. 092007. DOI: 10.1103/PhysRevD.89.092007. arXiv: 1312.5353 [hep-ex].

[31] R. Barate et al. "Search for the standard model Higgs boson at LEP". In: *Phys. Lett.* B565 (2003), pp. 61–75. DOI: 10.1016/S0370-2693(03)00614-2. arXiv: hep-ex/0306033 [hep-ex].

[32] TEVNPH Working Group. "Combined CDF and D0 Upper Limits on Standard Model Higgs Boson Production with up to 8.6 fb^{-1} of Data". In: 2011. arXiv: 1107.5518 [hep-ex]. URL: http://lss.fnal.gov/cgi-bin/find_paper.pl?conf-11-354.

[33] M. Baak et al. "Updated Status of the Global Electroweak Fit and Constraints on New Physics". In: *Eur. Phys. J.* C72 (2012), p. 2003. DOI: 10.1140/epjc/s10052-012-2003-4. arXiv: 1107.0975 [hep-ph].

[34] Vardan Khachatryan et al. "Precise determination of the mass of the Higgs boson and tests of compatibility of its couplings with the standard model predictions using proton collisions at 7 and 8 TeV". In: *Eur. Phys. J.* C75.5 (2015), p. 212. DOI: 10.1140/epjc/s10052-015-3351-7. arXiv: 1412.8662 [hep-ex].

[35] D. de Florian et al. "Handbook of LHC Higgs Cross Sections: 4. Deciphering the Nature of the Higgs Sector". In: (2016). DOI: 10.23731/CYRM-2017-002. arXiv: 1610.07922 [hep-ph].

[36] Georges Aad et al. "Combined Measurement of the Higgs Boson Mass in pp Collisions at $\sqrt{s} = 7$ and 8 TeV with the ATLAS and CMS Experiments". In: *Phys. Rev. Lett.* 114 (2015), p. 191803. DOI: 10.1103/PhysRevLett.114.191803. arXiv: 1503.07589 [hep-ex].

[37] F. Abe et al. "Observation of top quark production in $\overline{p}p$ collisions". In: *Phys. Rev. Lett.* 74 (1995), pp. 2626–2631. DOI: 10.1103/PhysRevLett.74.2626. arXiv: hep-ex/9503002 [hep-ex].

[38] S. Abachi et al. "Observation of the top quark". In: *Phys. Rev. Lett.* 74 (1995), pp. 2632–2637. DOI: 10.1103/PhysRevLett.74.2632. arXiv: hep-ex/9503003 [hep-ex].

[39] Vittorio del Duca and Eric Laenen. "Top physics at the LHC". In: *Int. J. Mod. Phys.* A30.35 (2015), p. 1530063. DOI: 10.1142/S0217751X1530063X. arXiv: 1510.06690 [hep-ph].

[40] Markus Cristinziani and Martijn Mulders. "Top-quark physics at the Large Hadron Collider". In: *J. Phys.* G44.6 (2017), p. 063001. DOI: 10.1088/1361-6471/44/6/063001. arXiv: 1606.00327 [hep-ex].

[41] Michael Russell. "Top quark physics in the Large Hadron Collider era". PhD thesis. Glasgow U., 2017. arXiv: 1709.10508 [hep-ph]. URL: https://inspirehep.net/record/1627892/files/arXiv:1709.10508.pdf.

[42] Sally Dawson et al. "Working Group Report: Higgs Boson". In: *Proceedings, 2013 Community Summer Study on the Future of U.S. Particle Physics: Snowmass on the Mississippi (CSS2013): Minneapolis, MN, USA, July 29-August 6, 2013*. 2013. arXiv: 1310.8361 [hep-ex]. URL: https://inspirehep.net/record/1262795/files/arXiv:1310.8361.pdf.

[43] https://atlas.web.cern.ch/Atlas/GROUPS/PHYSICS/CombinedSummaryPlots/TOP/.

[44] https://twiki.cern.ch/twiki/bin/view/CMSPublic/PhysicsResultsTOPSummaryFigures.

[45] Emanuele Bagnaschi et al. “Higgs Mass and Unnatural Supersymmetry”. In: *JHEP* 09 (2014), p. 092. DOI: 10.1007/JHEP09(2014)092. arXiv: 1407.4081 [hep-ph].

[46] Eva Halkiadakis, George Redlinger, and David Shih. “Status and Implications of Beyond-the-Standard-Model Searches at the LHC”. In: *Ann. Rev. Nucl. Part. Sci.* 64 (2014), pp. 319–342. DOI: 10.1146/annurev-nucl-102313-025632. arXiv: 1411.1427 [hep-ex].

[47] Patrick Draper and Heidi Rzehak. “A Review of Higgs Mass Calculations in Supersymmetric Models”. In: *Phys. Rept.* 619 (2016), pp. 1–24. DOI: 10.1016/j.physrep.2016.01.001. arXiv: 1601.01890 [hep-ph].

[48] Riccardo Barbieri and G. F. Giudice. “Upper Bounds on Supersymmetric Particle Masses”. In: *Nucl. Phys.* B306 (1988), pp. 63–76. DOI: 10.1016/0550-3213(88)90171-X.

[49] Matthew R. Buckley, Angelo Monteux, and David Shih. “Precision Corrections to Fine Tuning in SUSY”. In: (2016). arXiv: 1611.05873 [hep-ph].

[50] Lawrence J. Hall, David Pinner, and Joshua T. Ruderman. “A Natural SUSY Higgs Near 126 GeV”. In: *JHEP* 04 (2012), p. 131. DOI: 10.1007/JHEP04(2012)131. arXiv: 1112.2703 [hep-ph].

[51] Abdelhak Djouadi, Jean-Loic Kneur, and Gilbert Moultaka. “SuSpect: A Fortran code for the supersymmetric and Higgs particle spectrum in the MSSM”. In: *Comput. Phys. Commun.* 176 (2007), pp. 426–455. DOI: 10.1016/j.cpc.2006.11.009. arXiv: hep-ph/0211331 [hep-ph].

[52] S. Heinemeyer, W. Hollik, and G. Weiglein. “FeynHiggs: A Program for the calculation of the masses of the neutral CP even Higgs bosons in the MSSM”. In: *Comput. Phys. Commun.* 124 (2000), pp. 76–89. DOI: 10.1016/S0010-4655(99)00364-1. arXiv: hep-ph/9812320 [hep-ph].

[53] S. Heinemeyer, W. Hollik, and G. Weiglein. “The Masses of the neutral CP - even Higgs bosons in the MSSM: Accurate analysis at the two loop level”. In: *Eur. Phys. J.* C9 (1999), pp. 343–366. DOI: 10.1007/s100529900006. arXiv: hep-ph/9812472 [hep-ph].

[54] G. Degrassi et al. “Towards high precision predictions for the MSSM Higgs sector”. In: *Eur. Phys. J.* C28 (2003), pp. 133–143. DOI: 10.1140/epjc/s2003-01152-2. arXiv: hep-ph/0212020 [hep-ph].

[55] M. Frank et al. “The Higgs Boson Masses and Mixings of the Complex MSSM in the Feynman-Diagrammatic Approach”. In: *JHEP* 02 (2007), p. 047. DOI: 10.1088/1126-6708/2007/02/047. arXiv: hep-ph/0611326 [hep-ph].

[56] http://articles.adsabs.harvard.edu/cgi-bin/nph-iarticle_query?1933AcHPh...6..110Z&data_type=PDF_HIGH&whole_paper=YES&type=PRINTER&filetype=.pdf.

[57] https://arxiv.org/abs/1711.01693.

[58] Haakon Dahle. "A compilation of weak gravitational lensing studies of clusters of galaxies". In: (2007). arXiv: astro-ph/0701598 [astro-ph].

[59] Annamaria Borriello and Paolo Salucci. "The Dark matter distribution in disk galaxies". In: *Mon. Not. Roy. Astron. Soc.* 323 (2001), p. 285. DOI: 10.1046/j.1365-8711.2001.04077.x. arXiv: astro-ph/0001082 [astro-ph].

[60] Maxim Markevitch. "Chandra observation of the most interesting cluster in the universe". In: (2005). [ESA Spec. Publ.604,723(2006)]. arXiv: astro-ph/0511345 [astro-ph].

[61] Douglas Clowe et al. "A direct empirical proof of the existence of dark matter". In: *Astrophys. J.* 648 (2006), pp. L109–L113. DOI: 10.1086/508162. arXiv: astro-ph/0608407 [astro-ph].

[62] P. A. R. Ade et al. "Planck 2015 results. XIII. Cosmological parameters". In: *Astron. Astrophys.* 594 (2016), A13. DOI: 10.1051/0004-6361/201525830. arXiv: 1502.01589 [astro-ph.CO].

[63] Clifford Cheung et al. "Prospects and Blind Spots for Neutralino Dark Matter". In: *JHEP* 05 (2013), p. 100. DOI: 10.1007/JHEP05(2013)100. arXiv: 1211.4873 [hep-ph].

[64] Tao Han, Zhen Liu, and Aravind Natarajan. "Dark matter and Higgs bosons in the MSSM". In: *JHEP* 11 (2013), p. 008. DOI: 10.1007/JHEP11(2013)008. arXiv: 1303.3040 [hep-ph].

[65] Andreas Crivellin et al. "Light stops, blind spots, and isospin violation in the MSSM". In: *JHEP* 07 (2015), p. 129. DOI: 10.1007/JHEP07(2015)129. arXiv: 1503.03478 [hep-ph].

[66] Kim Griest and David Seckel. "Three exceptions in the calculation of relic abundances". In: *Phys. Rev.* D43 (1991), pp. 3191–3203. DOI: 10.1103/PhysRevD.43.3191.

[67] Gavin P. Salam. "Towards Jetography". In: *Eur. Phys. J.* C67 (2010), pp. 637–686. DOI: 10.1140/epjc/s10052-010-1314-6. arXiv: 0906.1833 [hep-ph].

[68] A. Abdesselam et al. "Boosted objects: A Probe of beyond the Standard Model physics". In: *Eur. Phys. J.* C71 (2011), p. 1661. DOI: 10.1140/epjc/s10052-011-1661-y. arXiv: 1012.5412 [hep-ph].

[69] A. Altheimer et al. "Jet Substructure at the Tevatron and LHC: New results, new tools, new benchmarks". In: *J. Phys.* G39 (2012), p. 063001. DOI: 10.1088/0954-3899/39/6/063001. arXiv: 1201.0008 [hep-ph].

[70] Jessie Shelton. "Jet Substructure". In: *Proceedings, Theoretical Advanced Study Institute in Elementary Particle Physics: Searching for New Physics at Small and Large*

Scales (TASI 2012): Boulder, Colorado, June 4-29, 2012. 2013, pp. 303–340. DOI: 10.1142/9789814525220_0007. arXiv: 1302.0260 [hep-ph].

[71] A. Altheimer et al. "Boosted objects and jet substructure at the LHC. Report of BOOST2012, held at IFIC Valencia, 23rd-27th of July 2012". In: *Eur. Phys. J.* C74.3 (2014), p. 2792. DOI: 10.1140/epjc/s10052-014-2792-8. arXiv: 1311.2708 [hep-ex].

[72] D. Adams et al. "Towards an Understanding of the Correlations in Jet Substructure". In: *Eur. Phys. J.* C75.9 (2015), p. 409. DOI: 10.1140/epjc/s10052-015-3587-2. arXiv: 1504.00679 [hep-ph].

[73] Matteo Cacciari. "Phenomenological and theoretical developments in jet physics at the LHC". In: *Int. J. Mod. Phys.* A30.31 (2015), p. 1546001. DOI: 10.1142/S0217751X1546001X. arXiv: 1509.02272 [hep-ph].

[74] Andrew J. Larkoski, Ian Moult, and Benjamin Nachman. "Jet Substructure at the Large Hadron Collider: A Review of Recent Advances in Theory and Machine Learning". In: (2017). arXiv: 1709.04464 [hep-ph].

[75] Jonathan M. Butterworth et al. "Jet substructure as a new Higgs search channel at the LHC". In: *Phys. Rev. Lett.* 100 (2008), p. 242001. DOI: 10.1103/PhysRevLett.100.242001. arXiv: 0802.2470 [hep-ph].

[76] Morad Aaboud et al. "Measurements of $t\bar{t}$ differential cross-sections of highly boosted top quarks decaying to all-hadronic final states in pp collisions at $\sqrt{s} = 13$ TeV using the ATLAS detector". In: (2018). arXiv: 1801.02052 [hep-ex].

[77] Albert M Sirunyan et al. "Search for dark matter in events with energetic, hadronically decaying top quarks and missing transverse momentum at $\sqrt{s} = 13$ TeV". In: (2018). arXiv: 1801.08427 [hep-ex].

[78] *Search for top squarks in final states with one isolated lepton, jets, and missing transverse momentum using 36.1fb^1 of $\sqrt{13}$ TeV pp collision data with the ATLAS detector*. Tech. rep. ATLAS-CONF-2017-037. URL: http://cds.cern.ch/record/2266170.

[79] Albert M Sirunyan et al. "Search for direct production of supersymmetric partners of the top quark in the all-jets final state in proton-proton collisions at $\sqrt{s} = 13$ TeV". In: *JHEP* 10 (2017), p. 005. DOI: 10.1007/JHEP10(2017)005. arXiv: 1707.03316 [hep-ex].

[80] Tilman Plehn and Michael Spannowsky. "Top Tagging". In: *J. Phys.* G39 (2012), p. 083001. DOI: 10.1088/0954-3899/39/8/083001. arXiv: 1112.4441 [hep-ph].

[81] Gregor Kasieczka. "Boosted Top Tagging Method Overview". In: (2018). arXiv: 1801.04180 [hep-ph].

[82] Michael Nielsen. *Neural Networks and Deep Learning*. URL: http://neuralnetworksanddeeplearning.com/.

[83] Ian Goodfellow, Yoshua Bengio, and Aaron Courville. *Deep Learning*. http://www.deeplearningbook.org. MIT Press, 2016.

[84] Yann LeCun, Yoshua Bengio, and Geoffrey Hinton. "Deep learning". In: *Nature* 521 (May 2015), 436 EP –. URL: http://dx.doi.org/10.1038/nature14539.

[85] Raia Hadsell et al. "Learning long-range vision for autonomous off-road driving". In: *Journal of Field Robotics* 26.2 (2009), pp. 120–144. ISSN: 1556-4967. DOI: 10.1002/rob.20276.

[86] Clément Farabet et al. "Scene Parsing with Multiscale Feature Learning, Purity Trees, and Optimal Covers". In: *CoRR* abs/1202.2160 (2012). arXiv: 1202.2160.

[87] Oriol Vinyals et al. "Show and Tell: A Neural Image Caption Generator". In: *CoRR* abs/1411.4555 (2014). arXiv: 1411.4555.

[88] Ali Farhadi et al. "Every Picture Tells a Story: Generating Sentences from Images". In: *Computer Vision – ECCV 2010*. Ed. by Kostas Daniilidis, Petros Maragos, and Nikos Paragios. Berlin, Heidelberg: Springer Berlin Heidelberg, 2010, pp. 15–29. ISBN: 978-3-642-15561-1. URL: https://www.cs.cmu.edu/~afarhadi/papers/sentence.pdf.

[89] Y. Taigman et al. "DeepFace: Closing the Gap to Human-Level Performance in Face Verification". In: *2014 IEEE Conference on Computer Vision and Pattern Recognition*. 2014, pp. 1701–1708. DOI: 10.1109/CVPR.2014.220.

[90] Kaiming He et al. "Delving Deep into Rectifiers: Surpassing Human-Level Performance on ImageNet Classification". In: *CoRR* abs/1502.01852 (2015). arXiv: 1502.01852.

[91] Josh Cogan et al. "Jet-Images: Computer Vision Inspired Techniques for Jet Tagging". In: *JHEP* 02 (2015), p. 118. DOI: 10.1007/JHEP02(2015)118. arXiv: 1407.5675 [hep-ph].

[92] Leandro G. Almeida et al. "Playing Tag with ANN: Boosted Top Identification with Pattern Recognition". In: *JHEP* 07 (2015), p. 086. DOI: 10.1007/JHEP07(2015)086. arXiv: 1501.05968 [hep-ph].

[93] Luke de Oliveira et al. "Jet-images ? deep learning edition". In: *JHEP* 07 (2016), p. 069. DOI: 10.1007/JHEP07(2016)069. arXiv: 1511.05190 [hep-ph].

[94] Pierre Baldi et al. "Jet Substructure Classification in High-Energy Physics with Deep Neural Networks". In: *Phys. Rev.* D93.9 (2016), p. 094034. DOI: 10.1103/PhysRevD.93.094034. arXiv: 1603.09349 [hep-ex].

[95] Patrick T. Komiske, Eric M. Metodiev, and Matthew D. Schwartz. "Deep learning in color: towards automated quark/gluon jet discrimination". In: *JHEP* 01 (2017), p. 110. DOI: 10.1007/JHEP01(2017)110. arXiv: 1612.01551 [hep-ph].

[96] Gregor Kasieczka et al. "Deep-learning Top Taggers or The End of QCD?" In: *JHEP* 05 (2017), p. 006. DOI: 10.1007/JHEP05(2017)006. arXiv: 1701.08784 [hep-ph].

[97] Andrew J. Larkoski et al. "Soft Drop". In: *JHEP* 05 (2014), p. 146. DOI: 10.1007/JHEP05(2014)146. arXiv: 1402.2657 [hep-ph].

[98] Tilman Plehn, Gavin P. Salam, and Michael Spannowsky. "Fat Jets for a Light Higgs". In: *Phys. Rev. Lett.* 104 (2010), p. 111801. DOI: 10.1103/PhysRevLett.104.111801. arXiv: 0910.5472 [hep-ph].

[99] Tilman Plehn et al. "Stop Reconstruction with Tagged Tops". In: *JHEP* 10 (2010), p. 078. DOI: 10.1007/JHEP10(2010)078. arXiv: 1006.2833 [hep-ph].

[100] Gregor Kasieczka et al. "Resonance Searches with an Updated Top Tagger". In: *JHEP* 06 (2015), p. 203. DOI: 10.1007/JHEP06(2015)203. arXiv: 1503.05921 [hep-ph].

[101] Jesse Thaler and Ken Van Tilburg. "Identifying Boosted Objects with N-subjettiness". In: *JHEP* 03 (2011), p. 015. DOI: 10.1007/JHEP03(2011)015. arXiv: 1011.2268 [hep-ph].

[102] *Top Tagging with New Approaches*. Tech. rep. CMS-PAS-JME-15-002. URL: https://cds.cern.ch/record/2126325/files/JME-15-002-pas.pdf.

[103] *Performance of Top Quark and W Boson Tagging in Run 2 with ATLAS*. Tech. rep. ATLAS-CONF-2017-064. URL: https://cds.cern.ch/record/2281054.

[104] ATLAS. *Identification of Hadronically-Decaying W Bosons and Top Quarks Using High-Level Features as Input to Boosted Decision Trees and Deep Neural Networks in ATLAS at $\sqrt{s}$ = 13 TeV*. Tech. rep. ATL-PHYS-PUB-2017-004. URL: https://cds.cern.ch/record/2259646.

[105] Gilles Louppe et al. "QCD-Aware Recursive Neural Networks for Jet Physics". In: (2017). arXiv: 1702.00748 [hep-ph].

[106] Jannicke Pearkes et al. "Jet Constituents for Deep Neural Network Based Top Quark Tagging". In: (2017). arXiv: 1704.02124 [hep-ex].

[107] Anja Butter et al. "Deep-learned Top Tagging with a Lorentz Layer". In: (2017). arXiv: 1707.08966 [hep-ph].

[108] Shannon Egan et al. "Long Short-Term Memory (LSTM) networks with jet constituents for boosted top tagging at the LHC". In: (2017). arXiv: 1711.09059 [hep-ex].

[109] Torbjrn Sjstrand et al. "An Introduction to PYTHIA 8.2". In: *Comput. Phys. Commun.* 191 (2015), pp. 159–177. DOI: 10.1016/j.cpc.2015.01.024. arXiv: 1410.3012 [hep-ph].

[110] J. de Favereau et al. "DELPHES 3, A modular framework for fast simulation of a generic collider experiment". In: *JHEP* 02 (2014), p. 057. DOI: 10.1007/JHEP02(2014)057. arXiv: 1307.6346 [hep-ex].

[111] Matteo Cacciari, Gavin P. Salam, and Gregory Soyez. "FastJet User Manual". In: *Eur. Phys. J.* C72 (2012), p. 1896. DOI: 10.1140/epjc/s10052-012-1896-2. arXiv: 1111.6097 [hep-ph].

[112] Andreas Hocker et al. "TMVA - Toolkit for Multivariate Data Analysis". In: *PoS* ACAT (2007), p. 040. arXiv: physics/0703039 [PHYSICS].

[113] T. Schaul, S. Zhang, and Y. LeCun. "No More Pesky Learning Rates". In: *ArXiv e-prints* (June 2012). arXiv: 1206.1106 [stat.ML].

[114] Matthew D. Zeiler. "ADADELTA: An Adaptive Learning Rate Method". In: *CoRR* abs/1212.5701 (2012). arXiv: 1212.5701.

[115] Diederik P. Kingma and Jimmy Ba. "Adam: A Method for Stochastic Optimization". In: *CoRR* abs/1412.6980 (2014). arXiv: 1412.6980.

[116] François Chollet et al. "Keras: Deep Learning library for Python - Convnets, recurrent neural networks, and more." In: (2015). URL: http://github.com/fchollet/keras.

[117] Martín Abadi et al. *TensorFlow: Large-Scale Machine Learning on Heterogeneous Systems*. Software available from tensorflow.org. 2015. URL: http://tensorflow.org/.

[118] Corinna Cortes et al. *Learning Curves: Asymptotic Values and Rate of Convergence,Advances in Neural Information Processing Systems 6*. http://papers.nips.cc/paper/803-learning-curves-asymptotic-values-and-rate-of-convergence.pdf. Morgan-Kaufmann, 1994.

[119] *Status of b-tagging and vertexing tools for 2011 data analysis*. Tech. rep. CMS-PAS-BTV-11-002. URL: https://cds.cern.ch/record/1395489.

[120] Andrea Rizzi, Fabrizio Palla, and Gabriele Segneri. *Track impact parameter based b-tagging with CMS*. Tech. rep. CMS-NOTE-2006-019. URL: https://cds.cern.ch/record/927385.

[121] M. Bahr et al. "Herwig++ Physics and Manual". In: *Eur. Phys. J.* C58 (2008), pp. 639–707. DOI: 10.1140/epjc/s10052-008-0798-9. arXiv: 0803.0883 [hep-ph].

[122] Johannes Bellm et al. "Herwig 7.0/Herwig++ 3.0 release note". In: *Eur. Phys. J.* C76.4 (2016), p. 196. DOI: 10.1140/epjc/s10052-016-4018-8. arXiv: 1512.01178 [hep-ph].

[123] A. Krizhevsky, I. Sutskever, and G. E. Hinton. "ImageNet Classification with Deep Convolutional Neural Networks". In: ().

[124] Ross B. Girshick. "Fast R-CNN". In: *CoRR* abs/1504.08083 (2015). arXiv: 1504.08083.

[125] Karen Simonyan and Andrew Zisserman. "Very Deep Convolutional Networks for Large-Scale Image Recognition". In: *CoRR* abs/1409.1556 (2014). arXiv: 1409.1556.

[126] Kaiming He et al. "Deep Residual Learning for Image Recognition". In: *CoRR* abs/1512.03385 (2015). arXiv: 1512.03385.

[127] Christian Szegedy et al. "Going Deeper with Convolutions". In: *CoRR* abs/1409.4842 (2014). arXiv: 1409.4842.

[128] I. J. Goodfellow et al. "Generative Adversarial Networks". In: *ArXiv e-prints* (June 2014). arXiv: 1406.2661 [stat.ML].

[129] Michela Paganini, Luke de Oliveira, and Benjamin Nachman. "CaloGAN: Simulating 3D High Energy Particle Showers in Multi-Layer Electromagnetic Calorimeters with Generative Adversarial Networks". In: (2017). arXiv: 1712.10321 [hep-ex].

[130] Luke de Oliveira, Michela Paganini, and Benjamin Nachman. "Controlling Physical Attributes in GAN-Accelerated Simulation of Electromagnetic Calorimeters". In: *18th International Workshop on Advanced Computing and Analysis Techniques in Physics Research (ACAT 2017) Seattle, WA, USA, August 21-25, 2017*. 2017. arXiv: 1711.08813 [hep-ex].

[131] Michela Paganini, Luke de Oliveira, and Benjamin Nachman. "Accelerating Science with Generative Adversarial Networks: An Application to 3D Particle Showers in Multi-Layer Calorimeters". In: (2017). arXiv: 1705.02355 [hep-ex].

[132] Luke de Oliveira, Michela Paganini, and Benjamin Nachman. "Learning Particle Physics by Example: Location-Aware Generative Adversarial Networks for Physics Synthesis". In: *Comput. Softw. Big Sci.* 1.1 (2017), p. 4. DOI: 10.1007/s41781-017-0004-6. arXiv: 1701.05927 [stat.ML].

[133] S. Agostinelli et al. "GEANT4: A Simulation toolkit". In: *Nucl. Instrum. Meth.* A506 (2003), pp. 250–303. DOI: 10.1016/S0168-9002(03)01368-8.

[134] Timothy Cohen, Marat Freytsis, and Bryan Ostdiek. "(Machine) Learning to Do More with Less". In: (2017). arXiv: 1706.09451 [hep-ph].

[135] Lucio Mwinmaarong Dery et al. "Weakly Supervised Classification in High Energy Physics". In: *JHEP* 05 (2017), p. 145. DOI: 10.1007/JHEP05(2017)145. arXiv: 1702.00414 [hep-ph].

[136] Eric M. Metodiev, Benjamin Nachman, and Jesse Thaler. "Classification without labels: Learning from mixed samples in high energy physics". In: *JHEP* 10 (2017), p. 174. DOI: 10.1007/JHEP10(2017)174. arXiv: 1708.02949 [hep-ph].

[137] Patrick T. Komiske et al. "Learning to Classify from Impure Samples". In: (2018). arXiv: 1801.10158 [hep-ph].

[138] Georges Aad et al. "Measurement of Spin Correlation in Top-Antitop Quark Events and Search for Top Squark Pair Production in pp Collisions at $\sqrt{s} = 8$ TeV Using the ATLAS Detector". In: *Phys.Rev.Lett.* 114.14 (2015), p. 142001. DOI: 10.1103/PhysRevLett.114.142001. arXiv: 1412.4742 [hep-ex].

[139] Georges Aad et al. "Search for Top Squark Pair Production in Final States with One Isolated Lepton, Jets, and Missing Transverse Momentum in $\sqrt{s}$ =8 TeV pp Collisions with the ATLAS Detector". In: *JHEP* 1411 (2014), p. 118. DOI: 10.1007/JHEP11(2014)118. arXiv: 1407.0583 [hep-ex].

[140] Georges Aad et al. "Search for Pair-Produced Third-Generation Squarks Decaying via Charm Quarks or in Compressed Supersymmetric Scenarios in pp Collisions at $\sqrt{s} = 8$ TeV with the ATLAS Detector". In: *Phys.Rev.* D90.5 (2014), p. 052008. DOI: 10.1103/PhysRevD.90.052008. arXiv: 1407.0608 [hep-ex].

[141] Georges Aad et al. "Measurement of the $t\bar{t}$ Production Cross-Section Using $e\mu$ Events with b-Tagged Jets in pp Collisions at $\sqrt{s} = 7$ and 8 TeV with the ATLAS Detector". In: *Eur.Phys.J.* C74.10 (2014), p. 3109. DOI: 10.1140/epjc/s10052-014-3109-7. arXiv: 1406.5375 [hep-ex].

[142] Georges Aad et al. "Search for Direct Pair Production of the Top Squark in All-Hadronic Final States in Proton-Proton Collisions at $\sqrt{s} = 8$ TeV with the ATLAS Detector". In: *JHEP* 1409 (2014), p. 015. DOI: 10.1007/JHEP09(2014)015. arXiv: 1406.1122 [hep-ex].

[143] Georges Aad et al. "Search for Direct Top-Squark Pair Production in Final States with Two Leptons in pp Collisions at $\sqrt{s} = 8$ TeV with the ATLAS Detector". In: *JHEP* 1406 (2014), p. 124. DOI: 10.1007/JHEP06(2014)124. arXiv: 1403.4853 [hep-ex].

[144] Georges Aad et al. "Search for Direct Top Squark Pair Production in Events with a Z Boson, b-Jets and Missing Transverse Momentum in $\sqrt{s} = 8$ TeV pp Collisions with the ATLAS Detector". In: *Eur.Phys.J.* C74.6 (2014), p. 2883. DOI: 10.1140/epjc/s10052-014-2883-6. arXiv: 1403.5222 [hep-ex].

[145] Georges Aad et al. "Search for Direct Third-Generation Squark Pair Production in Final States with Missing Transverse Momentum and Two b-Jets in $\sqrt{s} = 8$ TeV pp Collisions with the ATLAS Detector". In: *JHEP* 1310 (2013), p. 189. DOI: 10.1007/JHEP10(2013)189. arXiv: 1308.2631 [hep-ex].

[146] ATLAS collaboration. *A Search for $B - L$ R-Parity Violating Scalar Top Decays in $\sqrt{s} = 8$ TeV pp Collisions with the ATLAS Experiment.* eprint: {ATLAS-CONF-2015-015}.

[147] CMS Collaboration. *Exclusion Limits on Gluino and Top-Squark Pair Production in Natural SUSY Scenarios with Inclusive Razor and Exclusive Single-Lepton Searches at $\sqrt{s} = 8$ TeV.* eprint: {CMS-PAS-SUS-14-011}.

[148] Vardan Khachatryan et al. "Searches for Third Generation Squark Production in Fully Hadronic Final States in Proton-Proton Collisions at $\sqrt{s} = 8$ TeV". In: (2015). arXiv: 1503.08037 [hep-ex].

[149] Vardan Khachatryan et al. "Search for Supersymmetry Using Razor Variables in Events with b-Tagged Jets in pp Collisions at $\sqrt{s} = 8$ TeV". In: *Phys.Rev.* D91 (2015), p. 052018. DOI: 10.1103/PhysRevD.91.052018. arXiv: 1502.00300 [hep-ex].

[150] Vardan Khachatryan et al. "Search for Top-Squark Pairs Decaying into Higgs or Z Bosons in pp Collisions at $\sqrt{s}$=8 TeV". In: *Phys.Lett.* B736 (2014), pp. 371–397. DOI: 10.1016/j.physletb.2014.07.053. arXiv: 1405.3886 [hep-ex].

[151] Serguei Chatrchyan et al. "Search for Top-Squark Pair Production in the Single-Lepton Final State in pp Collisions at $\sqrt{s} = 8$ TeV". In: *Eur.Phys.J.* C73.12 (2013), p. 2677. DOI: 10.1140/epjc/s10052-013-2677-2. arXiv: 1308.1586 [hep-ex].

[152] Serguei Chatrchyan et al. "Search for Top Squark and Higgsino Production Using Diphoton Higgs Boson Decays". In: *Phys.Rev.Lett.* 112 (2014), p. 161802. DOI: 10.1103/PhysRevLett.112.161802. arXiv: 1312.3310 [hep-ex].

[153] CMS Collaboration. *Search for Top Squarks Decaying to a Charm Quark and a Neutralino in Events with a Jet and Missing Transverse Momentum.* eprint: {CMS-PAS-SUS-13-009}.

[154] Vardan Khachatryan et al. "Search for Pair-Produced Resonances Decaying to Jet Pairs in Proton-Proton Collisions at $\sqrt{s} = 8$ TeV". In: *Phys.Lett.* B747 (2015), p. 98. DOI: 10.1016/j.physletb.2015.04.045. arXiv: 1412.7706 [hep-ex].

[155] https://twiki.cern.ch/twiki/bin/view/AtlasPublic/SupersymmetryPublicResults.

[156] https://twiki.cern.ch/twiki/bin/view/CMSPublic/PhysicsResultsSUS.

[157] Zhenyu Han et al. "(Light) Stop Signs". In: *JHEP* 1208 (2012), p. 083. DOI: 10.1007/JHEP08(2012)083. arXiv: 1205.5808 [hep-ph].

[158] Michal Czakon et al. "Closing the Stop Gap". In: *Phys.Rev.Lett.* 113.20 (2014), p. 201803. DOI: 10.1103/PhysRevLett.113.201803. arXiv: 1407.1043 [hep-ph].

[159] Till Eifert and Benjamin Nachman. "Sneaky Light Stop". In: *Phys. Lett.* B743 (2015), pp. 218–223. DOI: 10.1016/j.physletb.2015.02.039. arXiv: 1410.7025 [hep-ph].

[160] Brian Batell and Sunghoon Jung. "Probing Light Stops with Stoponium". In: (2015). arXiv: 1504.01740 [hep-ph].

[161] Nilanjana Kumar and Stephen P. Martin. "LHC Search for Di-Higgs Decays of Stoponium and Other Scalars in Events with Two Photons and Two Bottom Jets". In: *Phys.Rev.* D90.5 (2014), p. 055007. DOI: 10.1103/PhysRevD.90.055007. arXiv: 1404.0996 [hep-ph].

[162] Chul Kim et al. "Production of Stoponium at the LHC". In: *Phys.Rev.* D89.7 (2014), p. 075010. DOI: 10.1103/PhysRevD.89.075010. arXiv: 1401.1284 [hep-ph].

[163] Daniele S.M. Alves et al. "Stops and $\not{E}_T$: The Shape of Things to Come". In: *Phys.Rev.* D87.3 (2013), p. 035016. DOI: 10.1103/PhysRevD.87.035016. arXiv: 1205.5805 [hep-ph].

[164] Ahmed Ismail et al. "Deconstructed Transverse Mass Variables". In: *Phys. Rev.* D91.7 (2015), p. 074002. DOI: 10.1103/PhysRevD.91.074002. arXiv: 1409.2868 [hep-ph].

[165] Can Kilic and Brock Tweedie. "Cornering Light Stops with Dileptonic m_{T2}". In: *JHEP* 1304 (2013), p. 110. DOI: 10.1007/JHEP04(2013)110. arXiv: 1211.6106 [hep-ph].

[166] Yevgeny Kats et al. "The Status of GMSB After 1/fb at the LHC". In: *JHEP* 1202 (2012), p. 115. DOI: 10.1007/JHEP02(2012)115. arXiv: 1110.6444 [hep-ph].

[167] Won Sang Cho et al. "Improving the Sensitivity of Stop Searches with On-Shell Constrained Invariant Mass Variables". In: *JHEP* 05 (2015), p. 040. DOI: 10.1007/JHEP05(2015)040. arXiv: 1411.0664 [hep-ph].

[168] Bhaskar Dutta et al. "Probing Compressed Top Squark Scenarios at the LHC at 14 TeV". In: *Phys.Rev.* D90.9 (2014), p. 095022. DOI: 10.1103/PhysRevD.90.095022. arXiv: 1312.1348 [hep-ph].

[169] Matthew R. Buckley, Tilman Plehn, and Michael J. Ramsey-Musolf. "Top Squark with Mass Close to the Top Quark". In: *Phys.Rev.* D90.1 (2014), p. 014046. DOI: 10.1103/PhysRevD.90.014046. arXiv: 1403.2726 [hep-ph].

[170] Kaoru Hagiwara and Toshifumi Yamada. "Equal-Velocity Scenario for Hiding Dark Matter at the LHC". In: *Phys.Rev.* D91.9 (2015), p. 094007. DOI: 10.1103/PhysRevD.91.094007. arXiv: 1307.1553 [hep-ph].

[171] Matteo Cacciari, Gavin P. Salam, and Gregory Soyez. "The Anti-k(t) jet clustering algorithm". In: *JHEP* 04 (2008), p. 063. DOI: 10.1088/1126-6708/2008/04/063. arXiv: 0802.1189 [hep-ph].

[172] Matteo Cacciari and Gavin P. Salam. "Dispelling the N^3 Myth for the k_t Jet-Finder". In: *Phys. Lett.* B641 (2006), pp. 57–61. DOI: 10.1016/j.physletb.2006.08.037. arXiv: hep-ph/0512210.

[173] Jacob Anderson et al. "Snowmass Energy Frontier Simulations". In: (2013). arXiv: 1309.1057 [hep-ex].

[174] ATLAS collaboration. *Performance Assumptions for an Upgraded ATLAS Detector at a High-Luminosity LHC*. eprint: {ATLAS-PHYS-PUB-2013-004}.

[175] ATLAS collaboration. *Tagging and Suppression of Pileup Jets with the ATLAS Detector*. eprint: {ATLAS-CONF-2014-018}.

[176] ATLAS collaboration. *Search for the $b\bar{b}$ Decay of the Standard Model Higgs Boson in Associated $(W/Z)H$ Production with the ATLAS Detector*. eprint: {ATLAS-CONF-2013-079}.

[177] Timothy Cohen et al. "Boosting Stop Searches with a 100 TeV Proton Collider". In: *JHEP* 1411 (2014), p. 021. DOI: 10.1007/JHEP11(2014)021. arXiv: 1406.4512 [hep-ph].

[178] Hsin-Chia Cheng, Ian Low, and Lian-Tao Wang. "Top Partners in Little Higgs Theories with T-Parity". In: *Phys.Rev.* D74 (2006), p. 055001. DOI: 10.1103/PhysRevD.74.055001. arXiv: hep-ph/0510225 [hep-ph].

[179] Haipeng An and Lian-Tao Wang. "Opening Up the Compressed Region of Stop Searches at 13 TeV LHC". In: (2015). arXiv: 1506.00653 [hep-ph].

[180] URL: https://indico.cern.ch/event/432527/.

[181] URL: https://twiki.cern.ch/twiki/bin/view/AtlasPublic.

[182] http://cms-results.web.cern.ch/cms-results/public-results/publications/.

[183] Jonathan L. Feng. "Naturalness and the Status of Supersymmetry". In: *Ann. Rev. Nucl. Part. Sci.* 63 (2013), pp. 351–382. DOI: 10.1146/annurev-nucl-102010-130447. arXiv: 1302.6587 [hep-ph].

[184] S. Dimopoulos and G. F. Giudice. "Naturalness constraints in supersymmetric theories with nonuniversal soft terms". In: *Phys. Lett.* B357 (1995), pp. 573–578. DOI: 10.1016/0370-2693(95)00961-J. arXiv: hep-ph/9507282 [hep-ph].

[185] Andrew G. Cohen, D. B. Kaplan, and A. E. Nelson. "The More minimal supersymmetric standard model". In: *Phys. Lett.* B388 (1996), pp. 588–598. DOI: 10.1016/S0370-2693(96)01183-5. arXiv: hep-ph/9607394 [hep-ph].

[186] Jared A. Evans et al. "Toward Full LHC Coverage of Natural Supersymmetry". In: *JHEP* 07 (2014), p. 101. DOI: 10.1007/JHEP07(2014)101. arXiv: 1310.5758 [hep-ph].

[187] Kamila Kowalska. "Phenomenological MSSM in light of new 13 TeV LHC data". In: (2016). arXiv: 1608.02489 [hep-ph].

[188] Chengcheng Han et al. "Top-squark in natural SUSY under current LHC run-2 data". In: (2016). arXiv: 1609.02361 [hep-ph].

[189] J. Alberto Casas et al. "What is a Natural SUSY scenario?" In: *JHEP* 06 (2015), p. 070. DOI: 10.1007/JHEP06(2015)070. arXiv: 1407.6966 [hep-ph].

[190] R. Barbier et al. "R-Parity violating supersymmetry". In: *Phys. Rept.* 420 (2005), pp. 1–202. DOI: 10.1016/j.physrep.2005.08.006. arXiv: hep-ph/0406039 [hep-ph].

[191] Matthew J. Strassler. "Possible effects of a hidden valley on supersymmetric phenomenology". In: (2006). arXiv: hep-ph/0607160 [hep-ph].

[192] Matthew J. Strassler and Kathryn M. Zurek. "Echoes of a hidden valley at hadron colliders". In: *Phys. Lett.* B651 (2007), pp. 374–379. DOI: 10.1016/j.physletb.2007.06.055. arXiv: hep-ph/0604261 [hep-ph].

[193] JiJi Fan, Matthew Reece, and Joshua T. Ruderman. "Stealth Supersymmetry". In: *JHEP* 11 (2011), p. 012. DOI: 10.1007/JHEP11(2011)012. arXiv: 1105.5135 [hep-ph].

[194] JiJi Fan, Matthew Reece, and Joshua T. Ruderman. "A Stealth Supersymmetry Sampler". In: *JHEP* 07 (2012), p. 196. DOI: 10.1007/JHEP07(2012)196. arXiv: 1201.4875 [hep-ph].

[195] Ryuichiro Kitano and Yasunori Nomura. "Supersymmetry, naturalness, and signatures at the LHC". In: *Phys. Rev.* D73 (2006), p. 095004. DOI: 10.1103/PhysRevD.73.095004. arXiv: hep-ph/0602096 [hep-ph].

[196] Rouven Essig and Jean-Francois Fortin. "The Minimally Tuned Minimal Supersymmetric Standard Model". In: *JHEP* 04 (2008), p. 073. DOI: 10.1088/1126-6708/2008/04/073. arXiv: 0709.0980 [hep-ph].

[197] Asimina Arvanitaki et al. "The Last Vestiges of Naturalness". In: *JHEP* 03 (2014), p. 022. DOI: 10.1007/JHEP03(2014)022. arXiv: 1309.3568 [hep-ph].

[198] Michele Papucci, Joshua T. Ruderman, and Andreas Weiler. "Natural SUSY Endures". In: *JHEP* 09 (2012), p. 035. DOI: 10.1007/JHEP09(2012)035. arXiv: 1110.6926 [hep-ph].

[199] Z. Chacko, Hock-Seng Goh, and Roni Harnik. "The Twin Higgs: Natural electroweak breaking from mirror symmetry". In: *Phys. Rev. Lett.* 96 (2006), p. 231802. DOI: 10.1103/PhysRevLett.96.231802. arXiv: hep-ph/0506256 [hep-ph].

[200] Gustavo Burdman et al. "Colorless Top Partners, a 125 GeV Higgs, and the Limits on Naturalness". In: *Phys. Rev.* D91.5 (2015), p. 055007. DOI: 10.1103/PhysRevD.91.055007. arXiv: 1411.3310 [hep-ph].

[201] Brando Bellazzini, Csaba Cski, and Javi Serra. "Composite Higgses". In: *Eur. Phys. J.* C74.5 (2014), p. 2766. DOI: 10.1140/epjc/s10052-014-2766-x. arXiv: 1401.2457 [hep-ph].

[202] G. F. Giudice and R. Rattazzi. "Theories with gauge mediated supersymmetry breaking". In: *Phys. Rept.* 322 (1999), pp. 419–499. DOI: 10.1016/S0370-1573(99)00042-3. arXiv: hep-ph/9801271 [hep-ph].

[203] Kiwoon Choi, Kyuwan Hwang, and Jae Sik Lee. "Constraints on R-Parity and B violating couplings in gauge mediated supersymmetry breaking models". In: *Phys.Lett.* B428 (1998), pp. 129–135. DOI: 10.1016/S0370-2693(98)00371-2. arXiv: hep-ph/9802323 [hep-ph].

[204] G Salam and Andreas Weiler. URL: http://collider-reach.web.cern.ch/collider-reach/.

[205] "Further searches for squarks and gluinos in final states with jets and missing transverse momentum at $\sqrt{s}$ =13 TeV with the ATLAS detector". In: (2016). ATLAS-CONF-2016-078. URL: https://cds.cern.ch/record/2206252.

[206] "Pursuit of new phenomena in final states with high jet multiplicity, high jet masses and missing transverse momentum with ATLAS at $\sqrt{s}$ = 13 TeV". In: (2016). ATLAS-CONF-2016-095. URL: https://cds.cern.ch/record/2212161.

[207] "Search for pair production of gluinos decaying via top or bottom squarks in events with b-jets and large missing transverse momentum in pp collisions at $\sqrt{s}$ = 13 TeV with the ATLAS detector". In: (2016). ATLAS-CONF-2016-052. URL: https://cds.cern.ch/record/2206134.

[208] "Search for supersymmetry with two same-sign leptons or three leptons using 13.2 fb^1 of $\sqrt{s} = 13$ TeV pp collision data collected by the ATLAS detector". In: (2016). ATLAS-CONF-2016-037. URL: https://cds.cern.ch/record/2205745.

[209] "Search for massive supersymmetric particles in multi-jet final states produced in pp collisions at $\sqrt{s}$ = 13 TeV using the ATLAS detector at the LHC". In: (2016). ATLAS-CONF-2016-057. URL: https://cds.cern.ch/record/2206149.

[210] "Search for new physics in a lepton plus high jet multiplicity final state with the ATLAS experiment using sqrt(s) = 13 TeV proton-proton collision data". In: (2016). ATLAS-CONF-2016-094. URL: https://cds.cern.ch/record/2211457.

[211] Jared A. Evans. "Flavors of Supersymmetry Beyond Vanilla". In: *Proceedings, 12th Conference on the Intersections of Particle and Nuclear Physics (CIPANP 2015): Vail, Colorado, USA, May 19-24, 2015*. 2015. arXiv: 1509.08504 [hep-ph]. URL: http://inspirehep.net/record/1395266/files/arXiv:1509.08504.pdf.

[212] Zhen Liu and Brock Tweedie. "The Fate of Long-Lived Superparticles with Hadronic Decays after LHC Run 1". In: *JHEP* 06 (2015), p. 042. DOI: 10.1007/JHEP06(2015)042. arXiv: 1503.05923 [hep-ph].

[213] Csaba Csaki et al. "Phenomenology of a Long-Lived LSP with R-Parity Violation". In: *JHEP* 08 (2015), p. 016. DOI: 10.1007/JHEP08(2015)016. arXiv: 1505.00784 [hep-ph].

[214] Jared A. Evans and Jessie Shelton. "Long-Lived Staus and Displaced Leptons at the LHC". In: *JHEP* 04 (2016), p. 056. DOI: 10.1007/JHEP04(2016)056. arXiv: 1601.01326 [hep-ph].

[215] Peter W. Graham, Surjeet Rajendran, and Prashant Saraswat. "Supersymmetric crevices: Missing signatures of R -parity violation at the LHC". In: *Phys. Rev.* D90.7 (2014), p. 075005. DOI: 10.1103/PhysRevD.90.075005. arXiv: 1403.7197 [hep-ph].

[216] Christopher Brust et al. "Identifying boosted new physics with non-isolated leptons". In: *JHEP* 04 (2015), p. 079. DOI: 10.1007/JHEP04(2015)079. arXiv: 1410.0362 [hep-ph].

[217] Nima Arkani-Hamed and Neal Weiner. "LHC Signals for a SuperUnified Theory of Dark Matter". In: *JHEP* 12 (2008), p. 104. DOI: 10.1088/1126-6708/2008/12/104. arXiv: 0810.0714 [hep-ph].

[218] Matthew Baumgart et al. "Non-Abelian Dark Sectors and Their Collider Signatures". In: *JHEP* 04 (2009), p. 014. DOI: 10.1088/1126-6708/2009/04/014. arXiv: 0901.0283 [hep-ph].

[219] Clifford Cheung et al. "Lepton Jets in (Supersymmetric) Electroweak Processes". In: *JHEP* 04 (2010), p. 116. DOI: 10.1007/JHEP04(2010)116. arXiv: 0909.0290 [hep-ph].

[220] Nima Arkani-Hamed, Markus A. Luty, and John Terning. "Composite quarks and leptons from dynamical supersymmetry breaking without messengers". In: *Phys. Rev.* D58 (1998), p. 015004. DOI: 10.1103/PhysRevD.58.015004. arXiv: hep-ph/9712389 [hep-ph].

[221] Maxime Gabella, Tony Gherghetta, and Joel Giedt. "A Gravity dual and LHC study of single-sector supersymmetry breaking". In: *Phys. Rev.* D76 (2007), p. 055001. DOI: 10.1103/PhysRevD.76.055001. arXiv: 0704.3571 [hep-ph].

[222] Ofer Aharony et al. "Inverted Sparticle Hierarchies from Natural Particle Hierarchies". In: *Phys. Rev.* D81 (2010), p. 085006. DOI: 10.1103/PhysRevD.81.085006. arXiv: 1001.0637 [hep-ph].

[223] Nathaniel Craig, Daniel Green, and Andrey Katz. "(De)Constructing a Natural and Flavorful Supersymmetric Standard Model". In: *JHEP* 07 (2011), p. 045. DOI: 10.1007/JHEP07(2011)045. arXiv: 1103.3708 [hep-ph].

[224] Edward Hardy and John March-Russell. "Retrofitted Natural Supersymmetry from a U(1)". In: *JHEP* 05 (2013), p. 120. DOI: 10.1007/JHEP05(2013)120. arXiv: 1302.5423 [hep-ph].

[225] Georges Aad et al. "Search for new phenomena in final states with large jet multiplicities and missing transverse momentum with ATLAS using $\sqrt{s} = 13$ TeV proton-proton collisions". In: *Phys. Lett.* B757 (2016), pp. 334–355. DOI: 10.1016/j.physletb.2016.04.005. arXiv: 1602.06194 [hep-ex].

[226] "Search for Black Holes with Early Run 2 Data". In: (2015). CMS-PAS-EXO-15-007. URL: https://cds.cern.ch/record/2116453.

[227] Vardan Khachatryan et al. "Search for new physics in events with high jet multiplicity and low missing transverse momentum in proton-proton collisions at $\sqrt{s} = 8$ TeV". In: *Submitted to: Phys. Lett.* (2016). arXiv: 1608.01224 [hep-ex].

[228] "Search for supersymmetry in events with jets and missing transverse momentum in proton-proton collisions at 13 TeV". In: (2016). CMS-PAS-SUS-16-014. URL: https://cds.cern.ch/record/2205158.

[229] "Search for squarks and gluinos in events with an isolated lepton, jets and missing transverse momentum at $\sqrt{s} = 13$ TeV with the ATLAS detector". In: (2016). ATLAS-CONF-2016-054. URL: https://cds.cern.ch/record/2206136.

[230] " An inclusive search for new phenomena in final states with one or more jets and missing transverse momentum at $\sqrt{s} = 13$ TeV with the α_T variable". In: (2016). CMS-PAS-SUS-16-016. URL: https://cds.cern.ch/record/2205163.

[231] "Search for new physics in the all-hadronic final state with the MT2 variable". In: (2016). CMS-PAS-SUS-16-015. URL: https://cds.cern.ch/record/2205162.

[232] J. Alwall et al. "The automated computation of tree-level and next-to-leading order differential cross sections, and their matching to parton shower simulations". In: *JHEP* 07 (2014), p. 079. DOI: 10.1007/JHEP07(2014)079. arXiv: 1405.0301 [hep-ph].

[233] W. Beenakker, R. Hopker, and M. Spira. "PROSPINO: A Program for the production of supersymmetric particles in next-to-leading order QCD". In: (1996). arXiv: hep-ph/9611232 [hep-ph].

[234] W. Beenakker et al. "Squark and gluino production at hadron colliders". In: *Nucl. Phys.* B492 (1997), pp. 51–103. DOI: 10.1016/S0550-3213(97)80027-2. arXiv: hep-ph/9610490 [hep-ph].

[235] W. Beenakker et al. "Stop production at hadron colliders". In: *Nucl. Phys.* B515 (1998), pp. 3–14. DOI: 10.1016/S0550-3213(98)00014-5. arXiv: hep-ph/9710451 [hep-ph].

[236] Rene Brun and Fons Rademakers. *ROOT - An Object Oriented Data Analysis Framework*. Proceedings AIHENP'96 Workshop, Lausanne, Sep. 1996, Nucl. Inst. & Meth. in Phys. Res. A 389 (1997) 81-86. URL: http://root.cern.ch/.

[237] René Brun et al. "GEANT Detector Description and Simulation Tool". In: (1994).

[238] Savas Dimopoulos, Kiel Howe, and John March-Russell. "Maximally Natural Supersymmetry". In: *Phys. Rev. Lett.* 113 (2014), p. 111802. DOI: 10.1103/PhysRevLett.113.111802. arXiv: 1404.7554 [hep-ph].

[239] Stephen P. Martin. "Nonstandard supersymmetry breaking and Dirac gaugino masses without supersoftness". In: *Phys. Rev.* D92.3 (2015), p. 035004. DOI: 10.1103/PhysRevD.92.035004. arXiv: 1506.02105 [hep-ph].

[240] Timothy Cohen, John Kearney, and Markus Luty. "Natural Supersymmetry without Light Higgsinos". In: *Phys. Rev.* D91 (2015), p. 075004. DOI: 10.1103/PhysRevD.91.075004. arXiv: 1501.01962 [hep-ph].

[241] Isabel Garcia Garcia, Kiel Howe, and John March-Russell. "Natural Scherk-Schwarz Theories of the Weak Scale". In: *JHEP* 12 (2015), p. 005. DOI: 10.1007/JHEP12(2015)005. arXiv: 1510.07045 [hep-ph].

[242] Antonio Delgado et al. "Natural Supersymmetry from Extra Dimensions". In: *Phys. Rev.* D94 (2016), p. 095017. DOI: 10.1103/PhysRevD.94.095017. arXiv: 1608.06470 [hep-ph].

[243] A. Heister et al. "Search for charginos nearly mass degenerate with the lightest neutralino in e+ e- collisions at center-of-mass energies up to 209-GeV". In: *Phys. Lett.* B533 (2002), pp. 223–236. DOI: 10.1016/S0370-2693(02)01584-8. arXiv: hep-ex/0203020 [hep-ex].

[244] G. Abbiendi et al. "Search for nearly mass degenerate charginos and neutralinos at LEP". In: *Eur. Phys. J.* C29 (2003), pp. 479–489. DOI: 10.1140/epjc/s2003-01237-x. arXiv: hep-ex/0210043 [hep-ex].

[245] S. Costantini. "Search for R-Parity violation at LEP". In: *Nucl. Phys. Proc. Suppl.* 109B (2002), pp. 242–247. DOI: 10.1016/S0920-5632(02)90039-3.

[246] R. Barate et al. "Search for R-Parity violating decays of supersymmetric particles in e^+e^- collisions at center-of-mass energies from 189-GeV to 202-GeV". In: *Eur. Phys. J.* C19 (2001), pp. 415–428. DOI: 10.1007/s100520100633. arXiv: hep-ex/0011008 [hep-ex].

[247] "Search for new physics in the compressed mass spectra scenario using events with two soft opposite-sign leptons and missing momentum energy at 13 TeV". In: (2016). CMS-PAS-SUS-16-025. URL: https://cds.cern.ch/record/2205866.

[248] "Searches for Long-lived Charged Particles in Proton-Proton Collisions at $\sqrt{s} = 13$ TeV". In: (2015). CMS-PAS-EXO-15-010. URL: https://cds.cern.ch/record/2114818.

[249] "A search for pair produced resonances in four jets final states in proton-proton collisions at $\sqrt{s}$=13 TeV with the ATLAS experiment". In: (2016). ATLAS-CONF-2016-084. URL: https://cds.cern.ch/record/2206277.

[250] CMS Collaboration. "Search for low-mass pair-produced dijet resonances using jet substructure techniques in proton-proton collisions at a center-of-mass energy of $\sqrt{s} = 13$ TeV". In: (2016). CMS-PAS-EXO-16-029. URL: https://cds.cern.ch/record/2231062.

[251] Serguei Chatrchyan et al. "Searches for light- and heavy-flavour three-jet resonances in pp collisions at $\sqrt{s} = 8$ TeV". In: *Phys. Lett.* B730 (2014), pp. 193–214. DOI: 10.1016/j.physletb.2014.01.049. arXiv: 1311.1799 [hep-ex].

[252] Georges Aad et al. In: (). DOI: 10.1103/PhysRevD.91.112016. arXiv: 1502.05686.

[253] Emanuel Nikolidakis and Christopher Smith. "Minimal Flavor Violation, Seesaw, and R-Parity". In: *Phys.Rev.* D77 (2008), p. 015021. DOI: 10.1103/PhysRevD.77.015021. arXiv: 0710.3129 [hep-ph].

[254] Csaba Csaki, Yuval Grossman, and Ben Heidenreich. "MFV SUSY: A Natural Theory for R-Parity Violation". In: *Phys.Rev.* D85 (2012), p. 095009. DOI: 10.1103/PhysRevD.85.095009. arXiv: 1111.1239 [hep-ph].

[255] Angelo Monteux. "Natural, R-parity violating supersymmetry and horizontal flavor symmetries". In: *Phys. Rev. D 88,* 045029 (2013), p. 045029. DOI: 10.1103/PhysRevD.88.045029. arXiv: 1305.2921.

[256] Patrick Meade, Matthew Reece, and David Shih. "Prompt Decays of General Neutralino NLSPs at the Tevatron". In: *JHEP* 05 (2010), p. 105. DOI: 10.1007/JHEP05(2010)105. arXiv: 0911.4130 [hep-ph].

[257] Jared A. Evans and Yevgeny Kats. "LHC Coverage of RPV MSSM with Light Stops". In: *JHEP* 04 (2013), p. 028. DOI: 10.1007/JHEP04(2013)028. arXiv: 1209.0764 [hep-ph].

[258] https://twiki.cern.ch/twiki/pub/CMSPublic/PhysicsResultsSUS/T2tt_limits_summary_cms_ICHEP16.pdf.

[259] Michelangelo L. Mangano et al. "Matching matrix elements and shower evolution for top-quark production in hadronic collisions". In: *JHEP* 01 (2007), p. 013. DOI: 10.1088/1126-6708/2007/01/013. arXiv: hep-ph/0611129 [hep-ph].

[260] Johan Alwall et al. "Comparative study of various algorithms for the merging of parton showers and matrix elements in hadronic collisions". In: *Eur. Phys. J.* C53 (2008), pp. 473–500. DOI: 10.1140/epjc/s10052-007-0490-5. arXiv: 0706.2569 [hep-ph].

[261] Johan Alwall, Simon de Visscher, and Fabio Maltoni. "QCD radiation in the production of heavy colored particles at the LHC". In: *JHEP* 02 (2009), p. 017. DOI: 10.1088/1126-6708/2009/02/017. arXiv: 0810.5350 [hep-ph].

[262] Junji Hisano, Kiichi Kurosawa, and Yasunori Nomura. "Natural effective supersymmetry". In: *Nucl. Phys.* B584 (2000), pp. 3–45. DOI: 10.1016/S0550-3213(00)00343-6. arXiv: hep-ph/0002286 [hep-ph].

[263] Angelo Monteux. "New signatures and limits on R-parity violation from resonant squark production". In: *JHEP* 03 (2016), p. 216. DOI: 10.1007/JHEP03(2016)216. arXiv: 1601.03737 [hep-ph].

[264] Patrick J. Fox, Ann E. Nelson, and Neal Weiner. "Dirac gaugino masses and supersoft supersymmetry breaking". In: *JHEP* 08 (2002), p. 035. DOI: 10.1088/1126-6708/2002/08/035. arXiv: hep-ph/0206096 [hep-ph].

[265] Graham D. Kribs and Adam Martin. "Supersoft Supersymmetry is Super-Safe". In: *Phys. Rev.* D85 (2012), p. 115014. DOI: 10.1103/PhysRevD.85.115014. arXiv: 1203.4821 [hep-ph].

[266] JiJi Fan et al. "Stealth Supersymmetry Simplified". In: *JHEP* 07 (2016), p. 016. DOI: 10.1007/JHEP07(2016)016. arXiv: 1512.05781 [hep-ph].

[267] Rakhi Mahbubani and Leonardo Senatore. "The Minimal model for dark matter and unification". In: *Phys. Rev.* D73 (2006), p. 043510. DOI: 10.1103/PhysRevD.73.043510. arXiv: hep-ph/0510064 [hep-ph].

[268] Junji Hisano et al. "WIMP dark matter in gauge-mediated SUSY breaking models and its phenomenology". In: *Phys. Lett.* B691 (2010), pp. 46–55. DOI: 10.1016/j.physletb.2010.05.081. arXiv: 1003.3648 [hep-ph].

[269] Timothy Cohen et al. "Singlet-Doublet Dark Matter". In: *Phys. Rev.* D85 (2012), p. 075003. DOI: 10.1103/PhysRevD.85.075003. arXiv: 1109.2604 [hep-ph].

[270] Clifford Cheung and David Sanford. "Simplified Models of Mixed Dark Matter". In: *JCAP* 1402 (2014), p. 011. DOI: 10.1088/1475-7516/2014/02/011. arXiv: 1311.5896 [hep-ph].

[271] Tomohiro Abe, Ryuichiro Kitano, and Ryosuke Sato. "Discrimination of dark matter models in future experiments". In: *Phys. Rev.* D91.9 (2015), p. 095004. DOI: 10.1103/PhysRevD.91.095004. arXiv: 1411.1335 [hep-ph].

[272] Lorenzo Calibbi, Alberto Mariotti, and Pantelis Tziveloglou. "Singlet-Doublet Model: Dark matter searches and LHC constraints". In: *JHEP* 10 (2015), p. 116. DOI: 10.1007/JHEP10(2015)116. arXiv: 1505.03867 [hep-ph].

[273] Ayres Freitas, Susanne Westhoff, and Jure Zupan. "Integrating in the Higgs Portal to Fermion Dark Matter". In: *JHEP* 09 (2015), p. 015. DOI: 10.1007/JHEP09(2015)015. arXiv: 1506.04149 [hep-ph].

[274] Shankha Banerjee et al. "WIMP Dark Matter in a Well-Tempered Regime: A case study on Singlet-Doublets Fermionic WIMP". In: (2016). arXiv: 1603.07387 [hep-ph].

[275] Takeo Moroi and Yasuhiro Okada. "Radiative corrections to Higgs masses in the supersymmetric model with an extra family and antifamily". In: *Mod. Phys. Lett.* A7 (1992), pp. 187–200. DOI: 10.1142/S0217732392000124.

[276] Takeo Moroi and Yasuhiro Okada. "Upper bound of the lightest neutral Higgs mass in extended supersymmetric Standard Models". In: *Phys. Lett.* B295 (1992), pp. 73–78. DOI: 10.1016/0370-2693(92)90091-H.

[277] K. S. Babu, Ilia Gogoladze, and Christopher Kolda. "Perturbative unification and Higgs boson mass bounds". In: (2004). arXiv: hep-ph/0410085 [hep-ph].

[278] K. S. Babu et al. "Higgs Boson Mass, Sparticle Spectrum and Little Hierarchy Problem in Extended MSSM". In: *Phys. Rev.* D78 (2008), p. 055017. DOI: 10.1103/PhysRevD.78.055017. arXiv: 0807.3055 [hep-ph].

[279] Stephen P. Martin. "Extra vector-like matter and the lightest Higgs scalar boson mass in low-energy supersymmetry". In: *Phys. Rev.* D81 (2010), p. 035004. DOI: 10.1103/PhysRevD.81.035004. arXiv: 0910.2732 [hep-ph].

[280] Peter W. Graham et al. "A Little Solution to the Little Hierarchy Problem: A Vector-like Generation". In: *Phys. Rev.* D81 (2010), p. 055016. DOI: 10.1103/PhysRevD.81.055016. arXiv: 0910.3020 [hep-ph].

[281] Stephen P. Martin. "Raising the Higgs mass with Yukawa couplings for isotriplets in vector-like extensions of minimal supersymmetry". In: *Phys. Rev.* D82 (2010), p. 055019. DOI: 10.1103/PhysRevD.82.055019. arXiv: 1006.4186 [hep-ph].

[282] Stephen P. Martin. "Quirks in supersymmetry with gauge coupling unification". In: *Phys. Rev.* D83 (2011), p. 035019. DOI: 10.1103/PhysRevD.83.035019. arXiv: 1012.2072 [hep-ph].

[283] Masaki Asano et al. "Non-anomalous Discrete R-symmetry, Extra Matters, and Enhancement of the Lightest SUSY Higgs Mass". In: *Phys. Lett.* B705 (2011), pp. 337–341. DOI: 10.1016/j.physletb.2011.10.025. arXiv: 1108.2402 [hep-ph].

[284] Motoi Endo et al. "Higgs Mass and Muon Anomalous Magnetic Moment in Supersymmetric Models with Vector-Like Matters". In: *Phys. Rev.* D84 (2011), p. 075017. DOI: 10.1103/PhysRevD.84.075017. arXiv: 1108.3071 [hep-ph].

[285] Jason L. Evans, Masahiro Ibe, and Tsutomu T. Yanagida. "Probing Extra Matter in Gauge Mediation Through the Lightest Higgs Boson Mass". In: (2011). arXiv: 1108.3437 [hep-ph].

[286] Takeo Moroi, Ryosuke Sato, and Tsutomu T. Yanagida. "Extra Matters Decree the Relatively Heavy Higgs of Mass about 125 GeV in the Supersymmetric Model". In: *Phys. Lett.* B709 (2012), pp. 218–221. DOI: 10.1016/j.physletb.2012.02.012. arXiv: 1112.3142 [hep-ph].

[287] Motoi Endo et al. "Higgs mass, muon g-2, and LHC prospects in gauge mediation models with vector-like matters". In: *Phys. Rev.* D85 (2012), p. 095012. DOI: 10.1103/PhysRevD.85.095012. arXiv: 1112.5653 [hep-ph].

[288] Motoi Endo et al. "Vacuum Stability Bound on Extended GMSB Models". In: *JHEP* 06 (2012), p. 060. DOI: 10.1007/JHEP06(2012)060. arXiv: 1202.2751 [hep-ph].

[289] Stephen P. Martin and James D. Wells. "Implications of gauge-mediated supersymmetry breaking with vector-like quarks and a 125 GeV Higgs boson". In: *Phys. Rev.* D86 (2012), p. 035017. DOI: 10.1103/PhysRevD.86.035017. arXiv: 1206.2956 [hep-ph].

[290] Motoi Endo et al. "Gauge Mediation Models with Vectorlike Matters at the LHC". In: *JHEP* 01 (2013), p. 181. DOI: 10.1007/JHEP01(2013)181. arXiv: 1212.3935 [hep-ph].

[291] Sho Iwamoto. "Supersymmetry after the Higgs discovery and its LHC phenomenology". In: (2013). arXiv: 1305.0790 [hep-ph].

[292] Yuichiro Nakai, Matthew Reece, and Ryosuke Sato. "SUSY Higgs Mass and Collider Signals with a Hidden Valley". In: *JHEP* 03 (2016), p. 143. DOI: 10.1007/JHEP03(2016)143. arXiv: 1511.00691 [hep-ph].

[293] Mohammad Abdullah and Jonathan L. Feng. "Reviving bino dark matter with vectorlike fourth generation particles". In: *Phys. Rev.* D93.1 (2016), p. 015006. DOI: 10.1103/PhysRevD.93.015006. arXiv: 1510.06089 [hep-ph].

[294] Mohammad Abdullah et al. "Heavy Bino Dark Matter and Collider Signals in the MSSM with Vector-like 4th-Generation Particles". In: *Phys. Rev.* D94 (2016), p. 095018. DOI: 10.1103/PhysRevD.94.095018. arXiv: 1608.00283 [hep-ph].

[295] M. G. Aartsen et al. "Improved limits on dark matter annihilation in the Sun with the 79-string IceCube detector and implications for supersymmetry". In: *JCAP* 1604.04 (2016), p. 022. DOI: 10.1088/1475-7516/2016/04/022. arXiv: 1601.00653 [hep-ph].

[296] M. Ackermann et al. "Searching for Dark Matter Annihilation from Milky Way Dwarf Spheroidal Galaxies with Six Years of Fermi Large Area Telescope Data". In: *Phys. Rev. Lett.* 115.23 (2015), p. 231301. DOI: 10.1103/PhysRevLett.115.231301. arXiv: 1503.02641 [astro-ph.HE].

[297] Vardan Khachatryan et al. "Search for dark matter, extra dimensions, and unparticles in monojet events in proton?proton collisions at $\sqrt{s} = 8$ TeV". In: *Eur. Phys. J.* C75.5 (2015), p. 235. DOI: 10.1140/epjc/s10052-015-3451-4. arXiv: 1408.3583 [hep-ex].

[298] Georges Aad et al. "Search for new phenomena in final states with an energetic jet and large missing transverse momentum in pp collisions at $\sqrt{s}$ =8 TeV with the ATLAS detector". In: *Eur. Phys. J.* C75.7 (2015). [Erratum: Eur. Phys. J.C75,no.9,408(2015)], p. 299. DOI: 10.1140/epjc/s10052-015-3517-3,10.1140/epjc/s10052-015-3639-7. arXiv: 1502.01518 [hep-ex].

[299] Serguei Chatrchyan et al. "Search for Dark Matter and Large Extra Dimensions in pp Collisions Yielding a Photon and Missing Transverse Energy". In: *Phys. Rev. Lett.* 108 (2012), p. 261803. DOI: 10.1103/PhysRevLett.108.261803. arXiv: 1204.0821 [hep-ex].

[300] Georges Aad et al. "Search for dark matter candidates and large extra dimensions in events with a photon and missing transverse momentum in *pp* collision data at $\sqrt{s} = 7$ TeV with the ATLAS detector". In: *Phys. Rev. Lett.* 110.1 (2013), p. 011802. DOI: 10.1103/PhysRevLett.110.011802. arXiv: 1209.4625 [hep-ex].

[301] Florian Staub. "SARAH 4 : A tool for (not only SUSY) model builders". In: *Comput. Phys. Commun.* 185 (2014), pp. 1773–1790. DOI: 10.1016/j.cpc.2014.02.018. arXiv: 1309.7223 [hep-ph].

[302] Werner Porod. "SPheno, a program for calculating supersymmetric spectra, SUSY particle decays and SUSY particle production at e+ e- colliders". In: *Comput. Phys. Commun.* 153 (2003), pp. 275–315. DOI: 10.1016/S0010-4655(03)00222-4. arXiv: hep-ph/0301101 [hep-ph].

[303] W. Porod and F. Staub. "SPheno 3.1: Extensions including flavour, CP-phases and models beyond the MSSM". In: *Comput. Phys. Commun.* 183 (2012), pp. 2458–2469. DOI: 10.1016/j.cpc.2012.05.021. arXiv: 1104.1573 [hep-ph].

[304] G. Belanger et al. "micrOMEGAs4.1: two dark matter candidates". In: *Comput. Phys. Commun.* 192 (2015), pp. 322–329. DOI: 10.1016/j.cpc.2015.03.003. arXiv: 1407.6129 [hep-ph].

[305] Marco Cirelli, Eugenio Del Nobile, and Paolo Panci. "Tools for model-independent bounds in direct dark matter searches". In: *JCAP* 1310 (2013), p. 019. DOI: 10.1088/1475-7516/2013/10/019. arXiv: 1307.5955 [hep-ph].

[306] Andrea De Simone, Gian Francesco Giudice, and Alessandro Strumia. "Benchmarks for Dark Matter Searches at the LHC". In: *JHEP* 06 (2014), p. 081. DOI: 10.1007/JHEP06(2014)081. arXiv: 1402.6287 [hep-ph].

[307] John F. Gunion et al. "The Higgs Hunter's Guide". In: *Front. Phys.* 80 (2000), pp. 1–448.

[308] Mark D. Goodsell, Kilian Nickel, and Florian Staub. "Two-Loop Higgs mass calculations in supersymmetric models beyond the MSSM with SARAH and SPheno". In: *Eur. Phys. J.* C75.1 (2015), p. 32. DOI: 10.1140/epjc/s10052-014-3247-y. arXiv: 1411.0675 [hep-ph].

[309] M. Goodsell, K. Nickel, and F. Staub. "Generic two-loop Higgs mass calculation from a diagrammatic approach". In: *Eur. Phys. J.* C75.6 (2015), p. 290. DOI: 10.1140/epjc/s10052-015-3494-6. arXiv: 1503.03098 [hep-ph].

[310] Ryuichiro Kitano and Yasunori Nomura. "A Solution to the supersymmetric fine-tuning problem within the MSSM". In: *Phys. Lett.* B631 (2005), pp. 58–67. DOI: 10.1016/j.physletb.2005.10.003. arXiv: hep-ph/0509039 [hep-ph].

[311] Ning Zhou, David Berge, and Daniel Whiteson. "Mono-everything: combined limits on dark matter production at colliders from multiple final states". In: *Phys. Rev.* D87.9 (2013), p. 095013. DOI: 10.1103/PhysRevD.87.095013. arXiv: 1302.3619 [hep-ex].

[312] Oliver Buchmueller et al. "Characterising dark matter searches at colliders and direct detection experiments: Vector mediators". In: *JHEP* 01 (2015), p. 037. DOI: 10.1007/JHEP01(2015)037. arXiv: 1407.8257 [hep-ph].

[313] Richard D. Ball et al. "Parton distributions with LHC data". In: *Nucl. Phys.* B867 (2013), pp. 244–289. DOI: 10.1016/j.nuclphysb.2012.10.003. arXiv: 1207.1303 [hep-ph].

[314] Ulrich Ellwanger, Cyril Hugonie, and Ana M. Teixeira. "The Next-to-Minimal Supersymmetric Standard Model". In: *Phys. Rept.* 496 (2010), pp. 1–77. DOI: 10.1016/j.physrep.2010.07.001. arXiv: 0910.1785 [hep-ph].

[315] Puneet Batra et al. "The Higgs mass bound in gauge extensions of the minimal supersymmetric standard model". In: *JHEP* 02 (2004), p. 043. DOI: 10.1088/1126-6708/2004/02/043. arXiv: hep-ph/0309149 [hep-ph].

[316] Alexander Maloney, Aaron Pierce, and Jay G. Wacker. "D-terms, unification, and the Higgs mass". In: *JHEP* 06 (2006), p. 034. DOI: 10.1088/1126-6708/2006/06/034. arXiv: hep-ph/0409127 [hep-ph].

[317] Torbjorn Sjostrand, Stephen Mrenna, and Peter Skands. "PYTHIA 6.4 Physics and Manual". In: *JHEP* 05 (2006), p. 026. arXiv: hep-ph/0603175.

[318] Michelangelo L. Mangano et al. "ALPGEN, A Generator for Hard Multiparton Processes in Hadronic Collisions". In: *JHEP* 0307 (2003), p. 001. arXiv: hep-ph/0206293 [hep-ph].

[319] S. Catani et al. "Longitudinally invariant K_t clustering algorithms for hadron hadron collisions". In: *Nucl. Phys.* B406 (1993), pp. 187–224. DOI: 10.1016/0550-3213(93)90166-M.

[320] Stephen D. Ellis and Davison E. Soper. "Successive combination jet algorithm for hadron collisions". In: *Phys. Rev.* D48 (1993), pp. 3160–3166. DOI: 10.1103/PhysRevD.48.3160. arXiv: hep-ph/9305266 [hep-ph].

[321] David Krohn, Jesse Thaler, and Lian-Tao Wang. "Jet Trimming". In: *JHEP* 02 (2010), p. 084. DOI: 10.1007/JHEP02(2010)084. arXiv: 0912.1342 [hep-ph].

[322] Benjamin Nachman et al. "Jets from Jets: Re-clustering as a tool for large radius jet reconstruction and grooming at the LHC". In: *JHEP* 02 (2015), p. 075. DOI: 10.1007/JHEP02(2015)075. arXiv: 1407.2922 [hep-ph].

[323] Paul Jackson, Christopher Rogan, and Marco Santoni. "Sparticles in Motion - getting to the line in compressed scenarios with the Recursive Jigsaw Reconstruction". In: (2016). arXiv: 1607.08307 [hep-ph].

[324] G. Belanger et al. "micrOMEGAs 3: A program for calculating dark matter observables". In: *Comput. Phys. Commun.* 185 (2014), pp. 960–985. DOI: 10.1016/j.cpc.2013.10.016. arXiv: 1305.0237 [hep-ph].